University of Southampton

# University of Southampton Research Repository

Copyright © and Moral Rights for this thesis and, where applicable, any accompanying data are retained by the author and/or other copyright owners. A copy can be downloaded for personal non-commercial research or study, without prior permission or charge. This thesis and the accompanying data cannot be reproduced or quoted extensively from without first obtaining permission in writing from the copyright holder/s. The content of the thesis and accompanying research data (where applicable) must not be changed in any way or sold commercially in any format or medium without the formal permission of the copyright holder/s.

When referring to this thesis and any accompanying data, full bibliographic details must be given, e.g.

Thesis: Hammed Olanrewaju Aminulai (2023) " Impact of Corrosion on Axial Load Bearing Capacity of Low-Strength Concrete Columns under Monotonic Compression and Cyclic Loading ", University of Southampton, Faculty of Engineering and Physical Sciences, Department of Civil, Maritime and Environmental Engineering, PhD Thesis.

University of Southampton

Faculty of Engineering and Physical Sciences (FEPS)

Civil, Maritime and Environmental Engineering (CMEE)

# Impact of Corrosion on Axial Load Bearing Capacity of Low-Strength Concrete Columns under Monotonic Compression and Cyclic Loading

By

**Hammed Olanrewaju Aminulai**

ORCID ID: 0000-0001-6185-5000

Thesis for the degree of Doctor of Philosophy in Engineering and the Environment

November 2023

# University of Southampton

## Abstract

Faculty of Engineering and Physical Sciences

Civil, Maritime and Environmental Engineering (CMEE)

Thesis for the doctor of Philosophy in Engineering and the Environment

**Impact of Corrosion on Axial Load Bearing Capacity of Low-Strength Concrete Columns under Monotonic Compression and Cyclic Loading**

by

Hammed Olanrewaju Aminulai

The durability of RC structures and bridges located in cold regions and marine environments is adversely affected by reinforcement corrosion, reducing the service lives, load-carrying capacities and seismic resistance. Several research studies have been undertaken to model the effect of corrosion on the behaviour of RC structures. However, many uncertainties exist due to problems in estimating the corrosion of the reinforcement within the concrete. This research thus explores the use of the X-ray CT scan technique to accurately estimate the volumetric mass loss resulting from the corrosion of a whole reinforcement cage embedded in RC columns and, at the same time, identify the location of pitting corrosion on the reinforcement bars. This will aid in the timely maintenance and retrofitting of degrading RC structures to prevent premature failure and collapse.

Furthermore, the impact of corrosion and reinforcement confinement on the nonlinear stress-strain responses of ageing low-strength confined corroded RC columns under axial monotonic and axial cyclic compressive loading was investigated experimentally. The corrosion of the RC columns were simulated in the laboratory using the constant current (2A) accelerated corrosion technique. The time to obtain the desired corrosion was estimated using Faraday's 2$^{nd}$ law of electrolysis. A total of 60 short RC columns with varying degrees of corrosion and three different confinement levels were tested during the investigations. Five different degrees of reinforcement corrosion (i.e., 0%, 5%, 10%, 20% and 30%) with three confinement ratios based on the transverse reinforcements' spacing are investigated under axial monotonic and axial cyclic compressive loads. The confinement ratios are assigned through the centre-to-centre spacing of the transverse reinforcement ($L$) and the diameter of the longitudinal reinforcement ($D$), known as the spacing-diameter, $L/D$ ratio. Hence, for the test, the three confinement ratios are high ($L/D$ = 5), medium ($L/D$ = 8) and low ($L/D$ = 13). The impact of corrosion and confinement on the inelastic buckling of the longitudinal reinforcements under loading was also investigated.

Corrosion of the reinforcement bars affects the effective confinement of the RC columns thereby reducing the ultimate strength of the columns. The strength of the highly confined reduced by about 38% at 30% mass loss while the mediumly and lowly confined reduced by about 39% and 70%, respectively. Hence, the better the confinement the less the impact of corrosion on the RC column and also the better the mechanical behaviour of the RC columns. Furthermore, circular columns have better load carrying capacity than the square columns as a result of the

uniform confinement of the transverse bar which provides a constant stress distribution of the concrete along the cross-section.

Finally, the numerical investigation was conducted on the confined corroded RC columns using the ABAQUS FEA software to validate the experimental results obtained from both axial and cyclic compressive loading. The numerical investigation accurately predicted the stress-strain response of the confined corroded RC columns under axial compressive monotonic loading. Furthermore, the location of the buckling of the longitudinal bars under load is clearly identified. This will aid in the parametric studies to develop constitutive models for low-strength concrete confined corroded RC columns.

# Table of Contents

# Table of Tables

Table of Tables

# Table of Figures

Table of Figures

Table of Figures

Table of Figures

# Research Thesis: Declaration of Authorship

Print name: **Hammed Olanrewaju Aminulai**

Title of thesis: **Impact of Corrosion on Axial Load Bearing Capacity of Low-Strength Concrete Columns under Monotonic Compression and Cyclic Loading**

I declare that this thesis and the work presented in it are my own and has been generated by me as the result of my own original research.

I confirm that:

1. This work was done wholly or mainly while in candidature for a research degree at this University;
2. Where any part of this thesis has previously been submitted for a degree or any other qualification at this University or any other institution, this has been clearly stated;
3. Where I have consulted the published work of others, this is always clearly attributed;
4. Where I have quoted from the work of others, the source is always given. With the exception of such quotations, this thesis is entirely my own work;
5. I have acknowledged all main sources of help;
6. Where the thesis is based on work done by myself jointly with others, I have made clear exactly what was done by others and what I have contributed myself;
7. Parts of this work have been published as:-

Journal Papers:

(1) **Aminulai, H. O.,** Robinson, A. F., Ferguson, N. S., & Kashani, M. M. (2023). Impact of corrosion on axial load capacity of ageing low-strength reinforced concrete columns with different confinement ratios. *Construction and Building Materials*, *384*, 131355. https://doi.org/https://doi.org/10.1016/j.conbuildmat.2023.131355

(2) **Aminulai, H. O.,** Robinson, A. F., Ferguson, N. S., & Kashani, M. M. (2023). Nonlinear behaviour of corrosion damaged low-strength short reinforced concrete columns under compressive axial cyclic loading. *Engineering Structures*, *289*, 116245. https://doi.org/https://doi.org/10.1016/j.engstruct.2023.116245

Research Thesis: Declaration of Authorship

Conference Papers:

1) **Aminulai, H. O.**, Ferguson, N., & Kashani, M. (2023a). Structural behaviour of axially loaded corroded low-strength RC columns with different confinement ratios. In *Life-Cycle of Structures and Infrastructure Systems* (pp. 3348-3355). CRC Press.
2) **Aminulai, H. O.**, Ferguson, N., & Kashani, M. (2023b). Structural response of corroded concrete columns with different rebar confinements under cyclic compressive loading. In *Life-Cycle of Structures and Infrastructure Systems* (pp. 3340-3347). CRC Press.

Signature: Date: 16/11/2023

# Dedication

In loving memory of my dad, Wakili Ayodeji Aminulai, who did everything for me to attain my goal but who unfortunately did not see it come to reality. May Almighty Allah grant him Aljanat Firdaus and forgive all his sins.

# Acknowledgements

First and foremost, Alhamdulillah! All praise and gratitude are for Allah – the Lord of the worlds, the Gracious, and the Merciful. He (Allah) gave me the unique opportunity to embark on this life-changing experience of undertaking my PhD studies. I acknowledge all His favours upon me throughout this journey and will remain eternally grateful to Him.

Secondly, I would like to express my profound gratitude to my principal supervisor, Dr Mohammed M. Kashani, who, throughout my studies, embodied professionalism, dedication and patience in discharging his duties. His expertise in corrosion of reinforcements in RC structures and research in general, along with his consistent support, proved a tremendous asset in propelling me through this journey, without which this feat would have been difficult or impossible to achieve. I hope the end of my PhD will not be the end of my working relationship with him, and I look forward to more collaborations on so many levels in the future. I also owe a debt of gratitude to my second supervisor, Dr Neil S. Ferguson, for his tremendous support and continuous advice throughout my PhD journey; I am very grateful indeed. Finally, I would like to thank the other Civil, Maritime and Environmental Engineering staff (Academics and non-academics). I appreciate my research groups (Infrastructure and Dynamics Groups) and the CDT-SIS at the University of Southampton for the opportunity to be part of them and present some of our findings. I did not forget to thank my progression review examiners, Dr Sheida Afshan, Dr Meisam Jalalvand and Dr Marco Baigueira, for their valuable feedback on the reviews.

On the family level, I would like to express my deepest gratitude to my lovely wife, Maimuna Aminulai, for walking every step of this journey with me. Her encouragement and support diminished the difference between my aspirations and achievements, and I am still in awe of how she managed it. I could not have done this without her strength and endurance. To my kids, Maryam, Umar and Mutmainnah, I thank you for your patience in putting up with my perpetual absences, which I must now make up for. My appreciation also goes to my mother and loving siblings and their spouses back in Nigeria for their encouragement, prayers and wise counsel throughout my studies.

I am very grateful to the management and staff of the Petroleum Technology Development Fund (PTDF) under the Federal government of Nigeria for sponsoring my PhD programme and the Federal University of Technology, Minna, for approving my study fellowship to achieve this goal. My sincere appreciation also goes to Prof. Salawu Sadiku (Vice-Chancellor, CUSTECH Osara) for being my adopted father, friend, mentor and boss. Worthy of special mention for their strong support and encouragement are Prof. Mukhtar Abdulkadir, Prof Abdullahi Mohammed, Dr Afis

Busari, Engr Y. S. Jibrin (FMW&H Abuja), and Engr Oludayo Oluyemi (Hancock, Ogundiya and Partners, Lagos).

I would also like to thank my PhD colleagues and friends with whom I enjoyed excellent working relationships and interesting research discussions. These include Dr Taufan Abadi, Hammish Moodley, Feysa Yildirim and Rebecca Presswood. Not forgetting the IP students (Saud Al-Busaidi, Shama Hamed Al-Khamisani, Thomas Frederich, and Hady Akl) and MSc students (Thirukumaran Gunasekaran and Sze Ning Tee) who worked with me during the preparation and testing of my samples. I would also appreciate the support of the technical and experimental officers in the LSTL and TSRL at the University of Southampton Boldrewood Campus.

I am also profoundly grateful to my friends from back home in Nigeria, including Engr Mohammed Tahir Abdulsalam, Engr Idowu Dawodu, Engr Awwal Tanko Umar, Engr Abdullahi (FMW&H), Engr Mojeed Adewunmi, Dr Mahmud Abubakar, Dr Yusuf Abdulazeez, Dr Hassan Abdulrahman, Dr Philip Abubakar, Engr Gabriel Ojelade, Babatunde Odubona, Olalekan Omolodun, Mrs Margaret Awobusuyi (My first teacher), Ifeanyi Ugbade, Sochi Onyewuchi and Shehu Mohammed to mention a few. My appreciation will not be complete without mentioning the friends I made while studying in Southampton. I want to thank Alex Kuzba, Theo Gryllis, Robyn Penny, Tania Guimares, Lisa Palmer, Maria Kostova, Martha Zgnilec, Sandra Padilla, Doville, Marina, Mariam Khosty, Micheala, Josana for their encouragement and advice towards the completion of my programme.

Finally, I would like to conclude this acknowledgement by apologising to those I may have forgotten to mention here. I sincerely appreciate every help I received throughout this journey because Prophet Muhammad (SAW) said in a famous hadith, "He who is not thankful to the creation, is not thankful to the creator”.

# Definitions and Abbreviations

A Ampere (Unit of current)

ACI American Concrete Institute

ASCE American Society of Civil Engineers

CDPM Concrete Damage Plasticity Model

CFRP Carbon Fibre Reinforced Polymer

CT scan Computed Tomography Scan

DAMAGEC Compressive damage at integration points

DAMAGET Tensile damage at integration points

DIC Digital Image correlation

ECM electrochemical methods

EM electromagnetic methods

EMI Electro-Mechanical Impedance

EW elastic wave methods

FE Finite Element

FEA Finite Element Analysis

FRP ` Fibre Reinforced Polymer

GFRP Glass Fibre Reinforced Polymer

HPFRC High-Performance Fibre Reinforced Concrete

IRT infrared thermography

ITZ Interfacial Transition Zone

LE Logarithmic strain component at integration point

NLFEA Non-Linear Finite Element Analysis

Definitions and Abbreviations

OSM Optical sensing methods

PE Plastic strain components at integration points

PEEQ Equivalent plastic strain at integration points

PZT Piezoelectric lead zirconate titanate

RAMS Risk assessment and method statements

RC Reinforced Concrete

RF reaction force at nodes

S Stress component at integration point

TSRL Testing and Structures Research Laboratory

U Spatial displacement at nodes

V Spatial velocity at nodes

$A_{sp}$ area of transverse reinforcement

$A_{sx}$ total area of transverse bars in the x-direction.

$A_{sy}$ total area of transverse bars in the y-direction

$d_s$ diameter of hoop bar centres

$E_c$ elastic (Young's) modulus of concrete

$E_{sec}$ secant modulus of confined concrete

$\varepsilon_c$ longitudinal compressive concrete strain

$\varepsilon_{cc}$ maximum confined concrete axial strain

$\varepsilon_{co}$ axial strain of unconfined concrete

$\varepsilon_{u_{corr}}$ ultimate strain of the corroded columns

$\varepsilon_{u_{pristine}}$ ultimate strain of the pristine columns

$\varepsilon_{sm}^{c}$ steel strains at the maximum tensile stress of corroded reinforcement

$\varepsilon_{sm}$ steel strains at the maximum tensile stress of corroded reinforcement (0.12)

$\varepsilon_{cu}$ ultimate strain of confined concrete

$f'_{cc}$ maximum confined concrete strength

$f'_{co}$ maximum strength of unconfined concrete

$f_{yh}$ yield strength of the transverse reinforcement

$f_{yh}^{c}$ yield strength of the corroded transverse reinforcement,

$k_e$ confinement effectiveness coefficient

$s$ vertical spacing of transverse bars

$s'$ vertical spacing between hoop bars

$\rho_{cc}$ ratio of the area of longitudinal reinforcement to the area of the core of section

$\rho_{cx}$ ratio of the area of longitudinal reinforcement to the area of the core of the section in the x-direction.

$\rho_{cy}$ ratio of the area of longitudinal reinforcement to the area of the core of the section in the y-direction.

$\rho_s$ ratio of the volume of transverse confining steel to the volume of confined concrete core

$\alpha$ stress correction coefficient

$\beta$ strain correction coefficient

$\beta_s$ ultimate strain reduction factor for corroded transverse reinforcement

$\varepsilon_{cu}$ ultimate strain of confined concrete

$X_{corr}$ corrosion level (mass loss of transverse reinforcement)

$\sigma_{u_{corr}}$ ultimate strength of the corroded columns

$\sigma_{u_{pristine}}$ ultimate strength of the pristine columns

Ψ Dilation angle

ϵ Flow potential eccentricity

μ Viscosity parameter

$\sigma_{b0}$ initial biaxial compressive yield stress

$\sigma_{c0}$ initial uniaxial compressive yield stress

$K_c$ ratio of the second stress invariant on the tensile meridian to the compressive meridian at the initial yield

# Chapter 1 Introduction

## 1.1 Background to the Study

Civil engineering structures primarily comprise a combination of concrete and steel, which may be in the form of reinforced concrete (RC), prestressed concrete (PC), or composite having one or more steel components leading to the formation of artefacts such as buildings (residential, communal, and industrial), bridges (highway, railway, and pedestrian), towers (communication, power, and water), dams, harbour, oil drilling platforms and others. RC is the most versatile material used in construction projects worldwide due to its component materials' availability and suitability for various construction applications Yeomans (2004). It combines concrete (very good in compression) with steel (strong in tension) to produce a composite material with both properties.

Ageing is a natural process in any infrastructure, but it has become an urgent and critical problem in recent years, resulting in the loss of a reliable lifespan of infrastructures. Many infrastructures all over the world are over 50 years old and suffer from extensive deterioration and degradation that affects their serviceability. The high costs associated with preserving the ageing structures, along with the limited funds allocated for their maintenance, pose significant technical and financial challenges. For example, the United States of America reported needing about $125 billion to repair ageing and existing bridges (ASCE, 2021). Ageing usually begins to appear in individual elements of the structures, leading to non-uniform or heterogeneous behaviour. The most well-known and widespread sign of structural ageing is related to the weakening of concrete mechanical properties

RC is affected by steel corrosion resulting from exposure to chloride ions and carbonation in marine and dry environments, respectively (Glass, 2003). Corrosion affects the durability of RC structures leading to a reduction in their service lives, load-carrying capacities and seismic resistance. Thus, its prevention is crucial in avoiding RC deterioration (Monticelli et al., 2016). Several methods have been proposed to prevent or reduce the impact of corrosion on RC structures, some of which include: the production of good quality concrete; design as per standards during the construction process; addition of pozzolans to RC in marine environments as these reduce the permeability and chloride ion diffusion within the RC structures (Glass, 2003).

Corrosion of RC bridge piers in marine environments and cold regions, where de-icing salts are often used on RC structures, is primarily non-uniform along the length of the piers/column, with the splash and tidal zone being more severe than the other parts. This is due to the combination

of effects such as chloride concentration, the abundance of oxygen and the wet-dry cycles of the surrounding water (Zhou et al., 2020).

Reinforcing steel embedded in concrete corrodes when the passivating film surrounding the steel becomes unstable and broken. This happens when the concentration of chloride ions on the reinforcing bars has reached a threshold value. This process becomes more evident in ageing structures with low-strength concrete and inadequate reinforcements. The rust products formed grow and exert pressure on the concrete cover causing it to crack and break (Figure 1.1). The cracks eventually extend to the surface of the concrete and allow further ingress of the chloride ions to the reinforcement surface, leading to pitting and generalised corrosion and reduction in the cross-section of the reinforcement bars.

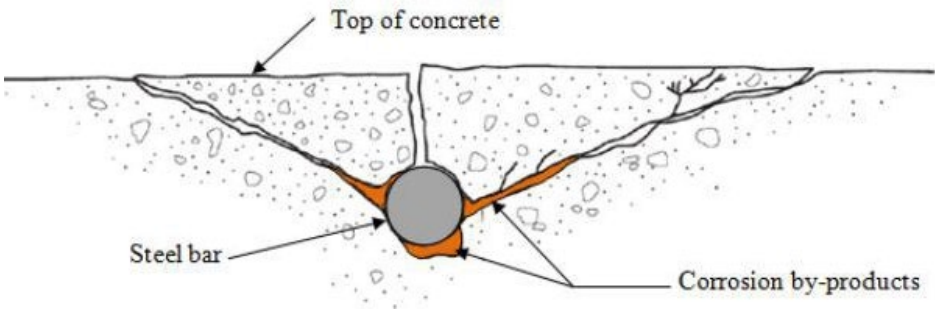


Figure 1.1: Cracking and spalling of concrete cover induced by corrosion (Elbusaefi, 2014)

The corrosion process makes the reinforcing steel thermodynamically unstable by depassivating the protective film surrounding the reinforcing steel. This depassivation leads to the formation of rust, which keeps growing volumetrically (approximately 3.5 times the size of the steel) in the space between the reinforcement and the concrete producing radial stresses on the concrete (Biswas et al., 2020). When these internal radial stresses exceed the tensile strength of concrete, cracks are formed between the corroded bars and the exterior surface of the concrete (Aboutaha et al., 2013). Generally, the degradation of RC structures may be divided into chemical and physical degradation as it concerns either the reinforcement or concrete. Figure 1.2 gives an overview of the mechanisms involved in the deterioration process.

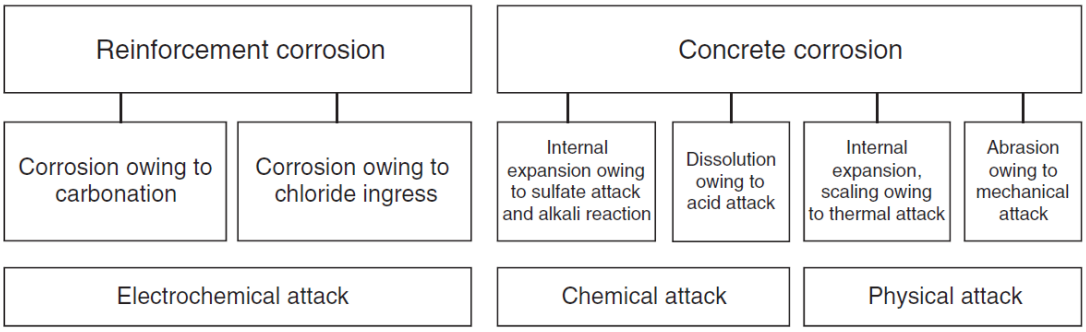


Figure 1.2: Overview of the basic mechanisms that lead to degradation (Gehlen et al., 2010)

The deterioration process described above is significantly pronounced in marine and highly seismic environments. Corrosion of reinforcing bars in RC structures reduces their load-carrying capacities and ductility, leading to a loss in serviceability, functionality and structural safety.

## 1.2 Corrosion of RC Structures

RC structures in cold regions are exposed to de-icing salts, which cause the reinforcement to corrode, leading to the degradation and collapse of the structure, resulting from a loss in its durability and structural capacity. This deterioration leads to the catastrophic failure of the structure by limiting its efficiency if uncontrolled (Broomfield, 2007). Steel corrosion in RC structures has resulted in massive economic loss due to the failure and degradation of such structures worldwide (Jia et al., 2020).

Repairing or replacing structures damaged by corrosion usually leads to a high cost. It is estimated, for example, that structurally damaged RC bridges in the United States will likely cost about $40 billion to repair or replace in 2018. In contrast, in Western Europe, such corrosion-damaged structures are estimated to cost approximately 5 billion Euros annually to repair (Markeset et al., 2006). In the UK, this cost is estimated to be about £1 billion per year in England and Wales alone, accounting for about 10% of the total corroded highway bridges (Wallbank, 1989). Generally, corrosion of ageing RC structures leads to the following broad damage types (Vu et al., 2016):

a) Spalling of the cover concrete
b) General or pitting loss of the steel rebar section
c) reduction in the compressive strength of the concrete
d) decreased bond strength between the reinforcement and the concrete

In addition to the broad classification of damages above, RC corrosion also changes the mechanical properties and ductility of the reinforcement, thereby leading to the collapse/failure of the structure (Vu et al., 2016).

The mechanism of RC corrosion may be described thus: degradation of RC structures occurs either through carbonation or chloride contamination individually or the combination of both processes. Many bridges in the cold region and marine environment suffer from the combination of both processes, with chloride-induced corrosion being the most significant. This degradation, once started, is sustained by the chemical action of chlorides in de-icing salts used during the winter (Fig. 1.3a) and exposure to chlorides in the water in the marine/aggressive environments (Fig. 1.3b). This corrosion results in the loss of both the longitudinal and transverse reinforcement (Fig.

1.4(a) and 1.4(b)). Loss of transverse reinforcement leaves the bridge column with little or no confinement and thus increases the tendency of buckling and failure of the bridge, especially in bridges with long columns/piers.


(a)


(b)

Figure 1.3: Bridge columns damaged by corrosion of reinforcing steel (a) due to de-icing chemical exposure and (b) in the marine environment (Mohammed, 2015)


(a)


(b)

Figure 1.4: Corrosion of longitudinal and transverse reinforcement (a) bridge pier columns (b) circular columns (Aboutaha et al., 2013)

Chloride-induced corrosion is the most prevalent degradation of RC structure located in marine and aggressive environments, causing corrosion of reinforcement and leading to the failure of the structures (Raupach & Schießl, 2001). In this case, chloride ions diffuse through the pores of the concrete cover to the reinforcement and induces corrosion of the reinforcement when the threshold limit of the chloride ion concentration exceeds a limit (Kashani, 2014) of about 0.026% by weight of concrete. The deterioration of the reinforcement leads to a loss in the bond between the concrete and reinforcement and the failure of the RC member (Stanish et al., 1999; Zhang et al., 2012).

## 1.3 Research Gap

The recent earthquake in Turkey showed many building collapses with low-strength (low-quality) concrete, inadequate reinforcement detailing and corroded reinforcements. Studies conducted after the disaster showed that most of the buildings and RC structures affected during the earthquakes were not adequately designed and constructed to resist vibrations resulting from the earthquake (Arya et al., 2014; Erdik et al., 2023; Kajastie, 2023; Neuman, 2023). The disaster was worsened by a widespread disregard and lack of implementation of building codes, which posed a significant risk to communities. The lack of adequate steel reinforcement meant buildings and RC structures were already brittle, causing them to collapse in the earthquakes (Ahmed, 2023). Hence, further investigation of the behaviour and response of low-strength RC structures to seismic loadings is needed.

The cost of repairing and replacing corrosion-damaged bridges in the USA is estimated at $40 billion. However, this figure only accounts for the effect of corrosion on about 50 percent of the total bridges in the country (Sprung et al., 2018). In industrialised countries, the main challenge is maintaining existing and ageing RC structures cost-effectively. Deterioration models estimate and predict the time to rehabilitate and repair ageing structures to reduce the risks of failure and catastrophic collapse. Unfortunately, due to the difficulty in predicting the actual behaviour of the materials, some of these assumptions do not accurately represent the processes involved in the corrosion of RC structures.

The overarching problem is that in predicting the actual performance of structures built with modern and innovative construction materials and construction processes, one can no longer rely on empirical long-term practical experience. This makes the need to study and understand the structural behaviour and response of ageing and deteriorating RC structures very important for researchers. The research into the nonlinear analysis of corrosion-damaged RC structures is an ongoing process due to the need to understand the responses of such structures under load (Azad et al., 2007; Du et al., 2007; Rodriguez et al., 2005). The structural response of RC members, when loaded and having the adverse effect of corrosion, has been investigated using nonlinear finite element analysis by many researchers (Dizaj & Kashani, 2022; Dizaj et al., 2018; Kashani et al., 2016a, 2016b; Mohammed et al., 2018).

Most previous studies on the numerical and experimental analysis of structural members concentrated on the response of such structures to monotonic loads. However, due to the location of many structures in marine, environmentally aggressive and high seismic regions, the investigation into the effect of cyclic loading on RC structures is increasing, leading to numerous work on the nonlinear behaviour of structural members to cyclic loading (Li et al., 2018; Liu et al., 2017; Meda et al., 2014; Ou & Chen, 2014; Ou et al., 2013; Ou et al., 2012). Although much has

been done in this research area, much remains to be done, especially on old RC structures in the seismic zone. The difficulties and complexities in estimating the corrosion of reinforcement in concrete (Kashani et al., 2019) introduce uncertainties in the accuracy and reliability of the numerous numerical models used to predict RC structures' performance and life cycle analysis.

In the past few decades, lots of experimental works on bending (Al-Saidy et al., 2016; Azad et al., 2010; Cairns et al., 2008; Dong et al., 2017; Gao et al., 2019; Hou et al., 2019; Yu et al., 2015; Zhu & François, 2015) and shear (El-Sayed et al., 2016; Wang et al., 2015; Ye et al., 2018) failure of corroded RC beams subjected to monotonic and cyclic static loading have been undertaken, while large-scale laboratory testing of rusty RC columns (rectangular and circular) subjected to the action of axial and cyclic loading are very few. Moreover, most of the research on experimental testing of corroded RC columns was based on the flexural failure of columns with little or no experimental work on shear-critical columns (Kashani et al., 2019). This is due to the complexity of the experimental testing of shear-critical columns. The setup for shear-critical testing requires a more advanced setting to avoid sudden collapse during testing.

Recent surveys into the failure of ageing and existing RC structures (Dizaj et al., 2021; Kam et al., 2011) in highly seismic areas revealed the susceptibility of such structures to even moderate seismic events due to a lack of proper seismic detailing and inadequate shear reinforcement leading to brittle failure of the structure (Del Zoppo et al., 2017). There is presently little or no experimental and numerical investigation of the response of low-strength RC columns to axial monotonic and cyclic loads.

The need for further research and experimental investigation into the structural response and behaviour of ageing low-strength corroded RC columns having different geometries (square and circular), reinforcing details, and considering different confinement ratios under various loading conditions (monotonic and cyclic) could not be over-emphasised. Therefore, this research will focus on the experimental investigation of low-strength concrete corroded RC columns with different confinement ratios and geometrical properties (square and circular) subjected to compressive cyclic and monotonic loading conditions.

## 1.4 Aim and objectives

This research investigates the effect of both cyclic and monotonic loading on the nonlinear response of ageing low-strength corroded RC structures in an aggressive/marine environment. This will involve conducting experimental tests and numerical investigations on corroded RC columns. Several kinds of research have been done to model the behaviour and response of corroded RC columns to monotonic and cyclic loading, but these were on normal and high-

strength concrete structures. However, many old and aged RC structures have low concrete strength which are further degraded by corrosion due to the environments. Therefore, understanding the behaviour and response of such structures to monotonic and cyclic loading became imperative for proper strengthening technique recommendations. This research will thus focus on the experimental investigations of low-strength RC columns.

The primary objectives of the research are:

i. To investigate the mechanical behaviour of ageing low-strength concrete circular and square RC columns under simultaneous reinforcement corrosion, confinement configurations and monotonic axial load with the combined effect of longitudinal bar buckling.
ii. To investigate the effect of corrosion and transverse reinforcement confinements on the nonlinear stress-strain response of RC columns under axial cyclic compressive loading with the combined impact of longitudinal bar buckling by analysing the failure modes, the load-deformation responses and the inelastic buckling of the longitudinal rebars.
iii. To conduct X-ray computed tomography (CT) scans on the corroded RC column specimens to examine the corrosion pattern on the longitudinal bars and estimate the actual volumetric mass loss resulting from the corrosion of the whole cage of reinforcement embedded in the RC samples.
iv. To investigate numerically the impact of corrosion and transverse reinforcement confinement on the stress-strain response of low-strength concrete confined corrosion-resistant RC columns and then compare and validate the results with experimental data relating to corrosion-damaged RC columns. This will aid the parametric studies in developing constitutive models for low-strength concrete confined corroded RC columns.

## 1.5 Structure of the thesis

This thesis presents the experimental investigation into the stress-strain behaviour of ageing low-strength concrete confined corroded RC columns, with different confinement ratios, under axial monotonic and cyclic loading. Furthermore, the estimation of the corrosion mass loss and identification of the location of pitting corrosion on the reinforcement with the X-ray CT scan technique was explored. The experimental results were afterwards validated with numerical analysis.

**Chapter 1** of the thesis covers the research background as well as the problem statement and justification of the study. A description of the research aims and objectives is also provided in this chapter.

The **second Chapter** gives an overview of the literature relevant to this research, including corrosion models, numerical simulations, experimental investigations of corroded RC elements, and non-destructive testing on corroded RC structures.

A detailed experimental investigation is presented in **Chapter 3,** examining the effect of axial monotonic loading upon the stress-strain behaviour of differently confined ageing low-strength concrete corroded RC columns. The corrosion was simulated in the laboratory environment using an accelerated corrosion procedure. A total of 30 RC columns (15 circular and 15 square) were designed and grouped into five different target degrees of reinforcement corrosion (i.e., 0%, 5%, 10%, 20% and 30%) with three confinement ratios (*L/D*=5, *L/D*=8 and *L/D*=13) under monotonic axial load.

**Chapter 4** discussed the experimental programme investigating the stress-strain response of low-strength corroded RC columns with different confinements and corrosion mass loss, as well as the buckling of longitudinal reinforcements to axial cyclic compressive load.

**Chapter 5** presents the novel use of the X-ray CT scan technique to investigate the corrosion pattern on the longitudinal reinforcement bars and the estimation of the corrosion mass loss in the whole reinforcement cage of the RC columns.

**Chapter 6** highlights and presents the numerical investigation of the stress-strain behaviour of low-strength concrete confined corroded RC columns using ABAQUS FEA software. The results were used to validate the data obtained from the experimental investigation presented in Chapters 3 and 4.

**Chapter 7** summarises the research's main conclusions and findings and provides recommendations for future research.

An overview of the thesis outline is shown in Fig. 1.5.

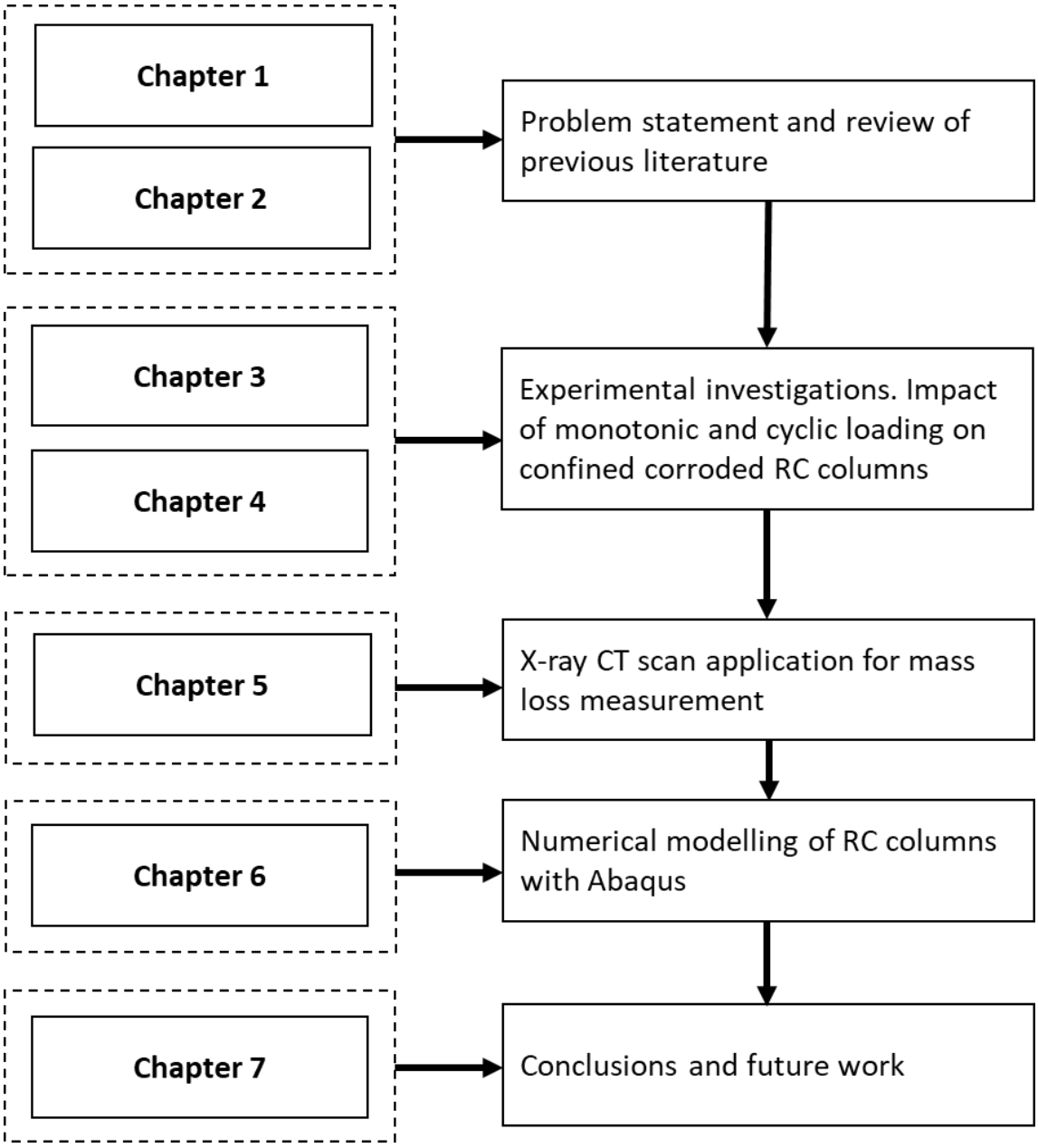


Figure 1.5: Overview of the thesis outline

# Chapter 2 Literature Review

This chapter reviews previous studies on the degradation of confined RC columns. The corrosion of steel reinforcement in RC structures, the corrosion deterioration models, previous works on numerical and analytical modelling, and confined concrete are explored. Previous experimental tests on corroded RC columns and the application of non-destructive tests such as X-ray Computed Tomography (CT) scans and Digital Image Correlation (DIC) measurements on RC structures are examined.

## 2.1 Ageing of RC Structures

Structures are generally designed for specific years based on the material composition and the expected load. As these structures age, the material starts to deteriorate due to their interaction with the environment, the imposed loads (static, cyclic and dynamic) and chemical aggressions, reducing strength and serviceability. The most significant environmental deterioration results from corrosion of reinforcement caused by carbonation and chloride ingress into the RC from the de-icing salts used in cold regions and the impact of the water on structures in the marine/aggressive environment.

Ageing structures are susceptible to materials degradation, resulting in considerable inspection, maintenance and repair expenses. It also leads to sudden failures when critical loading condition is exceeded, resulting in loss of lives; vulnerability to extreme loading from exposure to natural disasters such as earthquakes and hurricane (Al-Ostaz et al., 2009). The effects caused by ageing processes lead to the degradation of engineering properties, affecting the static and dynamic response of the structures, their resistance/capacity, failure mode, and the location of failure initiation. Thus, the ability of the structure to withstand various challenges from operation, environment and natural events may be reduced. Once the structural capacity falls below a given performance threshold, the structure may be repaired and strengthened, leading to a new initial capacity, diminishing progressively over time the ability to withstand future operating conditions.

Karapetrou et al. (2017), investigated the seismic vulnerability of RC structures to ageing by considering the effect of chloride-induced corrosion on corrosion initiation time and corrosion rate. Using different seismic code levels, two-dimensional incremental dynamic analysis was performed on uncorroded and corroded RC structural members. The investigation result showed that age significantly affects RC's seismic vulnerability over time, with a decrease in the overall performance of the structures.

The deterioration resulting from the ageing of RC structures makes such structures have inadequate seismic performance and suffer structural damage leading to failure and collapse when subjected to extreme ground motions. To mitigate this, RC structures are strengthened externally with fibre-reinforced polymers (FRP) such as carbon-fibre-reinforced polymers (CFRP) and glass-fibre-reinforced polymers (GFRP) and steel jackets.

Li et al. (2009), investigated the effectiveness of using CFRP and steel jackets on corroded RC columns. The columns, with variables such as different strengthening techniques, degree of rebar corrosion, axial load, CFRP sheets and steel jacket, were subjected to the combined effect of lateral cyclic displacement and constant axial load. The result showed that the columns strengthened with the combined CFRP and steel jacket had improved strength and ductility than those with only steel jackets or only with CFRP sheets.

Most old (aged) RC structures are designed and constructed without proper earthquake-resistant provisions (ductile detailing). As a result, the corrosion of the rebars in such structures further reduces strength and ductility. Joshi et al. (2015) conducted an experimental investigation (using 53 small-scale columns) into the effects of continuing corrosion on the strength and ductility of differently confined RC short columns while also strengthening the columns with ferrocement jacket and GFRP. The results of the tests showed that GFRP wraps performed better than ferrocement in improving the strength and ductility of RC structures as shown in Figure 2.1(a-d).

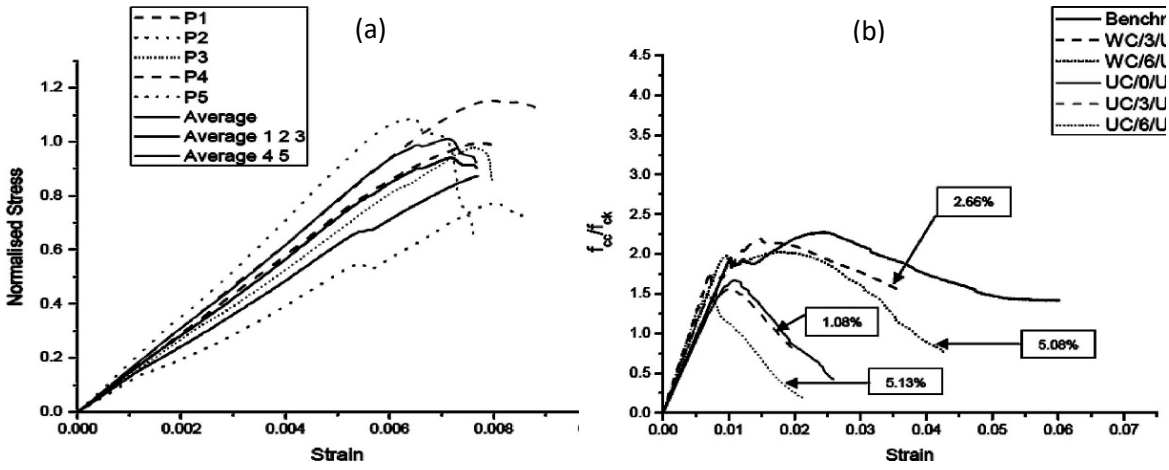

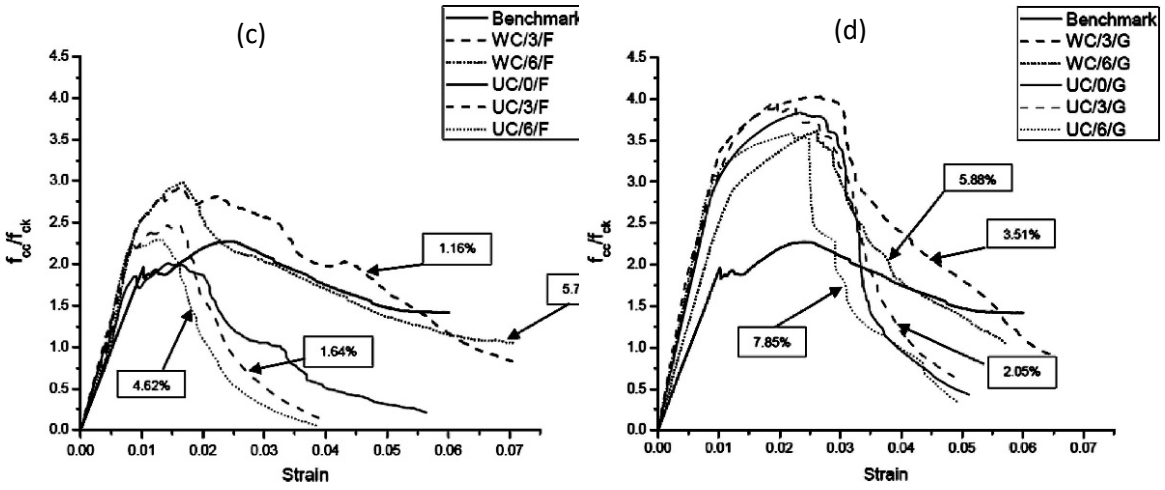


Figure 2.1: Stress-strain response of columns; (a) Normalised stress-strain curve for PCC specimens, (b) Effect of corrosion on unstrengthened specimens, (c) Effect of ferrocement strengthening on corroded specimens and (d) Effect of GFRP on corroded specimens (average corrosion indicated in figures) (Joshi et al., 2015).

Adequate confinement provided to a column increases its ductility and load-carrying capacity, as such new designs of RC structures has made provision for adequate transverse reinforcement needed for confinement. Also, old and ageing low-strength RC structures in high seismic and earthquake-prone areas should be strengthened with adequate FRPs to increase the strength and ductility and hence avoid collapse/failure of the structure.

## 2.2 Corrosion of Steel Reinforcement in RC Structures

Steel corrosion occurs when steel reacts with elements such as oxygen and hydrogen in the presence of water to form red iron oxide called rust, which is about two to four times the volume of the original steel and has none of the good mechanical properties of the original steel. Corrosion causes the steel to depassivate and loses the bond between the steel and the concrete, thereby leading to delamination and subsequent spalling and, if left unchecked, the collapse/failure of the structure. Steel corrosion in RC structures results in serious structural problems and irreparable damage, considerably impacting the world's technical, financial and societal needs (François et al., 2018). Corrosion of steel limits the serviceability of the structures and leads to structural failure/collapse of the structure (Fig. 2.2).

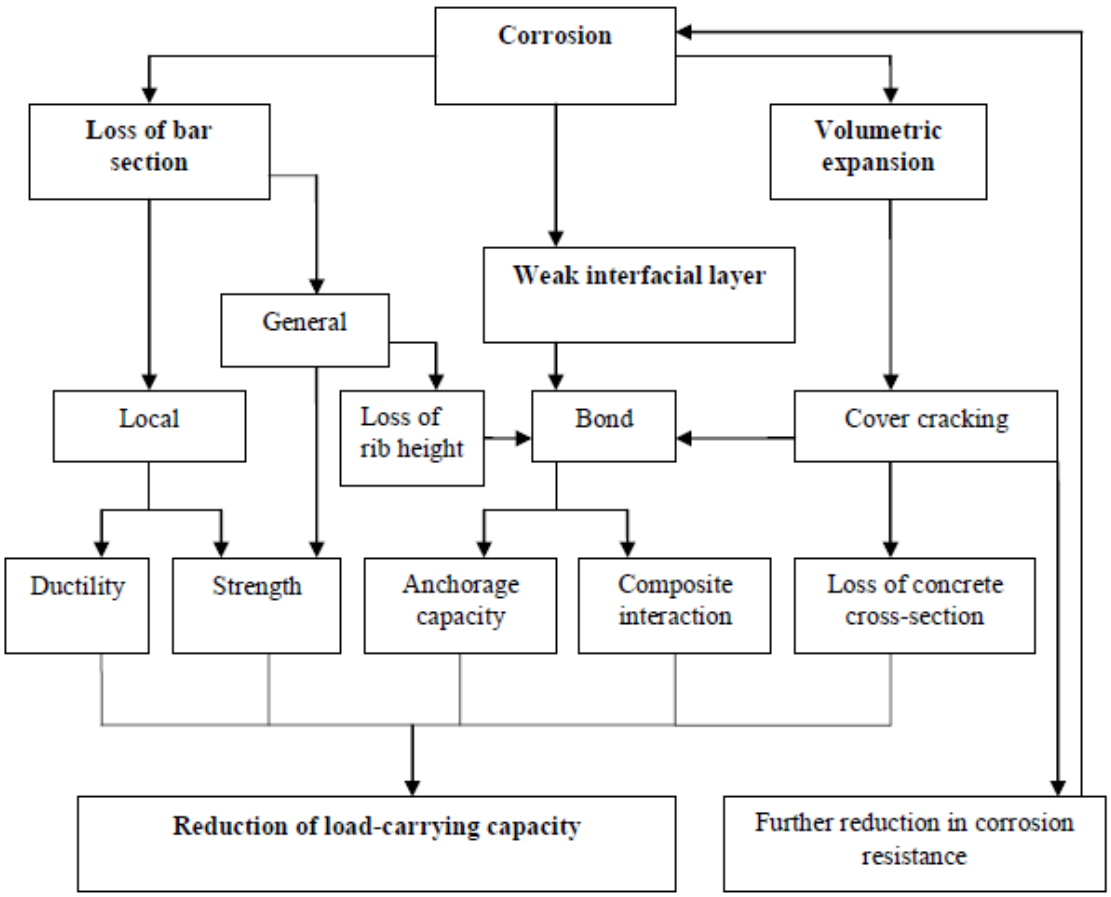


Figure 2.2: The consequence of reinforcement corrosion on RC Structures (Ayop & Cairns, 2013)

The collapse of some bridges in history has been adduced to the influence of corrosion. In May 2000, a concrete pedestrian walkway spanning a four-lane highway collapsed in North Carolina, injuring over 100 people. In 1967 (15th December), the Silver Bridge bridge connecting Point Pleasant, West Virginia, with Kanauga, Ohio, in the United States of America (USA), collapsed due to corrosion-induced deterioration, causing several fatalities. The Dickson Bridge in Montreal also became unusable in 1990 due to corrosion-induced deterioration (Glass, 2003). On 2 July 1965, the Kansas Avenue Bridge in the United States collapsed due to structural deterioration of the RC elements. The Mianus River Bridge in Greenwich, Connecticut, United States, collapsed on the 28th of June 1983 due to the corrosion of the pin and hanger supporting a span of the bridge.

According to Vu et al. (2016), the principal effects of corrosion on structural elements are:

i. loss of reinforcement cross-section,
ii. changing the mechanical properties and ductility of reinforcement,
iii. reduced compressive strength of the cracked cover concrete and
iv. reduction of bond strength at the reinforcement and concrete interface

Generally, corrosion of steel reinforcement bars in RC structures is induced either by carbonation (generalised), chlorides (localised or pitting), or stress cracking in prestressed wires, as shown in Figure 2.3.

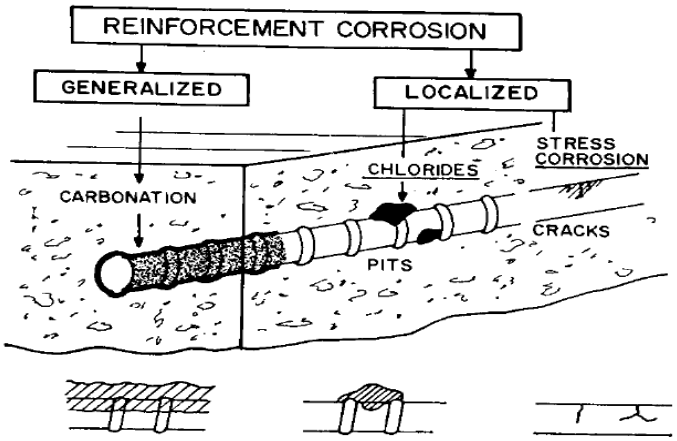


Figure 2.3: Types and morphology of the corrosion in concrete: generalised (carbonation), localised (chlorides) and stress cracking (prestressed wires) (ACI Committee 222, 2001; Mogire et al., 2018)

### 2.2.1 Carbonation induced corrosion of RC structures

Carbonation of concrete is the chemical reaction of calcium hydroxide (portlandite, $Ca(OH)_2$), in the cement matrix with carbon dioxide ($CO_2$) gas leading to the production of calcium carbonate (calcite, $CaCO_3$). Carbonation occurs when the $CO_2$ in the atmosphere reacts with the alkaline content of the concrete ($Ca(OH)_2$) in the presence of water to form calcium carbonate ($CaCO_3$). The concrete carbonation process is presented below (Equations 2.1 – 2.5) by Leber and Blakey (2017); Papadakis et al. (1989).

$$Ca(OH)_2 \rightarrow Ca^{2+}(aq) + 2OH^-(aq) \quad (2.1)$$

$$Ca^{2+}(aq) + 2OH^-(aq) + CO_2 \rightarrow CaCO_3 + H_2 \quad (2.2)$$

$$3CaO.2SiO_2.3H_2O + 3CO_2 \rightarrow 3CaCO_3.2SiO_2.3H_2O \quad (2.3)$$

$$3CaO.SiO_2 + \mu H_2O + 3CO_2 \rightarrow 3CaCO_3 + SiO_2.\mu H_2O \quad (2.4)$$

$$2CaO.SiO_2 + \mu H_2O + 3CO_2 \rightarrow 2CaCO_3 + SiO_2.\mu H_2O \quad (2.5)$$

The reaction leads to the depletion of the hydroxyl ions ($OH^-$) which lowers the pore water pH from above 12.5 to below 9.0 making the passive layer become unstable and allowing corrosion to occur in the presence of oxygen and water (Heiyantuduwa et al., 2006). It is difficult to predict the occurrence of carbonation-induced corrosion in RC structure as it is a much slower process

than chlorine-induced corrosion. Carbonation rates generally follow the parabolic kinetic equation given below:

$$d = At^{0.5} \quad (2.6)$$

where,

*d* = depth of carbonation

*t* = time

*A* = constant generally of the order 0.25 to 1.0mm.year$^{-1/2}$

### 2.2.2 Chloride-Induced Corrosion

Chloride-induced corrosion occurs in structures located in marine environments and those subjected to de-icing salts in cold climates. It involves the transportation of chloride through the concrete to the steel such that the corrosion can start once the threshold level is reached. The process of chloride-induced corrosion is described by Bentur et al. (1997).

$$\mathrm{Fe} \rightarrow \mathrm{Fe}^{2+} + 2\mathrm{e}^{-} \quad (2.7)$$

$$\mathrm{Fe}^{2+} + 2\mathrm{OH}^{-} \rightarrow \mathrm{Fe(OH)}_2 \quad (2.8)$$

$$4\mathrm{Fe(OH)}_2 + 2\mathrm{H}_2\mathrm{O} + \mathrm{O}_2 \rightarrow 4\mathrm{Fe(OH)}_3 \quad (2.9)$$

$$4\mathrm{e}^{-} + \mathrm{O}_2 + 2\mathrm{H}_2\mathrm{O} \rightarrow 4\mathrm{OH}^{-} \quad (2.10)$$

$$\mathrm{Fe}^{2+} + 2\mathrm{Cl}^{-} \rightarrow \mathrm{FeCl}_2 \quad (2.11)$$

$$\mathrm{FeCl}_2 + 2\mathrm{H}_2\mathrm{O} \rightarrow \mathrm{Fe(OH)}_2 + 2\mathrm{HCl} \quad (2.12)$$

During the reaction, the positively charged ferrous ions $Fe^{2+}$ pass into the solution while the negatively charged free electrons, $e^-$, pass through the steel into the cathode, which is absorbed by the electrolytes and combined with oxygen and water to form hydroxyl ions, $OH^-$. The hydroxyl ions combine with the ferrous ions to form the ferric hydroxide, which is converted by further oxidation to rust. Chloride-induced corrosion is a concern for RC structures located in a marine (Chloride-laden) environment or subjected to de-icing chemicals, as the movement of the chloride is much more rapid and leads to early degradation and failure of structures.

The process of chlorine-induced corrosion in RC structures involves two distinct phases: the initiation and propagation phases (Lounis & Amleh, 2004).

The corrosion initiation stage, also called the depassivation process, starts from placing concrete in RC structures to breaking the protective oxide film (passive film) on the reinforcing steel surface. It involves mainly the transport process of chloride through porous concrete cover to the reinforcing steel. The corrosion initiation time is a function of several parameters, including the depth of cover concrete, the concentration of chloride at the surface of RC section, the quality of concrete and the type of reinforcing steel (epoxy-coated black steel, galvanised steel, etc.).

The propagation stage begins with the formation of corrosion cells around the steel-concrete interface to the limiting state of corrosion-induced damage. Then, it involves much more complex procedures, such as electrochemical corrosion reaction and mechanical concrete cover cracking, which, if not controlled, could lead to the failure of the RC structures depending on several parameters such as the corrosion rate, environmental condition, natural hazards i.e. earthquake loading, quality of construction etc.

The impact of factors such as carbonation, bad construction, fatigue, freeze-thaw and insufficient grout on RC structures located in marine and highly seismic environments is less severe than chlorine–induced corrosion (Kashani, 2014), as shown in Figure 2.4

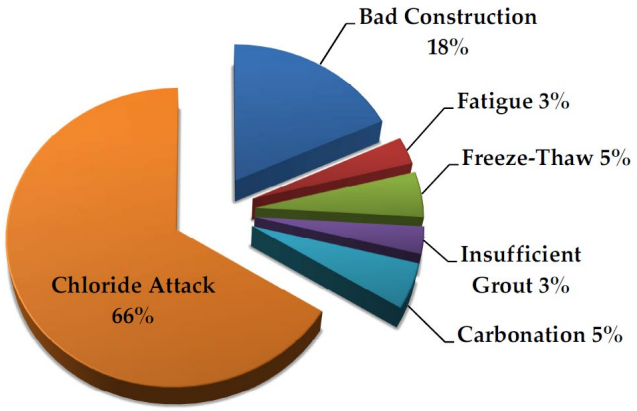


Figure 2.4: Significance of chloride-induced corrosion of RC structures (Kashani, 2014)

Chloride-induced corrosion is the primary cause of environmental deterioration in RC structures located in the marine environment; as such, its occurrence cannot be ignored. It starts when the chloride concentration reaches or exceeds 0.4% and 0.2% by weight of cement for chlorides cast into concrete and chlorides diffusing in, respectively (Apostolopoulos et al., 2013).

Much research has been done to investigate the effect of chloride-induced corrosion on RC structures. The impact of chloride-induced corrosion was investigated on the mechanical properties and pit depth of reinforcement corroded by direct exposure (immersion in a salt spray chamber) and embedding in concrete (Apostolopoulos et al., 2013). It was discovered that for the same mass loss, the degradation of the samples embedded in concrete is much more severe than

that exposed directly to chloride in terms of losses in yield strength, elongation, and the analysis of the pit depth.

Van Belleghem et al. (2018), investigated the autonomous healing of cracks using encapsulated polyurethane to reduce reinforcement corrosion. RC beams were exposed to chloride solutions for ten weeks, leading to pitting corrosion of the rebars. Applying self-healing concrete with low-viscosity polyurethane enhances the durability of RC structures in marine environments.

Khan et al. (2017) used mathematical models and probability to predict the service life of RC structures in chloride-laden environments. Fick's second law of diffusion was used to define the rate of chloride transport in concrete, while a stochastic model was introduced for corrosion initiation and cover cracking periods. The result showed that a lognormal distribution could be used to fit the initiation period and the cover cracking time. In contrast, a normal distribution could describe the necessary amount of rust formation during the corrosion process of RC structural elements.

### 2.2.3 Corrosion Deterioration Models

A lot of investigation is being done worldwide to predict the deterioration of RC structures affected by corrosion. Tuutti (1982) suggested a model for predicting the service lives of RC structures (Fig. 2.5) which relates the maximum acceptable corrosion level to the appearance of cracks. The length of the initiation period in the model is the time required for aggressive species to reach the reinforcement surfaces and trigger active corrosion. In contrast, the propagation period can be taken as the time elapse until repair becomes mandatory.

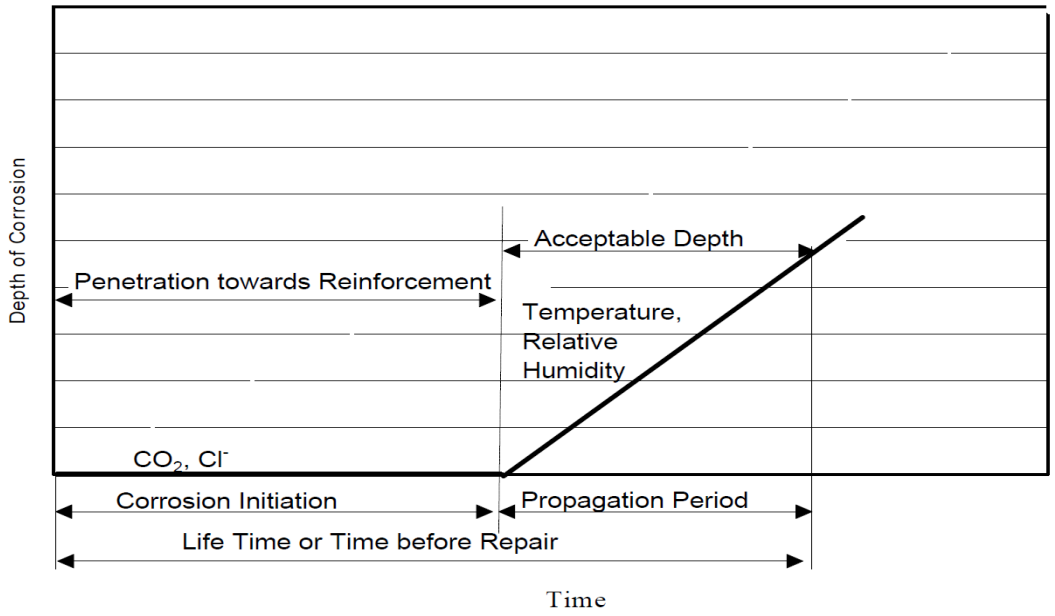


Figure 2.5: A schematic sketch of steel corrosion sequence in concrete (Tuutti, 1982).

Cady and Weyers (1984) developed a deterioration model for estimating the remaining life of a concrete bridge in a corrosive environment. The model was used to check the effect of salt-induced corrosion on the part of a deck to predict the corrosion of the entire bridge deck. It has three distinct phases (diffusion, corrosion and deterioration), as seen in Fig. 2.6.

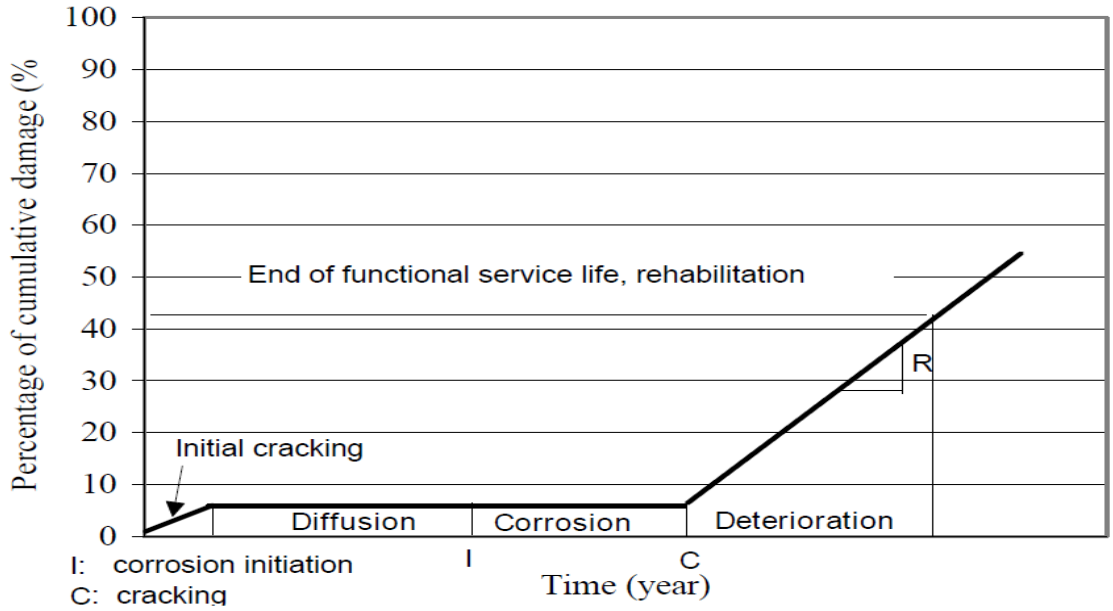


Figure 2.6: Chloride - Induced corrosion deterioration process for a concrete element with a mean cover depth of 50mm (Cady & Weyers, 1983)

The model's first phase (diffusion) describes the time it takes the chloride ions to penetrate the concrete cover and reach the steel surface. It is determined empirically with Fick's second law of diffusion, as shown below

$$\frac{\partial C}{\partial t} = \frac{\partial}{\partial x}\left[D\frac{\partial C}{\partial x}\right] \tag{2.13}$$

This equation was modified further by Crank (1975) using the following assumption:

Diffusion coefficient, $C = C_s$ and $C = 0$ for $x > 0$ at $t = 0$, this yields

$$C(x,t) = C_s\left(1 - \text{erf}\left(\frac{x}{2\sqrt{Dt}}\right)\right) \tag{2.14}$$

where

$C(x,t)$ = chloride concentration level at depth, x, and time, t,

*t* = time for diffusion

*x* = concrete cover depth

*erf* = statistical error function,

$C_s$ = surface chloride concentration by percentage weight of cement and

*D* = apparent diffusion coefficient (mm$^2$/year).

The second phase of the model, the corrosion phase, describes the period between the corrosion initiation and the cracking of the cover concrete. In contrast, the third phase, the deterioration phase, is when the degradation has reached the need to rehabilitate the structure.

Recently, many researchers have started to model the cracking of concrete cover induced by non-uniform corrosion of reinforcement. González et al. (1995) Compared the depth of pitting corrosion penetration on steel bars with the depth of general corrosion and found that the maximum penetration of pitting corrosion on the steel bar is equivalent to about four to eight times the penetration of general corrosion. Jang and Oh (2010) extended the experimental results of González et al. (1995) by investigating the effects of non-uniform corrosion on the cracking behaviour of concrete cover and discovered that expansive pressure exerted by corrosion on concrete cover adversely affects its stability. They also derived some equations for cracking pressures of concrete cover resulting from corrosion in terms of the degree of non-uniform corrosion for various cover-to-bar diameter. The various corrosion distribution considered in the work ranges from 1 – 8 and is shown in Figure 2.7 below. α is the ratio of the depth of non-uniform corrosion to that of uniform corrosion while t is the duration of the corrosion.

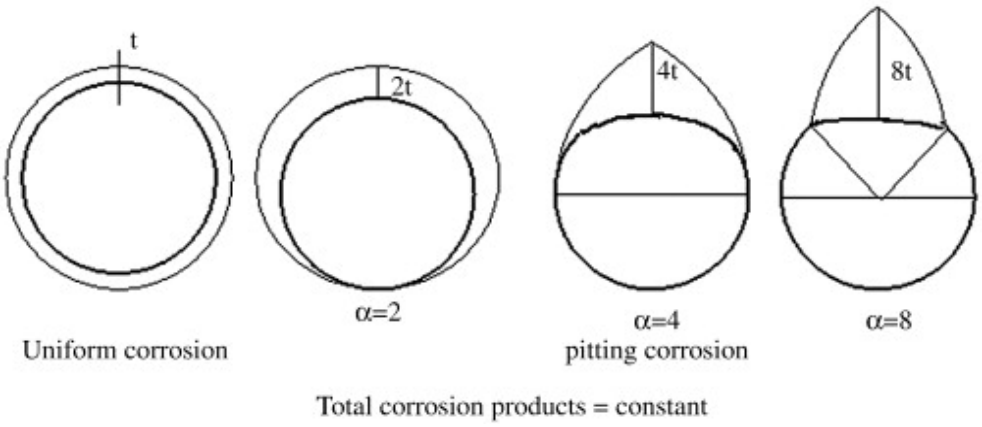


Figure 2.7: Various types of corrosion distribution for *α* = 1, 2, 4, and 8, respectively (Jang & Oh, 2010).

Cao et al. (2013) numerically simulated the interaction between corrosion-induced cover crack growth and corrosion propagation in RC structures using the coupled-micro and macro-cell corrosion and formulating the uniform thick-walled cylinder model. The microcells and macrocells process leads to uniform and pitting corrosion respectively as illustrated in Figure 2.8.

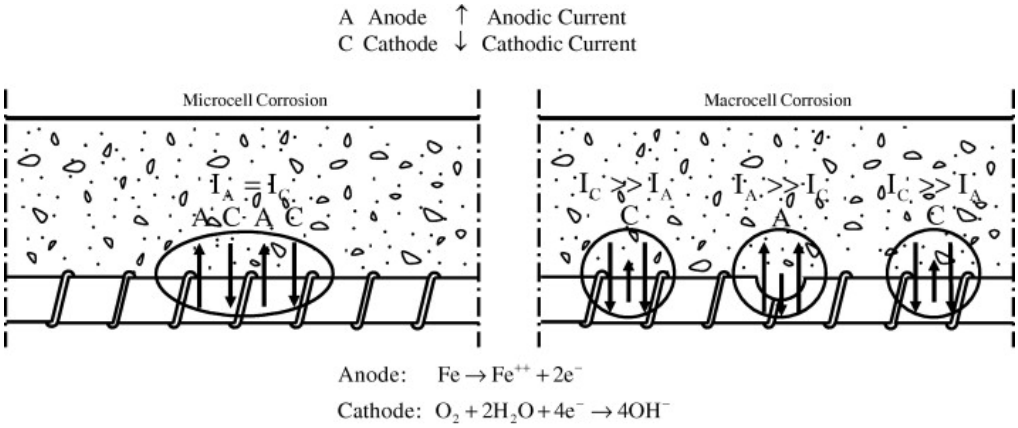


Figure 2.8: Microcell and macrocell corrosion (Cao et al., 2013).

The work used the thick-walled cylinder model shown below (Fig. 2.9) to investigate the degradation process and proposed equation 2.15 for the determination of the effective crack width opening on the concrete cover surface

$$w = 2\pi b.\left(\frac{2}{(\frac{b}{a})^2+1}\frac{u_{st}}{a} - \varepsilon_{cr}\right) \quad (2.15)$$

where,

w = crack width opening

$\varepsilon_{cr}$ = critical cracking strain

b = $R_c$ = Splitting crack front for a fully cracked thick-walled cylinder

$u_{st}$ = rust expansion beyond the porous zone

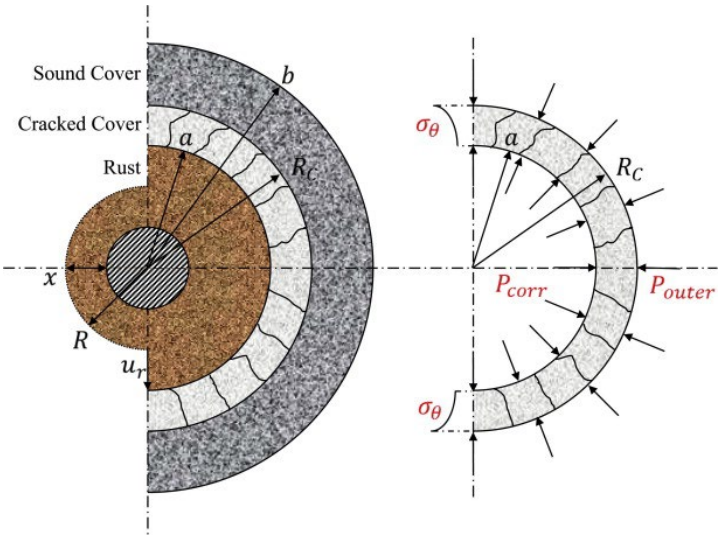


Figure 2.9 Uniform cracking model (Cao et al., 2013).

## 2.3 Numerical modelling of RC elements

Finite element (FE) has been used extensively by researchers to model and analyse the response of structural elements to loadings and deformations. These models, though, could not predict the behaviour of the RC elements correctly due to the difficulties and complexities involved in estimating the actual response of the structures. Nevertheless, these models pave the way for the improvement of FE analysis software such as ABAQUS, ANSYS and LS-DYNA by researchers for use in investigating the behaviour/response of RC elements (Al-Amin & Ahsan, 2012; Song & Lu, 2011; Yu et al., 2010a, 2010b; Zeng, 2016; Zeng, 2017).

### 2.3.1 Definition of plastic flow potential and yield function

Concrete is a complex material characterised by many parameters such as average compressive strength, average tension strength, crushing energy, fracture energy, etc. Usually, the values of these parameters are obtained through experiments (Le Minh et al., 2021). Several models have been proposed to describe the behaviour of concrete from the un-crack/un-crush stage to the failure stage. The damage concrete plasticity model (CDP) is widely used in all models. This model is employed in the ABAQUS manual (ABAQUS, 2019). The yield function in CDP is modified to account for the increased strength due to the effects of confinement. CDP is one of the possible constitutive models to predict the constitutive behaviour of concrete. It describes the constitutive behaviour of concrete by introducing scalar damage variables (Sümer & Aktaş, 2015). CDP can characterise the tensile and compressive response of concrete in Figure 2.10

The unloaded response of concrete specimens seems to be weakened because the elastic stiffness of the material appears to be damaged or degraded (Sümer & Aktaş, 2015). The degradation of the elastic stiffness on the strain-softening branch of the stress-strain curve is characterised by two damage variables (tensile damage ($d_t$) and compressive damage ($d_c$)) which can take values from zero to one. Zero represents the undamaged concrete material, while one represents a total loss of strength (ABAQUS, 2019). $E_0$ , is the initial (undamaged) elastic stiffness of the material and $\tilde{\varepsilon}_c^{pl}$, $\tilde{\varepsilon}_t^{pl}$, $\tilde{\varepsilon}_c^{in}$, $\tilde{\varepsilon}_t^{in}$, are the compressive plastic strain, tensile plastic strain, compressive inelastic strain and tensile inelastic strain respectively.

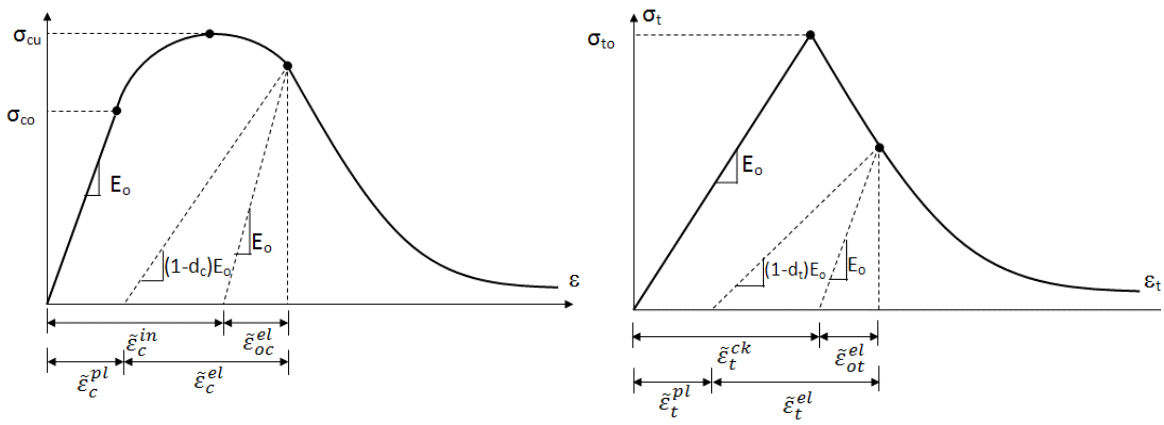


Figure 2.10. The behaviour of concrete under axial loading (a) compressive and (b) tensile (ABAQUS, 2019)

The stress-strain relations under uniaxial tension and compression are presented in Eq. (2.16) and Eq. (2.17) respectively.

$$\sigma_t = (1 - d_t) \cdot E_0 \cdot (\varepsilon_t - \tilde{\varepsilon}_t^{pl}) \tag{2.16}$$

$$\sigma_c = (1 - d_c) \cdot E_0 \cdot (\varepsilon_c - \tilde{\varepsilon}_c^{pl}) \tag{2.17}$$

The effective cohesion stresses determine the size of the yield (or failure) surface (Figure 2.11). In Abaqus the parameters required to define the yield surface consists of four constitutive parameters. The Poisson's ratio controls the volume changes of concrete for stresses below the critical value which is the onset of inelastic behaviour. Once the critical stress value is reached, concrete increases plastic volume under pressure (Chen, 2007). This behaviour is taken into account by defining a parameter called the angle of dilation.

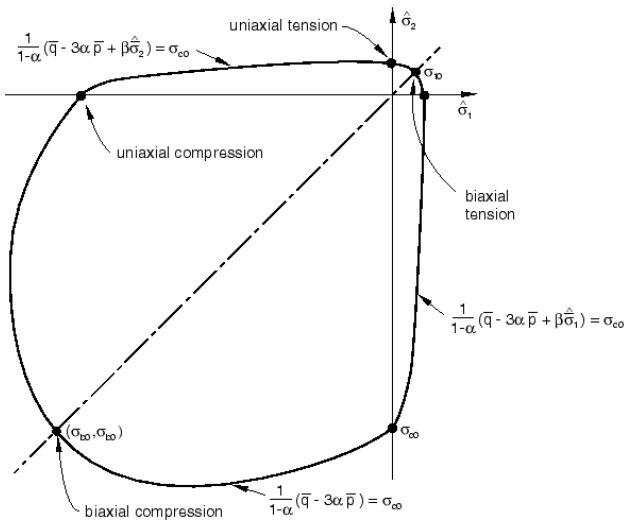


Figure 2.11. Biaxial yield surface in CDP Model (ABAQUS, 2019)

In the CDP model, ψ is the dilation angle measured in the p-q plane at high confining pressure, and in this study, it is determined with sensitivity analysis. єєis an eccentricity of the plastic potential surface with a default value of 0.1. The ratio of initial biaxial compressive yield stress to initial uniaxial compressive yield stress,$\sigma_{b0}/\sigma_{c0}$, with a default value of 1.16. Finally, $K_c$ is the ratio of the second stress invariant on the tensile meridian to the compressive meridian at the initial yield with a default value of 2/3 (ABAQUS, 2019). The parameter $K_c$ should be defined based on the full triaxial tests of concrete. Moreover, a biaxial laboratory test is necessary to determine the value of $\sigma_{b0}/\sigma_{c0}$.

Hany et al. (2016) used ABAQUS to model the stress-strain response of concrete columns and proposed a modified concrete damage plasticity model (CDPM) to predict the confined column's monotonic response accurately. The model developed applies to columns with different cross-sections and concrete with varying degrees of strength.

Morshed et al. (2016) performed nonlinear FEM on GFRP RC columns to investigate the post-peak behaviour and failure mode of short RC columns subjected to concentric loading. The numerical model was completed in ABAQUS using five specimens (3 GFRP and two steel RC columns). The result showed that the numerical model could accurately predict the peak load and post-peak behaviour of GFRP RC columns reliably.

Chi et al. (2017) presented a numerical work modifying the CDPM to accurately simulate the mechanical response of hybrid fibre reinforced concrete (HFRC). The FE software ABAQUS was used to investigate the fibre effect dependent on the damage evolution, yield criterion, hardening/softening law and plastic potential used in CDPM. The stress-strain relationship of CDPM in ABAQUS (Fig. 2.12 – 2.14) was modified with the resulting model validated against experimental results and found to be in close agreement.

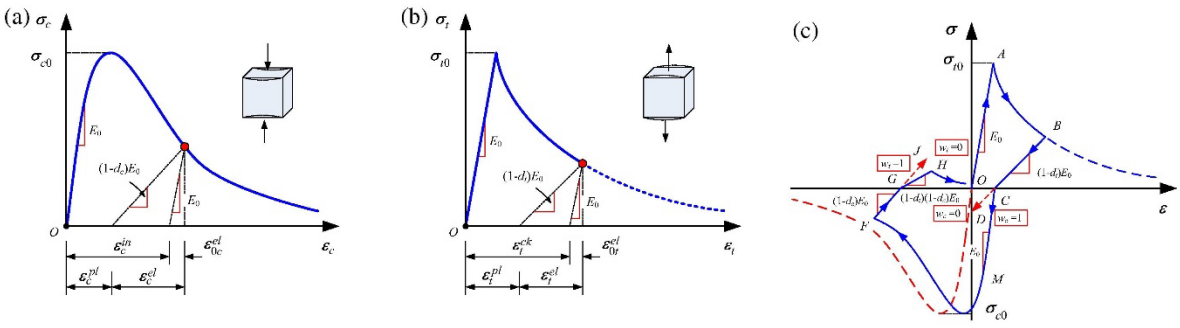


Figure 2.12: Stress-strain relationships of CDPM in ABAQUS, (a) compressive curve, (b) tensile curve, and (c) uniaxial load cycle (tension-compression-tension) response considering different values for the stiffness recovery factors (Chi et al., 2017)

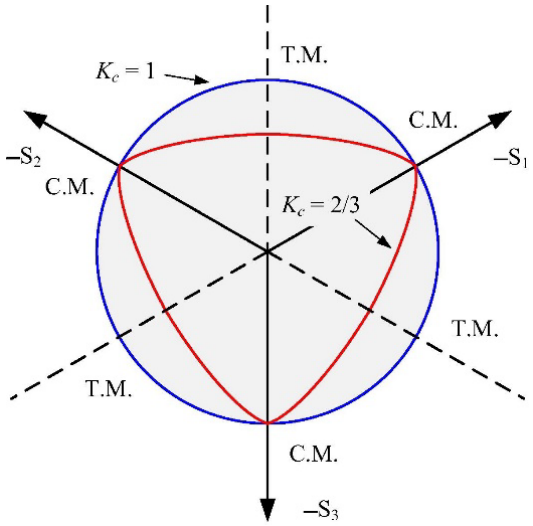


Figure 2.13: Deviatoric cross-sections of failure surface in ABAQUS (Chi et al., 2017).

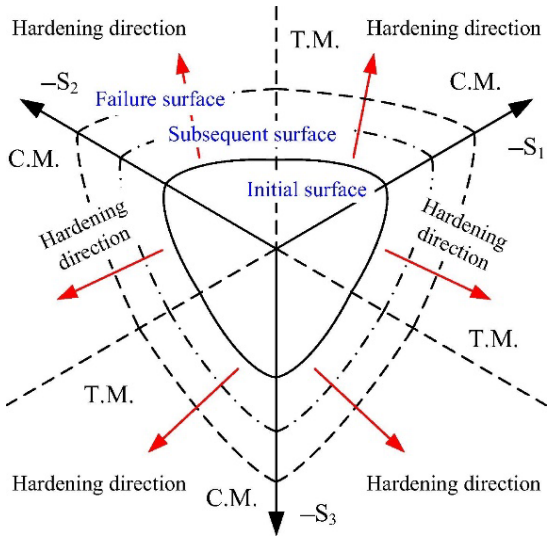


Figure 2.14: Isotropic hardening in the deviatoric plane in ABAQUS (Chi et al., 2017).

Mohammed et al. (2018) proposed a simplified nonlinear finite element analysis (NLFEA) to investigate the structural performance and residual capacities of aged beam-columns using slab-on-girder bridge columns subjected to the combined effect of rebar corrosion and external loads. The model established that critical sections identified at the design stage do not necessarily remain essential during the evaluation of an aged structure. Also, the efficiency and insensitivity of the NLFEA to controlling parameters of the nonlinear analysis indicate that it could be used for both the nonlinear static and/or dynamic analysis of corroded bridge elements.

Bossio et al. (2015) used FEM to simulate pitting or general corrosion on a cylindrical specimen reinforced with a single bar to demonstrate the possibility of extending the results to more complex RC members. The analysis also involved proposing an analytical model to evaluate the nonlinear development of stresses in the concrete and the crack propagation when rebars start to

corrode. The results showed that the maximum tensile stress is attained close to the bar in the circumferential direction, and the crack develops in the radial direction until it reaches the external surface of the concrete. Also, the results agreed with experimental results in the literature.

Salman and Al-Sherrawi (2018) used FEM to simulate and investigate the behaviour of using steel jackets to strengthen unloaded RC columns with design error and pre-loaded non-damaged RC columns. ABAQUS software was used in this analysis, with the results agreeing with previous experimental and analytical results. The proposed stress-strain relationship is:

$$\sigma_c = \frac{E_c \varepsilon_c}{1+(R+R_E-2)\left(\frac{\varepsilon_c}{\varepsilon_0}\right)-(2R-1)\left(\frac{\varepsilon_c}{\varepsilon_0}\right)^2+R\left(\frac{\varepsilon_c}{\varepsilon_0}\right)^3} \quad (2.18)$$

where,

$$R = \frac{R_E(R_\sigma-1)}{(R_\varepsilon-1)^2} - \frac{1}{R_\varepsilon}$$

$$R_E = \frac{E_c}{E_0}$$

$$E_0 = \frac{f_c}{\varepsilon_0}$$

$R_\sigma$ and $R_\varepsilon$ is assumed to be 4

$E_c$ = Elastic modulus ($E_c = 4700\sqrt{f_c}$ )

$\varepsilon_0$ = concrete strain corresponding to $f_c$ ($\varepsilon_0 = (0.2f_{cu} + 13.06) \times 10^{-4}$) - (Almusallam & Alsayed, 1995)

$f_{cu}$= concrete compressive strength

**Table 2.1: Summary of numerical modelling of RC structures**

| Study | Type of analysis | Type of structures | Rebar numbers and diameter | Sample sizes | Summary of results |
|---|---|---|---|---|---|
| **Yu et al., 2010a** | Drucker-Prager Model (D-P) in (ABAQUS) | circular columns confined with FRP jackets | | 152mm × 305mm | The D-P model in ABAQUS was modified to accurately predict actively and passively confined concrete. |
| **Yu et al., 2010b** | Concrete Damaged Plasticity Model (CDPM) in ABAQUS | Circular and square columns | | 152mm × 305mm circular and 150mm width square | The proposed CDPM agreed with the existing test results |
| **Al-Amin & Ahsan, 2012** | FE analysis using ANSYS | Rectangular columns | 4 and 8 number of rebars | 250×250mm, 300×300mm and 350×350mm and varying heights of 3000mm and 2400mm | The model could predict the response of columns similar to the provision of ACI code. |
| **Zeng, 2016** | FE analysis using ABAQUS | square RC columns | 8 No. of rebars | 305 × 305mm | The proposed model evaluates the behaviour of square RC columns under axial load. |
| **Hany et al. (2016)** | Concrete Damaged Plasticity Model (CDPM) in ABAQUS | Circular, square and rectangular columns | | | The modified CDPM showed an excellent agreement with the test data. |

| | | | | | |
|---|---|---|---|---|---|
| **Morshed et al. (2016)** | Concrete Damaged Plasticity Model (CDPM) in ABAQUS | Square RC columns with steel and GFRP bars | 19.1mm and 15.9mm | 350 × 350 × 1400mm | The model reproduced the columns' peak axial stress, deformation, post-peak behaviour and failure modes. |
| **Zeng, 2017** | Concrete Damaged Plasticity Model (CDPM) in ABAQUS | Square RC Columns with different configurations of transverse reinforcement | | | The FE model correctly predicts the response of confined RC columns by evaluating the effect of confinement reinforcement configuration. |
| **Chi et al. (2017)** | Modified concrete Damaged Plasticity Model (CDPM) in ABAQUS | Square RC columns with a large stub | 14mm bars with 8mm stirrups | 200 × 200mm column with 900 × 400 × 400mm stub | The modified model showed a close agreement between numerical predictions and test results. |
| **Salman and Al-Sherrawi (2018)** | Finite Element Model (FEM) using ABAQUS | Square and rectangular RC columns | 4 – 10mm bars with 6mm stirrups and 4 – 8mm bars with 6mm stirrups | 150 × 150 × 1000mm square column and 120 × 160 × 1000mm rectangular column | The FEM showed good agreement with the existing experimental and analytical results |

All the numerical methods modified the Concrete Damaged Plasticity Model (CDPM) in ABAQUS by adjusting parameters such as the flow rule, damage evolution, yield criterion, hardening and softening law and the plastic potential of RC elements to analyse their structural responses under load. It should be noted that most of the analyses were on pristine/plain concrete strengthened with FRP.

## 2.4 Experimental works on corrosion of RC elements

This section gives a brief of some of the experimental works that have been done on corroded RC beams and columns. In marine/aggressive environments, bridges suffer massive degradation, reducing their seismic capacity and durability. A lot of research has been done to investigate the structural behaviour of corroded rebars in RC structures located in marine environments, with the conclusion that the corrosion of rebars leads to a reduction in the ductility and load-carrying capacities of such members (Apostolopoulos & Papadopoulos, 2007; Apostolopoulos et al., 2006; Kashani et al., 2013a; Kashani et al., 2013b; Ma et al., 2012).

A state-of-the-art review of existing literature on experimental works on corroded beams and columns was carried out by Kashani et al. (2019) to ascertain the current state of knowledge on corroded RC structures. The review showed that there is quite a lot of experimental data available in the literature on large-scale testing of corroded RC beams in flexure and shear under monotonic and cyclic static loading. At the same time, there are very few experimental data and results on corroded RC columns, both circular and rectangular, under axial and lateral (monotonic and cyclic) loading. Also, experimental testing of corroded RC columns has been mainly on compression and flexure, with no experimental testing on the shear critical column.

### 2.4.1 Axial load testing of corroded RC columns

Ageing RC columns/piers generally fail through buckling the vertical reinforcement bars together with the crushing of core confined concrete and the fracture of the longitudinal bars (Kashani et al., 2019), resulting from inadequate confining transverse reinforcements. The failure becomes more critical in columns/piers in corrosion-laden environments where chloride-induced corrosion is prevalent and significantly affects the stress-strain behaviour of reinforcing bars. Therefore, numerous models are proposed to investigate the axial load-displacement behaviour of R.C. columns/piers in seismic regions (Hoshikuma et al., 1997; Z. Li et al., 2022; Liang et al., 2015; Mander et al., 1988; Saatcioglu & Razvi, 1992; Zeng, 2017).

Andisheh et al. (2021), conducted an experiment to investigate the effect of corrosion on the stress-strain response of confined concrete. They used 12 circular RC columns in the investigation (seven corroded and five non-corroded) with spiral confinement having different pitches. The corroded RC columns were categorized into four corrosion groups classified as non-corroded, low corrosion, high corrosion, and mechanical pitting corroded (Fig. 2.15).

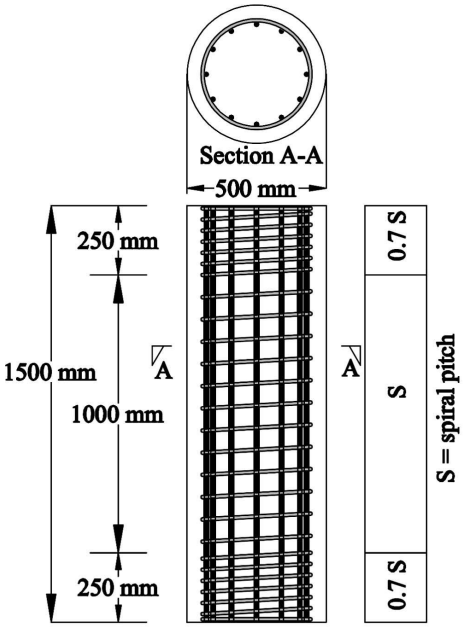


| Column Type | Spiral pitch S (mm) | Longitudinal reinforcement | | Confining reinforcement |
|---|---|---|---|---|
| | | Number | Diameter D (mm) | Diameter D (mm) |
| Low confined | 103 | 12 | 16 | 12 |
| Medium confined | 69 | 12 | 16 | 12 |
| High confined | 41 | 12 | 16 | 12 |

| Concrete | | | Steel |
|---|---|---|---|
| $f'_c$ (MPa) | Aggregate (mm) | Slump (mm) | Grade |
| 30 | 19 | 100 | 300 |

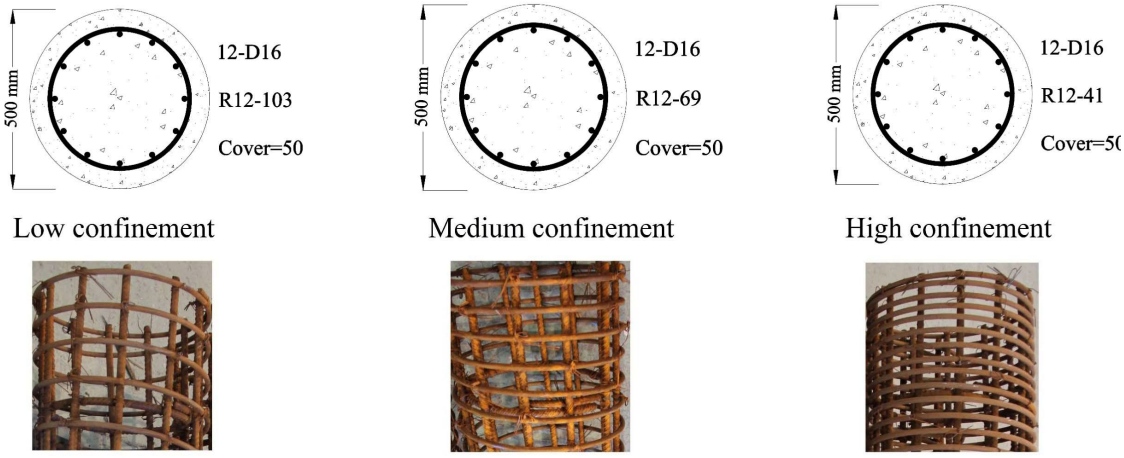


Figure 2.15: Details of the columns, confining reinforcement, and materials (Andisheh et al., 2021)

The experimental results were used to validate the proposed stress-strain model and shows good agreement with analytical models in the literature. Also, the corrosion of the confining steel results in a decrease in both the ultimate compressive strength and ultimate strain in the confined concrete, which caused significant changes to the shape of the stress-strain curves for RC columns (Fig. 2.16). The analytical model was developed based on the Mander (1983), Mander et al. (1988) and corrosion-induced deterioration models by Andisheh, Liu, et al. (2018); Andisheh et al. (2016a, 2016b); Andisheh, Scott, et al. (2018); Andisheh et al. (2019).

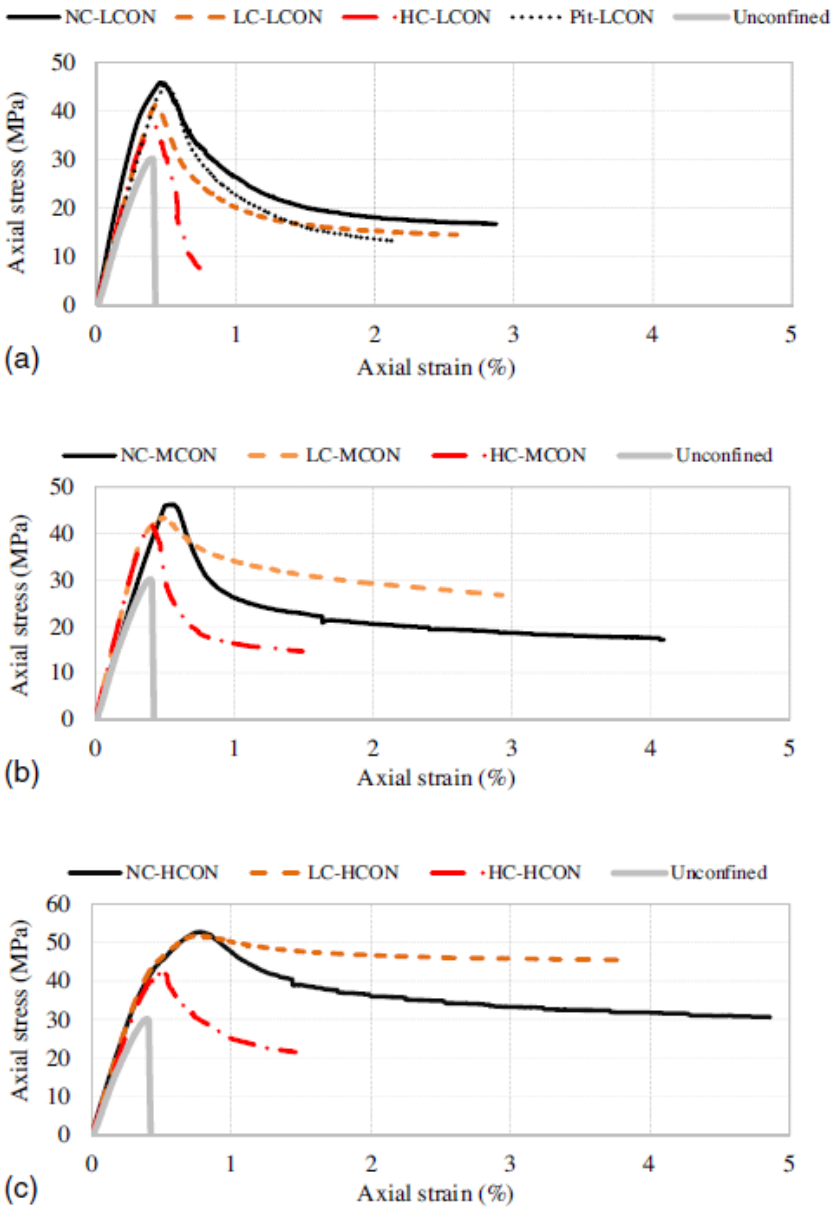


Figure 2.16: Stress-strain relationship of concrete with varying degrees of corrosion and confinement arrangements (Andisheh et al., 2021)

Liang et al. (2014) investigated experimentally and analytically the axial compressive load-carrying capacity and behaviour of square composite steel and concrete columns confined by multiple interlocking spirals. The columns were tested under monotonically increased axial load. The test results demonstrated that the composite columns with multiple spirals achieved great axial load-carrying capacity and deformability because of the excellent concrete confinement attributed to the numerous interlocking spirals and the structural steel section. Smaller spacing of the spirals and larger area of the highly confined concrete in the composite columns resulted in better strength and ductility.

Ma et al. (2022) investigated the effect of corrosion and different configurations of transverse reinforcement on the stress-strain behaviour of confined concrete in rectangular columns. A total of 27 RC columns categorised into three groups (Group A, Group B and Group C) based on cross-sectional shapes and configurations of transverse reinforcement, as illustrated in Fig. 2.17, were designed and tested. The columns were made with C35 concrete and subjected to 0%, 10% and 20% corrosion mass loss.

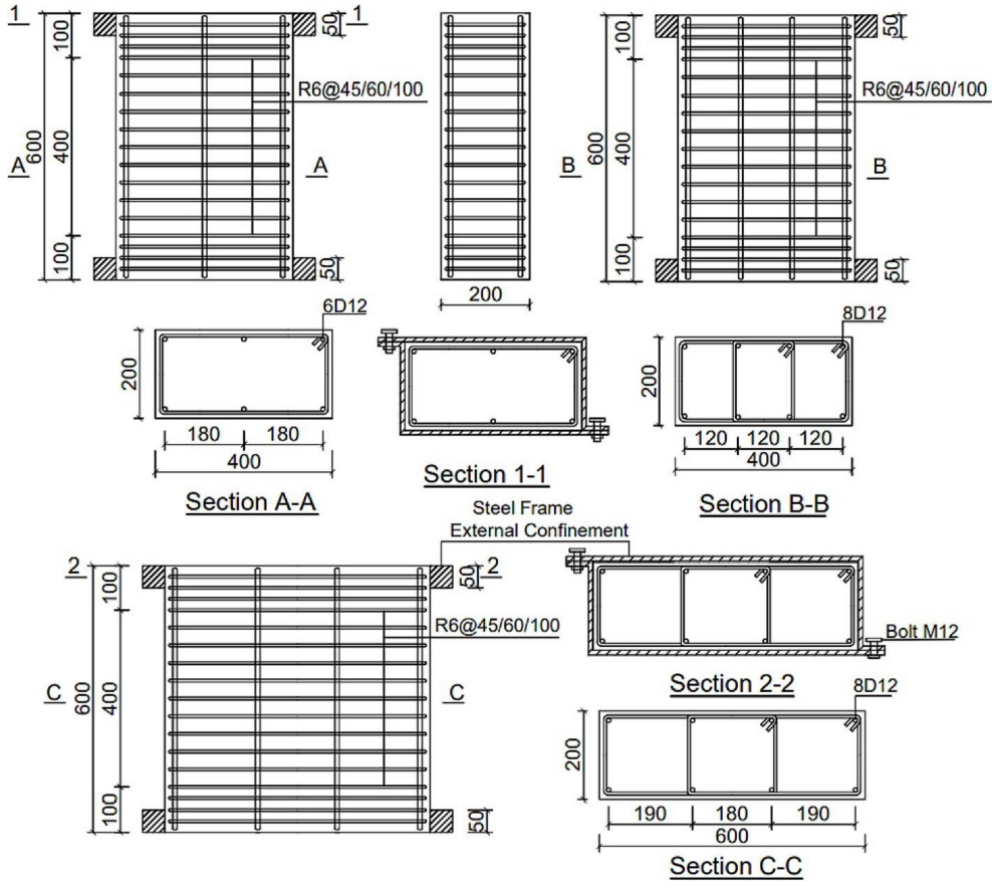


Figure 2.17: Specimen dimensions and reinforcement layouts (Ma et al., 2022)

The test result showed that corrosion degrees significantly influence the specimens' maximum stress and corresponding axial strain. Based on the test data and nonlinear regression analyses, empirical equations were proposed to account for the impacts of both reinforcement corrosion and the rectangular shape of transverse reinforcement on three critical characteristic parameters of the stress-strain curves, namely the maximum strength, the axial strain at maximum strength and the ultimate strain of confined concrete. Comparisons revealed that the proposed stress-strain model outperformed existing models and demonstrated good agreement with test results (Fig. 2.18).

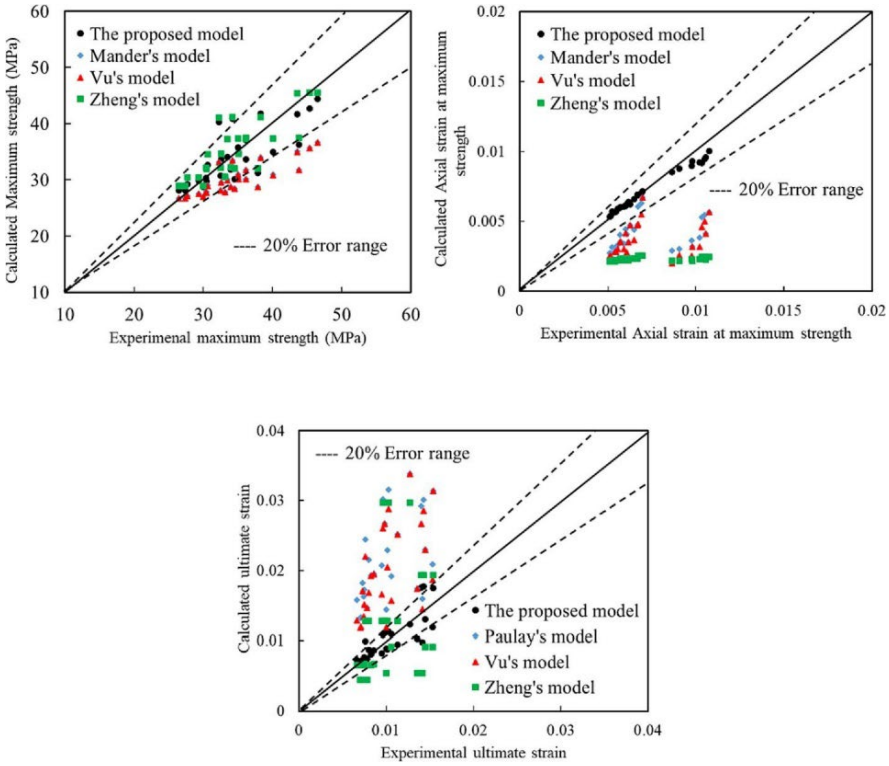


Figure 2.18: Comparisons of experimental and analytical results in terms of f′$_{cc}$, $\varepsilon_{cc}$ , and $\varepsilon_{cu}$ (Ma et al., 2022)

P. Li et al. (2022) investigated the effect of corrosion-induced damage on the mechanical properties of corroded RC columns repaired with large rupture strain fibre-reinforced polymer. A total of sixteen RC circular columns (Fig 2.19), made with 30MPa concrete, were corroded to different extents (0%, 5%, 10%, 15%, and 25%) by an electrochemical method (Fig 2.20) and then repaired by wrapping them with FRP (Fig 2.21). The repaired RC columns were afterwards subjected to monotonic axial compression tests.

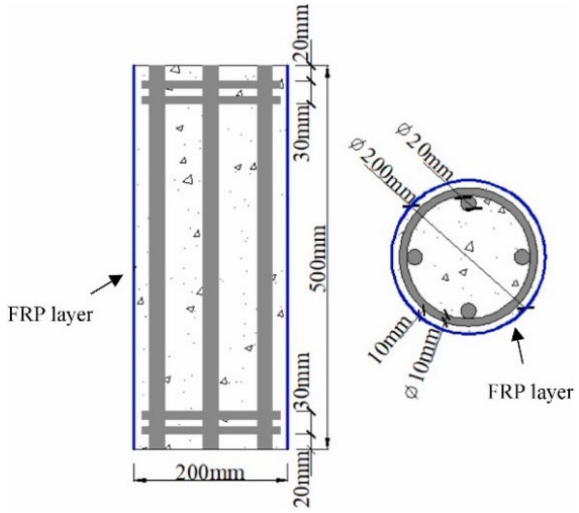


Figure 2.19: Schematic diagram of the specimens (P. Li et al., 2022)

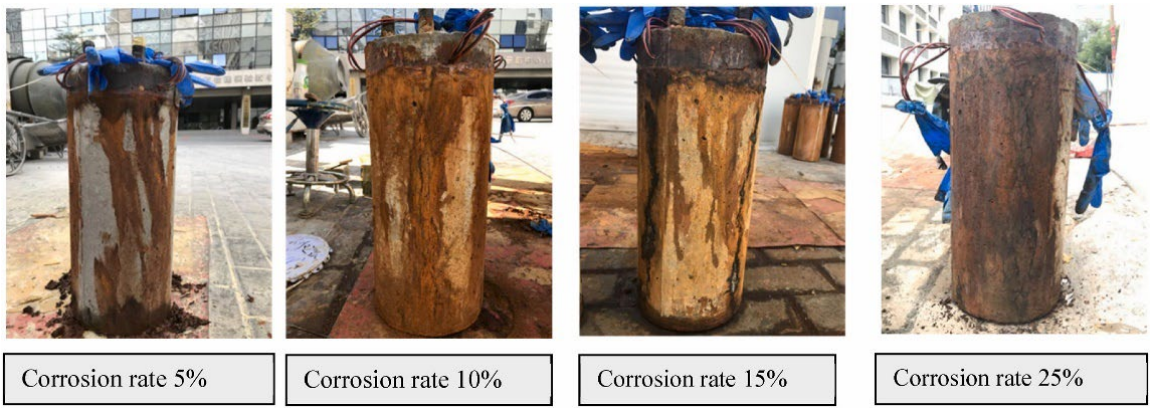


Figure 2.20: The RC column appearance after corrosion (P. Li et al., 2022)

Figure 2.21: FRP wrapping (P. Li et al., 2022)

The test results show that LRS-FRP confinement effectively enhanced the mechanical properties of corroded RC columns. However, corrosion weakened the rebar cross-sections and further damaged the confined inner concrete, significantly influencing the compressive strength and ductility of the repaired RC columns. In addition, rebar buckling was more pronounced at higher corrosion rates, which affected the hoop strain distribution of the FRP and further reduced its confinement effectiveness.

Zhang et al. (2022) investigated RC's confinement performance and stress-strain response with corroded reinforcement, considering key parameters such as corrosion levels, size effect, stirrup configurations, and effects of synchronized corrosion of the stirrups and longitudinal reinforcements. A total of 29 square RC columns, corroded through accelerated corrosion tests, were examined using axial compression evaluations. The theoretical corrosion levels of the stirrups ranged from 0% to 20%, with transverse reinforcements spacing between 50mm and 125mm (Fig. 2.22). The compressive strength of the unconfined concrete of the columns is 19.8MPa.

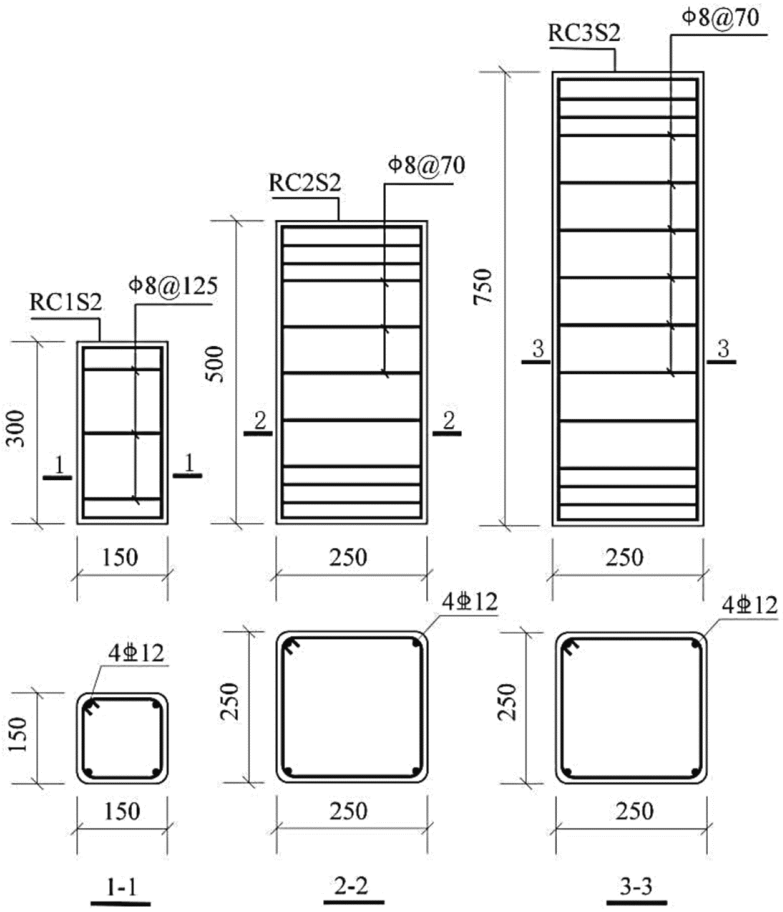


Figure 2.22: The geometry and reinforcement of the specimen (all the dimensions are in mm) (Zhang et al., 2022).

The test results revealed that the confinement behaviours were significantly affected by the severity of the corrosion of the stirrups, including the failure mode, bearing capacity and deformability. Also, the confinement performance is greatly influenced by the stirrup spacing and specimen sizes.

These experimental tests are mostly on normal or high-strength concrete structures, but many low-strength RC structures are aged 50 years and older worldwide. Therefore, studying their response/behaviour under load requires proper strengthening/repair methods.

**Table 2.2: Summary of Experimental studies on monotonic tests on corroded RC columns**

| References | Exposure type | No. of specimen and dimensions (mm) | Strength of concrete (MPa) | Rebar diameter (mm) | Corrosion rate and method | Summary of test results |
|---|---|---|---|---|---|---|
| **Joshi et al. (2015)** | accelerated corrosion condition (3.5% NaCl) | 53 square specimens (150 × 150 × 450mm) GFRP wrap | 37.1 – 41.3 | 12mm bars with 6mm stirrups | 0%, 3% and 6% (Faraday's law) | The strength and ductility of the strengthened confined concrete were affected by the corrosion of the tie reinforcements. GFRP wraps considerably improve corroded confined concrete's ductility and strength, compared to other wraps such as Ferrocement jacketing. |
| **Vu et al. (2017)** | accelerated corrosion condition (5% NaCl) | 36 specimens (200mm square and 200mm dia. circular with 600mm height) | 25.3 – 31.9 | 10mm bars with 6mm transverse reinforcements | 28 days (Gravimetric Method) | The ductility and strength of corroded columns reduce as the corrosion rate increases. The pitting corrosion can be noticed more in specimens with high corrosion rates. |

| | | | | | | |
|---|---|---|---|---|---|---|
| **Wu et al. (2019)** | accelerated corrosion condition (5% NaCl) | 20 square specimens (250 × 600mm) epoxy coating | 60.6 | 16mm bars with 16mm transverse reinforcements | 5%, 10% and 15% (Faraday's law) | The ultimate bearing capacity is reduced as the corrosion rate increases. Under the same load condition and corrosion rate, the maximum bearing capacity of columns with epoxy-coated stirrups is higher than those with standard stirrups. |
| **Andisheh et al. (2021)** | accelerated impressed current (AIC) corrosion (3.5% NaCl) | 12 circular RC columns (500mm dia. × 1500mm high) | 28 – 31 | 12 – 16mm main bars with 12mm spiral transverse reinforcements | Varying from 0% to 26.5% | The corrosion of the confining steel results in a decrease in the ultimate strength and strain. Also, the corrosion of the transverse reinforcement significantly increases the drop in the post-peak behaviour of the columns. |
| **Ma et al. (2022)** | accelerated corrosion (5% NaCl) | 27 rectangular RC columns (200 × 400mm, 200 × 600mm) and 600mm high | 24.94 | 6 - 12mm bars with 6mm transverse reinforcements at different spacings | 0%, 10% and 20% | The stress-strain model outperformed existing models and demonstrated good agreement with test results. |
| **P. Li et al. (2022)** | accelerated corrosion (5% NaCl) | 16 cylindrical RC columns (200mm dia. × 500mm high) | 38.3 | 4 - 20mm bars with 10mm | 0%, 5%, 10%, 15% and | The test results show that LRS-FRP confinement effectively enhanced the mechanical properties of corroded RC |

| | | | | | | |
|---|---|---|---|---|---|---|
| | | Confined with large rupture strain (LRS) fiber-reinforced polymer (FRP). | | transverse reinforcements | 25% (Faraday's law) | columns. Also, corrosion weakened the rebar cross-sections, which significantly influenced the compressive strength and ductility of the repaired RC columns. Furthermore, rebar buckling was more pronounced at higher corrosion rates, which affected the hoop strain distribution of the FRP and further reduced its confinement effectiveness. |
| **Zhang et al. (2022)** | accelerated corrosion condition (5% NaCl) | 29 square columns (150 × 150 × 300mm, 250 × 250 × 500mm and 250 × 250 × 750mm) | 19.8 and 22.7 | 4 - 12mm bars with 8mm transverse reinforcements | 5%, 10%, 15% and 20% (Faraday's law) | The test results revealed that the confinement behaviours were significantly affected by the severity of the corrosion of the stirrups, including the failure mode, bearing capacity, and deformability. |

### 2.4.2 Cyclic load experimental tests of corroded RC columns

Cyclic experiments are a significant method to provide insight into the seismic performance and response of the structural component. However, although it is recognized that the corrosion-induced damage on coastal bridge piers significantly affects the safety of the structures during the long-term service period, the damage mechanism and the mechanical behaviour are still seldom understood. Hence, several research studies have investigated the response of corroded RC columns to cyclic loading.

Guo et al. (2015) investigated the cyclic performance of RC piers with chloride-induced corrosion in a marine environment. The investigation involved using four specimens, one un-corroded and the other three having different levels of corrosion, to check the effects of corrosion damage on the seismic behaviour of RC piers. The detail of the RC piers used in the investigation is presented in Figure 2.23.

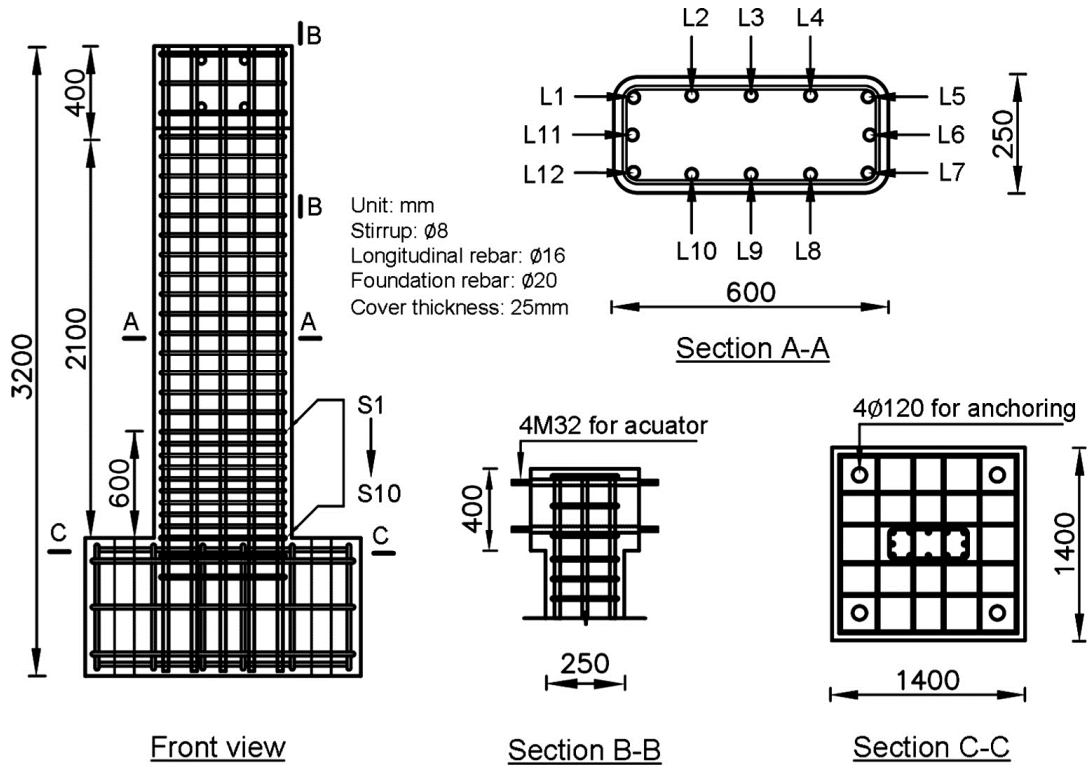


Figure 2.23: Schematic diagram of the specimen (Guo et al., 2015)

The columns were corroded to an estimated corrosion mass loss of 5%, 10% and 15% using the accelerated corrosion technique. The average compressive strength of the concrete used in the test was 42.9MPa. The test results revealed a higher degree of degradation for higher corrosion levels with a reduction in strength, ductility and energy dissipation capacity, all indicative of the seismic performance.

Yuan et al. (2017) investigated the effects of non-uniform corrosion on the cyclic behaviour of corroded bridge piers in the marine environment using the method of plastic hinge transfer by subjecting six RC circular bridge piers (Fig. 2.24) with varying degrees of corrosion to cyclic loads.

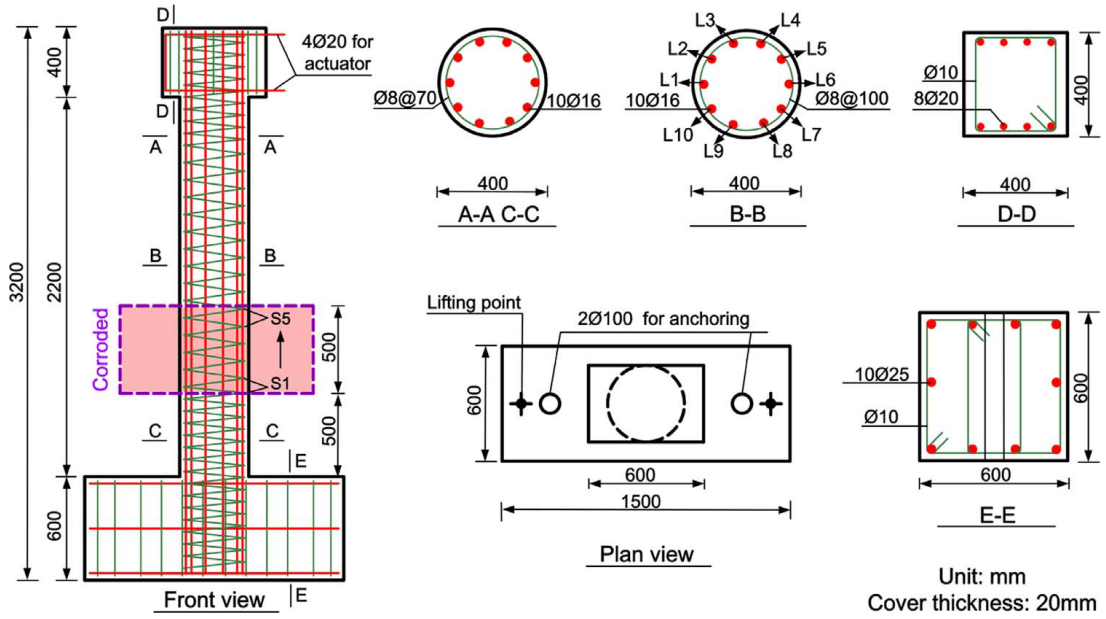


Figure 2.24: Schematic diagram of the RC columns (Yuan et al., 2017)

The thickness of the concrete cover was 20 mm, and the average compressive strength of the concrete was tested to be 36.3 MPa. The columns were subjected to constant current accelerated corrosion for 30, 60, 105, 130 and 150 days to achieve different corrosion degrees. The test results were used to validate an earlier publication by the authors. They showed that the seismic performance of corroded RC columns is greatly affected by non-uniform corrosion of the rebars (Fig. 2.25). Also, the performance of the bridge columns in the marine environment depends on the deterioration that occurs at the splash and tidal zone.

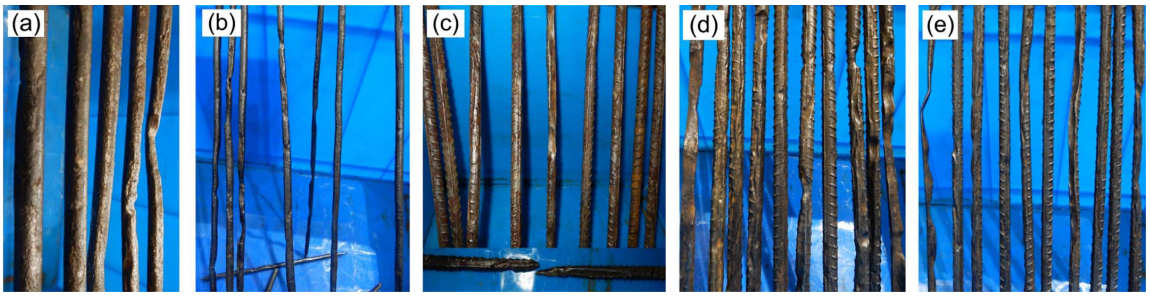


Figure 2.25: Close-up images of the corroded reinforcement: (a) D30-stirrups; (b) D60-stirrups; (c) D105-longitudinal bars; (d) D130-longitudinal bars; and (e) D150-longitudinal bars (Yuan et al., 2017)

Chlorine-induced corrosion significantly affects corroded RC structures' seismic performance, especially those located in marine and highly seismic regions. Wenting Yuan et al. (2018),

investigated the effect of non-uniform corrosion on bridge columns in the marine environment by applying biaxial quasi-static loads on the structural member. The experiment involved subjecting four bridge piers with varying corrosion degrees to biaxial pseudo-static cyclic loads with another corroded pier subjected to uniaxial load. The unconfined compressive strength of the concrete was 24.9MPa. The test result indicated that non-uniform corrosion in the splash and tide zones severely affects bridge piers' performance deterioration, with the effect more significant in the bi-axially loaded piers.

Rajput et al. (2019) Investigated the effect of high-performance fibre reinforced concrete (HPFRC) and glass fibre-reinforced polymer (GFRP) wraps on the seismic performance of corroded RC columns. The investigation used six full-scale columns (four corroded to 30% degree of corrosion and the other two uncorroded). The two un-corroded columns consisted of well-confined and under-confined (Figure 2.26). The results of the experiment showed that the corroded specimen retrofitted with only HPFRC jacket yielded a satisfactory recovery of strength and ductility in comparison to the un-corroded under-confined column, but showed lower ductility when compared with the seismically designed column specimen while wrapping of GFRP laminates further improved the performance of the specimens (Figure 2.27).

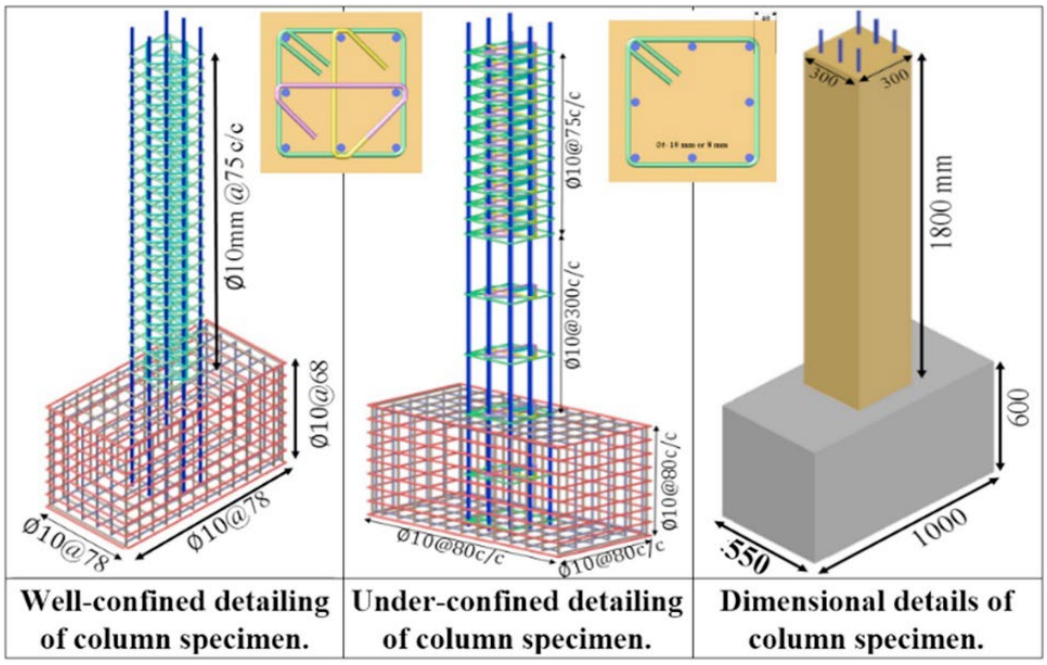


Figure 2.26: Reinforcement and dimensional details of specimens (Rajput et al., 2019)

Ma et al. (2012) conducted an experiment to investigate the seismic behaviour of 13 circular RC columns (Fig 2.27) with corrosion damage under cyclic loading. The corrosion loss applied in the investigation ranged from 0% to 15.1%, while the unconfined concrete's compressive strength was 32.4 MPa.

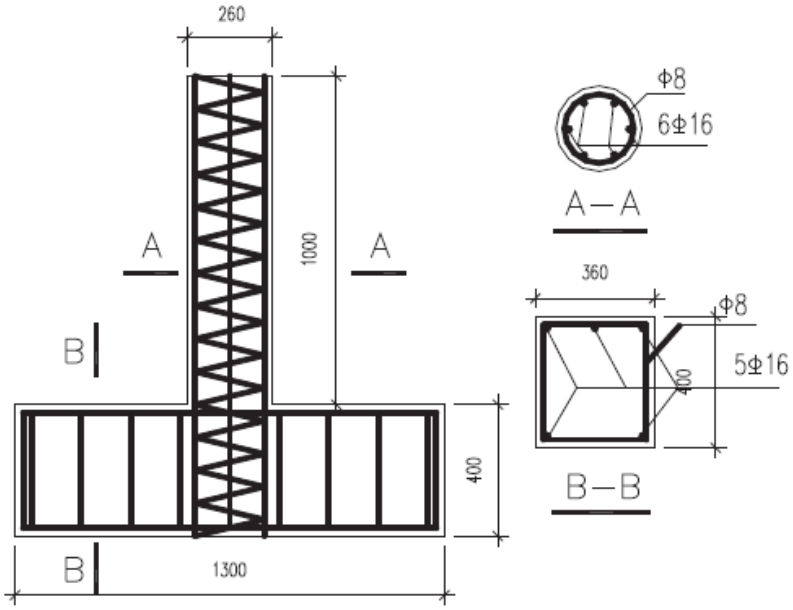


Figure 2.27: Details of test specimen (unit: mm). (Ma et al., 2012)

The experimental results demonstrated that increasing corrosion decreased the loading capacity, stiffness, ductility and energy dissipation capacity (Fig. 2.28). However, it was also found that the corroded specimens had almost the same energy dissipation capacity at the same displacement excursions when the mass loss was less than 14%.

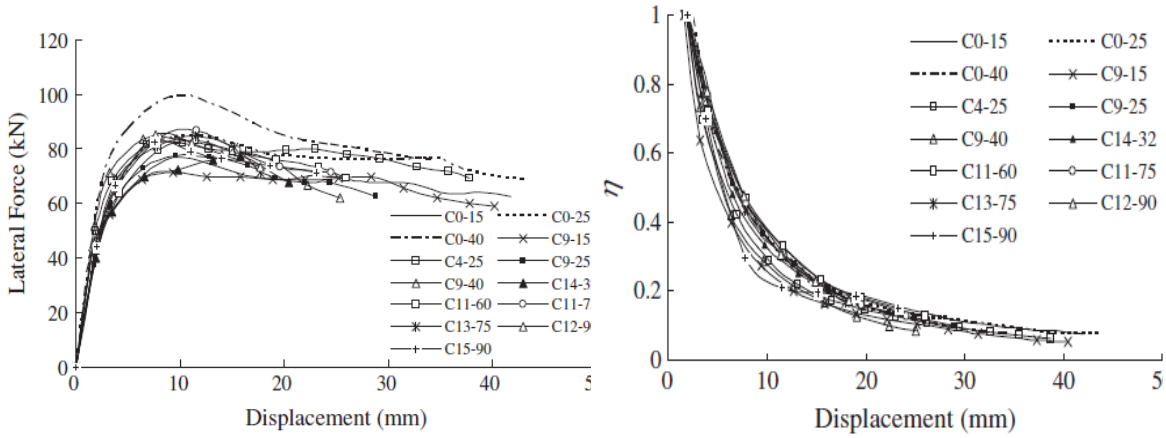


Figure 2.28: Response of the RC columns (a) Envelope curves (b) Stiffness degradation curves (Ma et al., 2012)

Li et al. (2009) experimentally investigated the effectiveness of applying carbon fibre-reinforced polymer (CFRP) sheets and steel jackets to upgrade corrosion-damaged reinforced concrete (RC) columns. The compressive strength of the concrete was 44.8MPa. The test results of 14 RC columns tested under combined lateral cyclic displacement and constant axial load indicated that the corrosion degree significantly affected the columns' behaviour. The column ductility was effectively improved by using the retrofit methods. It also showed that strengthening corroded RC columns with combined CFRP sheets and steel jackets effectively enhanced the seismic

performance of the columns and resulted in more stable hysteresis curves with lower strength degradations compared with the un-strengthened ones. It was also found that the corroded RC columns strengthened with combined CFRP sheets and steel jackets behaved better than those strengthened only with a single material.

Li et al. (2018) investigated the influence of seismic performance indicators such as bearing capacity, hysteresis characteristics, ductility, strength degradation, stiffness degradation and energy dissipation on the response of corroded RC columns. The compressive strength of the concrete used in the experiment was 50.3MPa. The experiment was performed on eight RC columns, and the results showed that the restraint of concrete provided by corroded stirrups is reduced, leading to a decline in seismic performance. With increasing stirrup corrosion, the failure limit displacement of columns decreases. The pinch phenomenon of the hysteresis curve gradually increases, the attenuation degree of strength and stiffness grows, and the ductility and energy-dissipation capacity is reduced. In contrast, the accumulated energy increases under the same control displacement. A method for predicting the lateral strength of reinforced concrete columns confined by corroded stirrups is presented based on the axial-shear-flexure interaction approach for conventional concrete columns, with modifications to consider the effect of stirrup corrosion. There was good agreement achieved between the test results and theoretical values.

Guohua et al. (2022) investigated the seismic performance of multiple reinforcement, high-strength concrete (MRHSC) columns having multiple transverse and longitudinal reinforcements in core areas. In the experiment, eight MRHSC columns were designed and subjected to a low cycle, reversed loading test as shown in Figure 2.29. The average compressive strength of the standard cubic specimens used in the columns was 54.3 MPa.

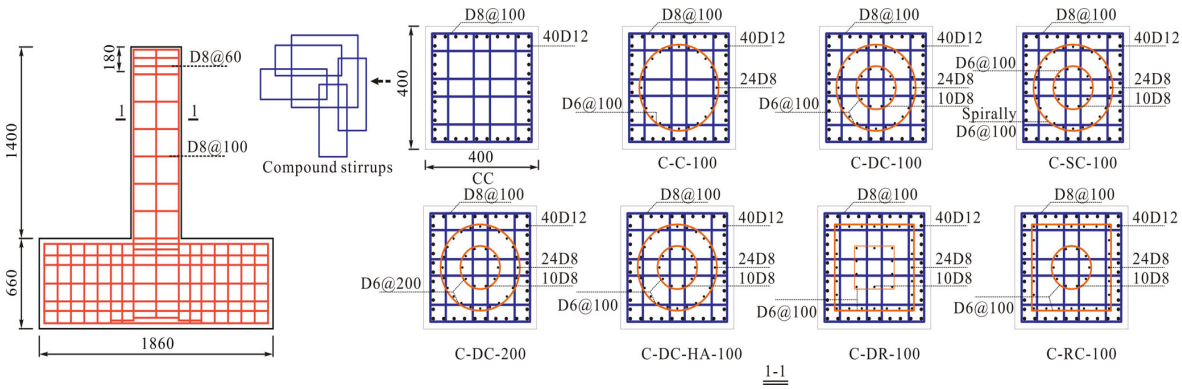


Figure 2.29: Design details of test specimens (Guohua et al., 2022).

The response, including the failure modes, hysteretic behaviour, lateral bearing capacity, and displacement ductility, was analyzed. The effects of the axial compression ratio, stirrup form, and stirrup spacing of the central reinforcement configuration on the seismic performance of the

columns were studied. The test results showed that these columns experienced two failure modes: shear failure and flexure-shear failure (Fig. 2.30). Also, as the axial compression ratio increased, the bearing capacity increased significantly, whereas the deformation capacity and ductility decreased.

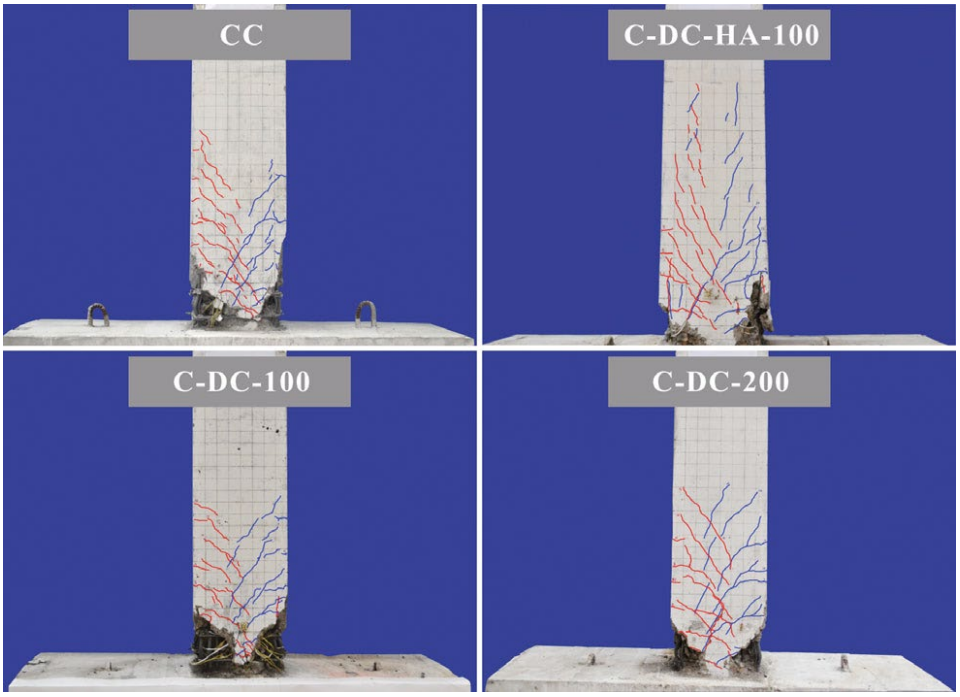


Figure 2.30: Crack distributions and failure modes (Guohua et al., 2022)

Luo et al. (2020) investigated the influence of corrosion on the seismic performance of RC columns. The investigations used eight full-scale RC columns (one uncorroded RC column, three RC columns with longitudinal reinforcement corrosion and four stirrup-corroded columns) (Fig. 2.31). The RC columns were corroded using the accelerated corrosion technique and subjected to repeated low-cycle loading. The compressive strength of the concrete used in the investigation at 28 days was 42.3MPa.

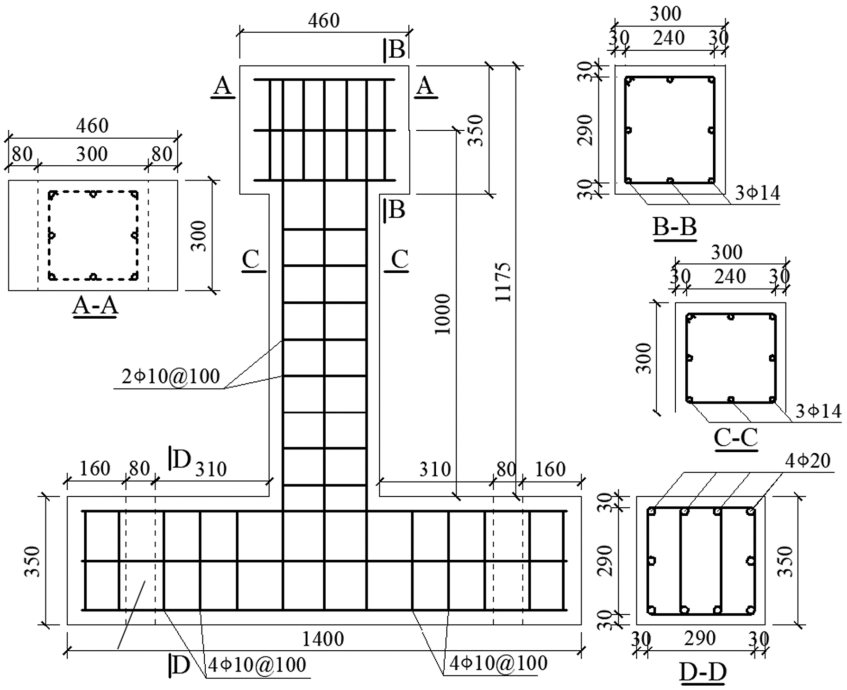


Figure 2.31: Column dimensions and reinforcement details (unit: mm) (Luo et al., 2020)

The experimental results show that with the increase in steel bars' corrosion degree, the pinch phenomenon of the hysteretic curve gradually increases, and the specimen's energy dissipation capacity, stiffness and plastic deformation capacity reduce significantly. The ductility and energy dissipation coefficient decreased by 20% and 36% (Fig. 2.32), respectively, when the stirrups corrosion ratio of the specimen reached 15.2%.

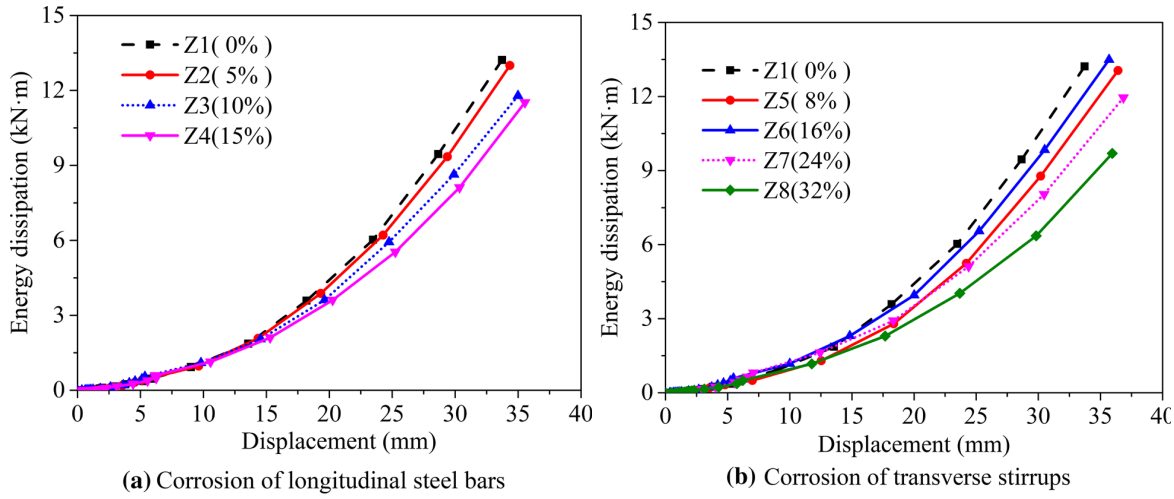


Figure 2.32: Cumulative energy dissipation curves of Z1–Z8 (Luo et al., 2020)

A shear failure surface was formed in the plastic hinge zone at the foot of the columns, which led to the change of failure mode from ductile bending failure to shear failure with poor ductility under the ultimate load for corroded columns. The influence of stirrup corrosion on the failure

mode of specimens is significant, but the effect of longitudinal reinforcement corrosion is negligible for samples with a corrosion ratio of 14.7%.

Zhang et al. (2023) investigated the seismic performance of RC columns of low-strength concrete. A total of 11 RC columns of low-strength concrete with different corrosion degrees were subjected to low-cycle repeated loading and axial compression ratios ranging from 0.25 to 0.75 (Fig. 2.33). The concrete strength was 15MPa. Furthermore, the junction between the stirrups and longitudinal bars was insulated with epoxy resins and insulating tape to prevent the corrosion of the stirrups. The impact of reinforcement corrosion on the failure modes, hysteretic behaviour, skeleton curve and energy dissipation were analysed and discussed.

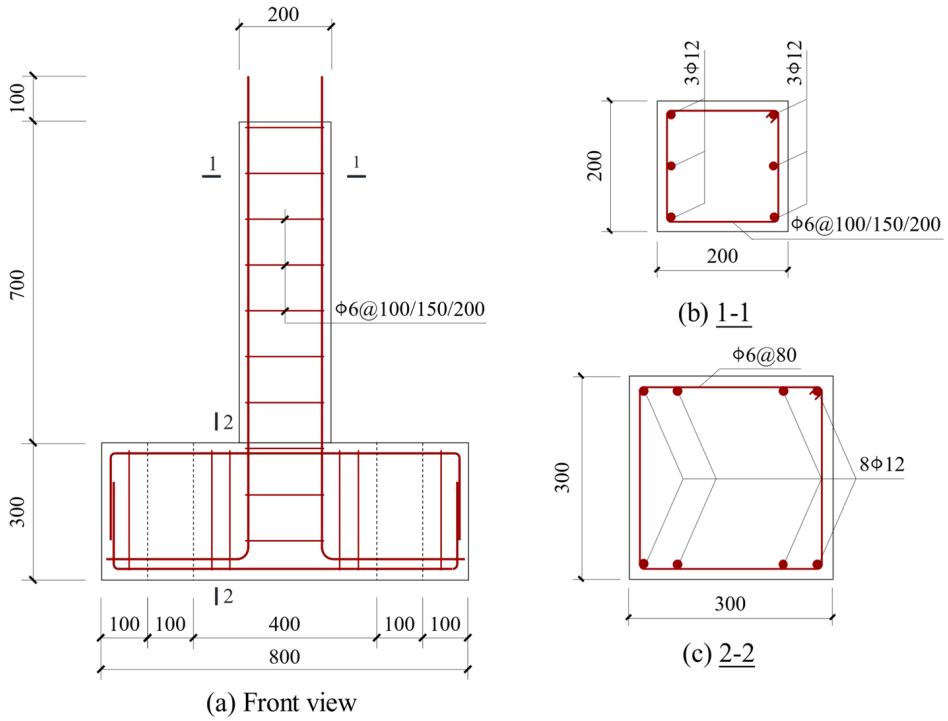


Figure 2.33: Dimensions and cross-sectional details of specimens (unit: mm)

The results showed the seismic performance of RC columns decreases rapidly with the increase of axial compression ratio and corrosion degree. As the axial compression ratio increases, the impact of reinforcement corrosion on the seismic performance is gradually weakened owing to the decreased contribution of longitudinal reinforcement bars to the load-carrying capacity. Furthermore, the impact of reinforcement corrosion is more obvious in RC columns of low-strength concrete with a larger reinforcement ratio.

Experimental tests on the cyclic performance of corroded RC columns and beams have been reported to have resulted in a reduction in the structural strength and ductility, which can affect the failure mode of such structures (Rinaldi et al., 2022; Zeng et al., 2022; Zhou et al., 2020; Zhou et al., 2023). However, it should be noted that all these works were on RC structures with normal

or high-strength concrete, with very few on low-strength concrete. Hence, most of the predictions on ageing and low-strength concrete RC structures were based on analytical models, which, though they have been used successfully, might not accurately predict the response of such structures under load.

**Table 2.3: Summary of Experimental studies on cyclic tests on corroded RC columns**

| Study | Exposure type | No. of specimen and dimensions (mm) | Strength of concrete (MPa) | Rebar diameter (mm) | Corrosion rate and method | Summary of test results |
|---|---|---|---|---|---|---|
| **Li et al. (2009)** | accelerated corrosion (3.5% NaCl) | 14 square RC column with CFRP and steel jackets | 44.8 | 4 - 14mm bars with 8mm transverse reinforcements | 17 – 20% | Corrosion considerably influences the behaviour of the strengthened columns. The strengthening is more effective in specimens with more corrosion. |
| **Ma et al. (2012)** | accelerated corrosion (3.5% NaCl) | 13 circular columns with large stub (260mm dia. and 1000mm high with 1300 × 360 × 400mm stub) | 32.4 | 6 - 16mm bars with 8mm transverse reinforcements | 0 – 15.1% | Higher corrosion levels and axial loads result in less stable hysteretic loops with more severe strength, stiffness degradations, and worse ductility. |
| **Meda et al. (2014)** | accelerated corrosion (3% NaCl) | Two square RC columns (300 × 300mm and 1500mm high with 700 × 700 × 100mm base) | 20 | 4 - 16mm bars with 8mm transverse reinforcements | 15% and 20% | The tests show how rebar corrosion can reduce structural ductility, so it could become a critical aspect, particularly for buildings in seismic regions. |

| | | | | | | |
|---|---|---|---|---|---|---|
| **Guo et al. (2015)** | accelerated corrosion (3.5% NaCl) | Four rectangular columns (250 × 600mm and 3200mm high with 1400 × 1400 × 700mm base) | 42.9 | 12 - 16mm bars with 8mm transverse reinforcements | 0, 5, 10 and 15% | Higher corrosion level leads to severe degradation of the seismic behaviour of concrete bridge piers, resulting in poor hysteretic responses, deterioration of stiffness and strength, and decreased displacement ductility and energy dissipation capacity. |
| **(Yuan et al., 2017)** | accelerated corrosion (4% NaCl) | Six circular columns (400mm dia. and 3200mm high with a 600 × 600 × 1500mm base) | 36.3 | 10 - 16mm bars with 8mm spiral reinforcements | 30, 60, 105, 130 and 150 days | The seismic performance of the non-uniformly corroded columns showed a slight variation before the transfer of the plastic hinge location. |
| **Wenting Yuan et al. (2018)** | accelerated corrosion (3.5% NaCl) | Five square RC columns (540 × 540mm and 2300mm high with 1400 × 1400 × 600mm base) | 24.9 | 24 - 14mm bars with 8mm transverse reinforcements | 0, 5, 15, 20 and 25% | The seismic performance of bridge piers is strongly affected by biaxial horizontal loads, and non-uniform corrosion makes the performance deterioration more severe. |

| | | | | | | |
|---|---|---|---|---|---|---|
| **Rajput and Sharma (2018a)** | accelerated corrosion (3.5% NaCl) | Six square RC columns (300 × 300mm and 1800mm high with 1000 × 600 × 550mm stub) | 29.9 – 33.2 | 8 - 16mm bars with 10mm transverse reinforcements | 10% and 15% | The investigation results show that reinforcement corrosion may defeat the purpose of providing transverse confinement in hinge regions of RC columns. |
| **Rajput et al. (2019)** | accelerated corrosion (3.5% NaCl) | Six square RC columns (300 × 300mm and 1800mm high with 1000 × 600 × 550mm stub) | 32.46 | 8 - 16mm bars with 10mm transverse reinforcements | 30% | High-performance fibre-reinforced concrete (HPFRC) was adequate in restoring the strength and deformability of corroded under-confined RC columns. However, the effect on the seismic performance of a well-confined RC column is not up to the code requirements. |
| **Luo et al. (2020)** | accelerated corrosion (5% NaCl) | Eight square RC columns (300 × 300mm and 1800mm high with 1000 × 600 × 550mm stub) | 42.3 | 8 - 14mm bars with 10mm smooth bars as transverse reinforcements | 5, 10 and 15% in longitudinal, with the transverse having 8, 16, 24 and 32% | The pinch phenomenon of the hysteretic curve gradually increases with the increase in steel bars' corrosion degree, resulting in a reduction in the specimen's energy dissipation, |

| | | | | | | |
|---|---|---|---|---|---|---|
| | | | | | | stiffness and plastic deformation capacity |
| **Zhou et al. (2020)** | accelerated corrosion (5% NaCl) | Twelve circular columns (300mm dia. and 1350mm high with an 800 × 410 × 300mm base) | 42.22 | 6 - 14mm bars with 8mm transverse reinforcements | 0, 2.5, 5, 10, 15 and 20% | The mechanical parameters of pier specimens degraded with increased corrosion. Also, the plastic hinge zone moved from the bottom of RC piers to the splash and tidal zones for severely corroded samples. |
| **Basdeki et al. (2022)** | accelerated corrosion (5% NaCl) | 34 prismatic RC columns, each with dimensions of 80 × 80 × 320mm | 30 | 16mm dia. bars | 15% | The negative consequences of corrosion on the hysteretic behaviour of steel reinforcing bars were highlighted. |
| **Rinaldi et al. (2022)** | accelerated corrosion (3% NaCl) | Four square RC columns (300 × 300mm and 1800mm high with 1500 × 750 × 500mm foundation) | 25 | 4 - 16mm bars with 8mm transverse reinforcements | 20% | The results of the cyclic experimental tests show how reinforcement corrosion (amount and morphology) can reduce structural strength and ductility and change the failure modes. |

| | | | | | | |
|---|---|---|---|---|---|---|
| **Zeng et al. (2022)** | | Six circular RC columns (390 dia. and 2340mm on 1300 × 580 × 800mm stub) | 37.1 | 8 - 16mm bars with 10mm smooth bars as transverse reinforcements | | |
| **Zhou et al. (2023)** | accelerated corrosion (3.5% NaCl) | Nine circular RC columns (250 dia. and 1200mm on 1400 × 450 × 450mm stub) | 33.8 | 8 - 16mm bars with 10mm smooth bars as transverse reinforcements | 10, 20, and 30% | The test results indicated that the severely corroded columns' ductility and energy dissipation capacity significantly increased by 48.5 % and 57.5 %, respectively. |
| **Zhang et al. (2023)** | accelerated corrosion (5% NaCl) | 11 square RC columns 200 × 200 × 700mm on a 300 × 300 × 800mm base beam) | 15 | 6 - 12mm bars with 6mm transverse reinforcements | 0, 5, 10, 15 and 20% | The seismic performance of RC columns decreases rapidly with the increase of axial compression ratio and corrosion degree. The impact of reinforcement corrosion is more obvious in RC columns of low-strength concrete with a larger reinforcement ratio. |

## 2.5 Confinement models for RC

In the RC bridge piers/columns designed to resist seismic vibrations, the plastic regions are provided with adequate transverse reinforcement to improve their ductility and prevent the buckling of longitudinal reinforcements. This confinement provides the compressed concrete with higher ductility and strength, which helps to prevent collapse and shear failure during vibrations (Mander et al., 1988). Thus, the higher the level of confining stress in the concrete, the more its gains in ductility and strength (Zeng, 2017).

Mander et al. (1988) presented a unified stress-strain model for confined concrete in rectangular or circular columns. The model was used for axial and cyclic loading and provides for the different configurations of ties by estimating the effective lateral confining stress. The model was based on the equation proposed in 1973 by Popovics and is shown in Figure 2.34 below.

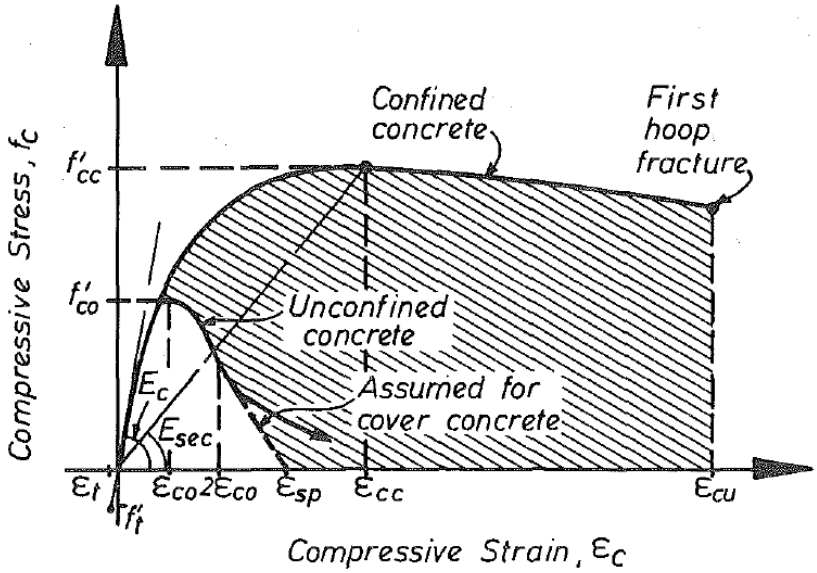


Figure 2.34: Stress-Strain Model Proposed for Monotonic Loading of Confined and Unconfined Concrete (Mander et al., 1988)

It should be noted that Mander et al. (1988) equations are for uncorroded confined concrete with the longitudinal compressive stress, $f_c$, expressed as

$$f_c = \frac{f'_{cc}xr}{r-1+x^r} \tag{2.19}$$

$$x = \frac{\varepsilon_c}{\varepsilon_{cc}} \tag{2.20}$$

$$r = \frac{E_c}{E_c - E_{sec}} \tag{2.21}$$

$$E_c = 5000\sqrt{f'_{co}} \tag{2.22}$$

$$E_{sec} = \frac{f'_{cc}}{\varepsilon_{cc}} \quad (2.23)$$

where,

$\varepsilon_c$ = longitudinal compressive concrete strain

$f'_{cc}$ = maximum confined concrete strength

$\varepsilon_{cc}$ = maximum confined concrete axial strain

$E_c$ = elastic modulus of concrete

$E_{sec}$= secant modulus of confined concrete

$f'_{co}$= maximum strength of unconfined concrete

There are a lot of confinement models for concrete columns proposed in the literature. It should be noted though that most of these confinement models are for uncorroded RC columns. Some of the confinement models for RC columns are presented in Table 2.1 below. The models in the table showed that the confined concrete behaviour is dependent on the unconfined concrete strength, the yield strength of the confinement reinforcement, the volumetric ratios of confinement to the concrete core and the confinement configuration (Liang et al., 2015).

**Table 2.4: Different confinement models for peak stress and strain of RC columns (Liang et al., 2015).**

| Researchers | Stress-strain models for confined concrete | |
|---|---|---|
| | **Peak stress, $f_{cc}$** | **Strain, $\varepsilon_{cc}$** |
| **Kent and Park, 1971** | $f_{co}$ | $0.002$ |
| **Vallenas *et al.*, 1977** | $f_{co}\left(1+0.0091(1-0.245\frac{s}{h''})\frac{(\rho_s+\frac{d''}{d}\rho_s)f_{yh}}{\sqrt{f_{co}}}\right)$ | $0.0024+0.005(1-\frac{0.734s}{h''})\frac{\rho_s f_{yh}}{\sqrt{f_{co}}}$ |
| **Sheikh and Uzumeri, 1980** | $f_{co}\times\left(1+\frac{{b_c}^2}{140P_{occ}}[\left(1-\frac{nC^2}{5.5{b_c}^2}\right)\left(1-\frac{s}{2b_c}\right)^2]\times\sqrt{\rho_s f_{yh}}\right)$ | $\varepsilon_{co}\times\left(1+\frac{248}{C}[1-5.0\times\left(\frac{s}{B}\right)^2]\frac{\rho_s f_{yh}}{\sqrt{f_{co}}}\right)$ |
| **Park *et al.*, 1982** | $f_{co}+\rho_s f_{yh}$ | $\varepsilon_{co}\times(1+\rho_s f_{yh}\,/\,f_{co})$ |
| **Mander *et al.*, 1988** | $f'_{cc}=f_{co}\left(-1.254+2.254\sqrt{1+\frac{7.94\,f_{le}}{f_{co}}}-2\frac{f_{le}}{f_{co}}\right)$ | $\varepsilon_{co}\left[1+5\left(\frac{f'_{cc}}{f'_{co}}-1\right)\right]$ |
| **Saatcioglu and Razvi, 1992** | $f_{cc}=f_{co}+k_1\,f_{le}$<br>$k_1=6.7(\,f_{le})^{-0.17}$<br>$f_{le}=k_2\,f_l$ | $\varepsilon_{co}\,(1+5K)$<br>$K=\frac{k_1\,f_{le}}{f'_{co}}$ |
| ***Hoshikuma *et al.*, 1997** | $f_{co}+3.8\alpha\rho_s f_{yh}$ | $0.002+0.033\beta\rho_s f_{yh}/f_{co}$ |
| **Bousalem and Chikh, 2006** | $f_{co}+0.4k_e\rho_{sh}f_{yh}\sqrt{f_{co}}$ | $\varepsilon_{co}\times[1+2.7\left(\frac{k_e\rho_{sh}f_{yh}}{\sqrt{f_{co}}}\right)]$ |

*$\alpha, \beta$ = modification factors dependent on the cross-sectional shape of the column for the Hoshikuma *et al*.'s model.

Corrosion of reinforcement affects the mechanical properties of reinforcement, thereby reducing the cross-sectional area and yield strength. This forms the basis of the work done by Vu et al. (2017), where the model by Mander et al. (1988) was modified by adjusting the volumetric ratio and yield strength of the transverse reinforcement to reflect the corrosion effect and hence the reduction in the lateral confining pressure. The modified equations are as follows:

Volumetric ratio, $\rho_{sc}$ ,

$$\rho_{sc} = (1 - X_{corr})\rho_s \tag{2.24}$$

where,

$X_{corr}$ = corrosion level (mass loss of transverse reinforcement)

$\rho_s$ = ratio of the volume of transverse confining steel to the volume of confined concrete core

$$\rho_s = \frac{A_{sp}\pi d_s}{\frac{\pi}{4}d_s^2 s} = \frac{4A_{sp}}{d_s s} \tag{2.25}$$

where,

$A_{sp}$ = area of transverse reinforcement

$d_s$ = diameter of hoop bar centres

$s$ = vertical spacing of transverse bars

This further impacted the yield strength of the transverse reinforcement, $f_{yh}$, as the area reduces. Thus, the expression for the yield strength of the corroded transverse reinforcement, $f_{yh}^c$, becomes

$$f_{yh}^c = (1 - \alpha_s X_{corr})f_{yh} \tag{2.26}$$

where,

$\alpha_s$= yield strength reduction factor (corroded transverse reinforcement = 0.005, Du *et al*. 2005; Stewart and Al-Harthy, 2008)

The reduced volumetric ratio and yield strength affect the confining stress, thereby leading to the reduction in the effective lateral confining pressure, $f_l'$, in the corroded section.

$$f_l' = \frac{1}{2}k_e \rho_{sc} f_{yh}^c \tag{2.27}$$

where,

$k_e$= confinement effectiveness coefficient (dependent on the geometry and configuration of the section)

The confinement effectiveness coefficient, $k_e$, for the circular columns is determined from the expression in Mander et al. (1988) using Figure 2.35.

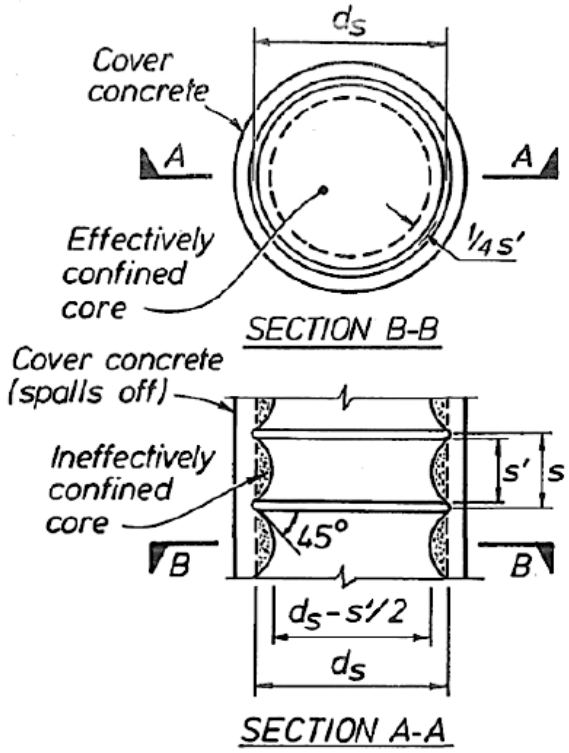


Figure 2.35: Confined Core for Circular Reinforcement (Mander et al., 1988)

$$k_e = \begin{cases} \dfrac{\left(1-\frac{s'}{2d_s}\right)^2}{1-\rho_{cc}} & for\ circular\ hoops \\ \dfrac{\left(1-\frac{s'}{2d_s}\right)}{1-\rho_{cc}} & for\ circular\ spirals \end{cases} \quad (2.28)$$

where,

$s'$=vertical spacing between hoop bars

$d_s$= diameter of hoop bar centres

$\rho_{cc}$ = ratio of the area of longitudinal reinforcement to the area of core of section

For a rectangular column, the confinement effectiveness coefficient, $k_e$, is determined from Figure 2.36 below:

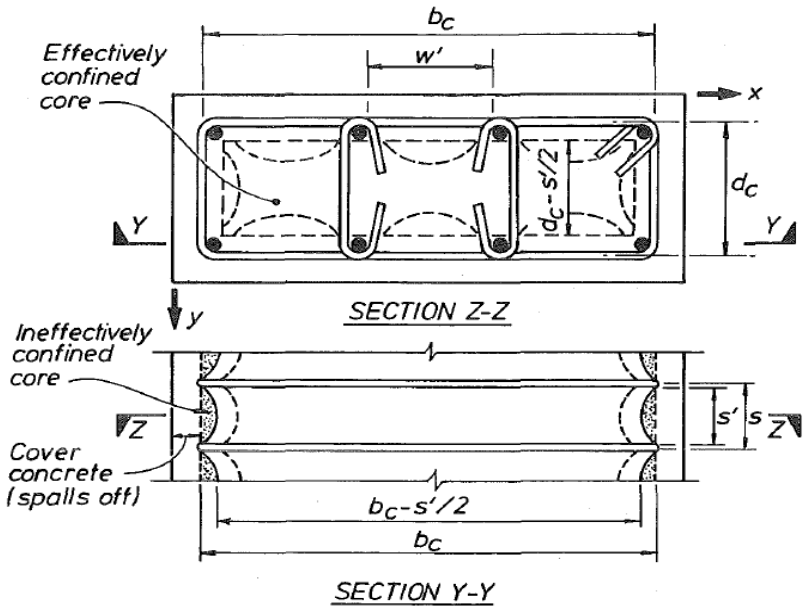


Figure 2.36: Confined Core for Rectangular Reinforcement (Mander et al., 1988)

$$k_e = \frac{\left(1-\sum_{i=1}^{n}\frac{(w_i')^2}{6b_c d_c}\right)\left(1-\frac{s'}{2b_c}\right)\left(1-\frac{s'}{2d_c}\right)}{(1-\rho_{cc})} \tag{2.29}$$

For rectangular RC columns with different confinement in the x and y directions, the effective lateral confining stress is determined from

$$f_{lx}' = k_e \rho_{cx} f_{yh}^c \tag{2.30}$$

and,

$$f_{ly}' = k_e \rho_{cy} f_{yh}^c \tag{2.31}$$

$$\rho_{cx} = \frac{A_{sx}}{s d_c} \tag{2.32}$$

$$\rho_{cy} = \frac{A_{sy}}{s b_c} \tag{2.33}$$

where,

$\rho_{cx}$ and $\rho_{cy}$, are the ratios of the area of longitudinal reinforcement to the area of the core of the section in the x and y directions, respectively.

$A_{sx}\ and\ A_{sy}$ = the total area of transverse bars in the x and y directions, respectively.

The compressive strength of corroded confined, $f_{cc}'$, is determined from Figure 2.37 for confined concrete without corrosion.

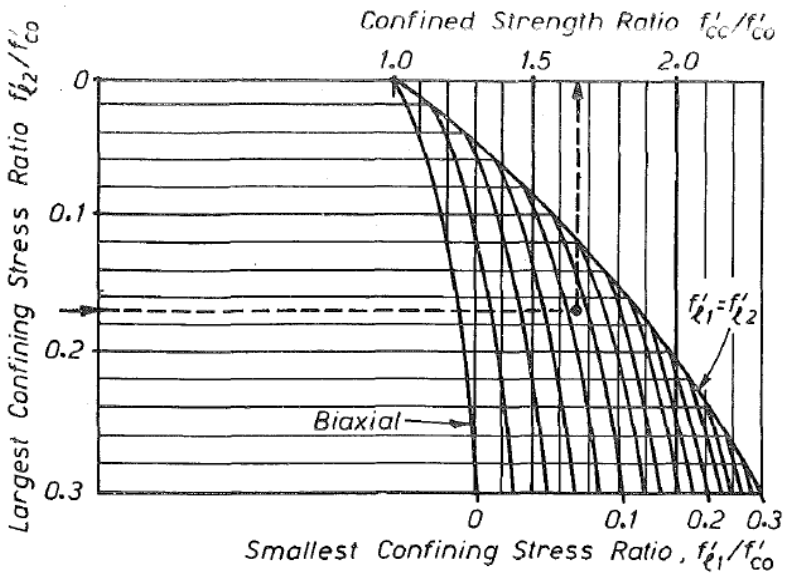


Figure 2.37: Confined Strength Determination from Lateral Confining Stresses for Rectangular Columns (Mander et al., 1988)

Applying the corrosion reduction factor on the confined concrete compressive strength reduces this to reflect the effect of corrosion.

The maximum confined strength, $f'_{cc}$,

$$f'_{cc} = (1 - \alpha X_{corr}) f'_{co} \left( -1.254 + 2.254 \sqrt{1 + \frac{7.94 f'_l}{f'_{co}}} - 2 \frac{f'_l}{f'_{co}} \right) \quad (2.34)$$

where,

$\alpha$ = stress correction coefficient ($\alpha = 0.19$, 0.40 and 0.51 for single hoop square, double hoop square and circular section with spiral hoops, respectively)

$f'_{co}$ = unconfined compressive strength of concrete

The axial strain of the corroded RC structure reduces significantly due to corrosion of the reinforcement. The axial strain for corroded confined concrete could be obtained by modifying the axial strain equation in Mander et al. (1988).

$$\varepsilon_{cc} = (1 - \beta X_{corr}) \varepsilon_{co} \left[ 1 + 5 \left( \frac{f'_{cc}}{f'_{co}} - 1 \right) \right] \quad (2.35)$$

where,

$\beta$= strain correction coefficient ($\beta$=0.49, 1.29 and 0.28 for single hoop square, double hoop square and circular section with spiral hoops, respectively)

$\varepsilon_{co}$= axial strain of unconfined concrete ($\varepsilon_{co}$= 0.002 if test data is not available)

The failure of transverse reinforcement will lead to the buckling failure of the longitudinal bars and, hence, the crushing of the core concrete. To mitigate this failure, the ultimate strain of confined concrete is estimated at the point where the fracture of the transverse reinforcement occurs. Vu et al. (2017) modified the empirical equation of Paulay and Priestley (1992) to include the corrosion effect on the ultimate strain of corrosion-confined concrete. The proposed equations are stated below (Equations 2.36 and 2.37)

$$\varepsilon_{cu} = 0.004 + (1 - X_{corr}) \frac{1.4\rho_{sc} f_{yh}^{c} \varepsilon_{sm}^{c}}{f_{cc}'} \tag{2.36}$$

$$\varepsilon_{sm}^{c} = (1 - \beta_s X_{corr}) \varepsilon_{sm} \tag{2.37}$$

where,

$\varepsilon_{sm}^{c}$= steel strains at the maximum tensile stress of corroded reinforcement

$\varepsilon_{sm}$= steel strains at the maximum tensile stress of corroded reinforcement (0.12)

$\beta_s$=ultimate strain reduction factor for corroded transverse reinforcement ($\beta_s$= 0.05, (Du et al., 2005)

In recent years, understanding the modelling and analysis of the degradation of RC structures has led to an improvement in models such as Druker-Prager and CDPM used in software for finite element analysis. For example, Zeng (2017) proposed a new uniaxial compressive stress-strain curve to analyse square RC columns confined with transverse reinforcement. The proposed CDPM was used in ABAQUS to analyse the behaviour of laterally confined RC columns with three different configurations (Fig. 2.38) of transverse reinforcement subjected to concentric loading.

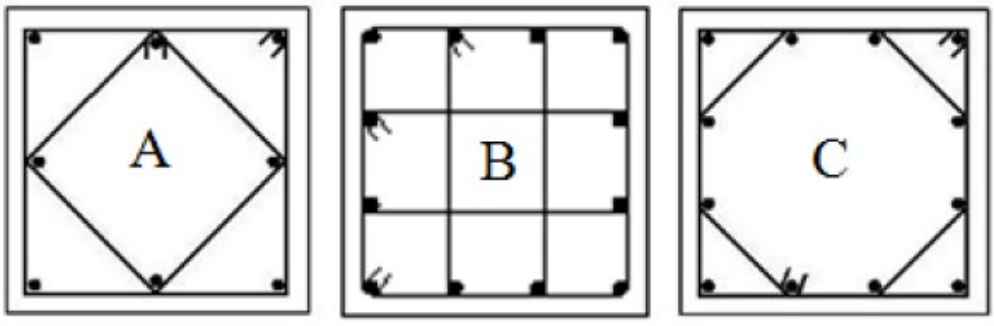


Figure 2.38: Configurations of Transverse Reinforcement. (Zeng, 2017)

The investigation showed that the column with configuration C has higher hydrostatic pressure than the other columns (A and B), as seen in Figure 2.39. Thus, the specimen with configuration C provides a better confinement effect on the core concrete than the other two after the peak load.

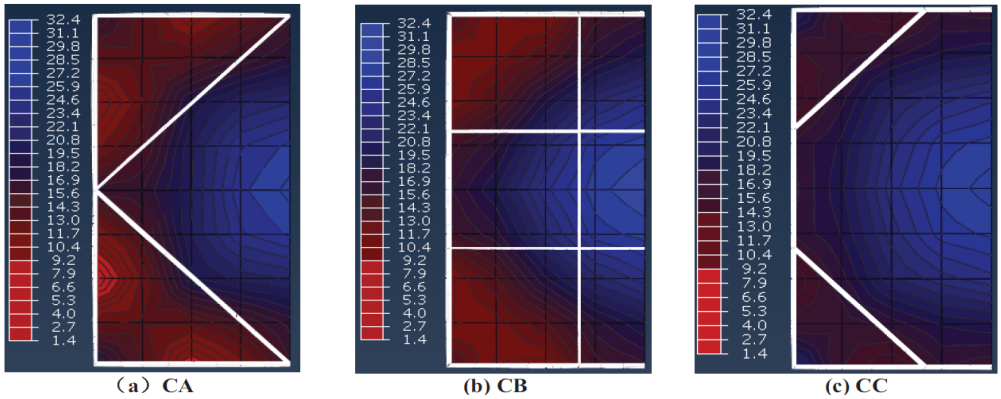


Figure 2.39: Contours of Hydrostatic Stress within Core at Middle Sections Corresponding to an Axial Strain of 0.02 (Zeng, 2017)

## 2.6 Non-Destructive Testing of RC Structures

Advanced non-destructive testing techniques in composite materials have received increasing attention because they allow for looking inside a material rather than examining its surface. This ability is of great importance since it enables engineers to characterise the internal fracture behaviour of materials, which can inform the development and validation of computer models. Moreover, non-destructive techniques can be used to assess the achieved material quality and control its properties during casting and after hardening (Shah & Ribakov, 2011, 2012).

Non-destructive tests are done on existing and ageing structures to assess the structural integrity and adequacy of such structures. Once done accurately, the test could also help predict and ascertain the time an RC structure requires for maintenance and rehabilitation. Some of the common methods of non-destructive tests done on RC structures are half-cell electrical potential, carbonation depth measurement, ultrasonic pulse velocity, radiographic testing, impact echo testing, impulse radar testing, infrared thermography, computed tomography (CT) scan and Digital Image Correlation (DIC), the electrical resistivity technique; electrochemical impedance spectroscopy; near-field microwave method; ground penetrating radar; X-ray and gamma-ray radiography; acoustic emission and the ultrasonic pulse velocity method. A comprehensive review of the application of these methods for testing cement-based composites has been recently presented by Shah and Ribakov (2011).

### 2.6.1 Computed Tomography (CT) Scan of RC Column

Microscale X-ray computed tomography (μXCT) is a non-destructive 3D imaging technique that allows accurate characterisation of the 3D nano-/micro-/meso-structure of different materials, including pores and cracks. Computed tomography has been used in medicine since the 1970s.

However, its application in material science is relatively new. It is being increasingly used to evaluate damage propagation, identify damage mechanisms and extract critical parameters of different types of materials (Maire & Withers, 2014).

The need to understand the internal microstructure of materials for accurate estimation and analysis of their behaviour under stress made it imperative for engineers to look at other assessment methods. For example, a computed Tomography (CT) scan is a very powerful method for studying the internal microstructure of materials (Vicente et al., 2019).

Recently, microscale X-ray computed tomography (µXCT), the 3D imaging technique routinely used in hospitals, has become popular in studying the behaviour of different materials and characterising their internal nano, micro and mesoscale structure (Maire & Withers, 2014). This is mainly because of its high resolution, non-destructive nature, and clear visualisation of multi-phase shapes, sizes and distribution, including pores and cracks. In addition, this technique allows the characterisation of the evolution of material behaviour by recording several scans at different time intervals under changing conditions.

#### 2.6.1.1 µXCT principles

Figure 2.40 illustrates the procedures of the µXCT as illustrated by Vicente et al. (2019). First, a sample is placed between the X-ray source and a detector. As the X-rays propagate through the sample, which is rotated axially through 360$^{o}$, they are attenuated or scattered depending on the sample density along the beam path. The detector captures the remaining X-rays transmitted through the sample and then builds a series of 2D digital radiographs (projections). Using a suitable reconstruction algorithm, a 3D volumetric image of the sample with variable greyscale is reconstructed from the radiographs. The grey values of each voxel (3D pixels) measure the material's absorptivity.

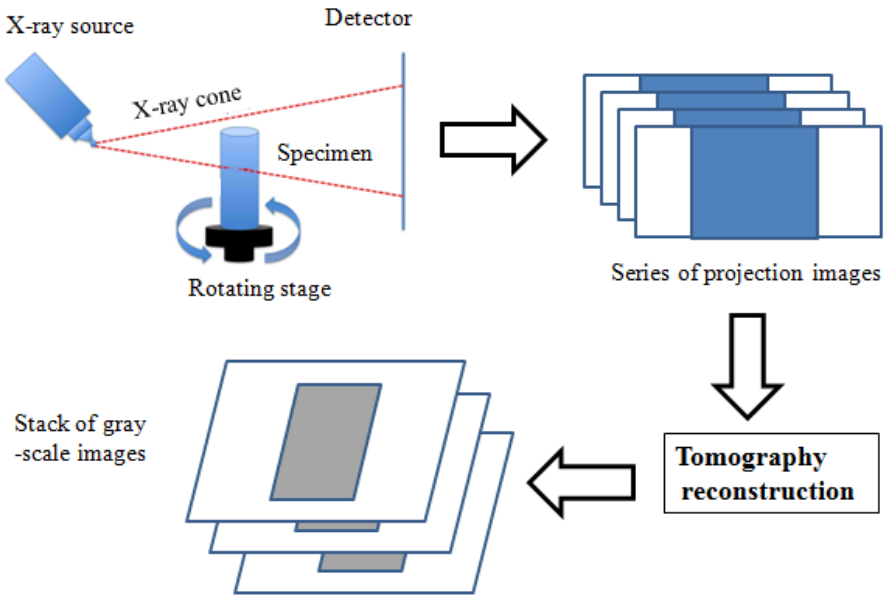


Figure 2.40: The setup of a CT scan (Vicente et al., 2019).

The X-ray radiation is characterised by its energy distribution (measured in kV) and intensity, which determines the penetrating power of the X-ray beam into a material. Higher energy X-rays can penetrate a greater thickness of the material or a similar thickness of denser material before being absorbed. However, high-energy X-rays are less sensitive to the differences in the densities of the material constituents. Therefore, the energy of the X-ray beam should be calibrated carefully according to the sample size and the density of the material to ensure the quality of the scanned images. A small electron beam or X-ray spot is essential to obtain sharp images. Spots of around 1µm diameter can be achieved with an applied voltage of up to 250kV. The material composition and its attenuation coefficient also significantly affect the quality of the µXCT images (Kruth et al., 2011).

At the beginning of the scan, the size of the image voxels should be calibrated to perform accurate and traceable dimensional measurements. This calibration allows the identification of a global scale factor that will be used to link voxel size to a unit of length. The calibration process is usually done by measuring a simple calibrated reference object. In addition, a large number of parameters, which have a significant influence on the scanning process, need to be determined at the beginning of the scan, such as source current, source voltage, the size and shape of the object, magnification, number of angular poses, exposure time, number of projections, number of positions and combining measurements with different current/voltage/target. Proper parameter selection may require iterative procedures and test measurements (Ketcham & Carlson, 2001; Kruth et al., 2011).

#### 2.6.1.2 Data reconstruction and segmentation

Image reconstruction is a mathematical process that aims to convert projection images collected by the detector into greyscale images. The grey values have a range determined by the computer system (e.g., 8-bit). The most commonly used reconstruction technique is filtered back projection, in which each view is successively superimposed over a square grid in the acquired initial direction. The resolution of the reconstruction is affected by many parameters such as voxel size, number of detector pixels in x and y directions, number of angular positions at which images are taken, and number of projection images taken in one angular pose (Ketcham & Carlson, 2001).

The 3D reconstruction is followed by edge detection and segmentation to determine the interfaces between the object and the surrounding air or between different material components. The object sample or material edges can be identified based on greyscale value thresholding. The grey edge value depends on the material quality and the radiation intensity. The presence of multiple materials complicates proper edge detection. The threshold values can be calculated and applied on a local transition area that includes only the two materials considered for the transition threshold rather than using the same threshold value over the entire sample (i.e., global thresholding). However, this requires lengthy procedures to identify accurate threshold values (Kruth et al., 2011).

The CT scan data could be exported to a FEM software package for further analysis and comparison with experimental data (Fig. 2.42). It could also show the crack distribution pattern inside a concrete specimen subjected to one form of deformation or another. In addition, researchers have used CT scans to investigate and establish the correlations between metals' internal microstructure and macroscopic response during mechanical testing (Awd, Stern, et al., 2018; Awd, Tenkamp, et al., 2018; Chen et al., 2020). The technology has also been extended to investigate the internal microstructure of concrete, most especially the porosity, which directly affects the durability, fatigue, fracture behaviour and freeze-thaw cycles (Balázs et al., 2017; Vicente et al., 2019; Vicente et al., 2021; Vicente et al., 2018).

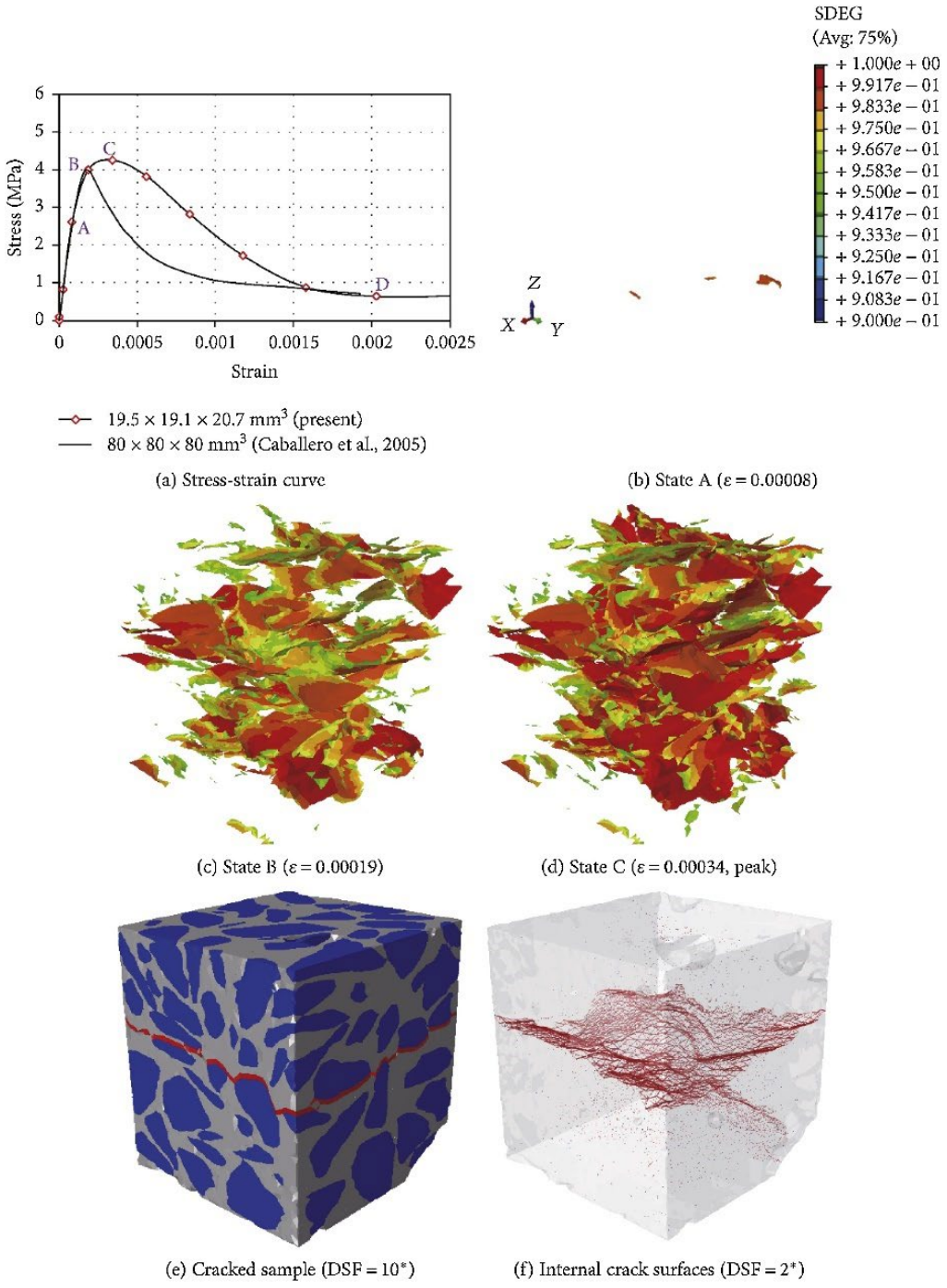


Figure 2.41: Stress-strain curve and damage propagation under tension ((Ren et al., 2018). DSF = displacement scale factor

Monitoring the corrosion of ageing RC structures can be a significant task due to the uncertainties surrounding its occurrence and propagation. Therefore, the X-ray CT scan and acoustic emission (AE) technique was used together to investigate the effect of corrosion-induced damage on the reinforcement-concrete interface of an existing RC structure by testing small reinforced mortar cylinders (Van Steen et al., 2017). The results of this investigation showed that the combination of the two methods gives a reliable estimate of the degradation mechanism of the corrosion process, which could be used further in numerical modelling.

Vicente et al. (2018) used the CT scan to study the crack patterns of fibre-reinforced concrete subjected to monotonic and low-cyclic fatigue loads using 40mm cubes made of steel fibre-reinforced concrete. First, the samples were loaded and scanned to acquire their 3D damage maps, which were then examined for the different crack patterns. The result of the investigation showed that the loading method does not affect the crack pattern of the tested cubes, as the damage maps are statistically similar.

The effective maintenance of ageing RC structure depends on accurately evaluating and detecting degradation caused by fatigue damage. Fan and Sun (2019) used industrial CT technology to detect and assess fatigue damage in concrete by conducting fatigue loading tests on cylindrical concrete specimens (50mm dia. and 100mm long) and observing the spatial distribution of the fatigue cracks generated. A new fatigue damage parameter (D) was developed based on the distribution of the fatigue crack in the concrete (Eq. 2.38)

$$D = \left(1 - \frac{1-P_n}{1-P_o}\right) / \left(\frac{P_o}{P_n}\right) = \frac{(P_n - P_o)P_n}{(1-P_o)P_o} \tag{2.38}$$

where,

$P_o$ = initial porosity of the concrete

$P_n$ = current porosity of the concrete

The damage parameter developed could be used to better characterise the material fatigue damage of concrete under compression as the micro parameters of fatigue cracks were accurately measured with the CT scanning done.

The use of CT scans in exploring the microstructural studies of materials used in various fields of engineering properties of materials has been growing in the past two decades. The need arises from the evidence of its successful applications in other areas of study to properly understand the internal distribution of stresses in materials. The technique has been used extensively in metal manufacturing, developing and improving composite materials, and pavement and asphalt production. CT scan technology of concrete output continuously evolves to include the deterioration and degradation of concrete materials and the responses under load. The table below summarises some of the work on using CT scans to investigate some properties of concrete.

**Table 2.5: Summary of application of CT scan on concrete materials**

| Study | Type of Study | Material tested | conclusions |
|---|---|---|---|
| **Balázs et al. (2017)** | Three-point bending tests on FRC beams (150 × 150 × 600 mm) | Concrete with varying quantities of steel fibres and different mixing durations | The specimens with longer mixing time but the same volume fraction of steel fibres resulted in higher residual flexural-tensile strength values that increased with increased fibre content. |
| **Van Steen et al. (2017)** | test on cylindrical mortar samples (27.7mm dia. and 58mm height | Mortar sample with a single smooth bar in the middle | Micro-CT, combined with other techniques such as the Acoustic Emission (AE) technique, result in a reliable visualization and characterization of the mechanical damage processes during the corrosion process |
| **Ren et al. (2018)** | Compressive tests on concrete cubes (20mm) | 20mm concrete cubes with 5mm average diameter of aggregates | The study demonstrates that combining the in situ micro XCT tests and image-based FE modelling is an effective technique to investigate the internal damage and fracture behaviour in multiphasic composites such as concrete |
| **Vicente et al. (2018)** | Monotonic and cyclic loading tests on concrete cubes (40mm) | self-compacting concrete reinforced with steel fibres | The results show that average damage maps for monotonically and cyclically tested cubes are statistically similar, confirming the hypothesis for steel fibre-reinforced concrete. |
| **Vicente et al. (2021)** | Using CT scan to investigate the porosity of concrete | self-compacting concrete reinforced with steel fibers | The result showed that CT can provide a great deal of information on the porosity of concrete, much more than that given by conventional procedures |

| | | | |
|---|---|---|---|
| **Wang et al. (2021)** | In-situ and real-time monitoring of the corrosion process of steel bars in concrete | RC with embedded single bar (carbon steel and corrosion-resistant bar) | The results show that the images collected by XCT can directly reflect the cracking position and the whole corrosion process of reinforced concrete |

### 2.6.2 Digital Image Correlation (DIC) measurement

The measurements of loaded samples with small and uniform strain deformations could easily be achieved with strain gauges and Linear Variable Differential Transformer (LVDT) devices, as they are easy to manufacture and have high sensitivities. However, most engineering structures are subjected to heterogeneous deformation and non-uniform deformation. Hence, strain gauges at discreet points may not correctly capture the information needed in the region of interest (Zhao et al., 2019). This problem is overcome with non-contact sample testing, with the DIC, one of the most recognised methods.

DIC is a non-destructive, non-contact full-field optical measurement technique capable of capturing digital images of the surface of an object to obtain the in-plane strains and out-of-plane deformations in its 2D and 3D configurations, respectively. It uses the correlation between images (reference and deformed) to measure the displacement. It is widely used in the field of solid mechanics to investigate the responses of structures to loadings.

Küntz et al. (2006) used the DIC technique to analyse the response/behaviour of in-situ shear crack in an RC bridge beam during a static loading test. The investigation was done on the Saint-Marcel Bridge. The result shows that crack loading varies with the position of the load and the sequence of application to the structure.

Jiang et al. (2017) examined the strain field of RC under accelerated corrosion using strain gauges and DIC. The RC sample used in the investigation was 100 × 100 × 300mm with a 10mm diameter carbon steel bar. The DIC equipment was set up to record the deformation as the sample was corroded (accelerated corrosion method), while the strain gauges were also attached to the rebar. The result showed an agreement between the two processes.

Rajagopal et al. (2018) used the 2D-DIC technique to assess the stress-strain behaviour of corroded steel reinforcement (Fig. 2.42). The stress-strain behaviour of 14 reinforcements (one

uncorroded and 13 naturally corroded obtained from a 15-year-old building) was investigated. The result of the investigation showed that the DIC provides more accurate measurements of the mechanical properties, as it was able to measure the local strain heterogeneity and separate the effects of geometrical variations from the material degradation.

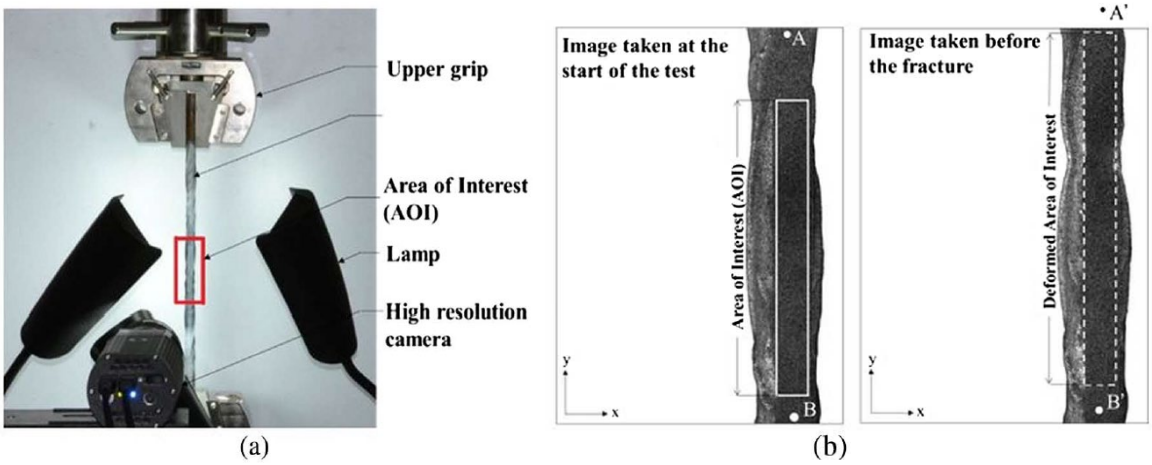


Figure 2.42: Capturing of images during deformation of test specimens: (a) experimental setup for 2D-DIC and (b) setting of camera frame (Rajagopal et al., 2018)

Chen et al. (2020) used the 3D-DIC to investigate the mechanical behaviour of reinforcement bars with localised pitting corrosion. The investigation was done on 61 reinforcement bars subjected to wetting and drying cycles in chloride solutions for over three years. The maximum corrosion level was determined with a 3D-scanning technique (Fig. 2.43). At the same time, the DIC was used to determine the displacement field and, thus, the engineering strain through the virtual extensometers created during the post-processing. The test result was used in proposing a time-dependent assessment of strain capacity considering the corrosion morphology evolution over time.

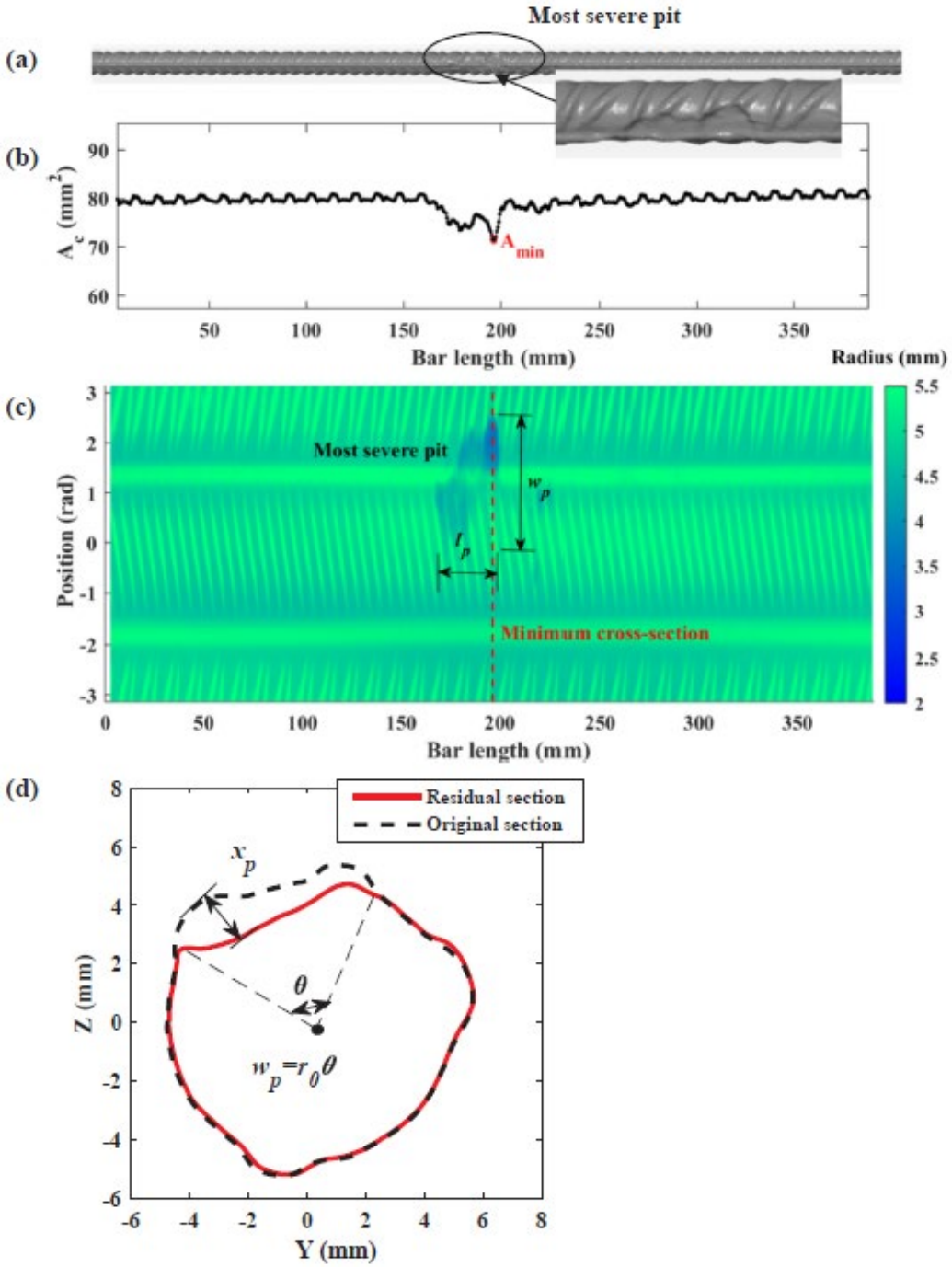


Figure 2.43: Example illustrating corrosion evaluation from 3D-scanning: (a) reconstructed bar surface from 3D-scanning; (b) longitudinal variation of the cross-sectional area along the scanned length; (c) 2D plot of the bar surface with a colour scale showing the magnitude of radius; (d) residual and original cross-sectional appearance at the minimum cross-section (Chen et al., 2020)

Wang et al. (2021) used X-ray computed tomography (XCT) and the DIC to research the internal monitoring of RC under accelerated corrosion of the Q235 carbon steel bar and corrosion-resistant steel bar. The study subjected concrete specimens mixed with seawater and reinforced by two steel bars, a Q235 carbon steel bar and a corrosion-resistant steel bar (Fig. 2.44) to

accelerated corrosion. X-ray computed tomography (XCT) was used for in situ and real-time monitoring of the corrosion process of the concrete.

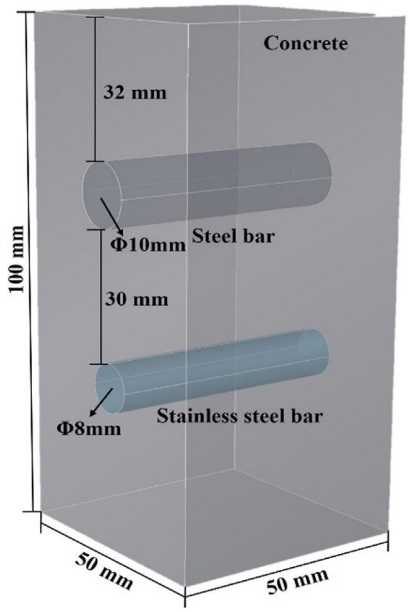


Figure 2.44: the 3D-diagram of the reinforced concrete (Wang et al., 2021)

The result showed that the XCT could monitor the cracking position and the whole process of RC corrosion, while the DIC could also quantify the strain generated. Also, the combination of XCT and DIC processes could assist in verifying existing cracking models on corrosion expansion.

**Table 2.6: Summary of application of DIC for investigation of the properties of corroded RC elements.**

| References | Type of Study | Conclusions |
|---|---|---|
| **Küntz et al. (2006)** | Investigate the in-situ behaviour of a shear crack in an RC beam during a static load test. | The results indicate that the crack loading varies significantly with load position and sequence of applications to the structure. |
| **Jiang et al. (2017)** | Investigating the strain evolution and crack pattern of RC attacked by corrosion | The results showed an agreement between the measurements with strain gauges and the DIC technique in the concrete strain field analysis induced by the corrosion of reinforced bars. |
| **Rajagopal et al. (2018)** | Assessment of the stress-strain behaviour of | The results show that the proposed method can provide more accurate estimates of |

| | | |
|---|---|---|
| | naturally corroded cold-twisted deformed (CTD) steel rebars | mechanical properties than the conventional methods. The developed method facilitates a better understanding of the stress-strain behaviour at the fracture location and other local points of interest on corroded steel rebars. |
| **Chen et al. (2020)** | Mechanical behaviour of reinforcement bars affected by pitting corrosion | The investigation revealed that the measured ultimate strain was dependent on the extensometer gauge length for a given corrosion pit |
| **Wang et al. (2021)** | Analyzing the inner expansion and strain variation of RC | The crack development was measured with considerable ease by the DIC. Also, the strain and stress field evolution in different areas of concrete reinforced by the steel bars was calculated. |

## 2.7 Conclusions

A review of the existing models for corrosion of RC structures, numerical analysis, experimental work, and corrosion effect for normal and high-strength concrete was presented. In addition, some of the results of previous experimental and numerical work on the corrosion of RC structural elements have been discussed.

The conclusions of the literature review and the gaps in the research identified can be summarised below:

1. Much experimental work is on the corrosion of RC beams subjected to flexure and shear under monotonic and cyclic loading.
2. There is a large volume of work on the modelling of confined concrete elements, with very few studies on corroded confined concrete columns.
3. Most experimental works on corroded confined RC columns were on normal and high-strength concrete structures, without any experimental work on low-strength RC columns.
4. There is limited experimental data on corroded RC columns, both circular and square cross-sections, under axial and lateral (monotonic and cyclic) loadings.

5. Also, previous experimental work on corroded RC columns has been mainly on flexure with no data on critical shear columns.
6. The use of non-destructive testing to examine the behaviour of corroded RC elements is limited in the literature.

The main contribution of this research will be to carry out experimental tests on low-strength corroded RC columns under monotonic and cyclic loading, representing ageing structures, considering different geometrical properties (square and circular) and different reinforcement configurations and shear span-to-depth ratios. The results will shed more light on pertinent questions like what configuration of the columns gives the best performance at different corrosion levels and the need for strengthening of ageing and low-strength RC columns.

# Chapter 3 Experimental investigation of the influence of axial compressive load on low-strength reinforced concrete corroded column[1,2]

## 3.1 Introduction

Chapter 2 showed that chloride-induced corrosion of reinforcing steel is the most common reason for the premature deterioration of RC structures in chloride-laden environments. Many of these old structures are located in highly seismic regions and are subjected to cyclic loading during an earthquake. Many ageing structures are also designed with inadequate confinement reinforcement for earthquake resistance. Hence, consideration needs to be given to their responses under seismic loading.

## 3.2 Ageing and corrosion of RC columns/piers

Ageing in reinforced concrete (RC) structures results in the loss of their strength via a slow, progressive and irreversible process over time. In addition, the ageing process results in the degradation of the engineering properties of structures by limiting their resistance to failure (Karapetrou et al., 2017; Yang et al., 2016). This failure is more pronounced in RC structures in aggressive and marine environments located in seismic regions subject to corrosion effects and poor quality of materials used in construction.

Corrosion of reinforcement in concrete is one of the most common and dangerous environmental deteriorations affecting the structural performance of ageing structures in chloride-laden and high seismic environments (Kashani, Alagheband, et al., 2015; Vu et al., 2017). It significantly reduces the diameter (Du et al., 2005), strength (Vu & Bing, 2018) and axial load-bearing capacity of reinforcing bars in corroded RC structures (Goksu & Ilki, 2016; Luo et al., 2020; Shen et al., 2021). Furthermore, as the corrosion products expand, they exert tensile stresses on the interface

[1] Aminulai, H. O., Robinson, A. F., Ferguson, N. S., & Kashani, M. M. (2023a). Impact of corrosion on axial load capacity of ageing low-strength reinforced concrete columns with different confinement ratios. *Construction and Building Materials*, *384*, 131355. https://doi.org/https://doi.org/10.1016/j.conbuildmat.2023.131355

[2] Aminulai, H. O., Ferguson, N., & Kashani, M. (2023a). Structural behaviour of axially loaded corroded low-strength RC columns with different confinement ratios. In *Life-Cycle of Structures and Infrastructure Systems* (pp. 3348-3355). CRC Press.

between reinforcement and concrete, resulting in corrosion cracks and subsequent spalling of the concrete cover (Shen et al., 2021). This reduces the concrete core confinement, leading to the degradation of strength and ductility and the long-term performance of the RC structure (Fang, 2020; Ma et al., 2022).

Extensive experimental and numerical studies have been carried out on corrosion-damaged RC components (Kashani et al., 2019; Meda et al., 2014; Rajput et al., 2019; Vecchi & Belletti, 2021; Yuan et al., 2017; Wenting Yuan et al., 2018; Wei Yuan et al., 2018). Moreover, many studies have been devoted to evaluating the seismic reliability of corroded RC components/structures (ABAQUS, 2019; Biondini et al., 2014; Guo et al., 2015; Li et al., 2009; Li et al., 2018; Ma et al., 2018; Ni Choine et al., 2016; Rajput et al., 2019; Rao et al., 2017b; Rodriguez et al., 1997; Yu et al., 2015; Zeng et al., 2022). The conclusion of these studies approves that corrosion of reinforcement increases the likelihood of catastrophic collapse in RC structures.

Ageing RC columns/piers generally fail through buckling of the vertical reinforcement bars together with the crushing of core confined concrete and the fracture of the longitudinal bars (Kashani et al., 2019), resulting from inadequate confinement from the transverse reinforcements. The failure becomes more critical in columns/piers in corrosion-laden environments where chloride-induced corrosion is prevalent and significantly affects the stress-strain behaviour of reinforcing bars. Therefore, numerous models are proposed to investigate the axial load-displacement behaviour of RC columns/piers in seismic regions (Aboutaha et al., 2013; Ma et al., 2022; Mohammed et al., 2018; Vu et al., 2016; Vu et al., 2017).

In the design of RC bridge piers/columns to resist seismic vibrations, the plastic regions are provided with adequate transverse reinforcement to improve their ductility and strength and prevent the buckling of longitudinal bars. This confinement reinforcement provides the compressed concrete with higher flexibility and stability, which helps to prevent collapse and shear failure during vibrations (Mander et al., 1988). Thus, the higher the level of confining stress in the concrete, the more its ductility and strength gain (Zeng, 2017). Several numerical and analytical models have been developed to investigate the effect of confinement of transverse reinforcement on the axial load capacity and stress-strain behaviour of RC columns (Hoshikuma et al., 1997; Liang et al., 2015; Mander et al., 1988; Saatcioglu & Razvi, 1992; Zeng, 2017). However, these models are primarily on plain RC columns without considering the effect of corrosion on the structural response of columns/piers. These models have been incorporated into design guidelines and codes for designing new RC bridge columns/piers. However, many old bridge columns are still with the old design without proper confinement. Therefore, the behaviour and

response of these old columns to combined effects of degradation and axial compressive load need to be investigated.

### 3.2.1 Research contribution and novelty of this chapter

Although the stress-strain behaviour of confined concrete in non-corroded RC columns has been comprehensively addressed (Andisheh et al., 2021), there are very few experimental studies on the effects of corrosion on the stress-strain behaviour of confined concrete columns, including the inelastic buckling of the longitudinal bars. Several researchers have used analytically developed stress-strain graphs of confined concrete subjected to corrosion for numerical applications without experimental verification (Ou et al., 2013; Ou & Nguyen, 2014). Also, most of the experimental works have been on normal and high-strength RC structures without many studies, if any, on old RC structures with low-strength concrete. However, many old RC structures still have low-strength concrete in seismic regions without seismic detailing. Hence, it is imperative to study the impact of corrosion on such old RC structures to understand their responses under load.

The corrosion of the rebars (longitudinal and transverse) in the concrete further decreases the mechanical performance of the corroded RC elements. As such, researchers modified some RC element models to reflect the corrosion effect on the stress-strain response of degraded RC columns. For example, Vu et al. (2017) adjusted the Mander et al. (1988) equation by adding the effect of corrosion on the volumetric ratio and yield strength of the transverse confining reinforcement, leading to a reduction in the adequate lateral confining pressure of the corroded column. Furthermore, Ma et al. (2022) extended the Mander et al. (1988) and Vu et al. (2017) models to reflect the corrosion effect on transverse reinforcements in rectangular columns.

Nevertheless, in most studies mentioned above, the influence of corrosion of the longitudinal and transverse rebars and different confinement configurations are not considered simultaneously. The corrosion test of reinforcement generally results in the loss of mechanical strength of RC members, while adequate confinement improves the ductility of RC members. Therefore, it is imperative to investigate the performance of RC columns under simultaneous reinforcement corrosion of the longitudinal and transverse reinforcement and the different confinement ratios.

The present study investigated the mechanical behaviour of ageing low-strength circular and square RC columns under simultaneous reinforcement corrosion, confinement configurations and monotonic axial load. 60 RC columns were designed and grouped into five different target degrees of reinforcement corrosion (i.e., 0%, 5%, 10%, 20% and 30%) with three confinement ratios (*L/D=5*, *L/D=8* and *L/D=13*) under compressive load (30 for monotonic axial and 30 for cyclic load). The different degrees of reinforcement corrosion were obtained by an accelerated

corrosion technique using the electrochemical process (Faraday's electrolysis technique). The effect of reinforcement corrosion and confinement ratios on the load-deformation responses of RC columns were analysed. The experimental results are further compared with analytical models in the literature.

## 3.3 Experimental design

### 3.3.1 Design of the specimens

The RC columns used in the investigation were designed to have a proposed strength of 20MPa to match the strength of ageing RC structures. The configuration and sizing of the specimen were limited to small RC columns, considering the maximum axial load capacity (compression) of the largest load capacity machine within the available existing experimental facility (TSRL, University of Southampton). The Instron Schenck G machine has a maximum axial load capacity of 630kN. The sizing of the specimens is shown in Table 3.1 below.

**Table 3.1. Sizing and load capacities of the test specimen**

| Parameters | Square column | Circular column |
|---|---|---|
| **Unconfined Concrete Strength (MPa)** | 20 | 20 |
| **Confined Concrete Strength (MPa)** | 30 | 30 |
| **Steel Strength (MPa)** | 500 | 500 |
| **Cross-section size (mm)** | 125 x 125 | 125 dia. |
| **Cross-section area ($mm^2$)** | 15625 | 12271.85 |
| **Number of longitudinal 10mm bars** | 4 | 5 |
| **Area of longitudinal bars ($mm^2$)** | 314.16 | 392.70 |
| **Total force (kN)** | 625.83 | 564.50 |

### 3.3.2 Specimen details material properties

A total of 60 RC columns (30 squares and 30 circulars) were designed for the experimental work, as shown in Figure 3.1 and cast into the square and circular columns. The square columns have a 125 × 125 × 600mm dimension incorporating four (4) No. 10mm diameter longitudinal bars, while the circular samples (125mm diameter × 600mm long) have five (5) No. 10mm longitudinal bars.

All the rebars in the columns were joined together with steel tie wires to ensure that the transverse and longitudinal bars corrode during the corrosion process. The columns were designed with three different confinement ratios in the middle 400mm zone, while the 100mm ends have transverse bars spaced at 25mm (Figure 3.1). Furthermore, the 100mm ends are wrapped with epoxy-coated GFRP to minimise the stress concentration damage at the top and bottom ends of the columns and ensure that the failure occurs at the RC columns' middle zone during loading.

The adequate confinement of concrete increases RC structures' ductility and load-carrying capacity (Zeng, 2017). Therefore, the RC short columns (square and circular) were designed to have three levels of confinements based on the spacing of the transverse reinforcements. The transverse reinforcement provides the needed confinement through the centre-to-centre spacing (L) in relation to the diameter of the longitudinal reinforcement (D), known as the L/D ratio. The columns in this research are thus designed with transverse reinforcement spaced as L/D = 5, L/D = 8 and L/D = 13 for the different levels of confinements, respectively and five targeted degrees of corrosion. The targeted degrees of corrosion range from 0% to 30% (i.e., 0%, 5%, 10%, 20% and 30%) as shown in Tables 3.2 and 3.3. The specimens were categorised according to their shape into circular and square (i.e., C and S), with the second numbers representing the level of confinements (5, 8 and 13). In contrast, the last numbers denote the estimated degree of corrosion (Tables 3.2 and 3.3). Furthermore, the letters B and A are used to denote samples used for axial monotonic and cyclic tests, respectively.

**Table 3.2. Experimental test matrix**

| **Circular columns** | | | **Square columns** | | |
|---|---|---|---|---|---|
| **Specimen label** | **Confinement level** | **Targeted corrosion (%)** | **Specimen label** | **Confinement level** | **Targeted corrosion (%)** |
| **C5B0** | 5 | 0 | **S5B0** | 5 | 0 |
| **C5B5** | 5 | 5 | **S5B5** | 5 | 5 |
| **C5B10** | 5 | 10 | **S5B10** | 5 | 10 |
| **C5B20** | 5 | 20 | **S5B20** | 5 | 20 |
| **C5B30** | 5 | 30 | **S5B30** | 5 | 30 |
| **C8B0** | 8 | 0 | **S8B0** | 8 | 0 |
| **C8B5** | 8 | 5 | **S8A5** | 8 | 5 |

| | | | | | |
|---|---|---|---|---|---|
| **C8B10** | 8 | 10 | **S8B10** | 8 | 10 |
| **C8B20** | 8 | 20 | **S8B20** | 8 | 20 |
| **C8B30** | 8 | 30 | **S8B30** | 8 | 30 |
| **C13B0** | 13 | 0 | **S13B0** | 13 | 0 |
| **C13B5** | 13 | 5 | **S13B5** | 13 | 5 |
| **C13B10** | 13 | 10 | **S13B10** | 13 | 10 |
| **C13B20** | 13 | 20 | **S13B20** | 13 | 20 |
| **C13B30** | 13 | 30 | **S13B30** | 13 | 30 |

**Table 3.3. Experimental test matrix for the axial cyclic compressive test**

| **Circular columns** | | | **Square columns** | | |
|---|---|---|---|---|---|
| **Specimen label** | **Confinement level** | **Targeted corrosion (%)** | **Specimen label** | **Confinement level** | **Targeted corrosion (%)** |
| **C5A0** | 5 | 0 | **S5A0** | 5 | 0 |
| **C5A5** | 5 | 5 | **S5A5** | 5 | 5 |
| **C5A10** | 5 | 10 | **S5A10** | 5 | 10 |
| **C5A20** | 5 | 20 | **S5A20** | 5 | 20 |
| **C5A30** | 5 | 30 | **S5A30** | 5 | 30 |
| **C8A0** | 8 | 0 | **S8A0** | 8 | 0 |
| **C8A5** | 8 | 5 | **S8A5** | 8 | 5 |
| **C8A10** | 8 | 10 | **S8A10** | 8 | 10 |
| **C8A20** | 8 | 20 | **S8A20** | 8 | 20 |
| **C8A30** | 8 | 30 | **S8A30** | 8 | 30 |
| **C13A0** | 13 | 0 | **S13A0** | 13 | 0 |
| **C13A5** | 13 | 5 | **S13A5** | 13 | 5 |
| **C13A10** | 13 | 10 | **S13A10** | 13 | 10 |
| **C13A20** | 13 | 20 | **S13A20** | 13 | 20 |
| **C13A30** | 13 | 30 | **S13A30** | 13 | 30 |

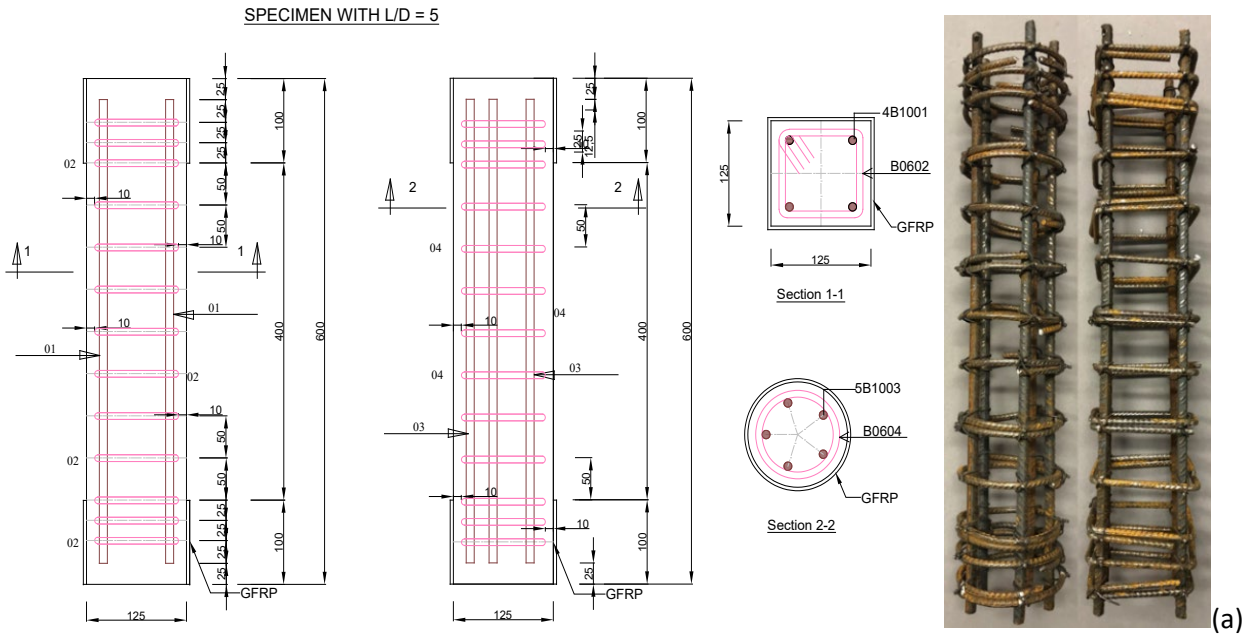
SPECIMEN WITH L/D = 5
4B1001
B0602
GFRP
Section 1-1
5B1003
B0604
GFRP
Section 2-2
GFRP
GFRP

(a)

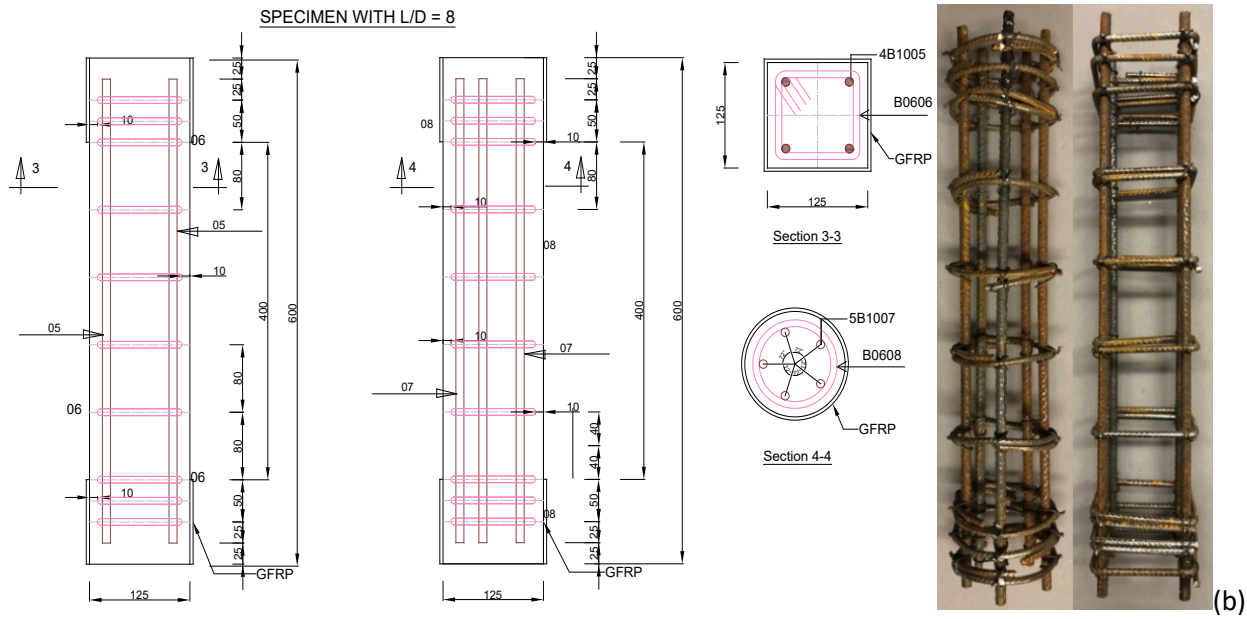
SPECIMEN WITH L/D = 8
4B1005
B0606
GFRP
Section 3-3
5B1007
B0608
GFRP
Section 4-4
GFRP
GFRP

(b)

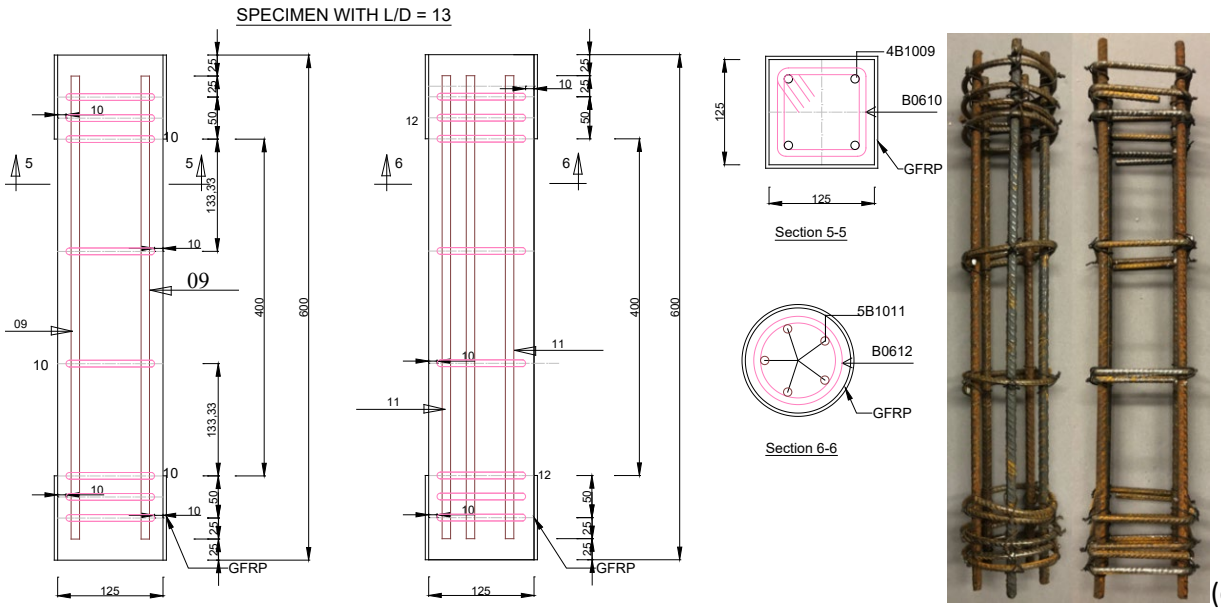


Figure 3.1: RC columns details showing the schematic drawing and reinforcement cages for the different confinement levels (a) High confined (*L/D = 5*) (b) Medium confined (*L/D = 8*) (c) Low confined (*L/D = 13*)

The longitudinal and transverse reinforcement used were the typical B500B British standard reinforcing bars. Tables 3.4 – 3.7 gives the schedule and bending configurations of the reinforcement bars and the summary of the reinforcement quantities used in producing the RC columns.

**Table 3.4. Bar bending schedule for high confined (*L/D = 5*) RC columns**

| location | Bar mark | Type and size | Number off. | Number in each | Total number | Length (mm) | Total length (mm) | Shape |
|---|---|---|---|---|---|---|---|---|
| **Square column** | 01 | B10 | 10 | 4 | 40 | 550 | 22,000 | 550 |
| | 02 | B06 | 10 | 13 | 130 | 545 | 70,850 | 62.5, 105, 105, L = 545mm |
| **Square column** | 03 | B10 | 10 | 5 | 50 | 545 | 27,500 | 550 |
| | 04 | B06 | 10 | 13 | 130 | 460 | 59,800 | 105, 130, L = 460mm |

**Table 3.5. Bar bending schedule for medium confined (*L/D = 8*) RC columns**

| location | Bar mark | Type and size | Number off. | Number in each | Total number | Length (mm) | Total length (mm) | Shape |
|---|---|---|---|---|---|---|---|---|
| **Square column** | 05 | B10 | 10 | 4 | 40 | 550 | 22,000 | 550 |
| | 06 | B06 | 10 | 10 | 100 | 545 | 54,500 | 82.5, 105, 105, L = 545mm |
| **Square column** | 07 | B10 | 10 | 5 | 50 | 545 | 27,500 | 550 |
| | 08 | B06 | 10 | 10 | 100 | 460 | 46,000 | 105, 130, L = 460mm |

**Table 3.6. Bar bending schedule for high confined (*L/D = 13*) RC columns**

| location | Bar mark | Type and size | Number off. | Number in each | Total number | Length (mm) | Total length (mm) | Shape |
|---|---|---|---|---|---|---|---|---|
| **Square column** | 01 | B10 | 10 | 4 | 40 | 550 | 22,000 | 550 |
| | 02 | B06 | 10 | 8 | 80 | 545 | 43,600 | 82.5, 105, 105, L = 545mm |
| **Square column** | 03 | B10 | 10 | 5 | 50 | 545 | 27,500 | 550 |
| | 04 | B06 | 10 | 8 | 80 | 460 | 36,800 | 105, 130, L = 460mm |

**Table 3.7. Summary of steel reinforcement required for the production of RC columns.**

| Type and size of bars | Total length (mm) | Total length (m) | Weight factor (kg/m) | Mass required. (kg) |
|---|---|---|---|---|
| **B10** | 150,500 | 150.5 | 0.616 | 92.708 |
| **B6** | 315,550 | 315.6 | 0.222 | 70.063 |

### 3.3.3 Confined concrete characteristics estimates of the RC columns.

#### 3.3.3.1 Confined circular RC columns:

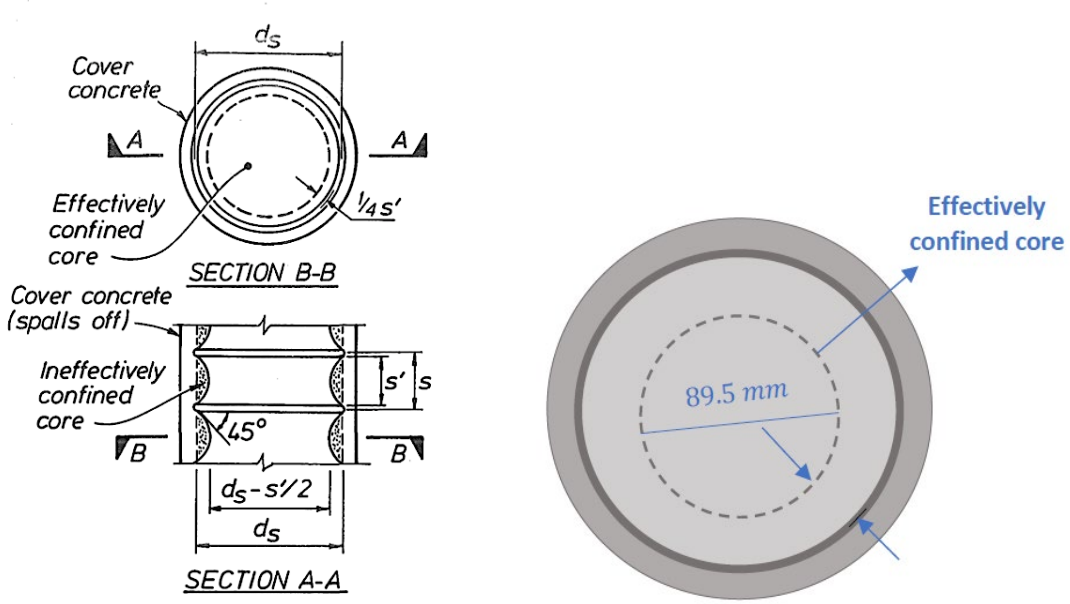


Figure 3.2: Area of the effectively confined core and the distance from the centre of the stirrup bar to the confined core line

The area of effectively confined core for the circular RC columns is estimated as below:

$d_s = 125 - 20 - 6 = 99mm$ for all the circular columns

$$\rho_{cc} = \frac{Area\ of\ longitudinal\ bars}{area\ of\ effectively\ confined\ concrete\ core}$$

$\rho_{cc} = \frac{5\,\pi\,(10)^2}{\pi\,(89.5)^2} = 0.0624$ for all the circular columns

**Table 3.8. The coefficients of the confinement effectiveness of circular RC columns at different degrees of confinement**

| Column Confinement level | Spacing between transverse bars, S' (mm) | Confinement effectiveness coefficient, $k_e$ (Eq. 2.28) |
|---|---|---|
| **High confined (L/D = 5)** | $50 - 6 = 44$ | 0.645 |
| **Medium confined (L/D = 8)** | $80 - 6 = 74$ | 0.418 |
| **Low confined (L/D = 13)** | $133 - 6 = 127$ | 0.137 |
| **Note: All L/D ratios have the same values of $d_s$ and $\rho_{cc}$** | | |

The values in Table 3.8 were used in Equation 2.24 to estimate the volumetric ratios of the circular columns, as shown in Table 3.9 below.

$$\rho_{c5} = \frac{4(\pi \times 6^2)}{4(99 \times 50)} = 0.0228$$

$$\rho_{c8} = \frac{4(\pi \times 6^2)}{4(99 \times 80)} = 0.0143$$

$$\rho_{c13} = \frac{4(\pi \times 6^2)}{4(99 \times 133.33)} = 0.0086$$

#### 3.3.3.2 Confined square RC columns:

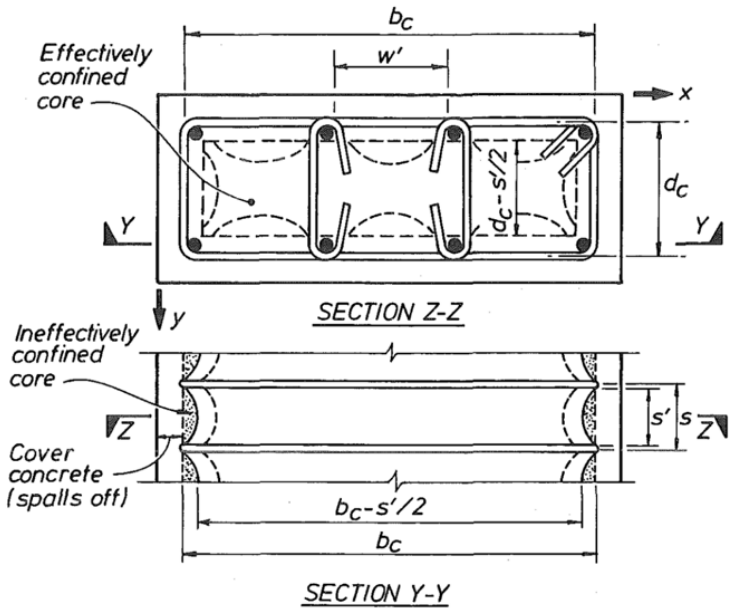


Figure 3.3: Confined core for rectangular cross-section (Mander et al., 1988)

The equations were for a rectangular, but this work involves square sections as such from Figure 3.3,

$b_c = d_c$ (Since square sections have all the sides equal) and $w' = 0$, then

$$k_e = \frac{\left(1 - \frac{s'}{2d_c}\right)^2}{1 - \rho_{cc}}$$

$d_c = 125 - 20 - 6 = 99mm$ for all the square columns

$$\rho_{cc} = \frac{Area\ of\ longitudinal\ bars}{area\ of\ effectively\ confined\ concrete\ core} = 0.0334$$ for all the square columns

The following coefficients and factors are obtained from Vu et al. (2017)

$\alpha_s =$ reduction factor for yield strength of corroded transverse bars $(0.005)$

$\alpha =$ stress correction coefficient (0.19 for a square section with single hoop)

$\beta =$ strain correction coefficient (0.49 for single hoop square sections)

$\varepsilon_{co} =$ maximum strain for unconfined concrete (taken as 0.002)

**Table 3.9. The coefficients of the confinement effectiveness of square RC columns at different degrees of confinement**

| Column Confinement level | Spacing between transverse bars, S' (mm) | Confinement effectiveness coefficient, ke (Eq. 2.29) |
|---|---|---|
| **High confined (L/D = 5)** | $50 - 6 = 44$ | 0.618 |
| **Medium confined (L/D = 8)** | $80 - 6 = 74$ | 0.395 |
| **Low confined (L/D = 13)** | $133 - 6 = 127$ | 0.123 |
| **Note: All L/D ratios have the same values of $d_c$ and $\rho_{cc}$** | | |

The values in Table 3.9 were used in Equation 2.24 to estimate the volumetric ratios of the square columns, as shown in Table 3.10 below.

$$\rho_{s5} = \frac{A_{sx}}{sd_c} = \frac{5856.32}{50\times99} = 1.1831$$

$$\rho_{s8} = \frac{A_{sx}}{sd_c} = \frac{5856.32}{80\times99} = 0.7394$$

$$\rho_{s13} = \frac{A_{sx}}{sd_c} = \frac{5856.32}{133\times99} = 0.4448$$

Table 3.10 below summarises the reinforcement configuration properties (longitudinal and transverse) of the circular and square RC columns.

**Table 3.10. The summary of confined concrete reinforcement details**

| Column type | Confinement level | Longitudinal reinforcement | | | Transverse reinforcement | | |
|---|---|---|---|---|---|---|---|
| | | Diameter (mm) | Number in column | Reinforcement ratio (%) | Diameter (mm) | Spacing (mm) | Volumetric ratio (%) |
| **Circular** | High confined (*L/D* = 5) | 10 | 5 | 5.1 | 6 | 50 | 2.28 |
| | Medium confined (*L/D* = 8) | 10 | 5 | 5.1 | 6 | 80 | 1.43 |
| | Low confined (*L/D* = 13) | 10 | 5 | 5.1 | 6 | 133.33 | 0.86 |
| **Square** | High confined (*L/D* = 5) | 10 | 4 | 3.21 | 6 | 50 | 1.18 |
| | Medium confined (*L/D* = 8) | 10 | 4 | 3.21 | 6 | 80 | 0.74 |
| | Low confined (*L/D* = 13) | 10 | 4 | 3.21 | 6 | 133.33 | 0.44 |

### 3.3.4 Concrete mix design

The mix design for the concrete specimen was done by following the steps outlined in Kett (2009). This involves proportioning the constituent material according to the targeted strength (20MPa) of the concrete and the weight of the materials. The materials needed for the experiments were determined using the appropriate water/cement ratio and the strength of the constituent materials as specified by the relevant BS codes and standards. The breakdown of the constituent materials required to cast the 60 specimens (30 square and 30 circular columns) for the monotonic and cyclic loading tests and 12 mass concrete is shown in Table 3.11. This estimate was used to order ready-mix concrete supplied for the work.

The concrete mix was designed as low-strength concrete representing a non-code conforming column with an expected mean compressive strength of 20MPa and a maximum aggregate size of 10mm. All the columns were cast with a nominal cover of 10mm. Concrete samples with the same configuration as the square and circular columns were taken for compressive strength tests during the casting.

**Table 3.11. weight of constituent material for concrete**

| Water (kg) | Cement (kg) | Fine aggregate (kg) | Coarse aggregate (kg) | Salt (5% cement content) (Kg) |
|---|---|---|---|---|
| 149.68 | 299.36 | 604.80 | 616.83 | 14.97 |

### 3.3.5 RC columns production

The reinforcement bars were marked, cut and bent at the Highfield campus of the University of Southampton. The rebars were cut as per the designed cross-sections of the square and circular columns, as presented in the bar bending schedule presented in Tables 3.4 – 3.7. The circular columns were cast using 125mm diameter pipes, cut to size, placed in a wooded base (Fig. 3.6), and held together by tie wires. The square columns were also cast with formwork made from 12mm thick plywood. The plywood was ordered cut to the required size as per the schedule in Figure 3.8 and cast in the old Civil Engineering laboratory at the Highfield campus of the University of Southampton. The RC columns were produced with ready-mix concrete from a local supplier in Southampton and placed in the formwork to harden. After a week, the hardened RC columns were removed from the formwork and subsequently immersed in water to cure for about three weeks. The procedure for the production of the columns is presented in the image below (Figs. 3.4 – 3.10).

Figure 3.4: Marking, cutting and tying the rebars

Figure 3.5: Completed Circular and Square reinforcements cages

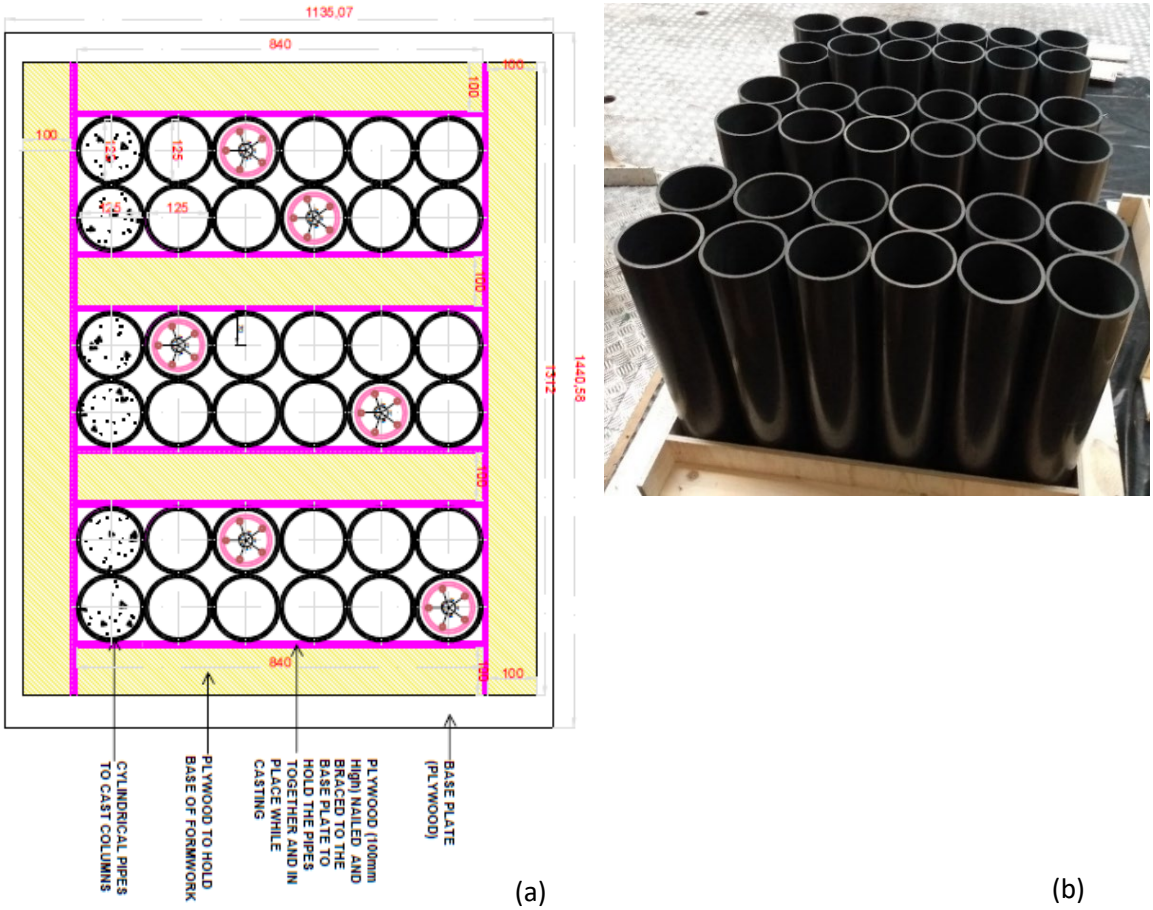


Figure 3.6: Arrangement of pipes for casting circular columns - 125mm diameter and 600mm high (a) Schematic drawing and (b) laboratory setup

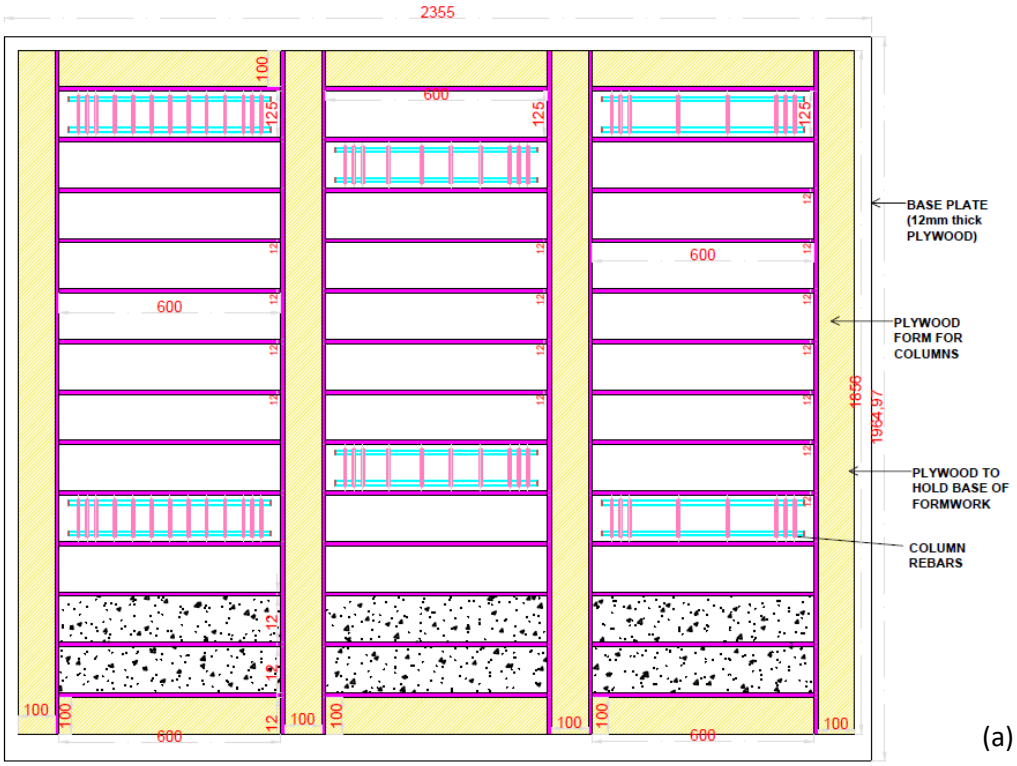


(a)

(b)

Figure 3.7: Arrangement of formworks for casting square columns - 125mm × 125mm and 600mm long (a) Schematic drawing and (b) laboratory setup

| S/No. | Dimension (mm) | Shape | Numbers Required. |
|---|---|---|---|
| 1. | 1850 x 125 | 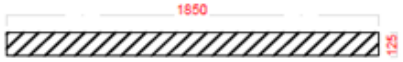  | 6 |
| 2. | 600 x 125 |   | 39 |
| 3. | 1850 x 100 |   | 4 |
| 4. | 600 x 100 |   | 6 |
| 5. | 1312 x 100 |   | 4 |
| 6. | 840 x 100 | 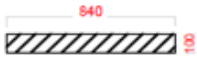  | 10 |

Figure 3.8: Schedule of wood needed for formwork


Figure 3.9: Completed Square and Circular RC samples


Figure 3.10: Curing the Square and Circular RC samples by complete immersion in water

## 3.4 Preliminary tests on constituent materials

### 3.4.1 Compressive strength test

The compressive strength test was done at the Testing and Structures Research Laboratory (TSRL), the University of Southampton, using the hydraulically powered 630kN Instron Schenk machine. The concrete columns were tested using the displacement control at a constant 2mm/min loading rate until failure. The samples used for the test were not the conventional cube/cylinder samples but had the same configurations as the reinforced ones. The square samples are 125 × 125 × 600mm in dimension, while the circular samples are 125mm diameter × 600mm long. The strain was estimated at the middle 400mm section, the same as the reinforced columns. Figure 3.11(a) shows the stress-strain response of the concrete, with the square columns having an average compressive strength of 12.03MPa while the circular columns have 9.90MPa compressive strength. Furthermore, Figure 3.11(b) is the failure mode of both the circular and square mass concrete after loading. The observed difference in the compressive strength of the columns is due to the failure mechanism, as some of the columns had a failure in the GFRP-strengthened ends.

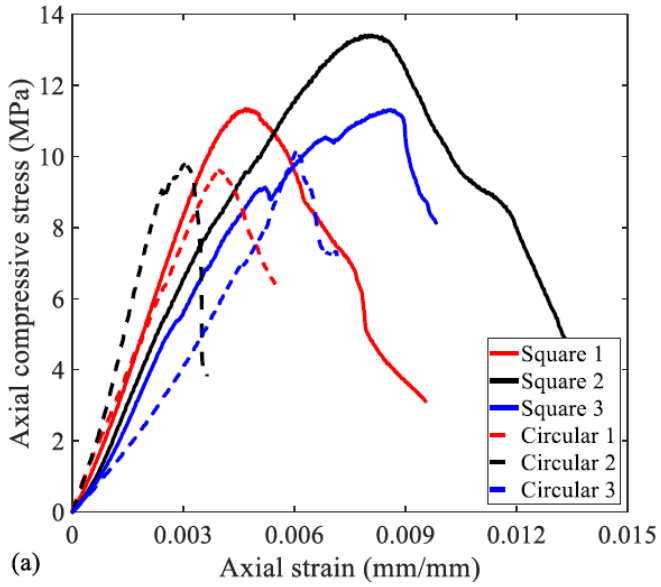



Figure 3.11: Mass concrete behaviour (a) compressive stress-strain response (b)observed failure after the test

### 3.4.2 Rebar tensile test

Tensile tests were conducted on the uncorroded transverse and longitudinal rebars using the Instron 8032 test machine with 100kN capacity and ±50mm travel at the Testing and Structures Research Laboratory (TSRL), the University of Southampton to determine the mechanical properties. Three reinforcement samples amongst the transverse and longitudinal rebars used in

the columns were selected for the tensile tests according to BS EN 10080:2005 (The British Standards, 2005) and BS 4449:2005+A3:2016 (The British Standards, 2016). In addition, the rebars were subjected to different loading rates before and after the yielding as specified in BS EN ISO 6892-1:2019 (The British Standards, 2020). At the same time, a 50mm dynamic extensometer with ±5mm maximum stroke measures the strain corresponding to the extension of the rebar. Figure 3.12(a) shows the experimental setup of the tensile test, while Figure 3.12(b) shows the failed rebar after the test.

The loading rates used in the test are estimated with the equation obtained from BS EN ISO 6892-1:2019 and stated below:

$$\text{Elastic region} = 0.00025/\sec \times L_c \tag{3.1}$$

$$\text{Yielding} = 0.0025/\sec \times L_c \tag{3.2}$$

$$\text{Plastic region} = 0.0067/\sec \times L_c \tag{3.3}$$

$$L_c = L_0 + (\frac{d}{2}) \tag{3.4}$$

where,

$L_c = \text{the parallel length of the test sample}$

$L_0 = \text{original gauge length}$

$d = \text{diameter of the test sample}$

The parallel length of the test sample is determined from Table 3.12 below.

**Table 3.12: Parallel length for circular cross-section test pieces (BS EN ISO 6892-1:2019)**

| **Coefficient of proportionality k** | **Diameter d (mm)** | **Original gauge length $L_0 = k\sqrt{S_0}$ (mm)** | **Minimum parallel length $L_c$ (mm)** |
|---|---|---|---|
| **5.65** | 20 | 100 | 110 |
| | 14 | 70 | 77 |
| | 10 | 50 | 55 |
| | 5 | 25 | 28 |

The tensile test was done on 250mm long 6mm (3 Nos) and 10mm (3 Nos) reinforcement bars to determine their yield and ultimate strengths and Young's modulus of elasticity (Fig. 3.13). The summary of the result is presented in Table 3.13 below.

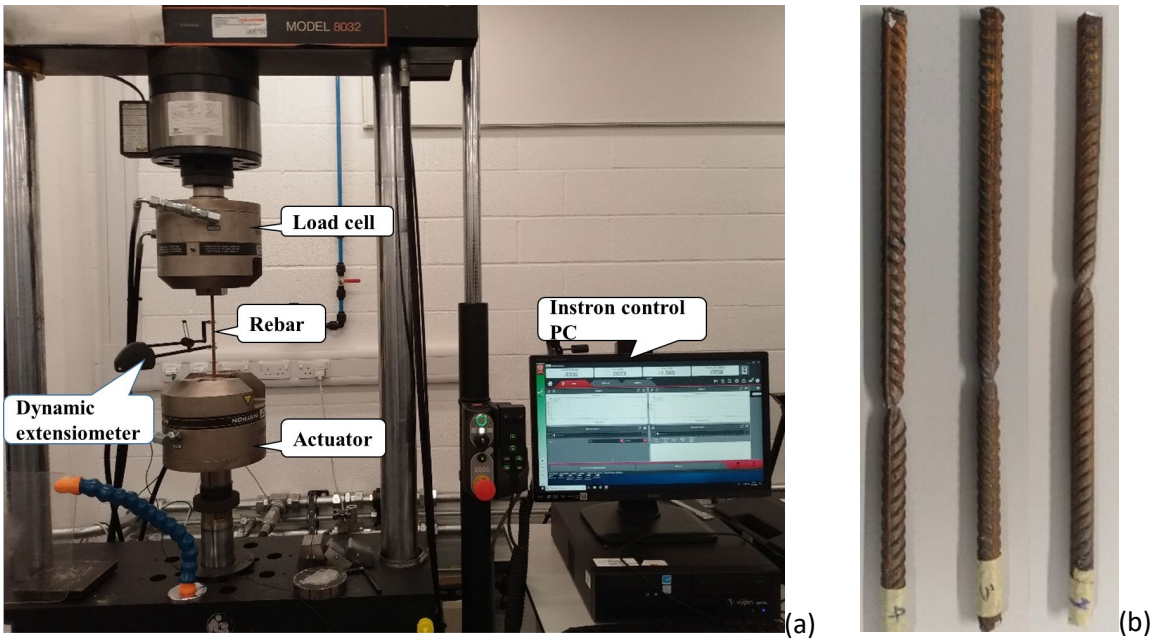


Figure 3.12: Tensile test of rebars (a) experimental setup (b) observed failure of 10mm bars

The stress-strain response of the rebars is shown in Figure 3.13, while the mechanical properties and code requirements summary are shown in Tables 3.13 and 3.14, respectively. The average yield, ultimate strengths and strain values obtained conform to the values specified for B500B rebars (The British Standards, 2016). Also, the variation in unit mass from the code specification (Table 3.14) for the rebars is 0.9% and 1.13% for the 6mm and 10mm bars, respectively and are considered insignificant (Kashani, 2014). The ductility of one of the 10mm bars was higher than the others as the bar failed outside the gauge length of the extensometer, thereby leading to the extensometer being unable to measure the actual extension of the bar under load.

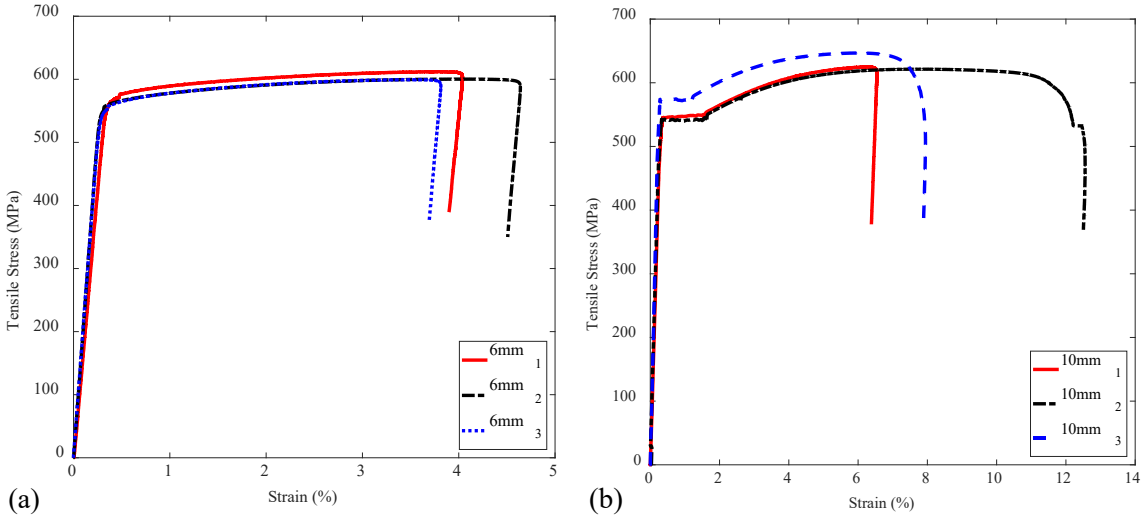


Figure 3.13: Tensile stress-strain behaviour of reinforcement bars (a) transverse (b) longitudinal

**Table 3.13: Mechanical properties of the uncorroded transverse and longitudinal bars**

| Reinforcement type | Symbol | Unit | 6mm (B6) | 10mm (B10) |
|---|---|---|---|---|
| **Yield Strength** | $f_y$ | MPa | 531.82 | 551.68 |
| **Ultimate strength** | $f_u$ | MPa | 603.05 | 630.11 |
| **Modulus of Elasticity** | E | GPa | 185.23 | 196.73 |
| **Yield Strain** | $\varepsilon_y = f_y/\mathbf{E}$ | | 0.00287 | 0.00280 |
| **Ultimate strain** | $\varepsilon_u$ | | 0.03356 | 0.06349 |
| **Strain ratio** | $\varepsilon_u/\varepsilon_y$ | | 11.69 | 22.67 |
| **Strength ratio** | $f_u/f_y$ | | 1.134 | 1.142 |
| **Average Total elongation at failure** | $\lambda_f$ | % | 4.16 | 8.49 |
| **Unit mass** | m | (kg/m) | 0.224 | 0.624 |

**Table 3.14: Minimum values of tensile properties of B500B reinforcement (**The British Standards, 2016**)**

| Reinforcement type | Symbol | Unit | 6mm (B6) | 10mm (B10) |
|---|---|---|---|---|
| **Yield Strength, $f_y$ (MPa)** | $f_y$ | MPa | 485 | 485 |
| **Strength ratio,** | $f_u/f_y$ | | 1.06 | 1.06 |
| **Average Total elongation at failure** | $\lambda_f$ | % | 4.0 | 4.0 |
| **Unit mass, m (kg/m)** | | | 0.222 | 0.617 |

### 3.4.3 Accelerated Corrosion Procedure

The natural corrosion process usually takes a more extended period, which could be several years or decades. As such, the electrochemical process known as the accelerated corrosion method is often adopted in the laboratory to simulate the corrosion process. The constant current and constant voltage methods of accelerated corrosion are commonly used. Much research has been done to investigate these corrosion methods' effectiveness in reproducing RC structures' corrosion process. Researchers have used the constant voltage (al-Swaidani & Aliyan, 2015; Deb & Pradhan, 2013; Kumar et al., 2012; Lee et al., 2000) and the constant current (El Maaddawy et al., 2005; El Maaddawy & Soudki, 2003; Kashani et al., 2013b; Pritzl et al., 2014; Talakokula et al., 2014) methods to simulate the corrosion process in the laboratory. The two methods were able to reproduce the corrosion of reinforcement in RC structures reasonably well. Still, the constant current method was found to give a better reproduction of the corrosion process than the constant voltage method (Altoubat et al., 2016).

The RC samples' corrosion was done using the constant current method of accelerated corrosion by passing a constant current of 2A through the reinforcing bars connected to the anode of the DC power supplies while also connecting the stainless-steel plate to the cathode. Then, the connected specimen is placed in a salt bath with 10% sodium chloride (NaCl) by water weight to simulate the corrosive environment. 5% sodium chloride by weight of the cement was added to the concrete mix during casting to improve the conductivity of the RC column during the accelerated corrosion process. The setup for the accelerated corrosion is shown in Figure 3.14 below.

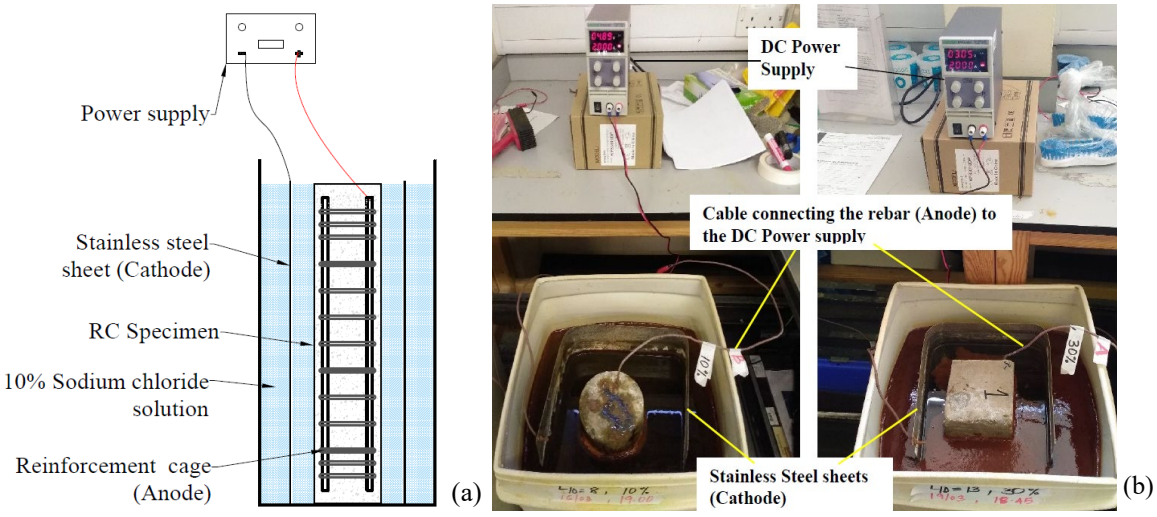


Figure 3.14. Accelerated corrosion procedure; (a) Schematic setup drawing, (b) laboratory setup, (c) corroded columns, and (d) corroded rebars after cleaning

The duration for the expected mass loss was estimated using Faraday's 2nd law of electrolysis (Kashani et al., 2013b) as follows (Eq. 3.5):

$$\Delta m = \left(\frac{M}{Z}\right)\left(\frac{Q}{F}\right) \tag{3.5}$$

where $\Delta m$ is the estimated mass loss (g), M is the molar mass of the iron (56g/mol), Z is the ionic charge for iron (valence electron transferred per ion = 2), and F is the Faraday's constant (96500 C/mol). Q is calculated from Eq. 3.6 below:

$$Q = \int_0^T I dt = IT \tag{3.6}$$

where I is the magnitude of the applied current (Ampere, A), T is the estimated time to achieve the desired corrosion (s),

$$\Delta m = \frac{MIT}{ZF} \tag{3.7}$$

The estimated mass loss and the duration needed to achieve the loss are presented in Tables 3.15 and 3.16 for the circular and square samples used in the monotonic and cyclic tests. Equation 3.7 estimates the expected corrosion mass loss, which could differ from the actual corrosion mass loss obtained after the corrosion process. Hence, the corroded bars are removed from the columns after testing by breaking the RC column. Then, the rebars were soaked in vinegar and cleaned with water and a wire brush to remove the surface's concrete and rust particles per ASTM G1-03 (ASTM, 2011). This brushing and cleaning procedure was also applied to the uncorroded specimen, and the cleaning effect was negligible on the base materials (Kashani et al., 2013b).

Afterwards, the actual mass loss due to corrosion is estimated by weighing the rebars and is estimated from Eq. 3.8:

$$\gamma = \frac{m_0 - m}{m} \times 100 \quad (3.8)$$

where $m_0$, is the mass per unit length of the uncorroded rebar, and $m$ is the mass per unit length of the rebar after cleaning. This equation gives an average corrosion loss (mass loss) along the length of the rebar. It should be noted that there were not any disconnections between the stirrups and longitudinal reinforcement, and hence, the current is applied to all the reinforcement at the same time.

**Table 3.15: Details of 125mm dia. circular RC columns and estimated duration for corrosion**

| S/No | Specimen ID | L/D | Corrosion Rate (%) | Loading | Total mass (kg) | Mass loss (kg) | Time for corrosion (Days) |
|---|---|---|---|---|---|---|---|
| **1** | C0 | 5 | 0 | Monotonic | 3.022 | 0 | 0 |
| **2** | C5 | | 5 | Monotonic | | 0.151 | 3.013 |
| **3** | C10 | | 10 | Monotonic | | 0.302 | 6.027 |
| **4** | C20 | | 20 | Monotonic | | 0.604 | 12.054 |
| **5** | C30 | | 30 | Monotonic | | 0.907 | 18.081 |
| **6** | C0 | | 0 | Cyclic | | 0 | 0 |
| **7** | C5 | | 5 | Cyclic | | 0.151 | 3.013 |
| **8** | C10 | | 10 | Cyclic | | 0.302 | 6.027 |
| **9** | C20 | | 20 | Cyclic | | 0.604 | 12.054 |
| **10** | C30 | | 30 | Cyclic | | 0.907 | 18.081 |
| **11** | C0 | 8 | 0 | Monotonic | 2.714 | 0 | 0 |
| **12** | C5 | | 5 | Monotonic | | 0.135 | 2.707 |
| **13** | C10 | | 10 | Monotonic | | 0.271 | 5.413 |
| **14** | C20 | | 20 | Monotonic | | 0.543 | 10.826 |
| **15** | C30 | | 30 | Monotonic | | 0.814 | 16.239 |
| **16** | C0 | | 0 | Cyclic | | 0 | 0 |
| **17** | C5 | | 5 | Cyclic | | 0.135 | 2.707 |
| **18** | C10 | | 10 | Cyclic | | 0.271 | 5.413 |

| S/No | Specimen ID | L/D | Corrosion Rate (%) | Loading | Total mass (kg) | Mass loss (kg) | Time for corrosion (Days) |
|---|---|---|---|---|---|---|---|
| **19** | C20 | | 20 | Cyclic | | 0.543 | 10.826 |
| **20** | C30 | | 30 | Cyclic | | 0.814 | 16.239 |
| **21** | C0 | 13 | 0 | Monotonic | 2.509 | 0 | 0 |
| **22** | C5 | | 5 | Monotonic | | 0.125 | 2.502 |
| **23** | C10 | | 10 | Monotonic | | 0.251 | 5.004 |
| **24** | C20 | | 20 | Monotonic | | 0.502 | 10.008 |
| **25** | C30 | | 30 | Monotonic | | 0.814 | 15.012 |
| **26** | C0 | | 0 | Cyclic | | 0 | 0 |
| **27** | C5 | | 5 | Cyclic | | 0.125 | 2.502 |
| **28** | C10 | | 10 | Cyclic | | 0.251 | 5.004 |
| **29** | C20 | | 20 | Cyclic | | 0.502 | 10.008 |
| **30** | C30 | | 30 | Cyclic | | 0.814 | 15.012 |

**Table 3.16: Details of 125mm x 125mm square RC columns and estimated duration for corrosion**

| S/No | Specimen ID | L/D | Corrosion Rate (%) | Loading | Total mass (kg) | Mass loss (kg) | Time for corrosion (Days) |
|---|---|---|---|---|---|---|---|
| **1** | S0 | 5 | 0 | Monotonic | 2.925 | 0 | 0 |
| **2** | S5 | | 5 | Monotonic | | 0.146 | 2.917 |
| **3** | S10 | | 10 | Monotonic | | 0.293 | 5.834 |
| **4** | S20 | | 20 | Monotonic | | 0.585 | 11.668 |
| **5** | S30 | | 30 | Monotonic | | 0.878 | 17.502 |
| **6** | S0 | | 0 | Cyclic | | 0 | 0 |
| **7** | S5 | | 5 | Cyclic | | 0.146 | 2.917 |
| **8** | S10 | | 10 | Cyclic | | 0.293 | 5.834 |
| **9** | S20 | | 20 | Cyclic | | 0.585 | 11.668 |
| **10** | S30 | | 30 | Cyclic | | 0.878 | 17.502 |

| | | | | | | | |
|---|---|---|---|---|---|---|---|
| **11** | S0 | 8 | 0 | Monotonic | 2.562 | 0 | 0 |
| **12** | S5 | | 5 | Monotonic | | 0.128 | 2.555 |
| **13** | S10 | | 10 | Monotonic | | 0.256 | 5.109 |
| **14** | S20 | | 20 | Monotonic | | 0.512 | 10.219 |
| **15** | S30 | | 30 | Monotonic | | 0.769 | 15.328 |
| **16** | S0 | | 0 | Cyclic | | 0 | 0 |
| **17** | S5 | | 5 | Cyclic | | 0.128 | 2.555 |
| **18** | S10 | | 10 | Cyclic | | 0.256 | 5.109 |
| **19** | S20 | | 20 | Cyclic | | 0.512 | 10.219 |
| **20** | S30 | | 30 | Cyclic | | 0.769 | 15.328 |
| **21** | S0 | 13 | 0 | Monotonic | 2.320 | 0 | 0 |
| **22** | S5 | | 5 | Monotonic | | 0.116 | 2.313 |
| **23** | S10 | | 10 | Monotonic | | 0.232 | 4.626 |
| **24** | S20 | | 20 | Monotonic | | 0.464 | 9.253 |
| **25** | S30 | | 30 | Monotonic | | 0.696 | 13.879 |
| **26** | S0 | | 0 | Cyclic | | 0 | 0 |
| **27** | S5 | | 5 | Cyclic | | 0.116 | 2.313 |
| **28** | S10 | | 10 | Cyclic | | 0.232 | 4.626 |
| **29** | S20 | | 20 | Cyclic | | 0.464 | 9.253 |
| **30** | S30 | | 30 | Cyclic | | 0.696 | 13.879 |

### 3.4.4 The wet layup of RC samples

The wet layup involves wrapping the top and bottom (100mm from both ends) of the samples with several layers of GFRP soaked in epoxy laminating resin (EL2) round the RC specimens (Fig. 3.15). The layers of GFRP are wrapped one after the other to stiffen the ends of the columns such that failure under compressive loading will occur in the middle section of the column. Typical mechanical properties of the epoxy resin and GFRP are presented in Table 3.17.

**Table 3.17. Mechanical properties of GFRP and epoxy resin (Xin et al., 2017)**

| Properties | GFRP | Epoxy resin |
|---|---|---|
| **Density (kg/m3)** | 2560 | 1160 |
| **Young's modulus (GPa)** | 74 | 3.35 |
| **Shear modulus (GPa)** | 30.8 | 75 |
| **Poisson's ratio** | 0.20 | 0.35 |
| **Compressive strength (MPa)** | 1450 | 120 |
| **Tensile Strength (MPa)** | 2150 | 80 |


Figure 3.15. Wet layup of RC Columns (a) Individual columns (b) Completed samples before testing

### 3.4.5 Axial load testing and instrumentation

This experiment studies the response of RC columns under axial monotonic compressive loading using the 630kN capacity Instron Schenck machine having a 250mm travel at the Testing and Structures Research Laboratory (TSRL) of the University of Southampton. The machine used an internal Linear Variable Differential Transformer (LVDT) that measures the displacement of the actuator during loading. The test is conducted at a constant loading rate of 1mm/min using the displacement control settings in the Instron Bluehill software. The setup of the experiment is shown in Figure 3.16(a).

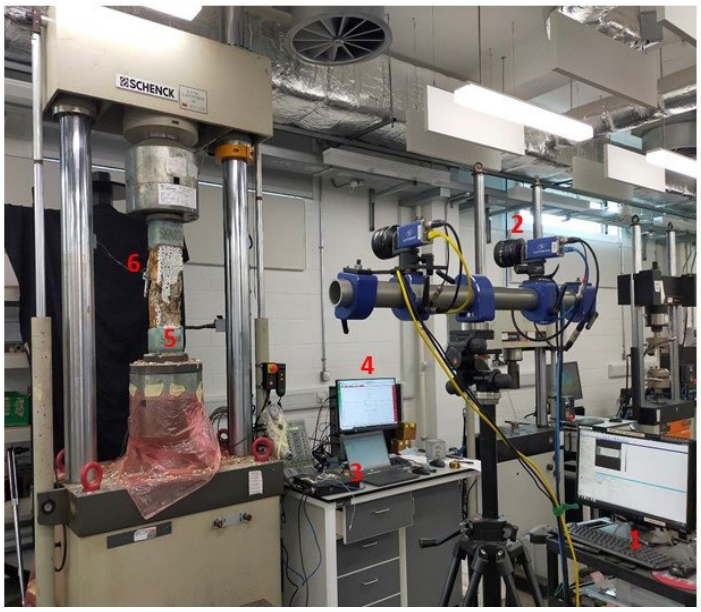


1 – DIC recording PC

2 – Stereo DIC cameras

3 – Strainsmart recording system

4 – Instron recording system

5 – RC sample

6 - LVDT

(a)

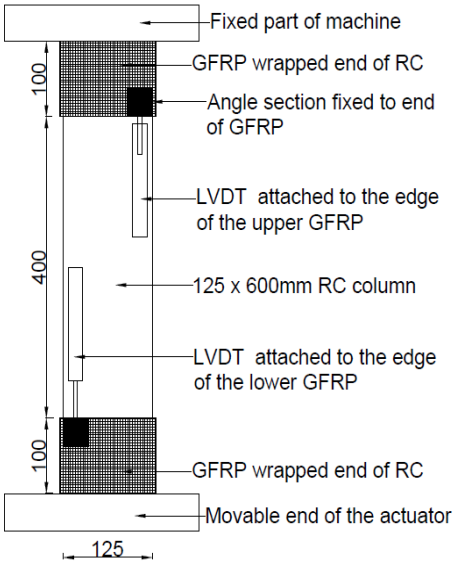


(b)

(c)


(d)

Figure 3.16: Experimental test setup (a) laboratory setup; (b) schematic of the LVDT connection; (c) Image of the LVDT connections to the R.C. samples and (d) R.C. sample with speckles for DIC

The displacement is measured with the LVDT, fixed to measure the displacement at the 400mm middle zone of the RC columns, and the stereo 3D Digital Image Correlation (DIC). The two LVDTs with 50mm stroke were clamped diagonally on the machine frame using magnetic robotic arms. They are fixed such that they touch the angle irons fixed to the edge of the Glass fibre-reinforced polymers (GFRP) strengthened ends of the RC columns (Fig. 3.16(b) and 3.16(c)). The LVDTs can thus measure the axial deformations in the middle 400mm section of the columns. The displacements from the LVDTs are recorded via a multichannel (Eight channels) data acquisition unit (Strainsmart 8000).

### 3.4.6 Stereo DIC setup and calibration

On the other hand, digital image correlation (DIC), a non-destructive non-contact full-field optical measurement technique capable of capturing digital images of the surface of an object, was used to obtain the in-plane strains and out-of-plane deformations in its 2D and 3D configurations. The DIC technique was deployed to capture the crack propagation and deformations on the RC columns under compressive load. The video imaging is performed using LaVision's Davis imaging software involving two cameras (Imager E-Lite 5M) fitted with Nikon AF Nikkor 28mm f/2.8D (28mm focal length and 2.8 maximum aperture) lenses. The cameras are calibrated to capture the RC column's out-of-plane and vertical displacements during loading using the dots marked on the columns (Fig. 3.16(d)). The images recorded are further processed using LaVision's Davis 10 software to see the strain distribution resulting from the applied loading. The parameters used in the DIC image acquisition and processing are presented in Table 3.18.

**Table 3.18. DIC processing parameters (Jones & Iadicola, 2018)**

| **Technique used** | **3D (Stereo) DIC** |
|---|---|
| **Camera name** | Imager E-lite 5M |
| **Focal length** | 28.4621mm |
| **RMS of fit** | 0.303396 pixel |
| **Size of dewarped image** | 1961 × 2479 pixel |
| **Subset** | 53 |
| **Step** | 17 |
| **Correlation criterion** | ZNSSD |
| **Shape function** | Quadratic |
| **Interpolation function** | Bi-cubic splines |
| **Strain** | |
| **Smoothing method** | Polynomial - Bilinear |
| **Resolution** | 3.45$\mu$m |
| **Calculation mode** | accurate |

## 3.5 Axial Monotonic Experimental Test Results and Discussions

### 3.5.1 Calculation of corrosion and mass loss ratio

The actual mass loss resulting from the corrosion of the reinforcements is estimated using Eq. 3.8. The results for the mass loss are illustrated in Tables 3.19 and 3.20 for the circular and square columns, respectively. The results indicate that the transverse stirrups had more severe corrosion than the longitudinal bar under the same constant current and duration (Q. Li et al., 2022). This results from the closeness of the transverse bars to the surface of the concrete, leading to a possibly higher concentration of chloride ions and an early start of corrosion (Gu et al., 2020). Furthermore, the diameter of the longitudinal rebar (10mm) was greater than that of the stirrups (6mm). In this regard, the mass loss ratio of transverse stirrups with smaller diameters was higher than that of the longitudinal rebar, according to Faraday's second law of electrolysis (Kashani et al., 2013b).

The localised corrosion of reinforcements results from applying a higher current at a shorter duration during the corrosion of rebars (Nguyen & Lambert, 2018). Hence, to obtain more general and uniform corrosion, low current is recommended at a shorter duration as the application of low current at a longer duration also results in localised corrosion (Nguyen & Lambert, 2018). In this work, a constant current of 2A was used for the accelerated corrosion of the RC columns. This results in corrosion current densities in Tables 3.19 and 3.20, with the square columns having higher corrosion densities in the sparsely confined columns than the circular columns with similar configurations. Figures 3.17 and 3.18 are the measured mass losses corresponding to the estimated mass losses for the circular and square columns, respectively. Furthermore, the applied current density is close to the 1mA/cm$^2$ recommended by Nguyen and Lambert (2018) for the laboratory simulation of corrosion of steel embedded in concrete.

**Table 3.19: Corrosion properties of circular columns**

| Specimen No. | Corrosion current density (mA/cm$^2$) | Corrosion duration (days) | Estimated mass loss (Eq. 3.7) (%) | Measured mass loss of longitudinal bars (Eq. 3.8) (%) | Measured mass loss of transverse bars (Eq. 3.8) (%) |
|---|---|---|---|---|---|
| **C5B0** | 0 | 0 | 0 | 0 | 0 |
| **C5B5** | 1.00 | 3.0 | 5 | 4.1 | 8.8 |
| **C5B10** | 1.00 | 6.0 | 10 | 7.3 | 21.2 |

| | | | | | |
|---|---|---|---|---|---|
| **C5B20** | 1.00 | 12.1 | 20 | 10.8 | 29.4 |
| **C5B30** | 1.00 | 18.1 | 30 | 20.6 | 39.8 |
| **C8B0** | 0 | 0 | 0 | 0 | 0 |
| **C8B5** | 1.16 | 2.7 | 5 | 4.9 | 13.0 |
| **C8B10** | 1.16 | 5.4 | 10 | 9.4 | 21.8 |
| **C8B20** | 1.16 | 10.8 | 20 | 16.5 | 41.4 |
| **C8B30** | 1.16 | 16.2 | 30 | 20.9 | 59.6 |
| **C13B0** | 0 | 0 | 0 | 0 | 0 |
| **C13B5** | 1.28 | 2.5 | 5 | 6.0 | 12.7 |
| **C13B10** | 1.28 | 5.0 | 10 | 12.5 | 30.1 |
| **C13B20** | 1.28 | 10.0 | 20 | 16.1 | 37.2 |
| **C13B30** | 1.28 | 15.0 | 30 | 27.6 | 45.9 |

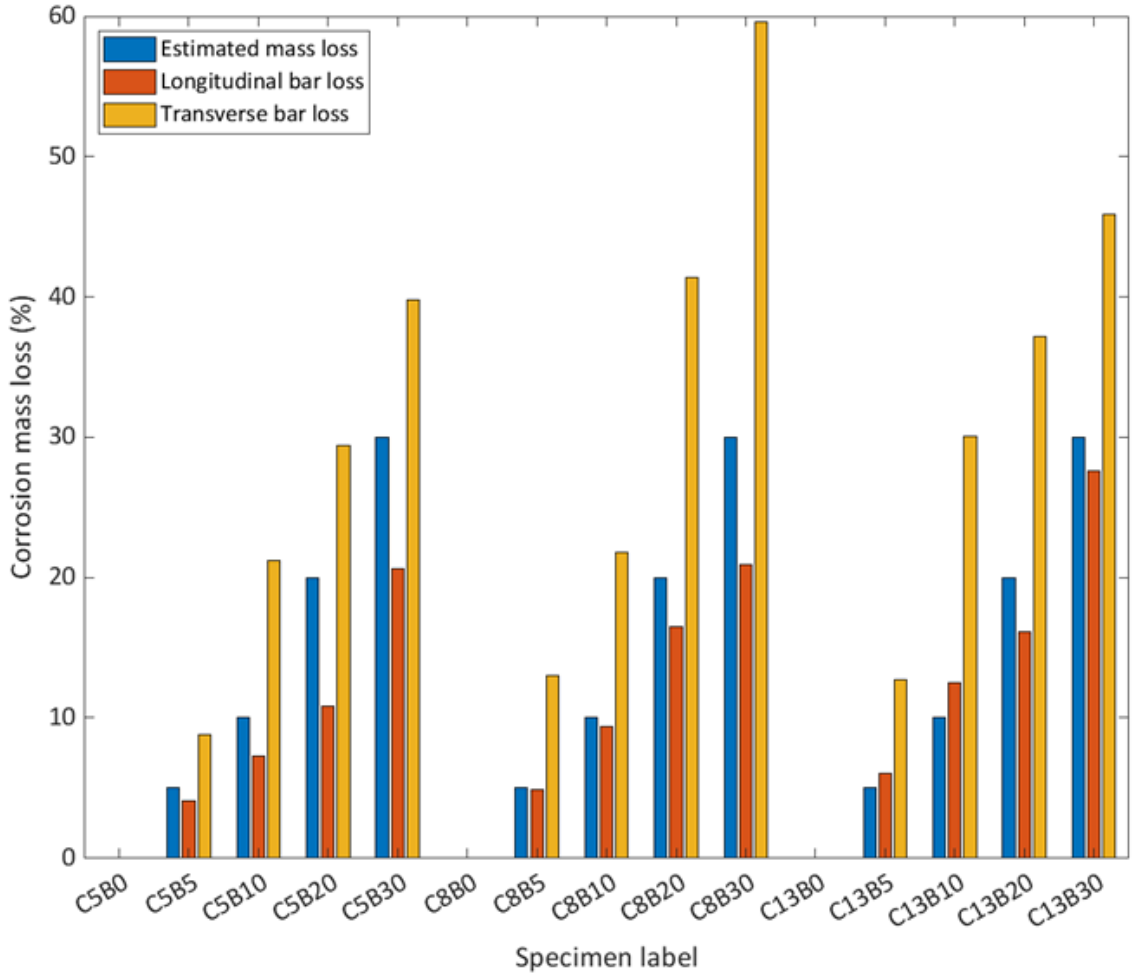


Figure 3.17: Corrosion mass loss estimate for circular columns for axial monotonic test

**Table 3.20: Corrosion properties of square columns**

| Specimen No. | Corrosion current density ($mA/cm^2$) | Corrosion duration (days) | Estimated mass loss (Eq. 3.7) (%) | Measured mass loss of longitudinal bars (Eq. 3.8) (%) | Measured mass loss of transverse bars (Eq. 3.8) (%) |
|---|---|---|---|---|---|
| **S5B0** | 0 | 0 | 0 | 0 | 0 |
| **S5B5** | 0.99 | 2.9 | 5 | 3.4 | 10.9 |
| **S5B10** | 0.99 | 5.8 | 10 | 6.8 | 17.1 |
| **S5B20** | 0.99 | 11.7 | 20 | 13.8 | 37.0 |
| **S5B30** | 0.99 | 17.5 | 30 | 18.4 | 46.3 |
| **S8B0** | 0 | 0 | 0 | 0 | 0 |
| **S8B5** | 1.17 | 2.6 | 5 | 4.7 | 13.4 |
| **S8B10** | 1.17 | 5.1 | 10 | 9.8 | 18.9 |
| **S8B20** | 1.17 | 10.2 | 20 | 16.7 | 39.4 |
| **S8B30** | 1.17 | 15.3 | 30 | 24.8 | 53.3 |
| **S13B0** | 0 | 0 | 0 | 0 | 0 |
| **S13B5** | 1.33 | 2.3 | 5 | 6.2 | 11.8 |
| **S13B10** | 1.33 | 4.6 | 10 | 8.8 | 17.4 |
| **S13B20** | 1.33 | 9.3 | 20 | 10.7 | 25.3 |
| **S13B30** | 1.33 | 13.9 | 30 | 20.2 | 30.3 |

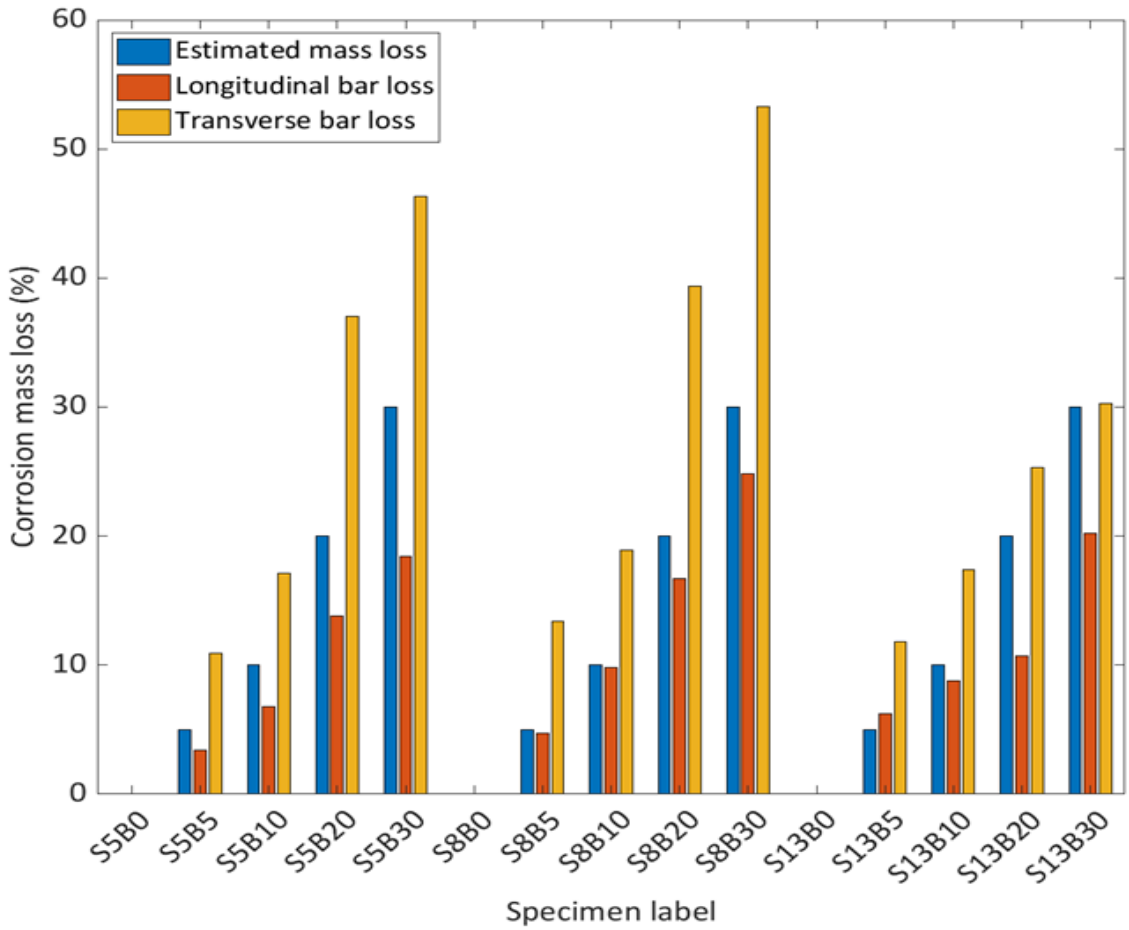


Figure 3.18: Corrosion mass loss estimate for square columns for axial monotonic test

### 3.5.2 Axial load testing of circular columns

The stress-strain response of the circular column to the applied axial compressive load is presented in Figure 3.19 (a-c). It should be noted that the stress-strain response plotted was from the LVDTs data, as the readings from the load cell of the hydraulic machine were ignored since it captures the deformation of the whole sample instead of the needed middle zone section. Similar behaviour was observed for all of the RC column samples. Vertical minor cracks were first developed on the concrete and, subsequently, became enlarged, resulting in the crushing and spalling of the concrete cover as the longitudinal bars buckled due to lateral expansion of the RC column. The observed compressive response of the columns is similar at the elastic range until yield and afterwards reduces beyond the peak load due to corrosion and confinements of the rebars (Dong et al., 2018). The axial load-carrying capacities of the columns generally decrease within each configuration of columns except in some cases where the control sample (0% corrosion) recorded low capacity due to the premature failure of the strengthening GFRP at the top/bottom of the column (Figure 3.20(a)). Also, the applied axial load results in the concrete cover's spalling (Figure 3.20(b)), buckling of the longitudinal bar (Figure 3.20(c)) and, in some cases, fracture of the transverse and longitudinal bars (Figure 3.20(d)). The observed buckling

position of the column varies with the different confinement configurations, with the *L/D*=5 and *L/D*=8 confined columns generally failing by buckling at the middle zone. In contrast, in the sparsely confined samples (*L/D*=13), the buckling occurs immediately below/above the GFRP zones (Figure 3.20(e)).

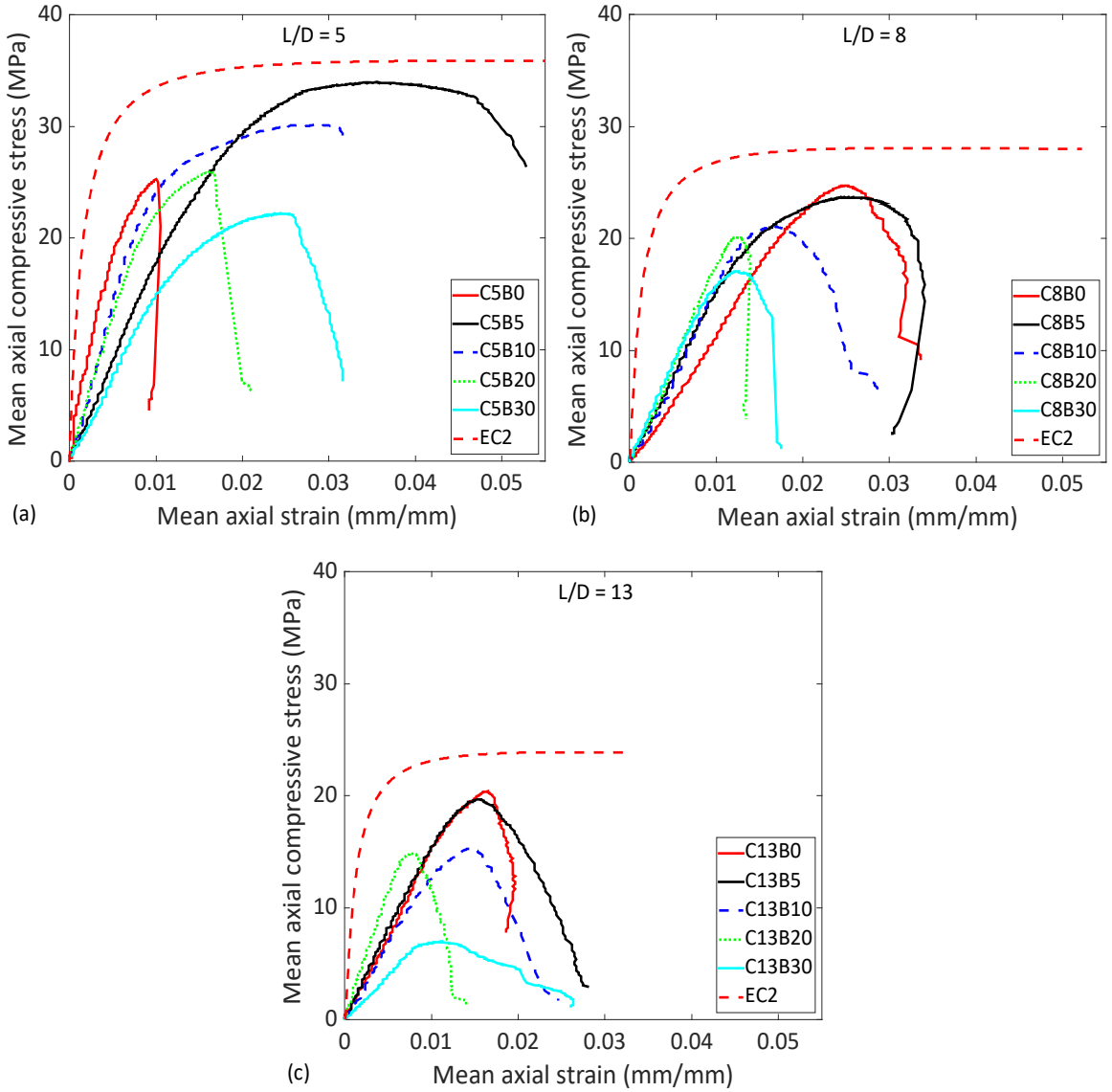


Figure 3.19: Compressive stress-strain responses of the circular columns (a) L/D = 5, (b) L/D = 8 and (c) L/D = 13

The difference in the initial stiffness observed in the stress-strain response curve of the RC columns is due to the impact of confinement and inelastic buckling. The concrete is low-strength, so the reinforcement confinement ratio significantly affects its compressive behaviour. Furthermore, the concrete does not provide any lateral restraint against buckling. Therefore, vertical bars are restrained against buckling by the transverse tie reinforcement. As a result, the concrete in test specimens with larger transverse tie spacing starts crushing, followed by a

buckling of vertical bars much earlier than the columns with more confinement ratio, i.e. closer transverse tie spacing. This has a significant impact on the initial stiffness of test specimens.

The corrosion mass loss of both the longitudinal and transverse bars results in the reduction of the ultimate strength and load-carrying capacity of the column. Consequently, columns with very close mass loss have their maximum strength quite close to each other. This trend is observed in all the different column configurations with an estimated mass loss between 10% and 20% (Fig. 3.15(a - c)).

### 3.5.3 Eurocode prediction of the ultimate strength of confined RC column

Due to the premature failure of some of the control samples during the monotonic loading, Eurocode 2 (The British Standard, 2005) was used to predict the RC columns' confined strength. The prediction showed that the compressive strength of the concrete used in the experiment is about 22MPa, which is very close to the concrete's proposed compressive strength (20MPa). The expressions used in the estimates of the ultimate stress for the confined RC columns are as follows:

$$f_{ck,c} = f_{ck}(1.0 + (5.0\frac{\sigma_2}{f_{ck}})) \quad \text{for} \quad \sigma_2 \leq 0.05 f_{ck} \tag{3.9}$$

$$f_{ck,c} = f_{ck}(1.125 + (2.5\frac{\sigma_2}{f_{ck}})) \quad \text{for} \quad \sigma_2 > 0.05 f_{ck} \tag{3.10}$$

Also, the corresponding strain is estimated from:

$$\varepsilon_{c2,c} = \varepsilon_{c2}(\frac{f_{ck,c}}{f_{ck}})^2 \tag{3.11}$$

$$\varepsilon_{cu2,c} = \varepsilon_{cu2} + (0.2\frac{\sigma_2}{f_{ck}}) \tag{3.12}$$

The stress-strain response of the corroded columns within each confinement's configuration was compared with the non-corroded ones (estimated using the EC2). It showed a gradual decrease in the columns' strength, stiffness and ductility as the corrosion loss increased. The corrosion of longitudinal and transverse bars reduces the column's ultimate strength and load-carrying capacity. Consequently, in the highly confined (*L/D*=5) columns, the maximum strengths varied relative to the increase in the corrosion mass loss (Fig. 3.15(a-c)). For example, the strength loss between the highly confined (uncorroded and corroded) columns was reduced by 5.35%, 15.97%, 27.74%, and 38.11% for the 5%, 10%, 20% and 30% estimated mass loss, respectively (Table 3.21). This trend is also observed in the mediumly confined columns (*L/D*=8) with a strength reduction range of 15.58%, 25.06%, 28.33%, and 39.08% for the 5%, 10%, 20% and 30% estimated mass loss,

respectively (Table 3.21). The lowly confined columns (*L/D*=13) have more disparities in their strength variations due to the combined effect of corrosion and inadequate confinements. The ultimate strength was reduced by 17.45%, 35.8%, 37.81%, and 70.78% for the 5%, 10%, 20% and 30% estimated mass loss, respectively (Table 3.21).

Furthermore, the axial compressive strain corresponding to the ultimate strength for each column varies compared to the axial strain of the uncorroded column estimated from the EC2 prediction (Table 3.21). In the highly confined column, the axial compressive strain was reduced by 25.17%, 40.34%, 65.92% and 49.03% for the 5%, 10%, 20% and 30% estimated mass loss, respectively (Table 3.21). This trend is similar in the mediumly confined (23% and 63%) and lowly confined RC columns (43% and 72%).

**Table 3.21. Ultimate stress and strain variation between uncorroded and corroded circular RC columns under axial compressive loading.**

| Sample label | Ultimate stress (MPa) | $\frac{\sigma_{u(uc)} - \sigma_{u(c)}}{\sigma_{u(uc)}} \times 100$ | Strain, $\varepsilon_u$ | $\frac{\varepsilon_{u(uc)} - \varepsilon_{u(c)}}{\varepsilon_{u(uc)}} \times 100$ |
|---|---|---|---|---|
| **C5B0** | 35.876 | 0 | 0.04783 | 0 |
| **C5B5** | 33.958 | 5.35 | 0.03579 | 25.17 |
| **C5B10** | 30.145 | 15.97 | 0.02854 | 40.34 |
| **C5B20** | 25.925 | 27.74 | 0.01630 | 65.92 |
| **C5B30** | 22.202 | 38.11 | 0.02438 | 49.03 |
| **C8B0** | 28.074 | 0 | 0.0336 | 0 |
| **C8B5** | 23.70 | 15.58 | 0.02576 | 23.34 |
| **C8B10** | 21.038 | 25.06 | 0.01704 | 49.28 |
| **C8B20** | 20.122 | 28.33 | 0.01244 | 62.98270536 |
| **C8B30** | 17.102 | 39.08 | 0.01237 | 63.18114881 |
| **C13B0** | 23.8832 | 0 | 0.0269 | 0 |
| **C13B5** | 19.715 | 17.45 | 0.01527 | 43.24469888 |
| **C13B10** | 15.334 | 35.8 | 0.01456 | 45.90979554 |
| **C13B20** | 14.852 | 37.81 | 0.00752 | 72.04908178 |
| **C13B30** | 6.978 | 70.78 | 0.01098 | 59.19847584 |

(a) (b) (c) (d) (e)

Figure 3.20: Observed failure modes of circular columns. (a) GFRP failure; (b) spalling of concrete cover; (c) rebar buckling at middle zone; (d) transverse bar fracture, and (e) buckling of longitudinal bars below the GFRP

The DIC tracks the RC columns' strain response and crack damage to the applied compressive load. Figure 3.21(a) shows the stress-strain response of one of the circular columns and the locations of the processed images (at yield stress, ultimate stress and beyond the ultimate stress). The processed images within the column's middle zone section showed the column's strain contour with the cracks, spalling of the cover concrete, and the buckling of the reinforcement captured. Figures 3.21(b - d) show the processed images with the Von Mises strain. These values correspond to the strain estimated from the LVDTs at yield stress, ultimate stress and beyond the ultimate stress.

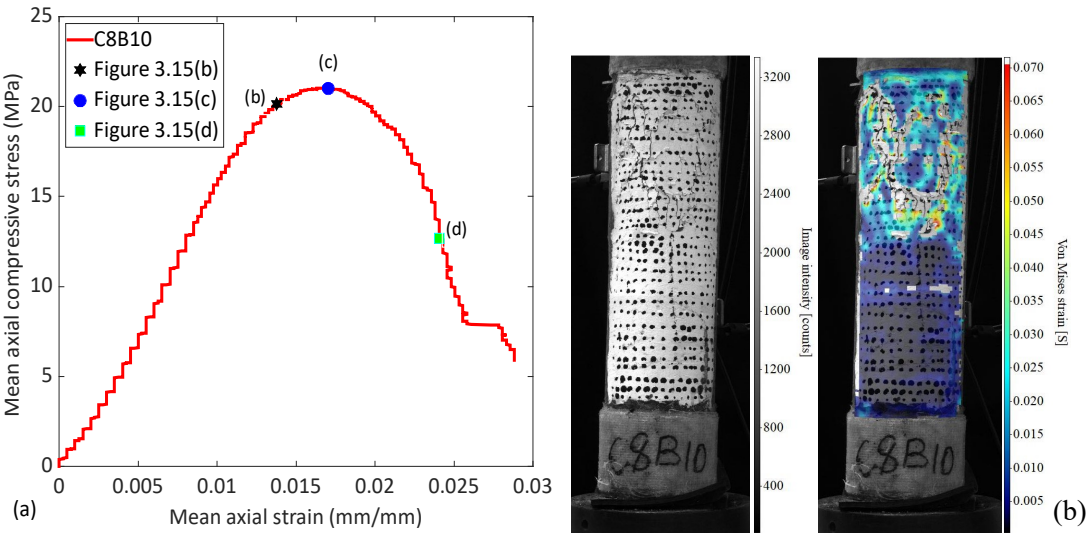

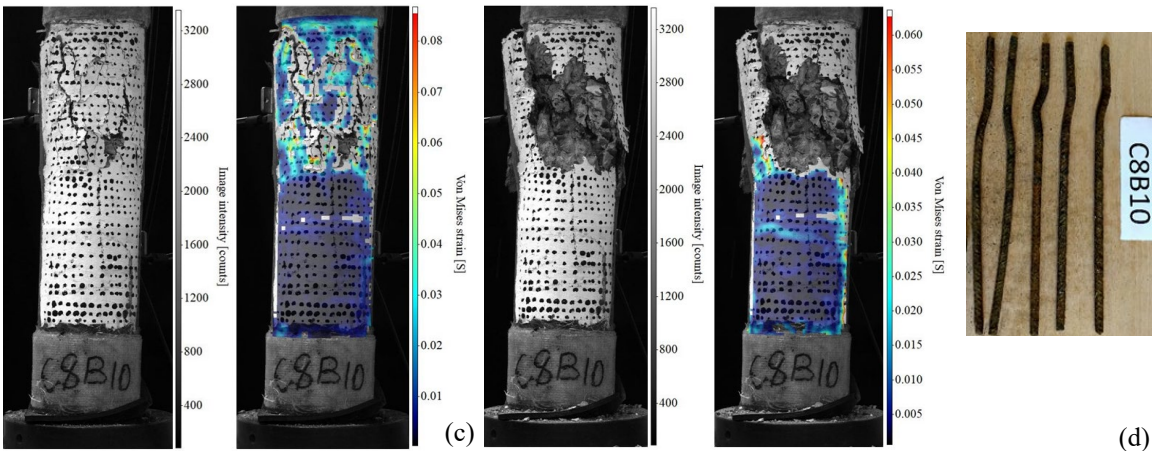


Figure 3.21. Processed DIC images of circular column (a) stress-strain response showing location of processed images (b) at yield stress, (c) at ultimate stress and (d) between ultimate stress and collapse

### 3.5.4 Axial load testing of square RC columns

The stress-strain response of the square columns to the applied axial compressive load is similar to the behaviour of the circular columns and is presented in Figure 3.22 (a-c). The more closely confined columns (*L/D = 5*) have higher load-carrying capacities, which reduces with increased corrosion mass loss. Also, some of the control samples (0% corrosion) recorded low capacities (Figures 3.22(b) and 3.22(c)) resulting from the failure of the strengthening GFRP at the top/bottom of the column (Figure 3.23(a)), leading to stress concentration and premature failure of the ends of the columns. The failure of the GFRPs occurs due to the sharp edges of the columns. Similar to the circular columns, the applied axial load results in the concrete cover's spalling, transverse bars fracture and longitudinal bars buckling.

Due to the premature failure of some of the control samples, resulting in the failure of the GFRPs at the end of the columns during the monotonic loading, Eurocode 2 (The British Standard, 2005) was used to predict the stress-strain response of the uncorroded confined RC columns. The expressions in equations 3.9 to 3.12 were used to estimate the ultimate stress of the confined RC columns and plotted with the corroded samples.

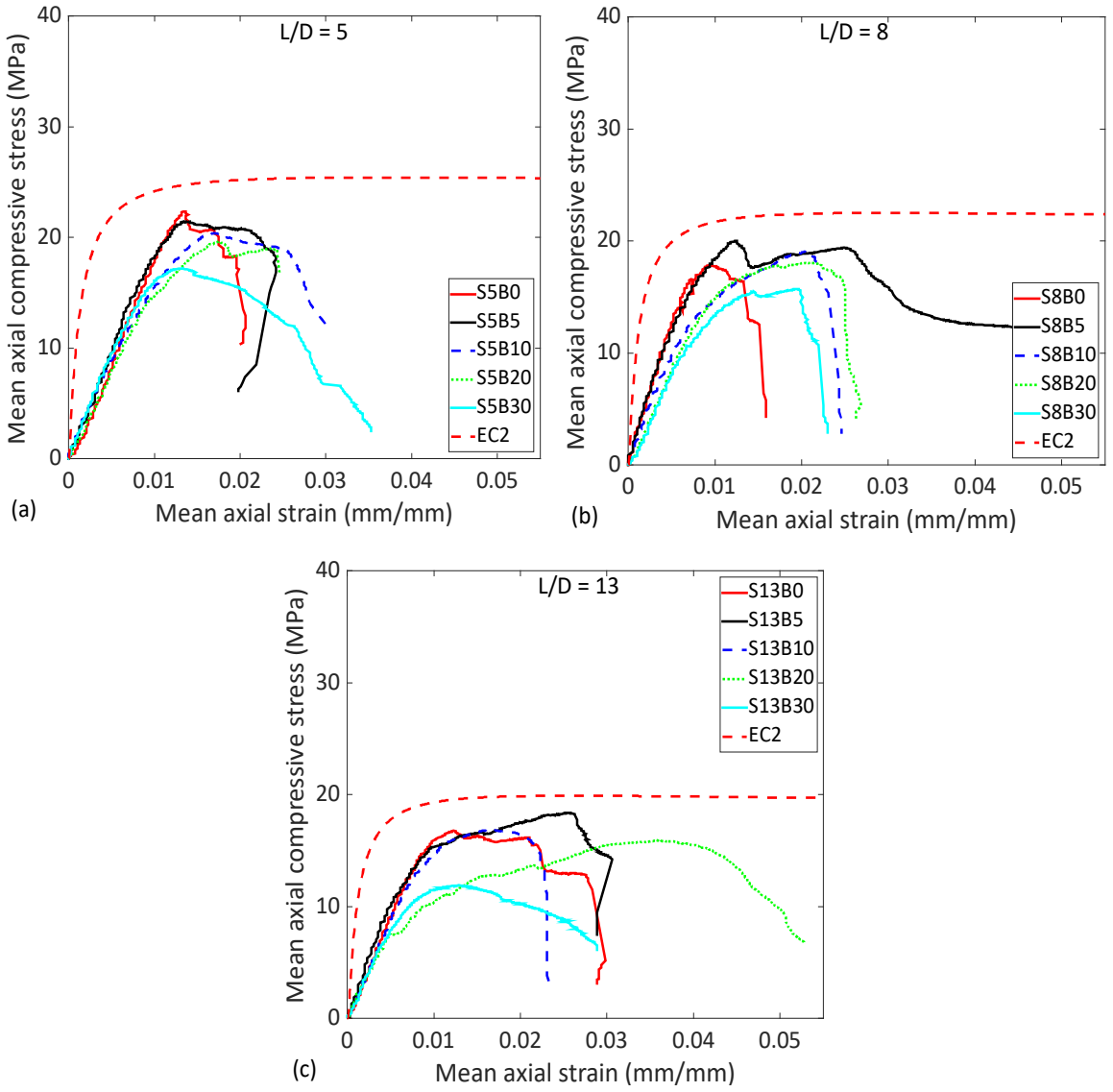


Figure 3.22. Axial compressive stress-strain responses of square columns (a) $L/D = 5$, (b) $L/D = 8$ and (c) $L/D = 13$

The stress-strain response of the corroded columns within each confinement's configuration was compared with the non-corroded ones (predicted using the EC2 expressions for confined concrete (Eqns. 3.9 – 3.12)). It showed a gradual decrease in the columns' strength, stiffness and ductility as the corrosion loss increased. The corrosion of longitudinal and transverse bars reduces the column's ultimate strength and load-carrying capacity. Consequently, in the highly confined (*L/D* = 5) columns, the maximum strengths varied relative to the increase in the corrosion mass loss (Fig. 3.18(a-c)). For example, the strength loss between the highly confined (uncorroded and corroded) columns was reduced by 15.5%, 19.79%, 22.74%, and 32.35% for the 5%, 10%, 20% and 30% estimated mass loss, respectively (Table 3.22). This trend is also observed in the mediumly confined columns (*L/D*=8) with a strength reduction range of 11%, 15.25%, 19.72%, and 29.97% for the 5%, 10%, 20% and 30% estimated mass loss, respectively (Table 3.22). The lowly confined

columns (*L/D* = 13) have more disparities in their strength variations due to the combined effect of corrosion and inadequate confinements. The ultimate strength was reduced by 7.6%, 15.36%, 19.94%, and 40.23% for the 5%, 10%, 20% and 30% estimated mass loss, respectively (Table 3.22). Furthermore, the axial compressive strain corresponding to the ultimate strength for each column varies compared to the axial strain of the uncorroded column estimated from the EC2 prediction (Table 3.22). In the highly confined column, the axial compressive strain was reduced by 64.41%, 54.94%, 53.51% and 64.59% for the 5%, 10%, 20% and 30% estimated mass loss, respectively (Table 3.21). A similar trend is observed in the strain response of the mediumly confined (between 31% and 59%) and lowly confined RC columns (between 2% and 49%).

**Table 3.22. Ultimate stress and strain variation between uncorroded and corroded square RC columns under axial compressive loading.**

| Sample label | Ultimate stress (MPa) | $\frac{\sigma_{u(uc)} - \sigma_{u(c)}}{\sigma_{u(uc)}} \times 100$ | Strain, $\varepsilon_u$ | $\frac{\varepsilon_{u(uc)} - \varepsilon_{u(c)}}{\varepsilon_{u(uc)}} \times 100$ |
|---|---|---|---|---|
| **S5B0** | 25.41 | 0 | 0.03756 | 0 |
| **S5B5** | 21.47 | 15.502 | 0.01337 | 64.41 |
| **S5B10** | 20.38 | 19.792 | 0.01692 | 54.944 |
| **S5B20** | 19.63 | 22.743 | 0.01746 | 53.514 |
| **S5B30** | 17.19 | 32.346 | 0.0133 | 64.592 |
| **S8B0** | 17.88 | 0 | 0.03 | 0 |
| **S8B5** | 20.02 | 11.0 | 0.01230 | 58.99 |
| **S8B10** | 19.06 | 15.25 | 0.02047 | 31.78 |
| **S8B20** | 18.06 | 19.72 | 0.02062 | 31.28 |
| **S8B30** | 15.75 | 29.97 | 0.01938 | 35.40 |
| **S13B0** | 19.89 | 0 | 0.0262 | 0 |
| **S13B5** | 18.38 | 7.6 | 0.02551 | 2.63 |
| **S13B10** | 16.83 | 15.35 | 0.01710 | 34.74 |
| **S13B20** | 15.92 | 19.94 | 0.03596 | -37.24 |
| **S13B30** | 11.89 | 40.22 | 0.01314 | 49.83 |

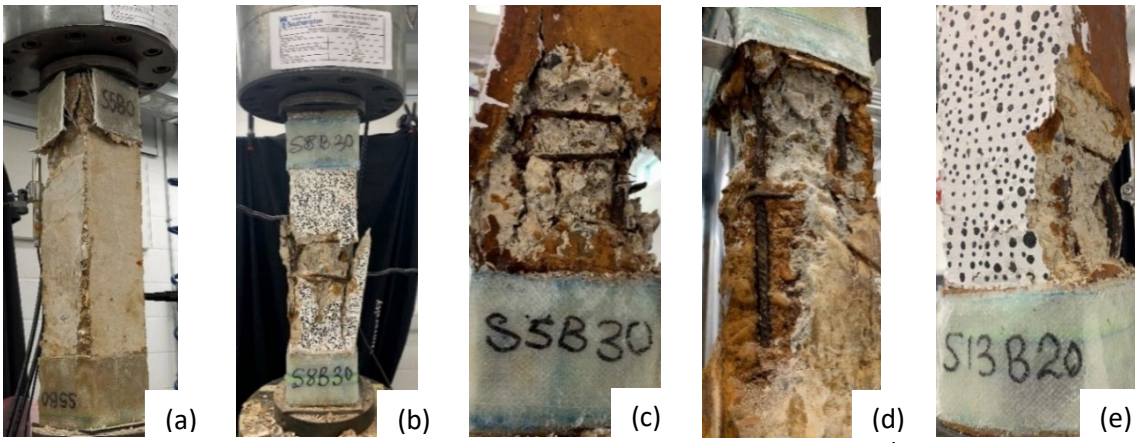


Figure 3.23: Observed failure modes of the square columns. (a) GFRP failure at the top; (b) spalling of concrete cover; (c) transverse bar fracture; (d) longitudinal bar fracture at pitting corrosion location; and (e) buckling of longitudinal bars above the GFRP

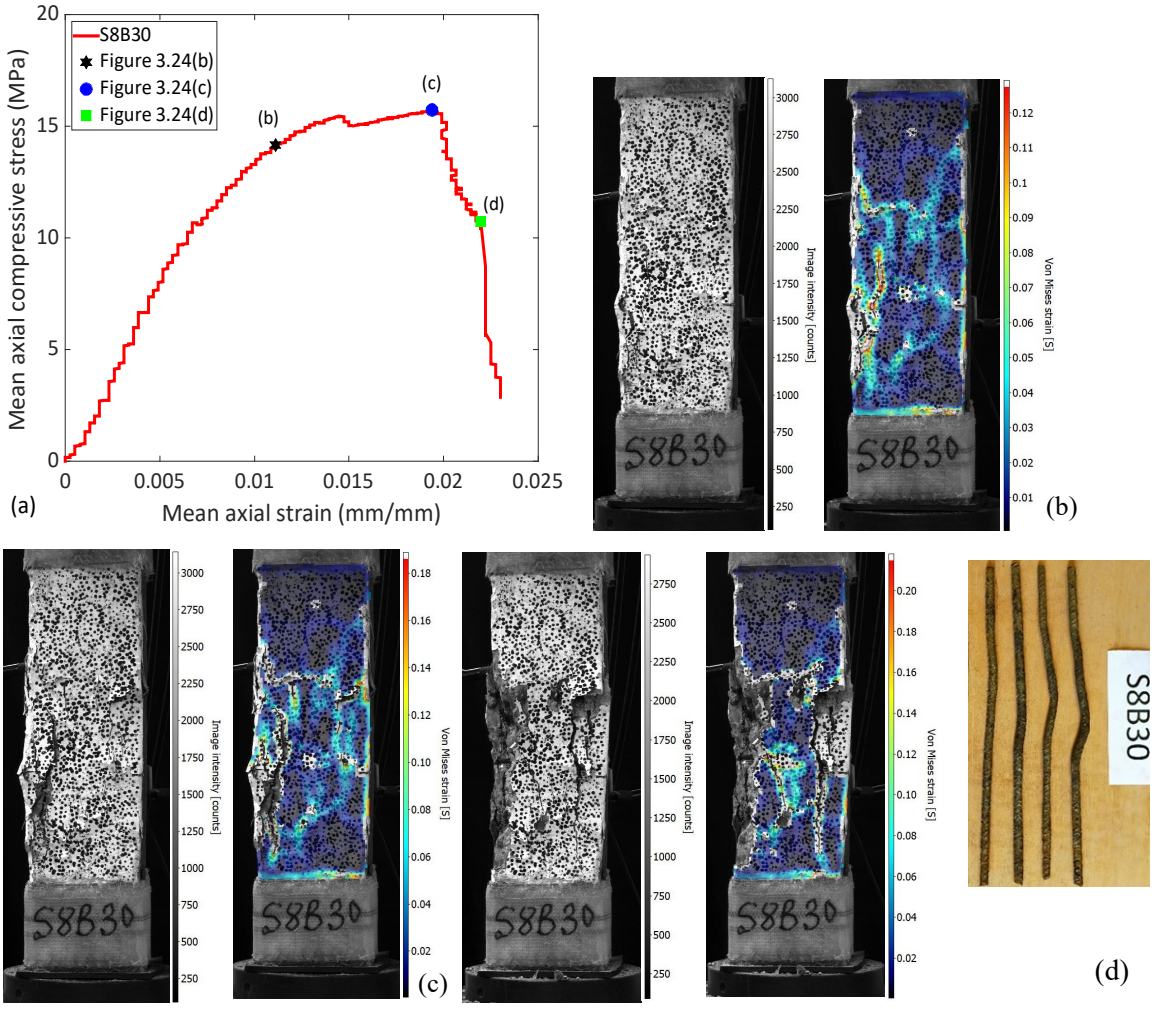


Figure 3.24: Processed DIC images of square column (a) stress-strain response showing location of processed images (b) at yield stress, (c) at ultimate stress and (d) between ultimate stress and collapse with the buckling at the end of the test

Figure 3.24(a) shows the stress-strain response of one of the square columns with an estimated 30% corrosion mass loss. Figures 3.24(b - d) are the processed images from the DIC at different locations during the compression test on the column. The processed images within the middle zone section of the column showed the images with and without the strain contour on the column with the crack propagation, spalling of the cover concrete and the reinforcement's buckling. Figure 3.20(d) further shows the buckled longitudinal bar after removal and cleaning.

It is observed that the circular columns generally have better axial load-carrying capacities and axial strain than the square columns (Dizaj & Kashani, 2020; Liang et al., 2015). This results from the effectiveness of the transverse ties in the circular column, which has more significant confinement effectiveness coefficients than the square columns(Liang et al., 2015).

### 3.5.5 Impact of corrosion on the strength of confined RC column

The strength loss resulting from the corrosion and confinement ratios of the R.C. columns is determined by normalising the ultimate strength of the corroded columns to the ultimate strength of the uncorroded. The estimated maximum strength of the uncorroded column is used in the normalisation due to premature failure of the tested uncorroded column. The ultimate strength is estimated from equation 3.13.

$$\sigma_u = \frac{\sigma_c\,(A_g - nA_s) + nA_s\sigma_s}{A_g} \tag{3.13}$$

where, $\sigma_c$ is the compressive strength of unreinforced concrete, $A_g$, is the cross-sectional area of the R.C. column, *n* is the number of longitudinal rebars, $A_s$, is the area of longitudinal rebar, and $\sigma_s$, is the ultimate strength of the rebar.

The normalised ultimate strength loss of the differently confined R.C. columns is plotted relative to the percentage of corrosion mass loss. Linear trend lines are fitted to the test data to estimate the strength reduction due to corrosion and confinement ratios. The R-square values obtained from the trend lines range from 0.95 to 0.90 for the circular columns at different confinement ratios (Figure 3.21(a)), while the variation for the square columns is from 0.99 to 0.96 (Figure 3.21(b)).

The ultimate strength of the confined corroded R.C. columns is reduced with an increase in the confinement degree and corrosion mass loss. For example, the well-confined circular columns with *L/D = 5* (Figure 3.25(a)) have a strength reduction range of 4.7%, 14%, 26% and 36.7% for the 4.1%, 7.3%, 10.8% and 20.6% corrosion mass loss, respectively. Also, the well-confined square columns with *L/D = 5* (Figure 3.25(b)) have a strength reduction range of 5.1%, 10.6%, 19.6% and

29.6% for the 3.4%, 6.8%, 13.8% and 18.4% corrosion mass loss, respectively. A similar trend is also observed in the medium level of confinement scenarios (*L/D = 8*) and sparsely confined (*L/D = 13*) columns, with the strength reduction increasing with an increase in the corrosion mass losses in the circular and square columns.

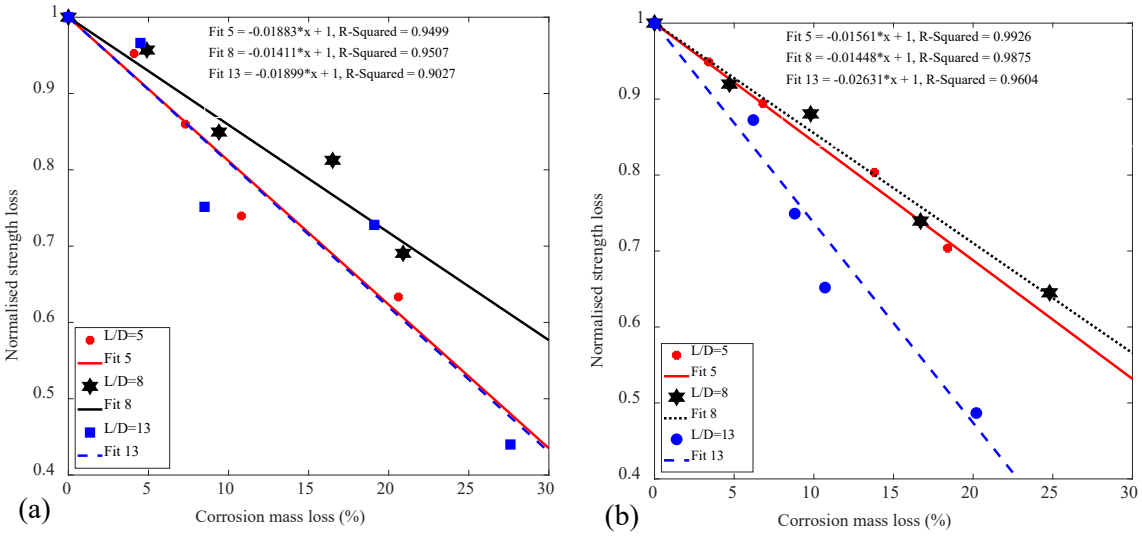


Figure 3.25. Normalised strength variation of the confined RC columns with corrosion mass loss (a) circular columns and (b) square columns

### 3.5.6 Impact of corrosion on inelastic buckling behaviour of vertical reinforcement

Corrosion generally reduces the cross-sectional areas of bars available to sustain the applied load (Kashani, 2017). This reduction becomes more severe in bars with pitting corrosion, resulting in localised reduction in the cross-sectional areas of the bars, leading to rebar fracture and localised buckling. The results of the tests on the corroded columns showed that the pitting effect is more significant as it leads to the buckling mechanism and reduction in the load-carrying capacity of the column. Longitudinal bars in columns with *L/D = 5* confinement had less buckling failure (Fig. 3.26(a-d)), especially at lower corrosion than bars from the *L/D = 8* (Fig. 3.26(e-g)) and *L/D =13* (Fig. 3.26(k-l)) configurations (Kashani et al., 2013b; Kashani, 2017). This buckling from the highly confined RC columns (*L/D = 5)* rebars at higher corrosion levels results from the unsymmetrical cross-sections arising from the pitting corrosion, causing imperfections in the bar and leading to additional bending moment and local stresses at the pitted sections (Kashani et al., 2013b; Kashani, 2017). Meanwhile, the buckling from the columns with *L/D = 8* and *L/D = 13* results from the combination of pitting corrosion and inadequate confinement provisions leading to premature yielding and squashing of the weakest section even at lower corrosion degrees (Kashani et al., 2015). Those columns with more uniformly distributed corrosion and a relatively

small mass loss showed similar behaviour to those with uncorroded bars with a more visible buckling at a higher compressive load (Kashani et al., 2013b).

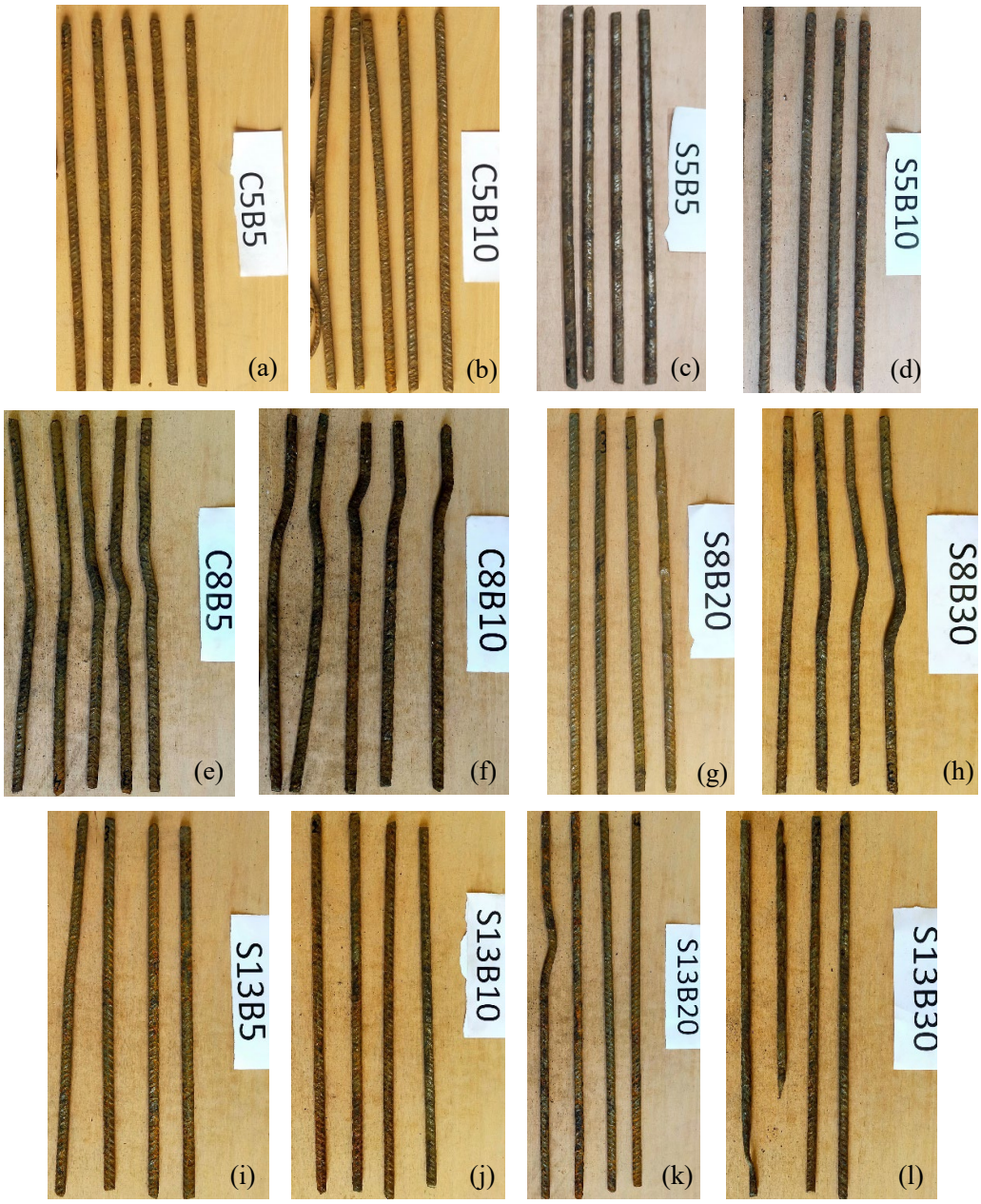


Figure 3.26. Observed buckling failure of the longitudinal reinforcement after testing; *L/D = 5* (a-d), *L/D = 8* (e-h) and *L/D = 13* (i-l)

### 3.5.7 Comparison of the response of circular and square RC columns

Figure 3.27 (a-l) compares the stress-strain response of the circular and square columns with similar confinement configurations and corrosion mass losses. The circular columns have higher axial compressive strength than the square columns (Figs. 3.27(a-i)) in almost all cases except in some of the low confined (*L/D = 13*) columns (Figs. 3.27(j-l)) where the effect of corrosion and

inadequate confinement affect the behaviour of the columns. This results from the uniform confinement of the circular columns, which gives rise to a uniform stress distribution of the concrete along the cross-section (Ayough et al., 2021; Colajanni et al., 2014; Liang et al., 2015; Liang & Sritharan, 2018). In contrast, the square columns have their stress concentration at the edges, sometimes leading to the failure of the GFRPs.

Corrosion of steel reinforcement and confinement results in the loss of stiffness and reduced ductility of the RC columns. Generally, the highly confined columns (*L/D = 5*) with minor corrosion mass loss have a higher ductility (especially the circular columns) than columns in the medium level of confinement (*L/D = 8*) and low confinement (*L/D =13*) at the same corrosion levels. This behaviour is observed to be the same in the columns within the same configurations as the corrosion level increases.

Furthermore, the columns' ductility was reduced with increased confinement levels in all columns. This behaviour is also similar to the corrosion mass losses, where an increase in the corrosion loss results in a decrease in the ductility of the column in almost all the different confinement configurations.

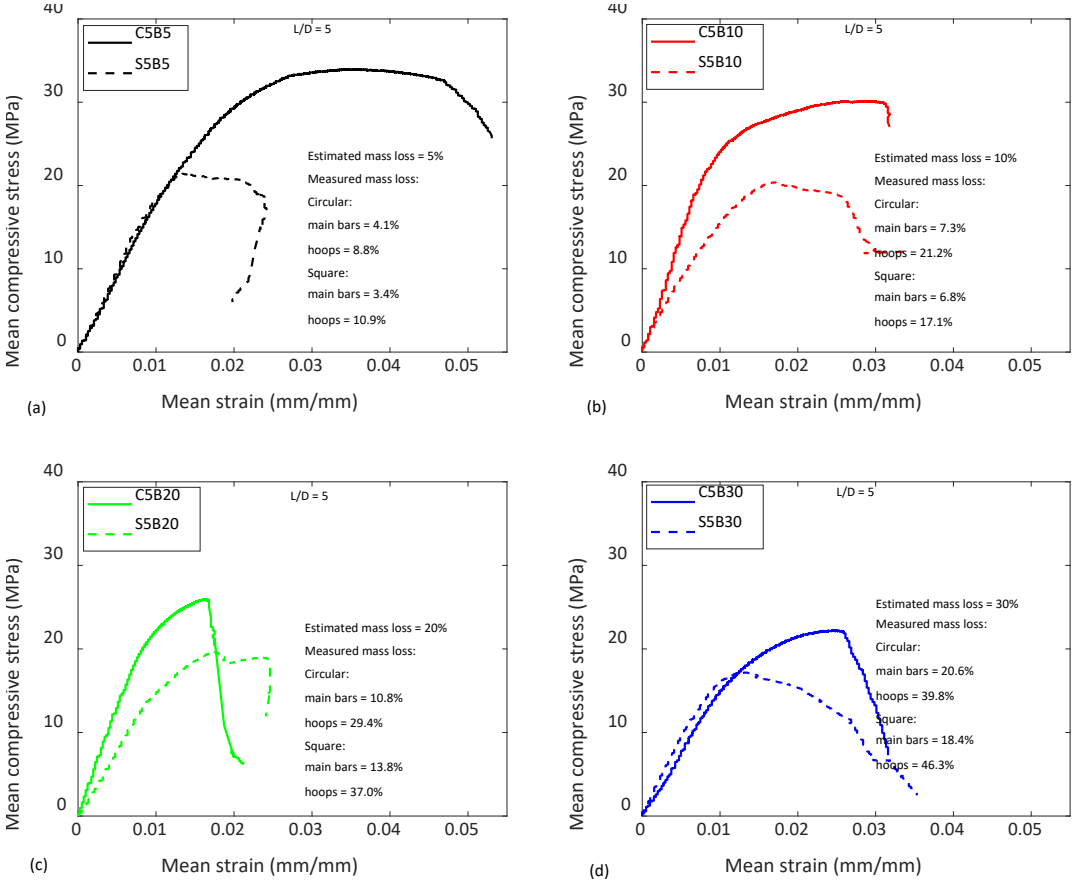

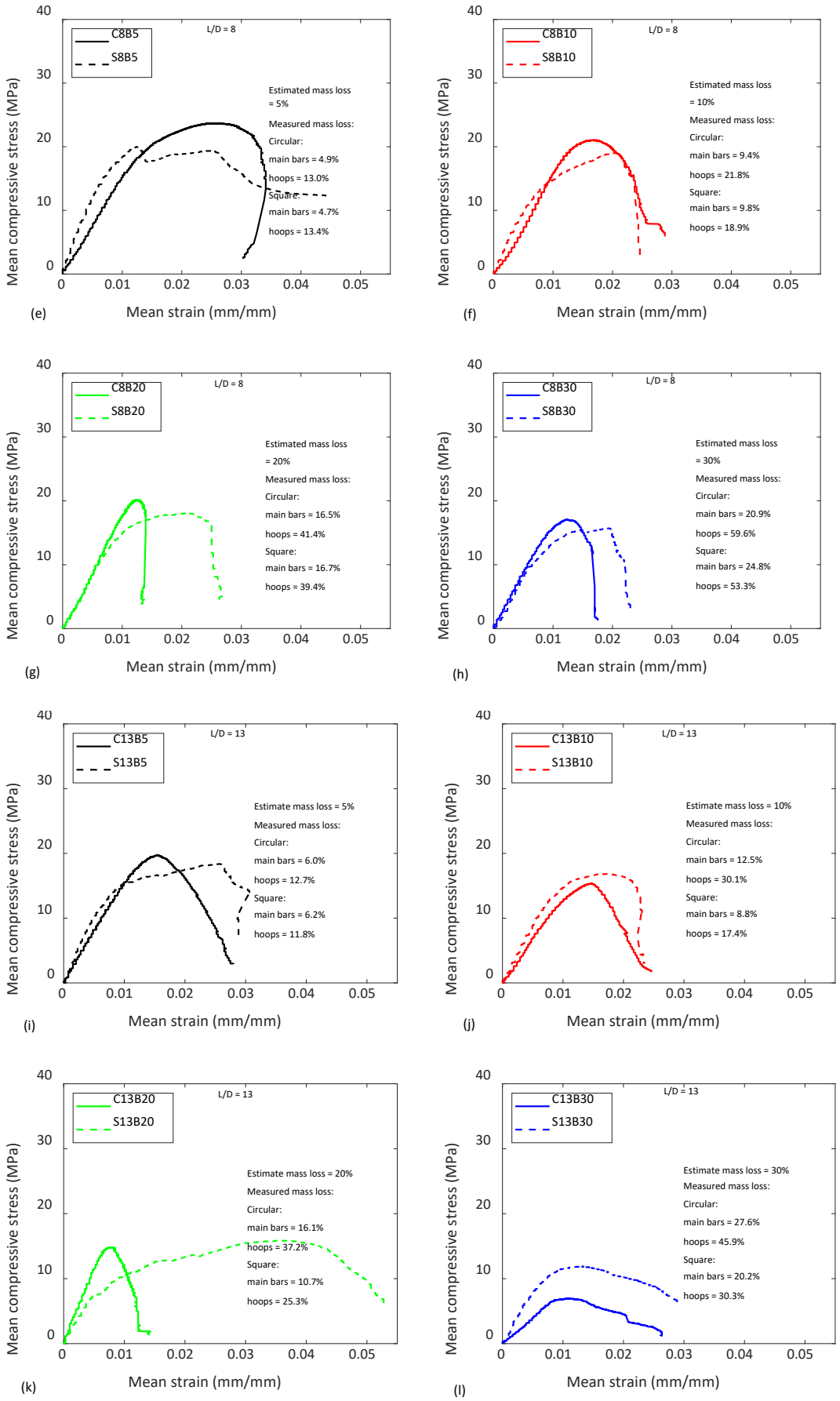


Figure 3.27. Comparison of the response of circular and square columns with varying corrosion and confinement levels; *L/D = 5* (a-d), *L/D = 8* (e-h) and *L/D = 13* (i-l)

### 3.5.8 Comparison of Existing Analytical Models with Experimental Results

Various models have been proposed to investigate the stress-strain response of confined concrete. These analytical models were developed from observations in experimental studies with several adjustments to account for the confinement of the concrete core. Mander et al. (1988) unified stress-strain model, which is based on the multiaxial properties of concrete, is the most popular confined concrete model. The model defined an effective lateral confining stress dependent on the transverse and longitudinal bars. However, despite its popularity, the model does not include the effect of reinforcement corrosion, resulting in its inapplicability for corroded RC structures.

Several researchers have used analytically developed stress-strain graphs of confined concrete subjected to corrosion for numerical applications without experimental verification (Ou et al., 2013; Ou & Nguyen, 2014). For example, Coronelli and Gambarova (2004) validated their numerical model through comparison with available test data on supported beams. Still, the analytically proposed stress-strain model of confined concrete used in their numerical simulation was not validated experimentally.

In this work, three existing stress-strain models on corroded R.C. columns with varying degrees of corrosion and different column configurations were compared with the experimental results. The models (Andisheh et al., 2021; Hoshikuma et al., 1997; Ma et al., 2022; Vu et al., 2017) adopted modified that from Mander et al. (1988) to reflect the effect of corrosion on the strength of confined concrete by adjusting the yield strengths of the transverse reinforcement. The expressions of the existing models are shown in Table 3.23. All the proposed models considered the effect of corroded transverse reinforcement on the peak strength and the ultimate strain without considering the impact of the corrosion of the longitudinal rebar. The models show the satisfying performance of predicting the ultimate condition of the corroded RC columns with different degrees of deterioration of the stirrup (P. Li et al., 2022).

To compare the experimental data with these models, the ultimate strength from each of the RC columns tested is adjusted by removing the stress resulting from the longitudinal bars from the maximum strength of the RC columns. Hence, the strength of confined concrete is estimated from equation 3.14.

$$\sigma_c = \frac{(\sigma_g \times A_g) - nA_s\sigma'_{yc}}{A_g - nA_s} \tag{3.14}$$

The yield strength of the longitudinal bar is adjusted to reflect the corrosion and buckling effect using the equation (equation 3.15) proposed by Kashani et al. (2013b).

$$\sigma'_{yc} = \sigma_y(1 - \beta\gamma) \quad (3.15)$$

where, $\sigma'_{yc}$, is the yield stress of corroded bars in compression, $\beta = 0.005$ for $L/D \leq 5$, $\beta = 0.0065$ for $5 < L/D \leq 10$, $\beta = 0.0125$ for $L/D > 10$ and $\gamma$, is the corrosion mass loss determined in Eq. 3.4

**Table 3.23. Ultimate strength and strain of analytical models**

| Model | Ultimate strength | Ultimate strain | Column type |
|---|---|---|---|
| Vu et al. (2017) | $\sigma_{cc} = (1 - \alpha X_{corr}) \cdot \sigma'_{co} \cdot (-1.254 + 2.254 \cdot \sqrt{1 + (\frac{7.94 f'_l}{\sigma'_{co}})} - 2 \cdot \frac{f'_l}{\sigma'_{co}})$ <br> $\alpha = 0.51$ | $\varepsilon'_{cu} = 0.004 + (1 - X_{corr}) \cdot \frac{2.8 \cdot \varepsilon^c_{sm} \cdot f'l}{fcc}$ <br> $\varepsilon^c_{sm} = (1 - \tau X_{corr}) \varepsilon_{sm}$ | Square and circular |
| Hoshikuma et al. (1997) | $\sigma_{cc} = \sigma_{co}(1.0 + 3.8\alpha \frac{\rho_s f_{yh}}{f_{co}})$ <br> $\alpha = 1.0$ and $0.2$ for circular and square sections | $\varepsilon'_{cu} = 0.002 + 0.033\beta \frac{\rho_s f_{yh}}{\sigma_{co}}$ <br> $\beta = 1.0$ and $0.4$ for circular and square sections | Square and circular |
| Ma et al. (2022) | $\sigma'_{cc} = \sigma'_{co}(-1.6 + 2.6\sqrt{1 + (\frac{10 f'_{lc}}{\sigma'_{co}})} - 2 \cdot \frac{f'_{lc}}{\sigma'_{co}})$ | $\varepsilon'_{cu} = 0.004 + (1 - 0.559 X_{corr}) \frac{0.216 \beta_{xy} \rho_{sc} f_{yhc} \varepsilon_{sm}}{\sigma'_{cc}}$ | rectangular |
| Andisheh et al. (2021) | $\sigma'_{cc} = \sigma'_{co} \cdot \left(2.254 \cdot \sqrt{1 + (\frac{7.94 f'^c_l}{\sigma'_{co}})} - 2 \cdot \frac{f'^c_l}{\sigma'_{co}}) - 1.254\right)$ | $\varepsilon'_{cu} = 0.004 + (\frac{1.4 \cdot \rho_s f_{yh} \varepsilon^c_{su}}{\sigma'^c_{cc}})$ | Circular |

**$\alpha$, is the stress correction coefficient; $\varepsilon^c_{sm}$, is the steel strains at the maximum tensile stress of corroded transverse reinforcement; $\varepsilon_{sm}$, is the ultimate strain of uncorroded transverse reinforcement; $\tau$, is the reduction factor for the ultimate strain of uncorroded reinforcement; $f'_l$, is the lateral confining pressure of the R.C. column; $\sigma'_{co}$, compressive strength of uncorroded reinforcement**

The ultimate strength equations for the models in Table 3.23 were used to predict the strength of the RC columns. The predicted values are tabulated for the circular and square columns in Tables 3.24 and 3.25. These values were plotted against the experimental values in Figure 3.24.

**Table 3.24: Predicted analytical values for circular columns from different models and the experimental value**

| Column Configuration | Experiment | Vu et al. (2017) | Hoshikuma et al. (1997) | Ma et al. (2022) | Andisheh et al. (2021) |
|---|---|---|---|---|---|
| **High confined (*L/D = 5*)** | 18.01 | 24.83 | 24.56 | 33.23 | 24.83 |
| | 17.11 | 23.94 | 23.46 | 31.88 | 22.90 |
| | 14.81 | 23.23 | 22.59 | 29.84 | 20.22 |
| | 11.34 | 22.48 | 21.69 | 28.40 | 18.49 |
| | 8.85 | 20.37 | 19.23 | 26.44 | 16.33 |
| **Medium confined (*L/D = 8*)** | 9.40 | 17.82 | 15.74 | 22.27 | 17.82 |
| | 7.67 | 17.08 | 15.06 | 20.99 | 15.87 |
| | 7.03 | 16.39 | 14.44 | 20.08 | 14.57 |
| | 6.02 | 15.34 | 13.50 | 17.92 | 11.82 |
| | 5.16 | 14.71 | 12.93 | 15.70 | 9.42 |
| **Low confined (*L/D = 13*)** | 4.90 | 11.72 | 10.89 | 12.86 | 11.72 |
| | 4.49 | 11.25 | 10.49 | 12.49 | 10.73 |
| | 3.40 | 10.74 | 10.05 | 11.96 | 9.43 |
| | 3.09 | 10.48 | 9.82 | 11.74 | 8.91 |
| | 1.64 | 9.61 | 9.07 | 11.47 | 8.29 |

**Table 3.25: Predicted analytical values for square columns from different models and the experimental value**

| Column Configuration | Experiment | Vu et al. (2017) | Hoshikuma et al. (1997) | Ma et al. (2022) | Andisheh et al. (2021) |
|---|---|---|---|---|---|
| **High confined (L/D = 5)** | 13.60 | 22.15 | 13.58 | 27.65 | 22.15 |
| | 11.15 | 21.74 | 13.44 | 26.32 | 20.83 |
| | 10.58 | 21.33 | 13.31 | 25.54 | 20.09 |
| | 10.26 | 20.50 | 13.03 | 22.88 | 17.69 |
| | 9.11 | 19.95 | 12.84 | 21.54 | 16.55 |
| **Medium confined (L/D = 8)** | 13.60 | 16.89 | 12.70 | 19.56 | 16.89 |
| | 10.98 | 16.54 | 12.55 | 18.68 | 15.89 |
| | 9.87 | 16.16 | 12.40 | 18.31 | 15.49 |
| | 8.97 | 15.66 | 12.20 | 16.87 | 14.00 |
| | 7.87 | 15.07 | 11.96 | 15.86 | 13.02 |
| **Low confined (L/D = 13)** | 13.60 | 13.14 | 12.21 | 13.74 | 13.14 |
| | 8.94 | 12.92 | 12.06 | 13.55 | 12.73 |
| | 7.97 | 12.83 | 11.99 | 13.46 | 12.53 |
| | 7.47 | 12.76 | 11.95 | 13.33 | 12.26 |
| | 5.35 | 12.43 | 11.72 | 13.25 | 12.09 |

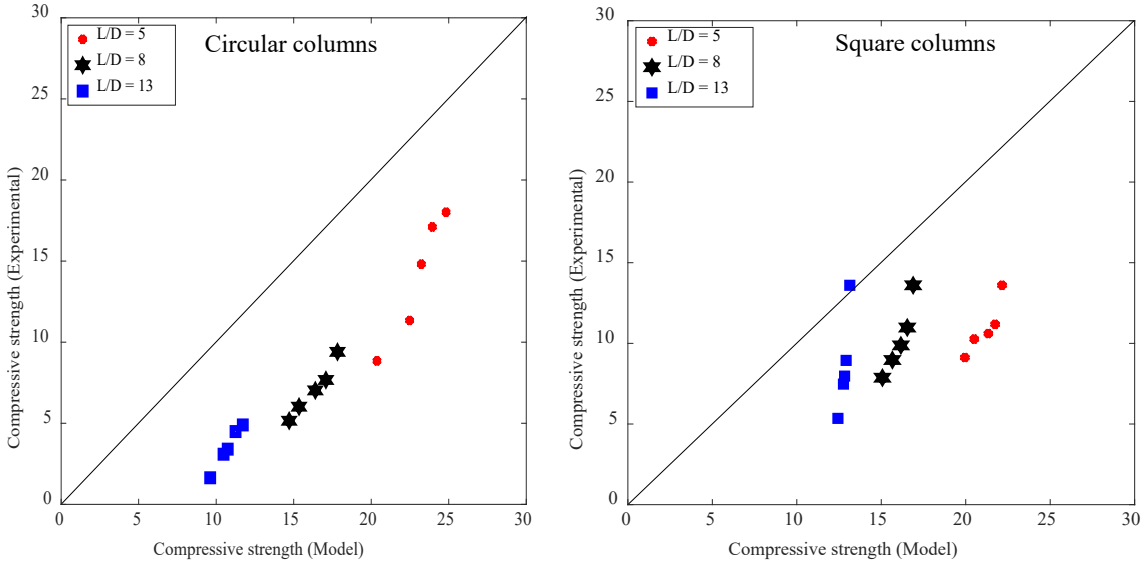


(a) Vu et al. (2017) model

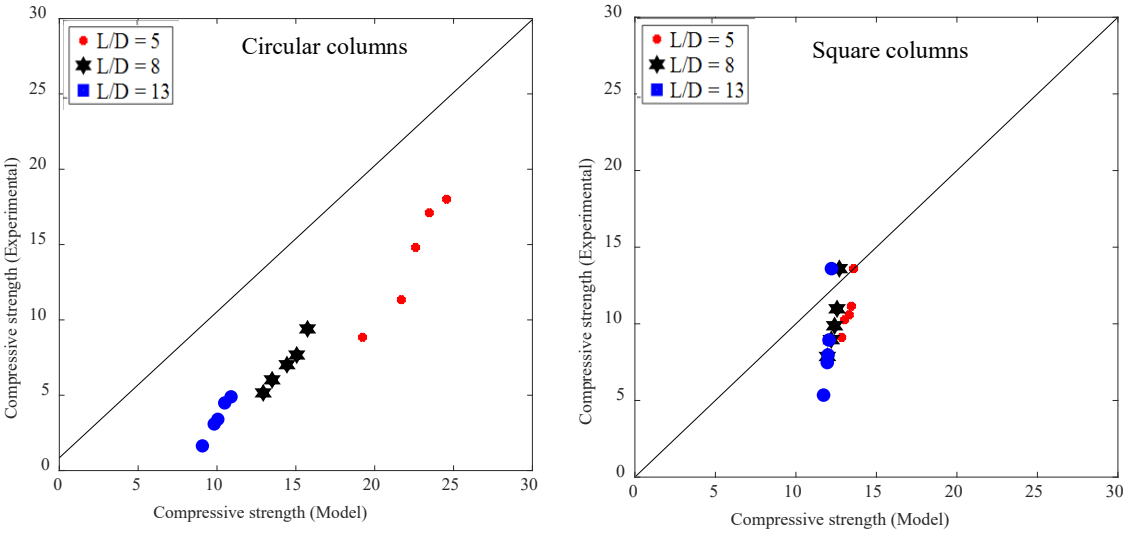


(b) Hoshikuma et al. (1997) model

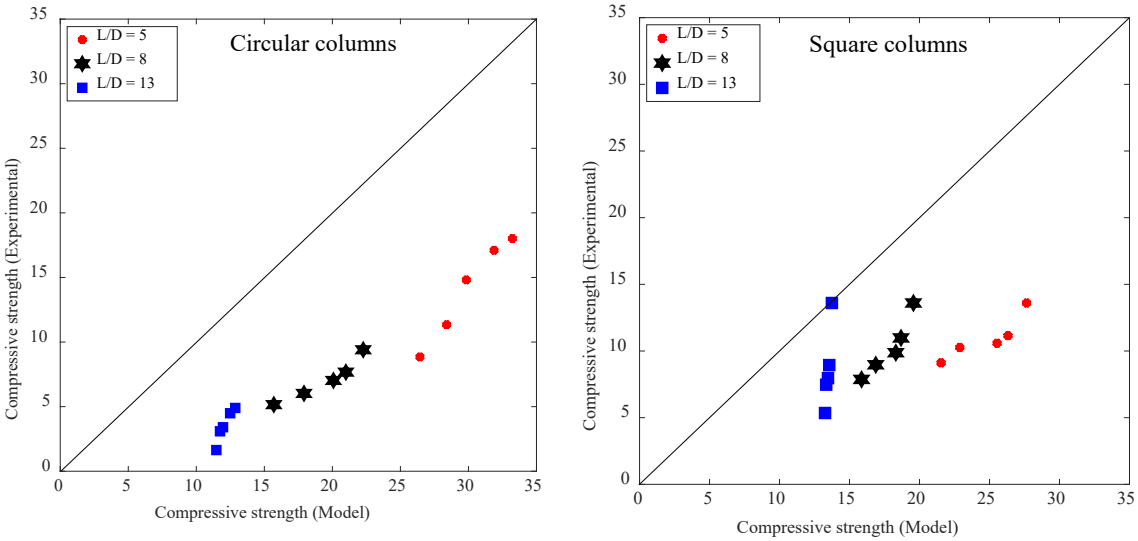


(c) Ma et al. (2022) model

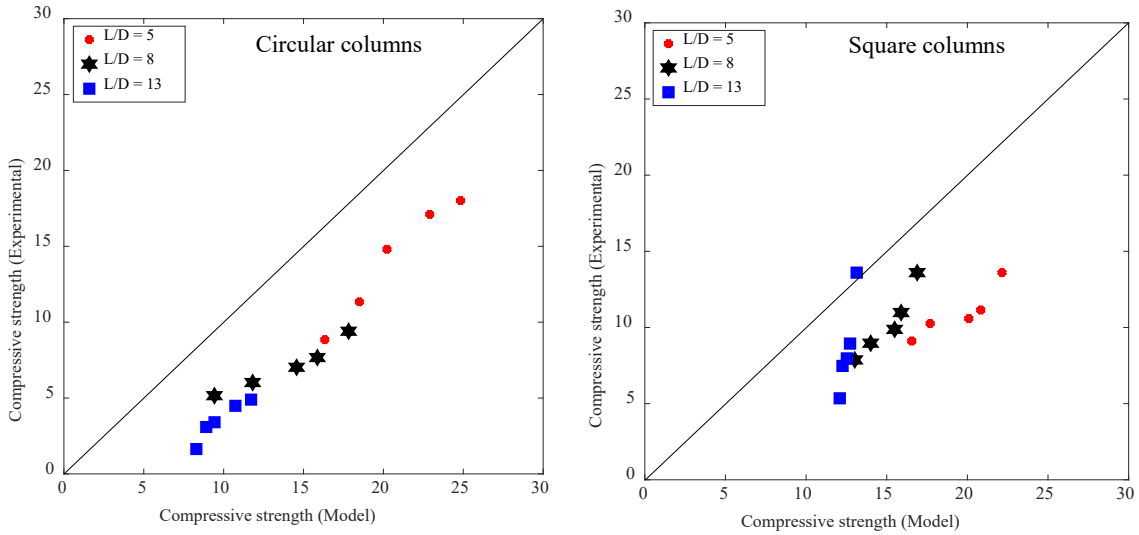


(d) Andisheh et al. (2021) model

Figure 3.28. Comparison of existing confined concrete models and experimental results of ultimate compressive strength

Figure 3.28 shows the performance of the selected existing analytical models in predicting the compressive strength of confined corroded R.C. columns. It can be seen from the above comparison that the current analytical models overestimate the peak strength of the confined columns. This is because the ultimate strength of confined concrete columns depends on the strength of the unconfined concrete, the dimensions of the core and the amount and configuration of transverse reinforcements. Thus, the observation of high ultimate strength in the analytical models to the experimental data results from the low compressive strength of the concrete used in the experimental tests. Furthermore, the response of confined concrete columns to lateral pressure is affected by changes in the cross sections. Hence, columns with circular cross-sections have higher strength capacity, which is about double that of the circular cross-sections when subjected to the same lateral confining pressure. These differences in the lateral confining pressures result from the irregular distribution of pressure in the cross-section of the rectangular columns. In addition, the predictions of the strength of the square columns are not too different from the experimental data.

## 3.6 Conclusions

The effects of corrosion on the axial load capacity of differently confined RC columns have been studied experimentally. The parameters investigated in this study are corrosion mass loss on the stress-strain response of differently confined circular and square RC columns representing typical shapes of bridge piers. The experiment was done on 30 short RC columns divided into two groups of fifteen circulars and fifteen squares, subdivided into five groups according to the expected

corrosion mass loss from the accelerated corrosion process and three groups considering the spacing of their transverse confining rebars. The primary conclusions drawn from the analysis of the experimental data are as follows.

1. The circular columns have higher axial cyclic load-carrying capacities, gradually decreasing with increased corrosion and confinement than the square columns. The well-confined circular RC columns (*L/D* = 5) have 35.88MPa, 33.96MPa, 30.15MPa, 25.93MPa and 22.20MPa axial compressive load carrying capacities for the 0%, 5%, 10%, 20% and 30% corrosion losses respectively. Meanwhile, the square columns with the same confinement and corrosion losses have 25.41MPa, 21.47MPa, 20.38MPa, 19.63MPa and 17.19MPa axial compressive load-carrying capacities. A similar trend was observed in the medium-confined and low-confined columns, with the circular columns having higher capacities than the square columns. This results from the effectiveness of the transverse ties in the circular column, which has more significant confinement effectiveness coefficients than the square columns.
2. Corrosion of transverse confining steel affects the strength and deformability of confined concrete. The effectiveness of confinement reinforcements in confining the core concrete reduces as the corrosion increases. The strength of the highly confined circular column was reduced by 5.35%, 15.97%, 27.74%, and 38.11% for the 5%, 10%, 20% and 30% corroded columns to the EC2 estimated uncorroded column. Similarly, the mediumly confined and lowly confined columns have strength reduction varying between 15% to 39% and 17% to 70%, respectively.
3. The degree of corrosion experienced by transverse reinforcement is more severe than longitudinal reinforcements at the same current densities. In the highly confined circular RC columns, the transverse reinforcement corrosion losses are 8.8%, 21.2%, 29.4% and 39.8%, while the longitudinal bars have corrosion losses of 4.1%, 7.3%, 10.8% and 20.6% for the 5%, 10%, 20% and 30% corrosion estimates. This results from the closeness of the transverse bars to the surface of the concrete, leading to a possibly higher concentration of chloride ions and an early start of corrosion of the transverse bars. Similar trends are observed in the other confinement configurations in both the circular and square RC columns..
4. Local buckling is more severe for specimens with high corrosion rates, and buckling always occurs in areas with more rust products. This is evidence that the local buckling of the rebar is strongly related to its corrosion condition, and the part where the cross-sectional area is weakened by corrosion is more likely to cause buckling of the longitudinal rebar and collapse of the structure.

5. The inelastic buckling mechanism of bars is affected by non-uniform pitting corrosion. The observed buckling modes showed that the buckling mechanism of corroded bars is a function of the mass loss due to corrosion and the distribution of pits along the bar length. Hence, the bars with more corrosion mass loss experienced more buckling and fracture than columns at low corrosion.
6. The existing analytical models overestimate the ultimate strength of ageing low-strength confined corroded RC columns. Hence, there is a need for more experimental tests on low-strength concrete to develop a new model that will correctly predict the strength of such columns.

# Chapter 4 Nonlinear Behaviour of Corrosion Damaged Low-Strength Reinforced Concrete Columns under Axial Cyclic Compressive Loading[3,4]

## 4.1 Introduction

The nonlinear stress-strain behaviour of low concrete strength corroded RC columns under monotonic axial compression load with different confinement ratios and varying degrees of corrosion was discussed in Chapter 3. It was found that an increase in corrosion mass loss and inadequate transverse reinforcement confinement results in a substantial reduction in the load-carrying capacity of corroded columns. Furthermore, it results in the inelastic buckling of the longitudinal bars, especially at high corrosion loss. Much research has been done on the effect of chloride-induced corrosion on the seismic performance of RC structures (Chapter 2). However, they are primarily on normal and high-strength RC structures. However, many ageing low-strength RC structures exist in high seismic zones; investigating their response to cyclic loading is pertinent to understanding their behaviour under cyclic load and providing adequate maintenance and rehabilitation plans to prevent their collapse.

## 4.2 Degradation and cyclic response of RC Columns

Numerous RC elements (beams and columns) vulnerable to severe damage and collapse during seismic events were constructed before the 1970s in areas of high seismicity. Significant load redistributions occur between failing and surrounding elements as damage progresses in a structure during a seismic event. The challenge for structural engineers is to accurately determine whether an existing structure can satisfy life-safety or collapse-prevention performance objectives after a severe earthquake, which depends on how well the degrading behaviour of failing elements and the associated load redistributions can be estimated (LeBorgne & Ghannoum, 2012).

[3] Aminulai, H. O., Robinson, A. F., Ferguson, N. S., & Kashani, M. M. (2023b). Nonlinear behaviour of corrosion damaged low-strength short reinforced concrete columns under compressive axial cyclic loading. *Engineering Structures*, *289*, 116245. https://doi.org/https://doi.org/10.1016/j.engstruct.2023.116245

[4] Aminulai, H. O., Ferguson, N., & Kashani, M. (2023b). Structural response of corroded concrete columns with different rebar confinements under cyclic compressive loading. In *Life-Cycle of Structures and Infrastructure Systems* (pp. 3340-3347). CRC Press.

In practice, deterioration of columns often results in a high risk of the collapse of RC structures, for the reason that as one of the paramount structural members, the columns almost support all of the vertical loads, as well as some frequent lateral loads (Darwin et al., 2016). Thus, the performance of columns under various loading and environmental conditions has always been one of the major concerns during the whole service life (Rodrigues et al., 2013; Torres-Acosta & Martınez-Madrid, 2003). To date, the crucial parameters that affect the mechanical properties of RC columns have been well understood and documented, and important among these factors include the concrete strength, thickness of the concrete cover, axial compression ratio, and slenderness (Bažant & Kwon, 1994; Dhakal & Maekawa, 2002; Huang et al., 2015). However, existing studies have shown that in the case of harsh environments, considerable degradations of the mechanical properties of RC columns, in terms of the ultimate bearing capacity, ductility, dynamic responses, etc., are still generally observed due to the reinforcement corrosion and concrete spalling, although the protection measures are satisfied with the requirements of design codes (Boumarafi et al., 2015; Li et al., 2020; Prachasaree et al., 2018).

There have been several studies investigating the mechanical response of RC columns in seismic regions (Dai et al., 2021; P. Li et al., 2022; Q. Li et al., 2022; Rajput & Sharma, 2018b). Some of these studies are on uncorroded RC samples subject to the combined effect of axial and lateral cyclic load (Choi & Lee, 2022; Z. Li et al., 2022; Matthews et al., 2022; Rajput & Sharma, 2018b), while others are numerical work to predict the mechanical behaviour of corroded bars in RC columns (Apostolopoulos et al., 2018; Basdeki et al., 2022; Rajput & Sharma, 2018a).

The previous experimental investigations are mostly on normal and high-strength concrete. Still, many old and ageing bridges/structures have low-strength columns/piers and improper confinement based on the old design in earthquake-prone regions. The effect of corrosion and inadequate confinement on such weak and old RC structures must be investigated to understand their response to axial cyclic loading. In addition, there is a shortfall in research on the seismic performance of ageing RC columns with low concrete strength subject to the combined effect of corrosion and varying confinement levels, particularly in investigations on their load-carrying and deformation capacities.

## 4.3 Research contribution and novelty of this chapter

The use of cyclic experimental testing is effective in providing insight into the seismic performance of a structural component. However, although it is recognised that corrosion-induced degradation on coastal bridge piers significantly affects the performance of the structures during the long-term service period (Guo et al., 2015), the damage mechanism and the

mechanical behaviour of low-strength concrete structures are still not well understood. Therefore, this chapter discussed the effect of corrosion and confinement on the nonlinear cyclic behaviour of ageing low-strength RC columns.

Corrosion of reinforcement significantly affects the nonlinear response of bridge piers/columns subject to seismic and axial loadings, where the buckling of vertical bars in plastic hinge regions is the governing parameter. It is well known that bending moment combined with axial compression force will induce considerable strain on the edge of a section. This generates large tensile stresses in the RC structure, followed by high compression will cause the reinforcing bars to buckle, resulting in concrete crushing or spalling (Yang et al., 2020). Reinforcement buckling inside RC structures is a more complex phenomenon due to the confining effect of the surrounding concrete than buckling of bare reinforcing bars. Recent studies have shown that multiple local parameters influence the buckling response of reinforcing bars inside RC structures compared to a plain reinforcing bar (Kashani et al., 2016b; Kashani et al., 2018; Nojavan et al., 2017). The buckling response of bars inside RC members primarily depends on the resistance offered by the cover concrete and transverse reinforcement to bars against buckling.

While several studies have been dedicated to investigating the structural vulnerability of corrosion-damaged RC members, there is a significant lack in the literature on the influence of corrosion damage, confinement levels and cross-sectional shape on the seismic behaviour of ageing RC bridge columns/piers. Several numerical and analytical models have investigated the effects of corrosion and transverse reinforcement confinements on seismic performance and failure modes of RC members with normal-strength concrete (Kashani et al., 2016a, 2016b; Kashani et al., 2018; Su et al., 2015). However, they have not investigated ageing RC members with low-strength concrete. Therefore, there is a need for experimental investigation of the nonlinear cyclic response of corroded low-strength RC columns with various confinement ratios under cyclic compressive loading.

Axial cyclic behaviour of short columns is important in developing uniaxial constitutive models for corrosion damaged concrete (with various confinement), which can be used in modelling nonlinear seismic behaviour of corroded structures. All the uniaxial constitutive models for concrete with various confinement ratios have been developed in past using similar tests. Hence, the present study investigates, for the first time, the nonlinear behaviour of low-strength circular and square RC columns under simultaneous reinforcement corrosion, confinement configurations and cyclic compressive load. Five degrees of reinforcement corrosion (i.e., 0%, 5%, 10%, 20% and 30%) with three confinement ratios based on the spacing of the transverse reinforcements are investigated under cyclic compressive load. The confinement ratios are assigned through the

centre-to-centre spacing of the transverse reinforcement (L) and the diameter of the longitudinal reinforcement (*D*), known as the spacing-diameter, *L/D* ratio. Hence for the test, the three confinement ratios are high (*L/D* = 5), medium (*L/D* = 8) and low (*L/D* = 13). The accelerated corrosion technique obtained different degrees of reinforcement corrosion. The failure modes of the RC columns, the load-deformation responses of RC columns and the inelastic buckling of the longitudinal reinforcements were analysed.

## 4.4 Experimental Campaign

### 4.4.1 Specimen details and material characterisation

Chapter 3 (3.2.1) described that the specimens (15 circular and 15 square RC columns) were made with British standard B500B ribbed thread steel bars. The configurations of the samples and the targeted corrosion mass losses are presented in Table 3.3 (Chapter 3), while Table 3.10 (Chapter 3) shows the confinement reinforcement details for the different levels of confinement.

### 4.4.2 Axial cyclic compressive strength of concrete

Similar to the concrete used in the monotonic test in Chapter 3 (3.4.1), the concrete was designed as low-strength concrete, representing ageing RC structures. The axial cyclic compressive strength test was done at the Testing and Structures Research Laboratory (TSRL), the University of Southampton, using the servo-hydraulic 630kN Instron Schenk machine. The concrete columns were tested using the cyclic loading protocol with displacement control at a constant loading rate of 0.1mm/sec until failure. Figure 4.1(a) shows the stress-strain response of the unreinforced concrete samples, with the square samples (S1, S2 and S3) having an average compressive strength of 13.8 MPa while the circular sample (C1) has 12.6 MPa. Furthermore, the concrete columns show similar failure patterns, having diagonal cracks in the middle of the column (Figure 4.1(b))

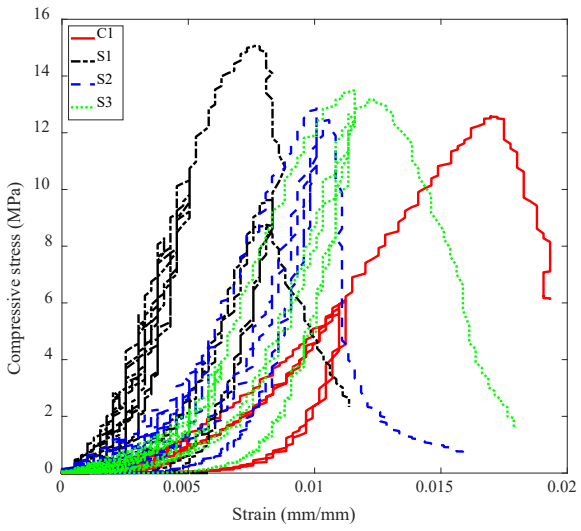


(a)

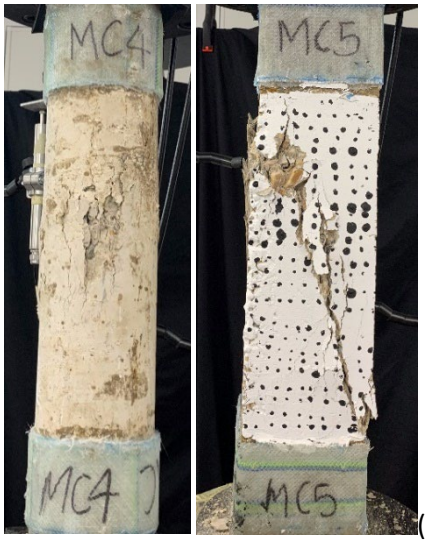


(b)

Figure 4.1: Mass concrete behaviour (a) stress-strain response (b) observed failure after test

### 4.4.3 Axial compressive cyclic loading protocol and instrumentation

The RC columns were tested under axial compressive cyclic loading. The loading protocol was set to have 20 cycles with ten different mean strains, each strain peak repeating twice, as shown in Figure 4.2. The mean strain was estimated from the displacement values of the test done on corroded RC under monotonic loading in Chapter 3. The load was applied using the displacement control condition using the servo-hydraulic Instron Schenck 630kN testing machine within TSRL. The first five lower strain peaks were applied at a 0.1mm/sec loading rate, while the remaining were at 0.15mm/sec. The cyclic loading protocol was set up using the Instron Wavematrics software (Instron, 2018).

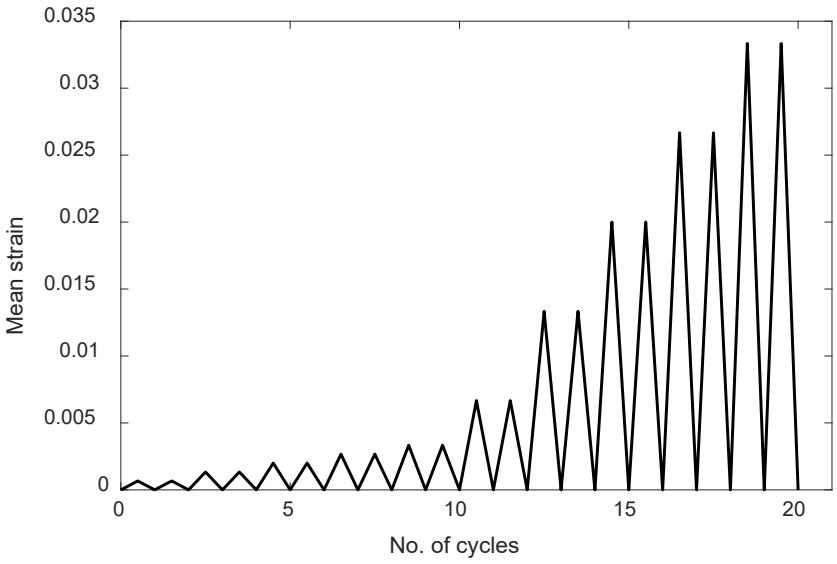


Figure 4.2: Cyclic compressive loading protocol

The RC columns were tested under axial cyclic compressive load using displacement control with a lower loading rate for the first ten cycles. After that, the remaining cycles were at a slightly higher rate until the failure of the RC columns. Furthermore, the test was conducted under complete axial cyclic compression loading, with each loading cycle repeated twice without going into the tension loading zone. The servo-hydraulic machine used an internal Linear Variable Differential Transformer (LVDT) that measures the displacement of the actuator during loading. In contrast, a load cell measures the corresponding load resulting from the applied displacement. The setup of the experiment is presented in Figure 4.3(a).

The displacement at the middle 400mm zone of the RC columns is measured with the LVDTs fixed to the edge of the Glass fibre-reinforced polymers (GFRP) strengthened ends and the stereo 3D Digital Image Correlation (DIC). The two LVDTs with 50mm strokes were fixed such that they touch the angle irons fixed to the edge of the Glass fibre-reinforced polymers (GFRP) strengthened ends of the RC columns (Figures 4.3(b) and 4.3(c)). This ensures that the LVDTs measure the axial deformations in the middle 400mm section of the columns, which are recorded via a multichannel data acquisition unit (Strainsmart 8000).

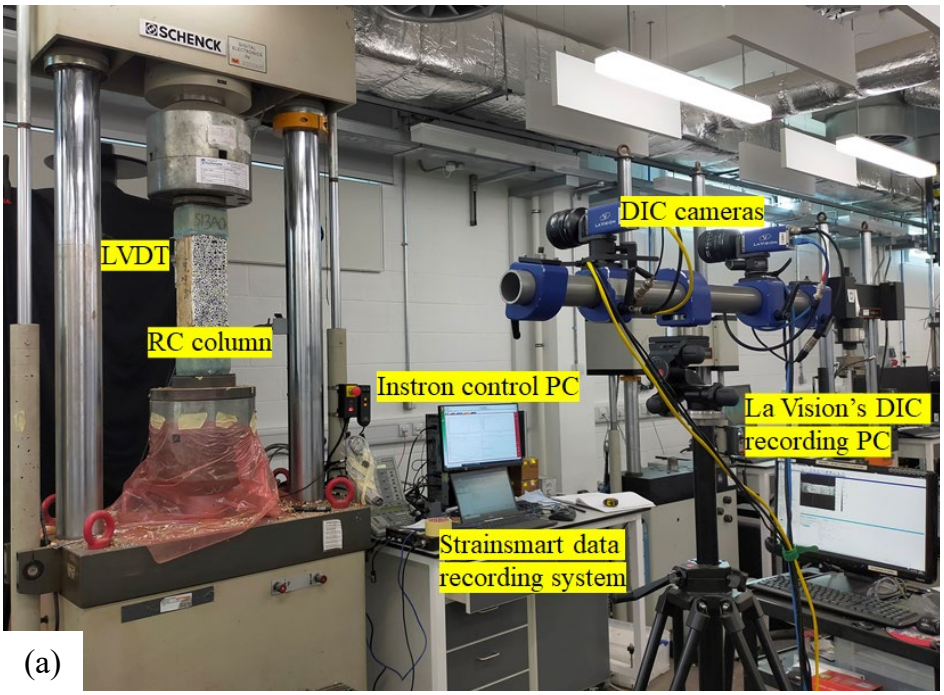


(a)

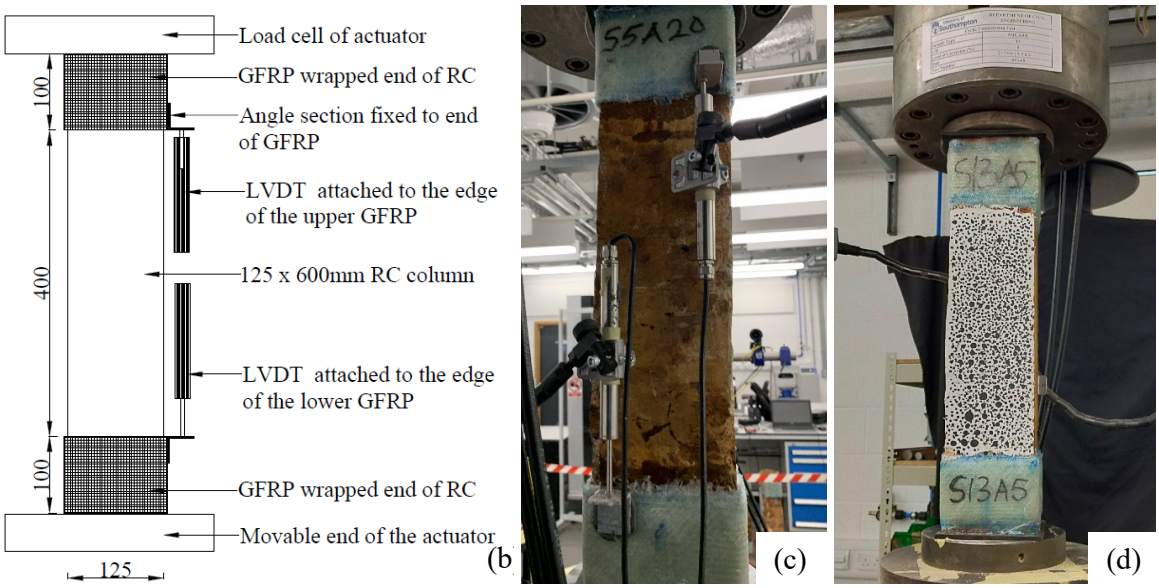


Figure 4.3: Experimental test setup (a) laboratory setup; (b) schematic of the LVDT connection; (c) Image of the LVDT connections to the RC samples and (d) RC sample with speckles for DIC processing

Furthermore, the DIC technique, as applied in section 3.2.9 was used to investigate the strain distribution in the middle section of the RC column. The cameras were calibrated to capture the RC column's out-of-plane and vertical displacements during loading using the dots marked on the columns (Figure 4.4(d)). The images recorded are further processed using LaVision's Davis 10 software to see the strain distribution resulting from the applied loading. The parameters used in the DIC image acquisition and processing are presented in Table 3.7 (Chapter 3).

## 4.5 Experimental Results and Discussion

### 4.5.1 Calculation of corrosion and mass loss ratio

Table 4.1 shows the corrosion density and the duration for each column used in this experiment. The actual mass losses resulting from the corrosion of the reinforcements are estimated using Eq. 3.4 and are illustrated in Figures 4.4 and Table 4.2 for the circular columns. Furthermore, Figure 4.5 and Table 4.3 give the square columns' corrosion estimates. Similar to the results of the monotonic test presented in Chapter 3, the stirrups rebars had more severe corrosion than the longitudinal bar under the same constant current and duration (Q. Li et al., 2022). The observed mass loss resulting from the accelerated corrosion process is like the results presented in Tables 3.8 and 3.9 (section 3.4.1)

**Table 4.1. Accelerated corrosion parameters for RC columns.**

| Specimen No. | Corrosion current density ($mA/cm^2$) | Corrosion duration (days) | Specimen No. | Corrosion current density ($mA/cm^2$) | Corrosion duration (days) |
|---|---|---|---|---|---|
| **C5A0** | 0 | 0 | **S5A0** | 0 | 0 |
| **C5A5** | 1.00 | 3.0 | **S5A5** | 0.99 | 2.9 |
| **C5A10** | 1.00 | 6.0 | **S5A10** | 0.99 | 5.8 |
| **C5A20** | 1.00 | 12.1 | **S5A20** | 0.99 | 11.7 |
| **C5A30** | 1.00 | 18.1 | **S5A30** | 0.99 | 17.5 |
| **C8A0** | 0 | 0 | **S8A0** | 0 | 0 |
| **C8A5** | 1.16 | 2.7 | **S8A5** | 1.17 | 2.6 |
| **C8A10** | 1.16 | 5.4 | **S8A10** | 1.17 | 5.1 |
| **C8A20** | 1.16 | 10.8 | **S8A20** | 1.17 | 10.2 |
| **C8A30** | 1.16 | 16.2 | **S8A30** | 1.17 | 15.3 |
| **C13A0** | 0 | 0 | **S13A5** | 0 | 0 |
| **C13A5** | 1.28 | 2.5 | **S13A5** | 1.33 | 2.3 |
| **C13A10** | 1.28 | 5.0 | **S13A10** | 1.33 | 4.6 |
| **C13A20** | 1.28 | 10.0 | **S13A20** | 1.33 | 9.3 |
| **C13A30** | 1.28 | 15.0 | **S13A30** | 1.33 | 13.9 |

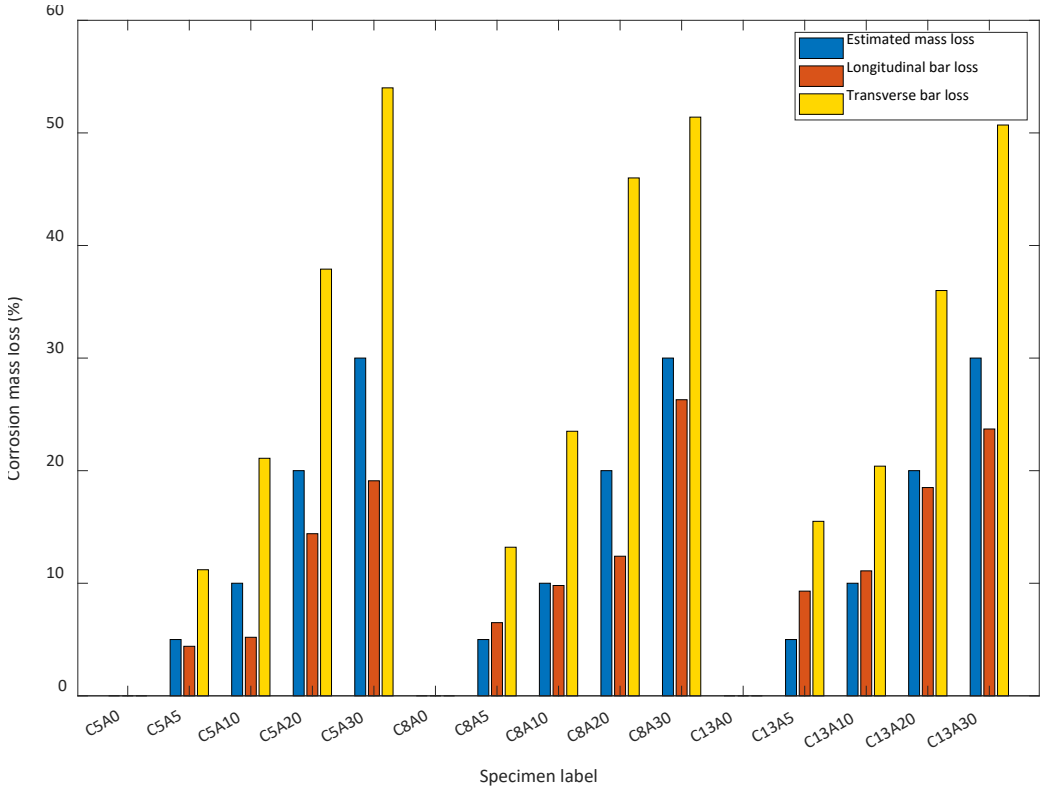


Figure 4.4: Corrosion mass loss estimate for circular columns

**Table 4.2. Summary of the circular RC columns' predicted and measured corrosion mass losses.**

| Specimen No. | Corrosion current density ($mA/cm^2$) | Corrosion duration (days) | Estimated mass loss (Eq. 3.7) (%) | Measured mass loss of longitudinal bars (Eq. 3.8) (%) | Measured mass loss of transverse bars (Eq. 3.8) (%) |
|---|---|---|---|---|---|
| **C5A0** | 0 | 0 | 0 | 0 | 0 |
| **C5A5** | 1.00 | 3.0 | 5 | 4.4 | 11.2 |
| **C5A10** | 1.00 | 6.0 | 10 | 5.2 | 21.1 |
| **C5A20** | 1.00 | 12.1 | 20 | 14.4 | 37.9 |
| **C5A30** | 1.00 | 18.1 | 30 | 19.1 | 54.0 |
| **C8A0** | 0 | 0 | 0 | 0 | 0 |
| **C8A5** | 1.16 | 2.7 | 5 | 6.5 | 13.2 |
| **C8A10** | 1.16 | 5.4 | 10 | 9.8 | 23.5 |
| **C8A20** | 1.16 | 10.8 | 20 | 12.4 | 46.0 |
| **C8A30** | 1.16 | 16.2 | 30 | 26.3 | 51.4 |
| **C13A0** | 0 | 0 | 0 | 0 | 0 |
| **C13A5** | 1.28 | 2.5 | 5 | 9.3 | 15.5 |
| **C13A10** | 1.28 | 5.0 | 10 | 11.1 | 20.4 |
| **C13A20** | 1.28 | 10.0 | 20 | 18.5 | 36.0 |

| | | | | | |
|---|---|---|---|---|---|
| **C13A30** | 1.28 | 15.0 | 30 | 23.7 | 50.7 |

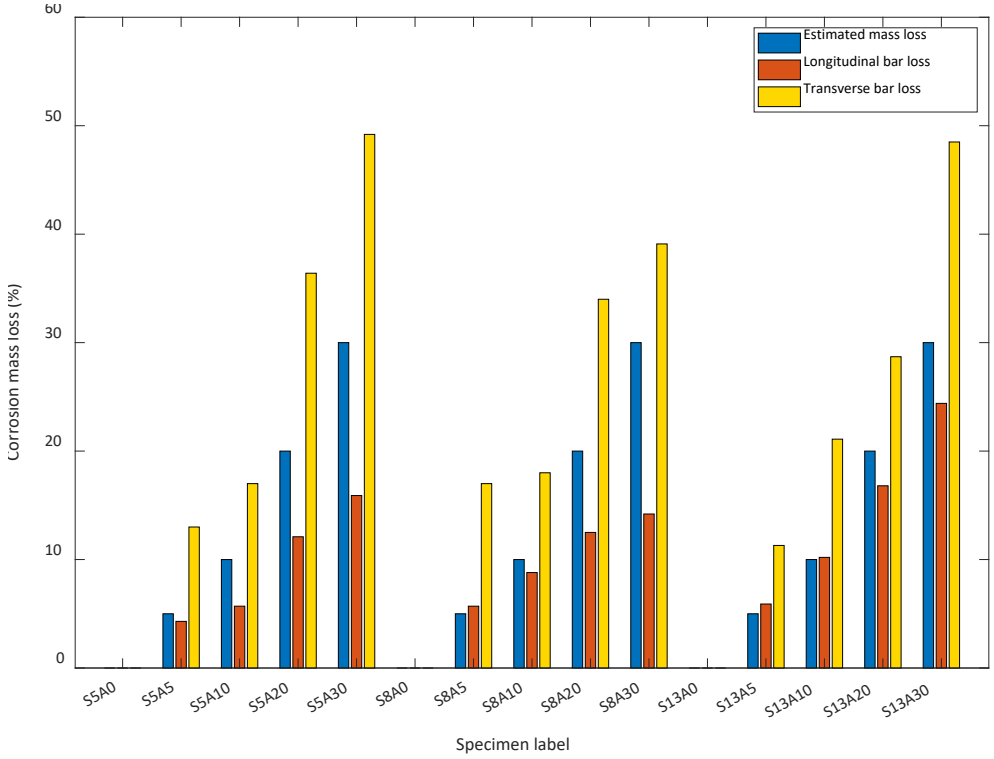


Figure 4.5: Corrosion mass loss estimate for square columns

**Table 4.3. Summary of the square RC columns' predicted and measured corrosion mass losses.**

| Specimen No. | Corrosion current density (mA/cm²) | Corrosion duration (days) | Estimated mass loss (Eq. 3.7) (%) | Measured mass loss of longitudinal bars (Eq. 3.8) (%) | Measured mass loss of transverse bars (Eq. 3.8) (%) |
|---|---|---|---|---|---|
| **S5A0** | 0 | 0 | 0 | 0 | 0 |
| **S5A5** | 0.99 | 2.9 | 5 | 4.3 | 13.0 |
| **S5A10** | 0.99 | 5.8 | 10 | 5.7 | 17.0 |
| **S5A20** | 0.99 | 11.7 | 20 | 12.1 | 36.4 |
| **S5A30** | 0.99 | 17.5 | 30 | 15.9 | 49.2 |
| **S8A0** | 0 | 0 | 0 | 0 | 0 |
| **S8A5** | 1.17 | 2.6 | 5 | 5.7 | 17.0 |
| **S8A10** | 1.17 | 5.1 | 10 | 8.8 | 18.0 |
| **S8A20** | 1.17 | 10.2 | 20 | 12.5 | 34.0 |
| **S8A30** | 1.17 | 15.3 | 30 | 14.2 | 39.1 |
| **S13A5** | 0 | 0 | 0 | 0 | 0 |
| **S13A5** | 1.33 | 2.3 | 5 | 5.9 | 11.3 |

| | | | | | |
|---|---|---|---|---|---|
| **S13A10** | 1.33 | 4.6 | 10 | 10.2 | 21.1 |
| **S13A20** | 1.33 | 9.3 | 20 | 16.8 | 28.7 |
| **S13A30** | 1.33 | 13.9 | 30 | 24.4 | 48.5 |

### 4.5.2 Axial compressive cyclic testing of circular RC columns

The stress-strain responses of the circular columns to the applied axial cyclic compressive load are presented in Figure 4.6 (a-l). These stress-strain responses were plotted from the LVDTs data since it shows the deformation of the 400mm middle zone section rather than the readings from the machine load cell that captures the deformation of the whole column under loading. The cyclic responses of the corroded columns under loading were compared with the corresponding behaviour of the non-corroded columns in each confinement configuration.

The RC column samples all have similar stress-strain responses under axial cyclic load. The deformation started with minor vertical cracks, which subsequently enlarged with further loading, leading to spalling of the concrete cover as the longitudinal bars buckled due to lateral expansion of the RC columns. The observed cyclic responses of the RC columns are similar at the elastic range until yield and afterwards become nonlinear beyond the peak stress due to the corrosion and confinements of the rebars.

The hysteretic curve of the corroded columns within each confinement's configuration was compared with the non-corroded ones. It showed a gradual decrease in the columns' strength, stiffness and ductility as the corrosion loss increased. The corrosion of longitudinal and transverse bars reduces the column's ultimate strength and load-carrying capacity. Consequently, columns with very close mass loss in the highly confined (L/D=5) columns have their maximum strengths relative to each other, especially at low corrosion between 5% and 10% (Fig. 4.6(a - d)). For example, the strength loss between the highly confined (uncorroded and corroded) columns was reduced by 13%, 22%, 26%, and 37% for the 5%, 10%, 20% and 30% estimated mass loss, respectively (Table 4.4). This trend is also observed in the mediumly confined columns (L/D=8) with a strength reduction range between 5% to 50% (Fig. 4.6(e - h) and Table 4.4) and lowly confined columns (L/D=13) having between 10% to 48% reduction (Fig. 4.6(i - l) and Table 4.5).

Furthermore, the axial strain corresponding to the ultimate strength for each column varies compared to the axial strain of the uncorroded column (Table 4.4). In the highly confined column, the axial strain was reduced by 42%, 30%, 16% and 44% for the 5%, 10%, 20% and 30% estimated mass loss, respectively (Table 4.4). This trend is similar in the mediumly confined (2% and 47%) and lowly confined RC columns (1% and 31%).

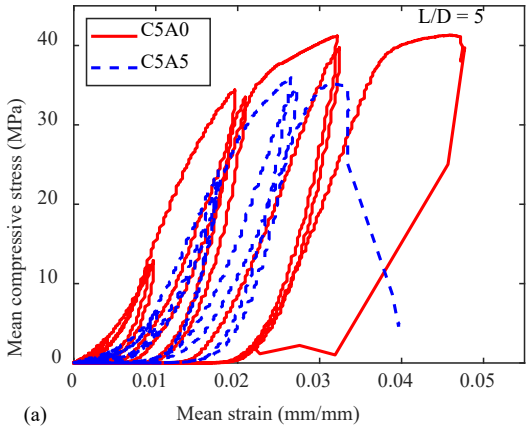
L/D = 5
C5A0
C5A5
Mean compressive stress (MPa)
Mean strain (mm/mm)

(a)

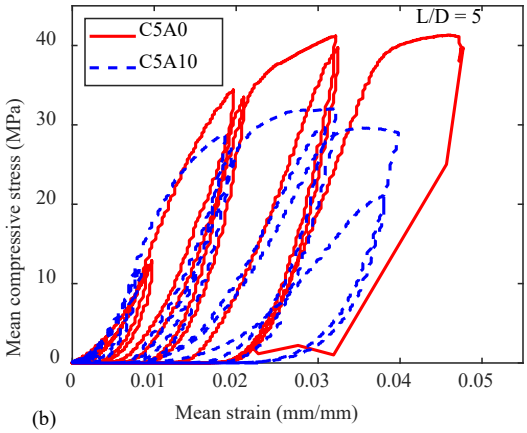
L/D = 5
C5A0
C5A10
Mean compressive stress (MPa)
Mean strain (mm/mm)

(b)

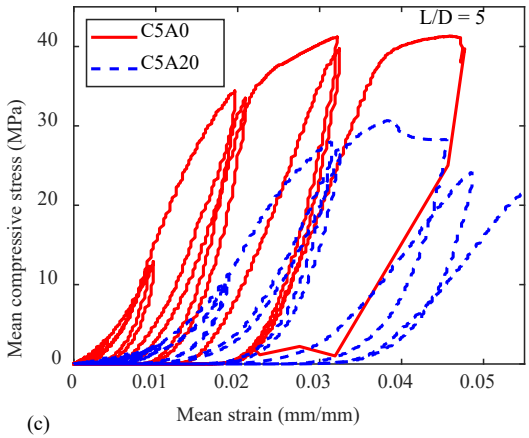
L/D = 5
C5A0
C5A20
Mean compressive stress (MPa)
Mean strain (mm/mm)

(c)

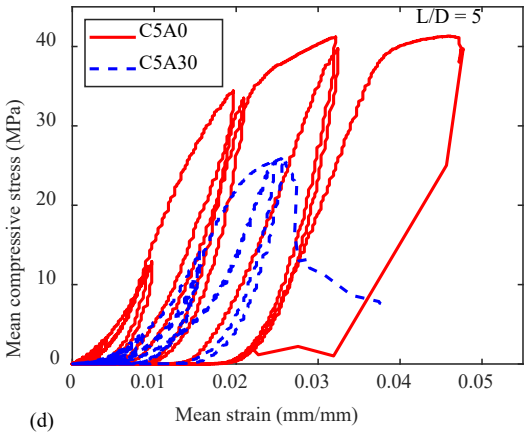
L/D = 5
C5A0
C5A30
Mean compressive stress (MPa)
Mean strain (mm/mm)

(d)

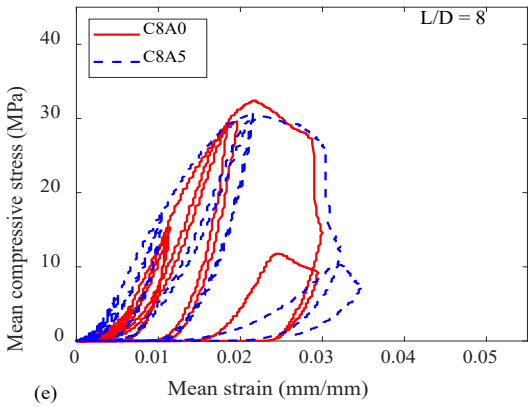
L/D = 8
C8A0
C8A5
Mean compressive stress (MPa)
Mean strain (mm/mm)

(e)

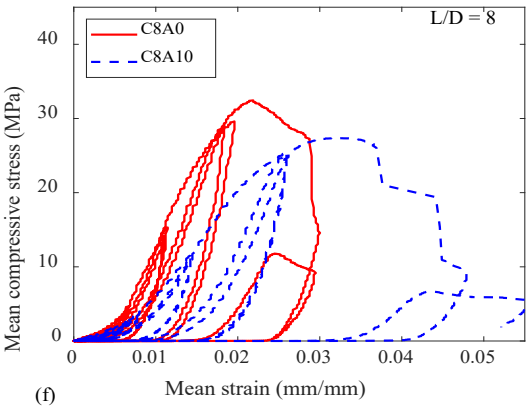
L/D = 8
C8A0
C8A10
Mean compressive stress (MPa)
Mean strain (mm/mm)

(f)

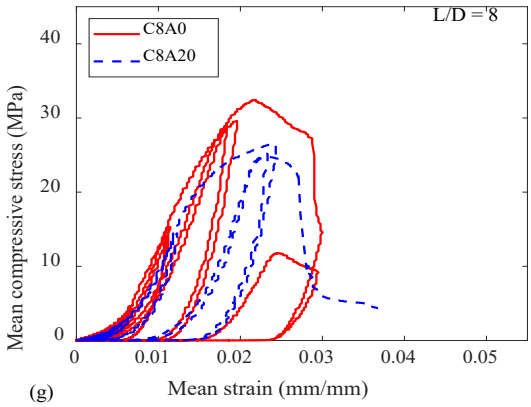
L/D = 8
C8A0
C8A20
Mean compressive stress (MPa)
Mean strain (mm/mm)

(g)

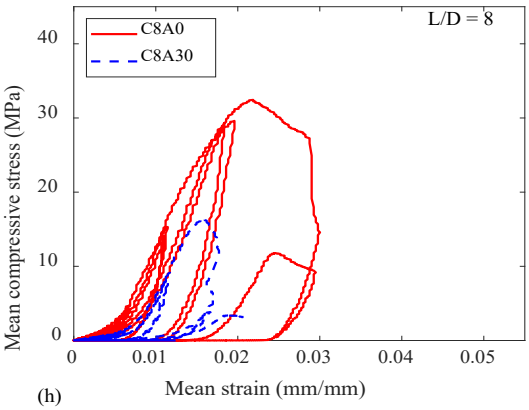
L/D = 8
C8A0
C8A30
Mean compressive stress (MPa)
Mean strain (mm/mm)

(h)

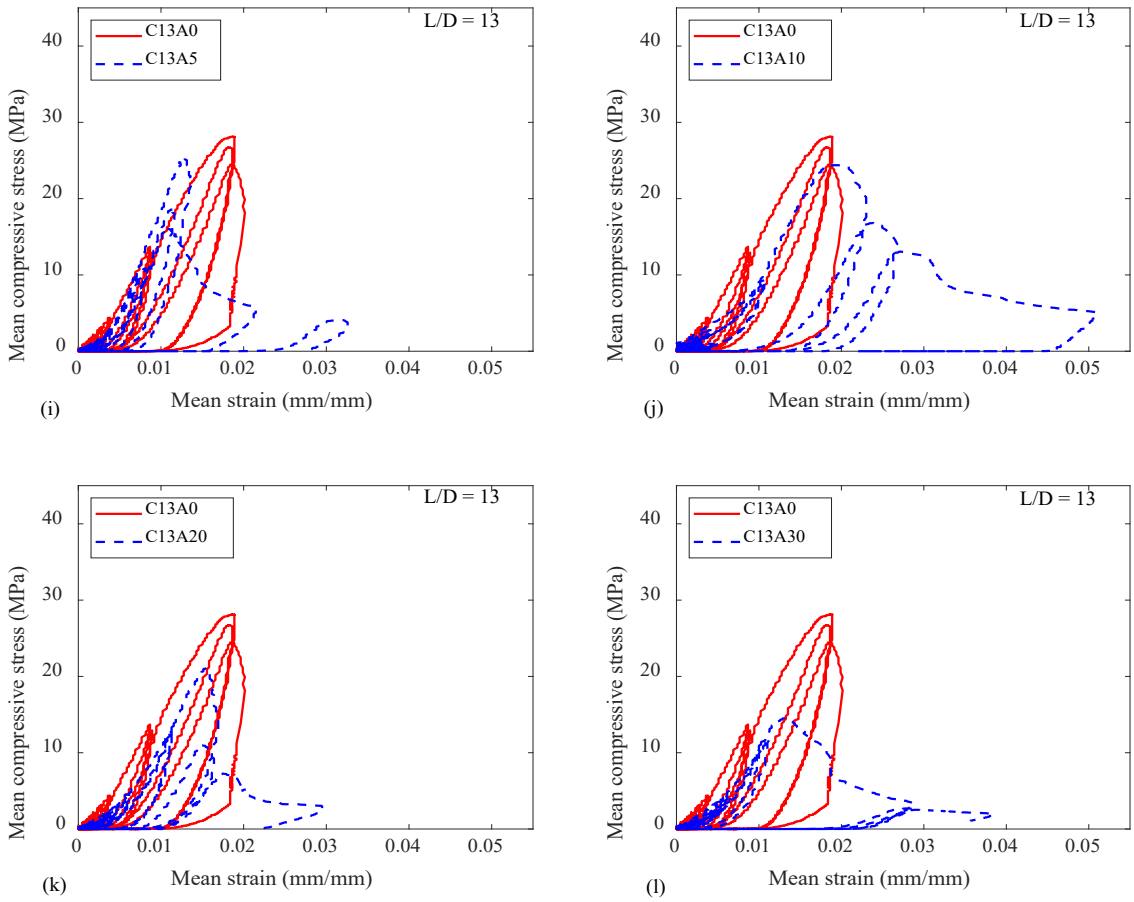


Figure 4.6. Axial cyclic compressive stress-strain response of low-strength confined RC circular columns; *L/D* = 5 (a-d), *L/D* = 8 (e-h) and *L/D* = 13 (i-l)

**Table 4.4. Variation of ultimate stress and axial compressive strain between uncorroded and corroded circular RC columns.**

| Sample label | Ultimate stress, $\sigma_u$ (MPa) | $\frac{\sigma_{u(uc)} - \sigma_{u(c)}}{\sigma_{u(uc)}} \times 100$ | Strain, $\varepsilon_u$ | $\frac{\varepsilon_{u(uc)} - \varepsilon_{u(c)}}{\varepsilon_{u(uc)}} \times 100$ |
|---|---|---|---|---|
| **C5A0** | 41.325 | 0 | 0.0459 | 0 |
| **C5A5** | 35.928 | 13.060 | 0.02669 | 41.89 |
| **C5A10** | 32.040 | 22.468 | 0.03214 | 30.002 |
| **C5A20** | 30.656 | 25.817 | 0.03836 | 16.457 |
| **C5A30** | 25.920 | 37.278 | 0.02558 | 44.291 |
| **C8A0** | 32.443 | 0 | 0.02188 | 0 |
| **C8A5** | 30.630 | 5.588 | 0.02152 | 1.663 |
| **C8A10** | 27.356 | 15.680 | 0.03217 | 47.008 |

| | | | | |
|---|---|---|---|---|
| **C8A20** | 26.488 | 18.355 | 0.02431 | 11.095 |
| **C8A30** | 16.343 | 49.626 | 0.01596 | 27.066 |
| **C13A0** | 28.116 | 0 | 0.01862 | 0 |
| **C13A5** | 25.423 | 9.578 | 0.01288 | 30.843 |
| **C13A10** | 24.381 | 13.284 | 0.01878 | 0.877 |
| **C13A20** | 21.115 | 24.90 | 0.01538 | 17.387 |
| **C13A30** | 14.552 | 48.243 | 0.01308 | 29.779 |

The applied axial cyclic compressive load results in the premature failure of some of the highly confined columns resulting from the GFRP failure at the top/bottom of the column (Fig. 4.7(a-d)). Furthermore, the applied load led to concrete cover spalling and hence buckling of the longitudinal bars and, in some cases, fracture of the transverse bar (Fig. 4.7(e, h and j)) in some columns. The longitudinal bars buckled mostly at the expected middle 400mm zone, with some columns having shear buckling due to inadequate confinement (Fig. 4.7 (k and o)), loss of confinement resulting from pitting corrosion (Fig. 4.7 (j)), and the transverse bars' fracture (Fig. 4.7(h and i)).

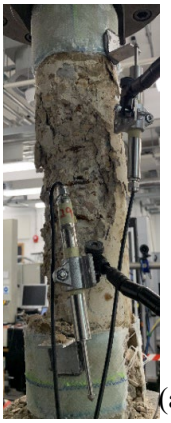
(a)


(b)


(c)


(d)


(e)

(f)

(g)


(h)


(i)


(j)

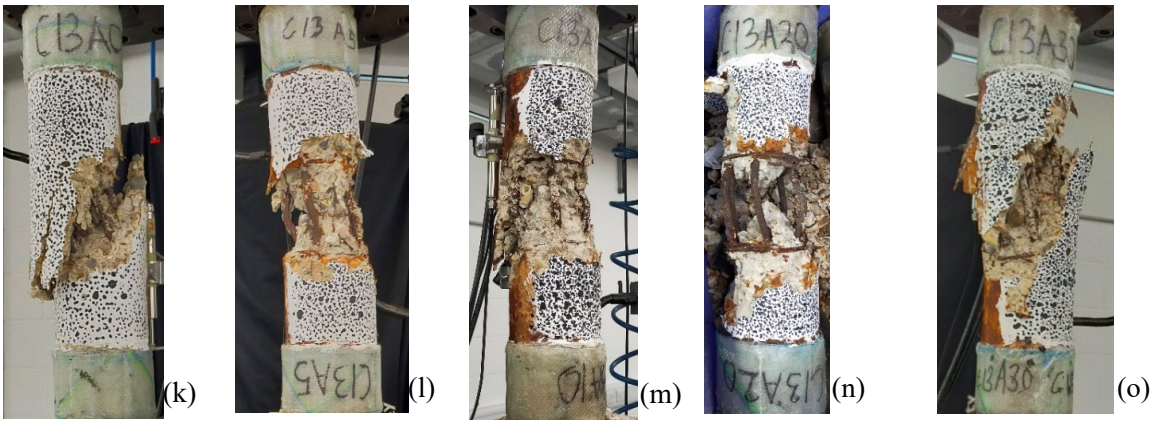


Figure 4.7: Observed failure modes of circular columns with the different corrosion levels and confinement ratios; *L/D*=5 (a - e), *L/D* = 8 (f - j) and *L/D* = 13 (k - o)

The DIC tracks the RC columns' strain response and cracks damage to the applied compressive load. Figure 4.8(a) shows the stress-strain response of one of the circular columns and the locations of the processed images (at yield stress, ultimate stress and beyond the ultimate stress). The processed images within the column's middle zone section showed the column's strain contour with the cracks, spalling of the cover concrete, and the buckling of the reinforcement captured. Figures 4.8(b - d) are the Von Mises strain processed from the captured images during loading. These values correspond to the strain estimated from the LVDTs at yield stress, ultimate stress and beyond the ultimate stress.

The DIC image process showed that it could not adequately capture the crack propagation on the circular columns during testing due to the curvature of the column, especially at lower loads (Figure 4.8(b)).

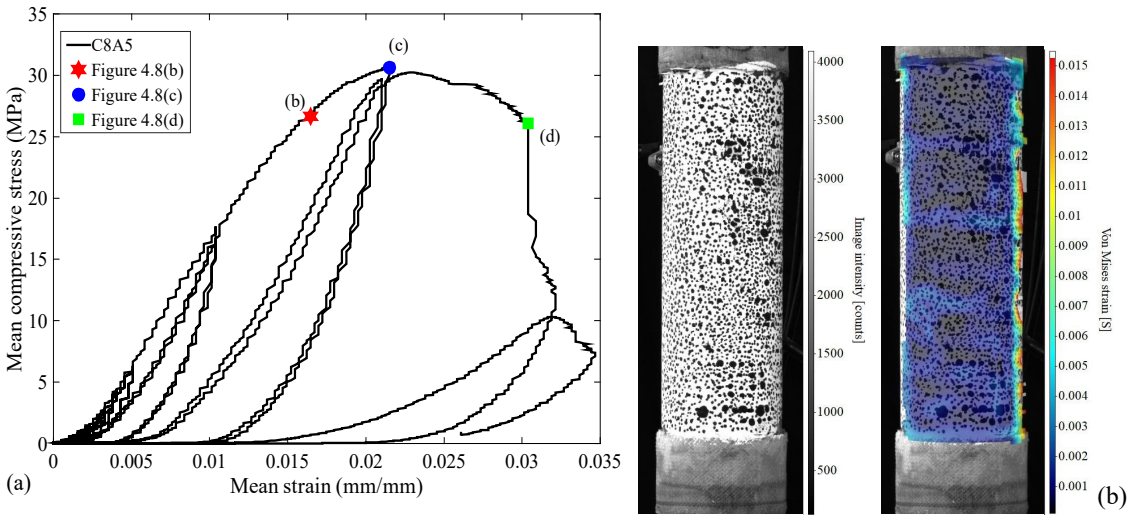

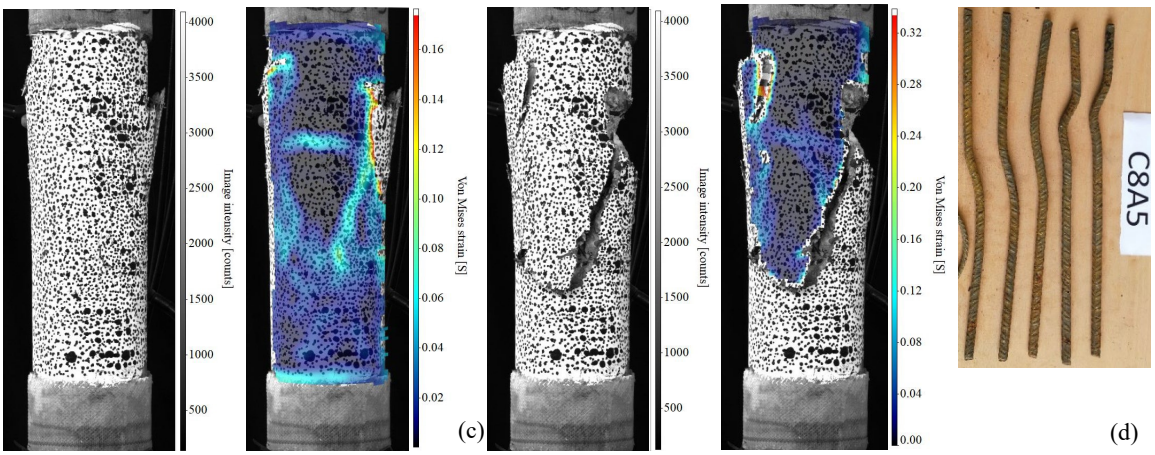


Figure 4.8: Processed DIC images of circular column (a) stress-strain response showing location of processed images (b) at yield stress, (c) at ultimate stress and (d) between ultimate stress and collapse

### 4.5.3 Axial compressive cyclic testing of square RC columns

Similar to the circular columns, the stress-strain relationship showed identical behaviour within the elastic region in all the columns until the yield stress, beyond which the confinement configurations and increase in the corrosion degree resulted in a subsequent decrease in the load-carrying capacities. The stress-strain responses of the columns to the applied axial compressive load are presented in Figure 4.9 (a-l). The cyclic responses of the corroded columns were compared with the corresponding behaviour of the non-corroded columns in each confinement configuration. The columns all have similar stress-strain responses under axial cyclic load. The deformation started with minor vertical cracks, which subsequently enlarged with further loading, leading to the spalling of the concrete cover and, eventually, the buckling of the longitudinal bars.

The hysteretic curve of the corroded columns within each confinement's configuration was compared with the non-corroded ones. It showed a gradual decrease in the columns' strength, stiffness and ductility as the corrosion loss increased. The strength of the RC columns decreased due to the combined effects of buckling the longitudinal bars and crushing the concrete. The corrosion of both longitudinal and transverse bars reduces the column's ultimate strength and load-carrying capacity. Consequently, columns with very similar mass loss in all the confinement configurations have their maximum strengths relative to each other, especially at low corrosion between 5% and 10% (Fig. 4.9(a - l). The strength reduction from corrosion in the highly confined columns was 13%, 18%, 25%, and 31% for the 5%, 10%, 20% and 30% (Table 4.5) estimated mass loss, respectively. This trend is also observed in the medium levels of confinement columns (*L/D=8*) with a strength reduction range between 7% to 23% (Fig. 4.9(e - h) and Table 4.5) and

low-level confined columns (*L/D=13*) having between 4% to 29% reduction (Fig. 4.9(i - l) and Table 4.5).

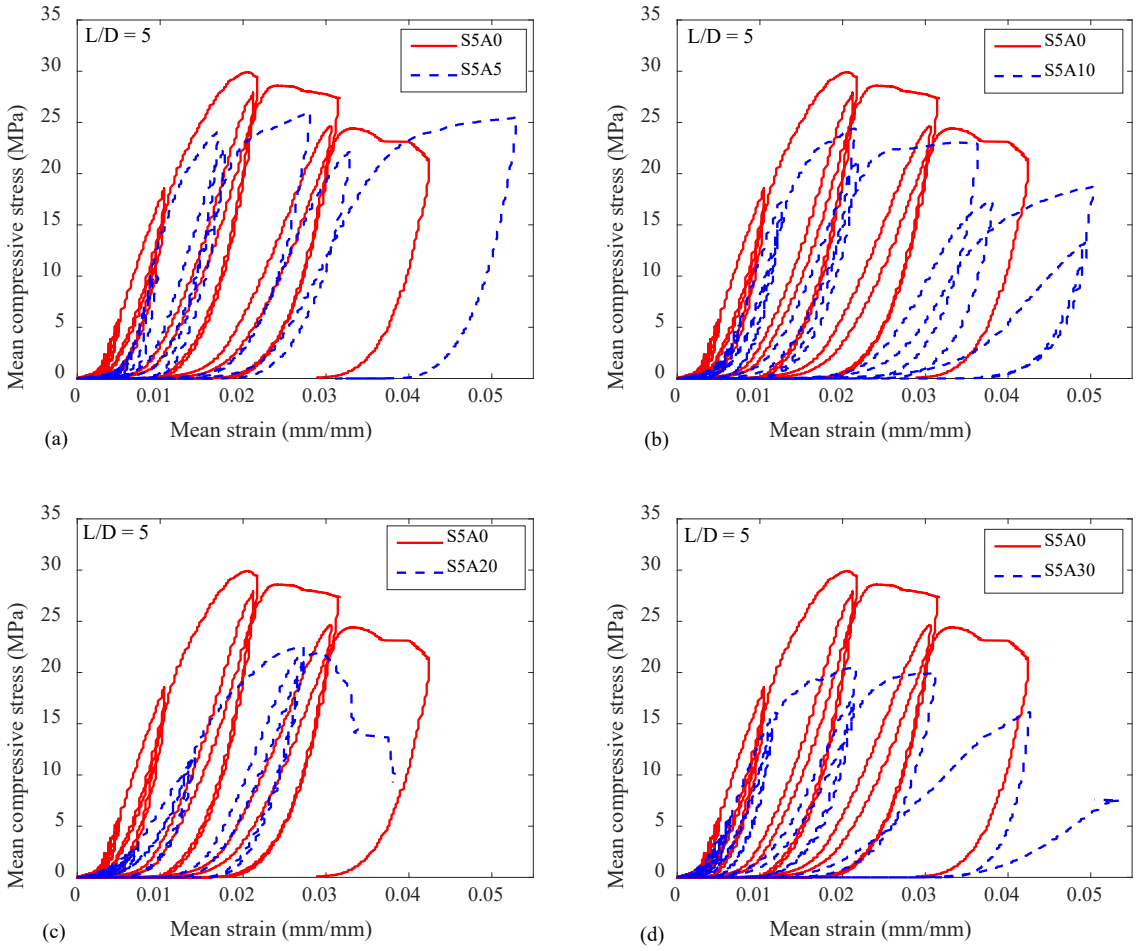

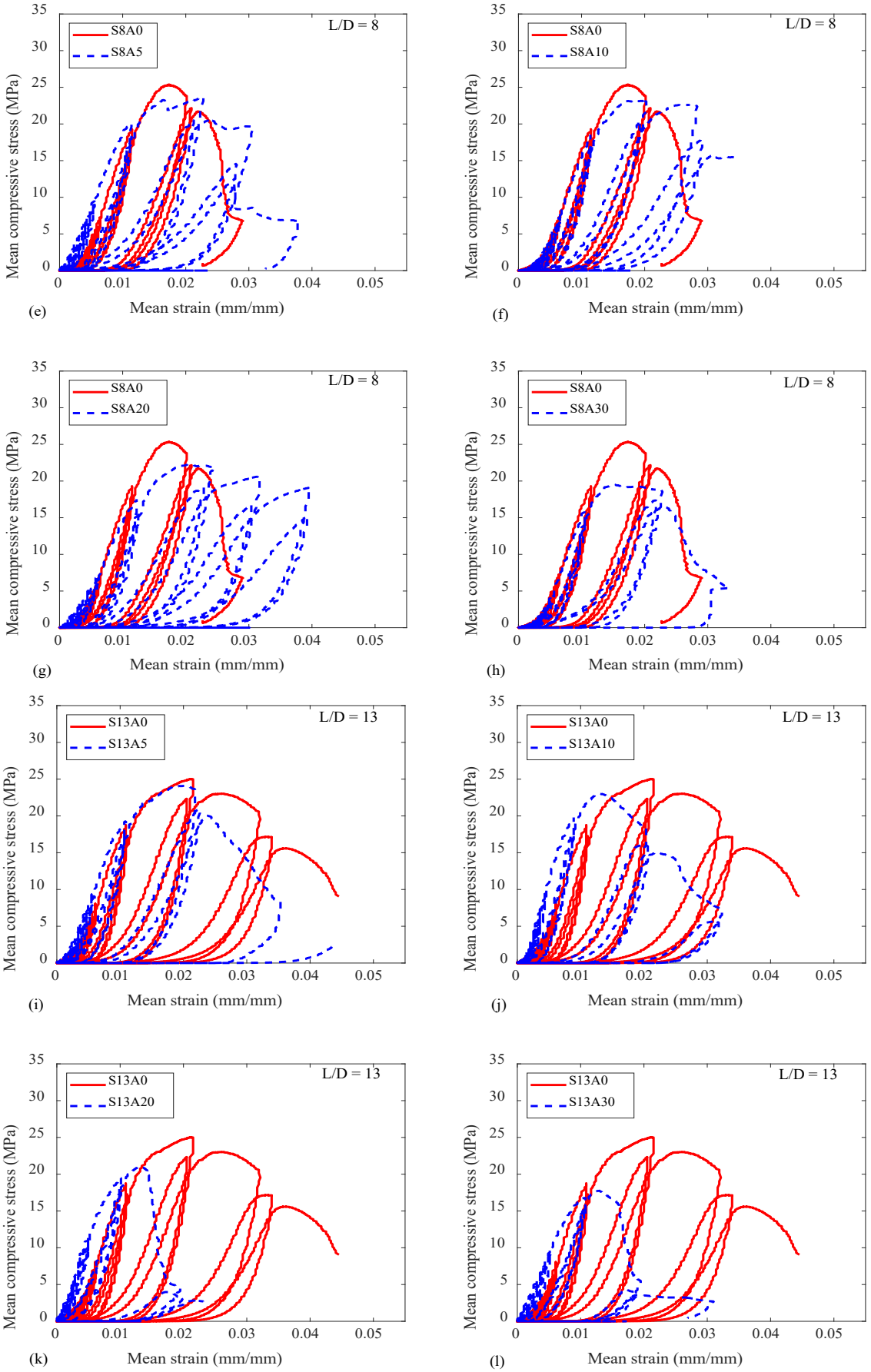


Figure 4.9: Axial cyclic compressive stress-strain response of low-strength confined RC square columns; *L/D* = 5 (a-d), *L/D* = 8 (e-h) and *L/D* = 13 (i-l)

Table 4.5 also shows the strain variations corresponding to the ultimate strength between the uncorroded and corroded RC columns. The strain varies between 3% and 36% in the highly confined column. Also, the strain variation in the medium-confined columns is between 11% and 31%, while the lowly confined columns strain varies between 5% and 39%.

**Table 4.5. Variation of ultimate stress and strain between uncorroded and corroded square RC columns.**

| Sample label | Ultimate stress (MPa) | $\frac{\sigma_{u(uc)} - \sigma_{u(c)}}{\sigma_{u(uc)}} \times 100$ | Strain, $\varepsilon_u$ | $\frac{\varepsilon_{u(uc)} - \varepsilon_{u(c)}}{\varepsilon_{u(uc)}} \times 100$ |
|---|---|---|---|---|
| **S5A0** | 29.914 | 0 | 0.0207 | 0 |
| **S5A5** | 25.982 | 13.144 | 0.02808 | 35.616 |
| **S5A10** | 24.44 | 18.3 | 0.02159 | 4.254 |
| **S5A20** | 22.484 | 24.839 | 0.0273 | -31.879 |
| **S5A30** | 20.499 | 31.473 | 0.02133 | -3.068 |
| **S8A0** | 25.399 | 0 | 0.01735 | 0 |
| **S8A5** | 23.649 | 6.872 | 0.02278 | 31.348 |
| **S8A10** | 23.143 | 8.863 | 0.01949 | 12.375 |
| **S8A20** | 22.289 | 12.227 | 0.02052 | 18.289 |
| **S8A30** | 19.496 | 23.224 | 0.01538 | 11.312 |
| **S13A0** | 25.005 | 0 | 0.02127 | 0 |
| **S13A5** | 24.081 | 3.697 | 0.02 | 5.952 |
| **S13A10** | 22.996 | 8.036 | 0.01345 | 36.584 |
| **S13A20** | 20.971 | 16.134 | 0.01325 | 37.709 |
| **S13A30** | 17.751 | 29.011 | 0.01308 | 38.507 |

Similar to the circular columns, the applied axial cyclic load results in the concrete cover's spalling (Fig. 4.10(b)), transverse bars fracture (Fig. 4.10 (d and j)) and longitudinal bars buckling (Fig. 4.10(a, m, n and o)). Also, some of the non-corroded columns (0% corrosion) have failure of the strengthening GFRP at the top/bottom of the column (Fig. 4.10 (c, f, g and i)), leading to stress concentration and premature failure of the ends of the columns. The failure of the GFRPs occurs due to the sharp edges of the square columns.


Figure 4.10: Observed failure modes of square columns with different corrosion levels and confinement ratios; *L/D* = 5 (a - e), *L/D* = 8 (f - j) and *L/D* = 13 (k - o)

Figure 4.11(a) shows the stress-strain response of one of the low confined square RC columns with an estimated 20% corrosion mass loss. Figures 4.11(b - d) are the processed images from the DIC at different locations during the compression testing on the column. The processed DIC images within the middle zone section of the column show the images with and without the strain contour on the column with the crack propagation, spalling of the cover concrete, and the reinforcement's buckling. Figure 4.11(d) further shows the buckled longitudinal bars at the end of the test after removal and cleaning.

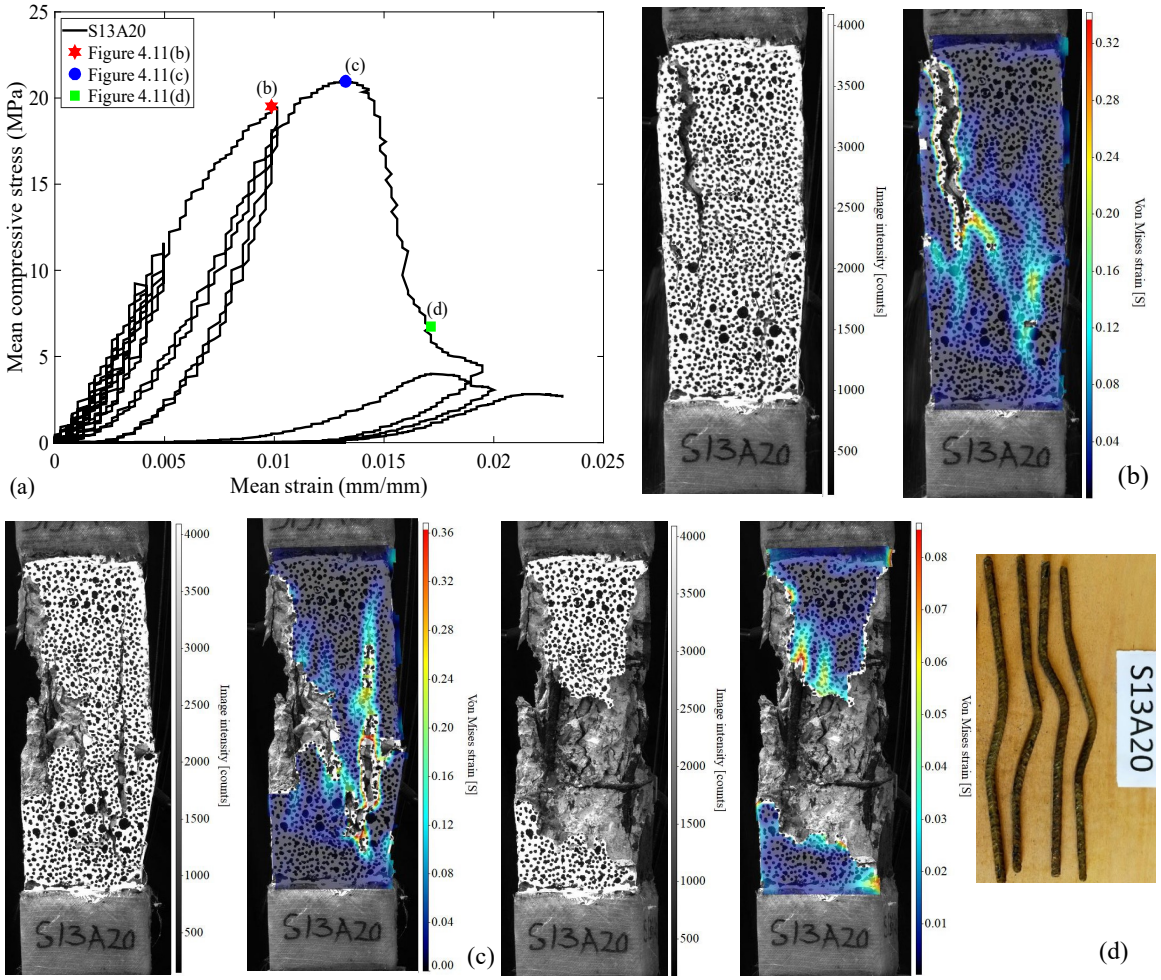


Figure 4.11: Processed DIC images of square column (a) stress-strain response showing location of processed images (b) at yield stress, (c) at ultimate stress and (d) between ultimate stress and collapse with the buckling at the end of the test

### 4.5.4 Impact of corrosion on cumulative energy dissipation capacity

The experimental studies on the cyclic behaviour of corroded beams and columns (Akiyama et al., 2011; Ma et al., 2018; Ma et al., 2012; Ou et al., 2012) showed that buckling and/or fracture of corroded bars significantly affects the global response and plastic rotation capacity and plastic hinging mechanisms of the corroded RC elements. Consequently, in the seismic assessment and evaluation of existing corroded structures, consideration needs to be given to the buckling of the rebars, even if the structure is designed initially to have sufficient confinement reinforcement.

The plots of the normalised accumulated hysteretic energy versus the number of cycles are presented in Figure 4.12. For each column, the cumulative energy dissipated at each loading cycle is normalised against the total cumulative energy dissipated at failure. Figure 4.12(a-c) shows the influence of corrosion on the accumulated energy dissipation of circular RC columns with different

confinement configurations. In contrast, Figure 4.12(d-f) shows the impact of corrosion on the accumulated energy dissipation of square RC columns. The plots showed similar behaviour for all the columns with very low energy dissipated at the smaller cycles and a steep increase in the dissipated energy after the 10th cycle. The steep increase in the dissipated energy is more significant at high corrosion and low confinement in both the circular and square columns though the circular columns have better energy dissipated. It should be noted that extensive corrosion lead to a large reduction in the energy dissipated by a column as such the highly corroded columns are more likely to have brittle failure than the uncorroded columns (Dai et al., 2021).

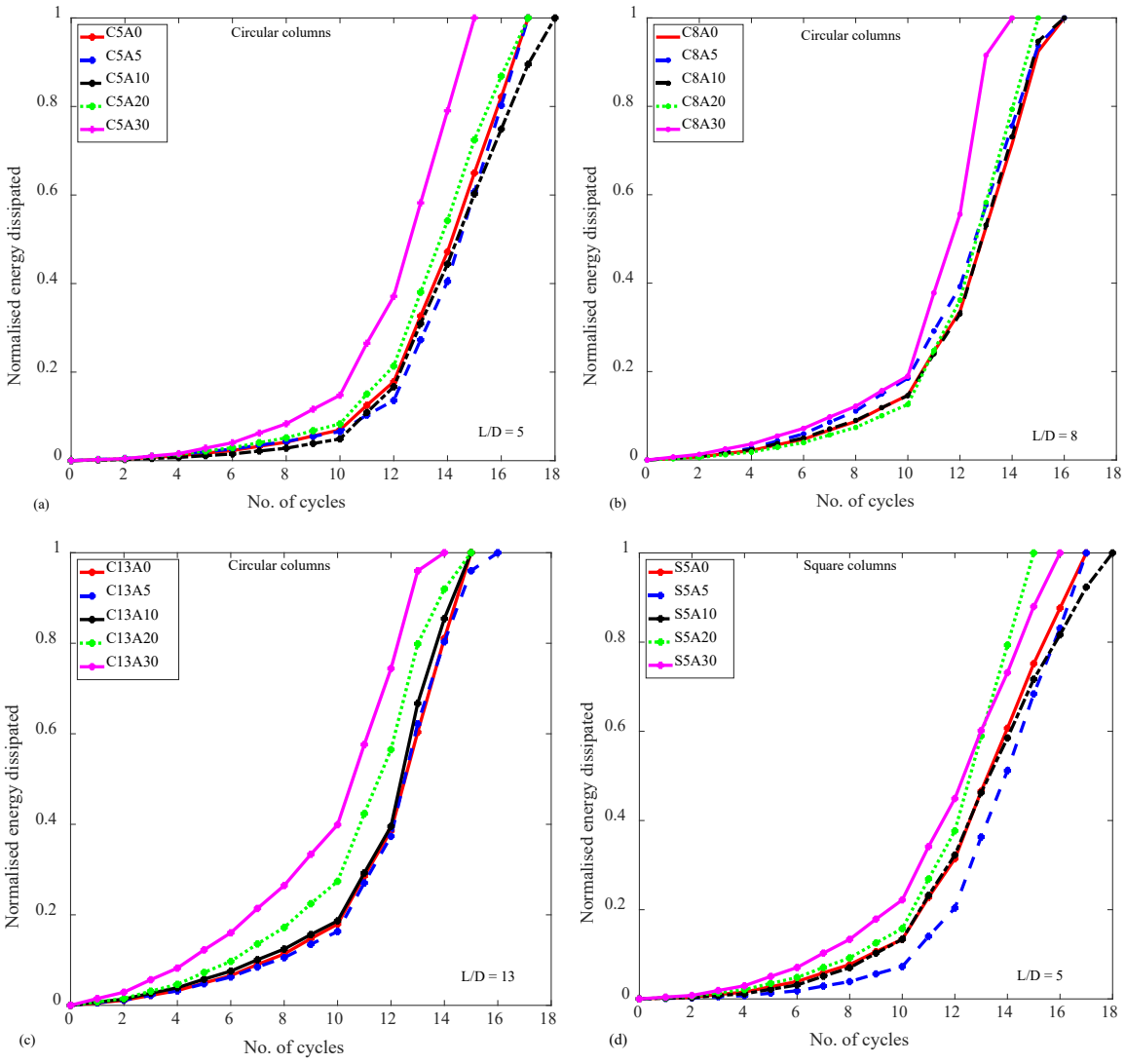

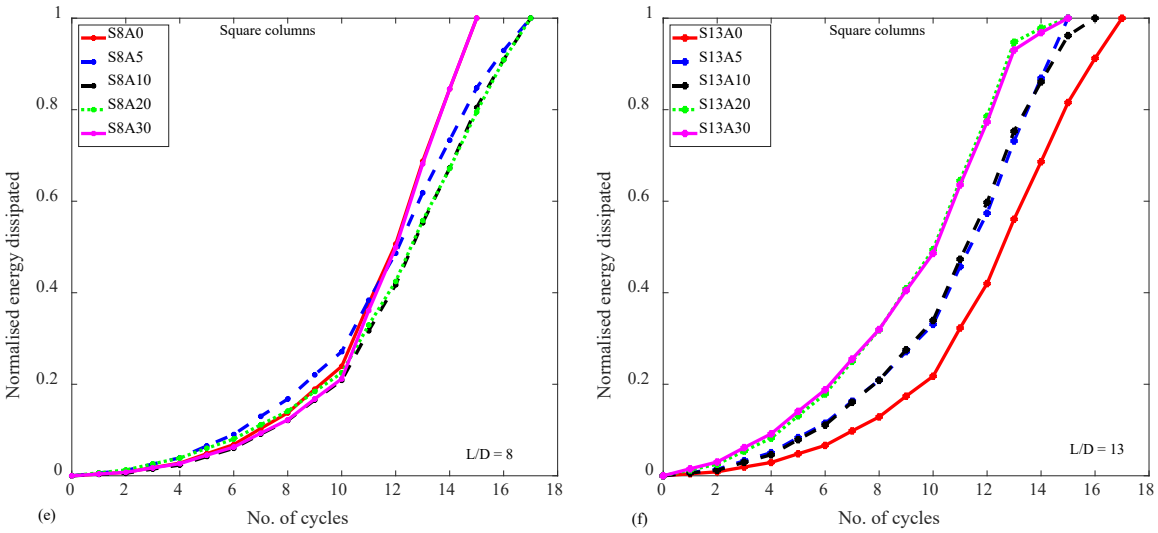


Figure 4.12: Normalised dissipated energy of the RC columns; circular (a) *L/D* = 5, (b) *L/D* = 8 and (c) *L/D* = 13; square (d) *L/D* = 5, (e) *L/D* = 8 and (f) *L/D* = 13

**Table 4.6. Variation in cumulative energy dissipation of RC columns with corrosion.**

| Sample details | Cumulative energy dissipated | Percentage dissipation energy loss | Sample details | Cumulative energy dissipated | Percentage dissipation energy loss |
|---|---|---|---|---|---|
| **C5A0** | 231.42 | 0 | **S5A0** | 197.57 | 0 |
| **C5A5** | 177.62 | 23.245 | **S5A5** | 151.06 | 23.542 |
| **C5A10** | 202.22 | 12.614 | **S5A10** | 174.77 | 11.540 |
| **C5A20** | 168.06 | 27.376 | **S5A20** | 105.83 | 46.435 |
| **C5A30** | 122.68 | 46.988 | **S5A30** | 134.42 | 31.963 |
| **C8A0** | 155.29 | 0 | **S8A0** | 140.25 | 0 |
| **C8A5** | 166.10 | 6.961 | **S8A5** | 178.83 | -27.509 |
| **C8A10** | 126.48 | 18.554 | **S8A10** | 171.01 | -21.9324 |
| **C8A20** | 119.66 | 22.944 | **S8A20** | 167.62 | -19.521 |
| **C8A30** | 45.46 | 70.724 | **S8A30** | 106.62 | 23.97699 |
| **C13A0** | 129.08 | 0 | **S13A0** | 177.82 | 0 |
| **C13A5** | 102.37 | 20.697 | **S13A5** | 152.62 | 14.17202 |
| **C13A10** | 89.71 | 30.502 | **S13A10** | 147.97 | 16.7868 |
| **C13A20** | 90.45 | 29.929 | **S13A20** | 129.39 | 27.23374 |
| **C13A30** | 67.40 | 47.785 | **S13A30** | 112.76 | 36.59005 |

Table 4.6 shows the percentage variation of the cumulative energy dissipated by each corroded column to the uncorroded column. The percentage reductions in the cumulative energy dissipated by the highly confined circular columns are 23.2%, 12.6%, 27.4% and 47% for the 5%, 10%, 20% and 30%, respectively. A similar trend was observed in the highly confined square columns, with the reductions varying between 11.5% and 46.4% between the uncorroded and corroded columns. Like the highly confined columns, the mediumly and lowly confined columns also had varying degrees of reductions in their cumulative energy dissipated relative to the corrosion mass loss and the level of confinements.

### 4.5.5 Impact of corrosion on buckling of vertical reinforcement

Corrosion generally reduces the cross-sectional area of the bars available to sustain the applied load (Kashani, 2017). This reduction becomes more severe in bars with pitting corrosion, resulting in localised reduction in the cross-sectional areas of the bars, leading to rebar fracture and localised buckling (Kashani et al., 2013a). The results of the tests on the corroded columns showed that the pitting effect is more significant, as it leads to the buckling mechanism and reduction in the load-carrying capacity of the column. Longitudinal bars in columns with $L/D$ = 5 confinement (Fig. 4.13(a-c)) had less noticeable buckling failure, especially in the circular columns and at lower corrosion degrees than bars from the $L/D$ = 8 and $L/D$ = 13 configurations (Kashani et al., 2013b; Kashani, 2017). This buckling from the columns with $L/D$ = 5 (Fig. 4.13(d)) rebars at higher corrosion levels results from the unsymmetrical cross-sections arising from the pitting corrosion, causing imperfections in the bar and leading to additional bending moment and local stresses at the pitted sections (Kashani et al., 2013a; Kashani et al., 2013b). Meanwhile, the buckling from the columns with $L/D$ = 8 and $L/D$ = 13 results from the combination of pitting corrosion and inadequate confinement provisions leading to premature yielding and squashing of the weakest section even at lower corrosion degrees (Kashani et al., 2015). Those columns with more uniformly distributed corrosion and a relatively small mass loss showed similar behaviour to those with uncorroded bars with a more visible buckling at higher compressive load (Kashani et al., 2013b).

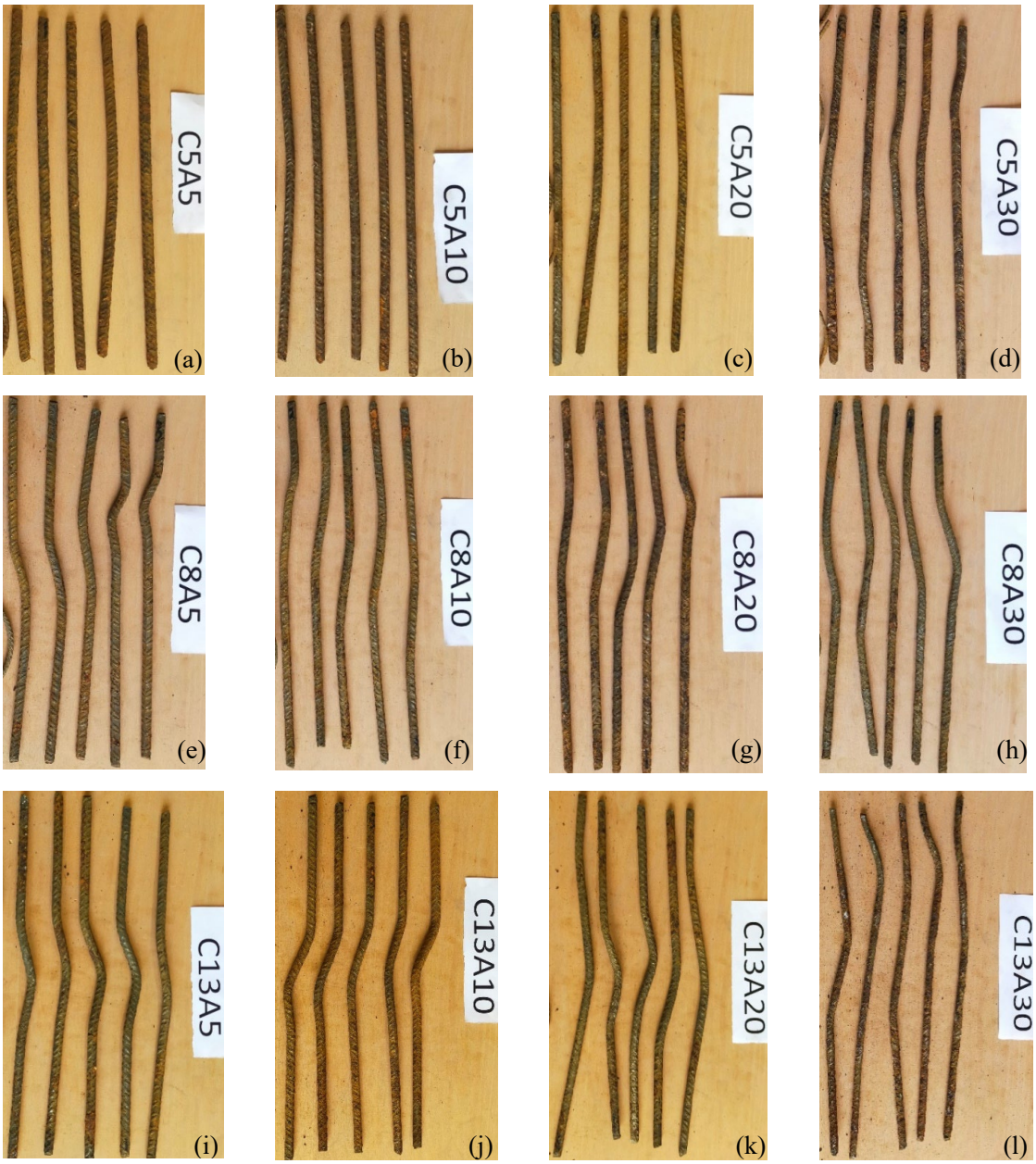


Figure 4.13: Observed buckling failure of the longitudinal reinforcement in the circular columns; *L/D* = 5 (a-d), *L/D* = 8 (e-h) and *L/D* = 13 (i-l)

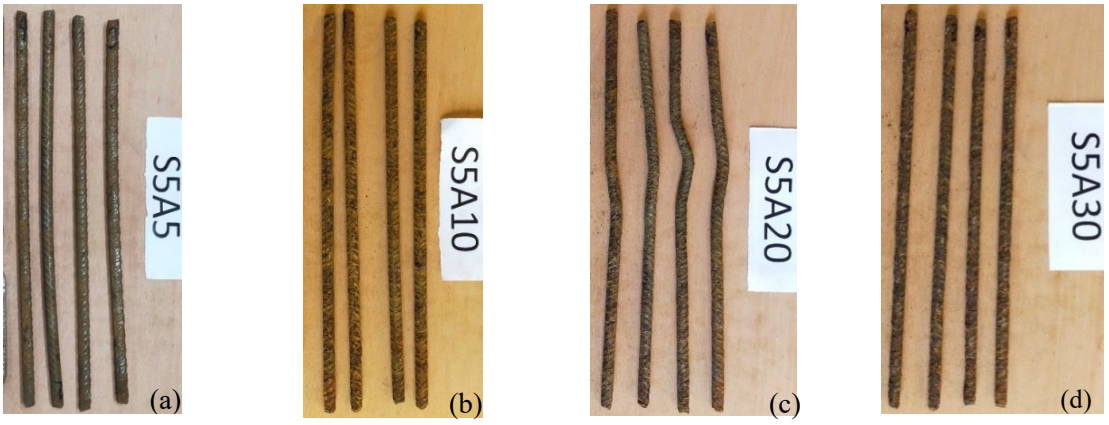

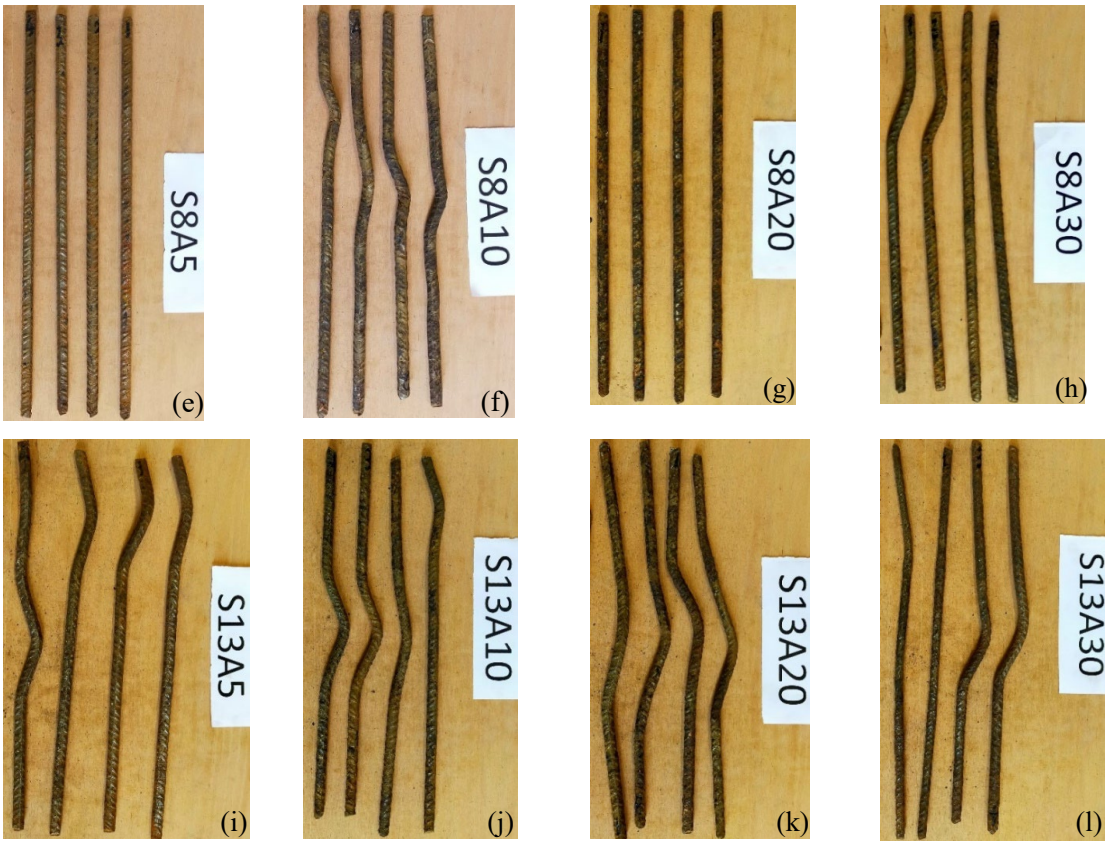


Figure 4.14: Observed buckling failure of the longitudinal reinforcement in the square columns; *L/D* = 5 (a-d), *L/D* = 8 (e-h) and *L/D* = 13 (i-l)

### 4.5.6 Impact of corrosion on the strength and strain of confined RC column

The strength loss resulting from the corrosion and confinement ratios of the RC columns is determined by normalising the ultimate strength of the corroded columns ($\sigma_{u_{corr}}$), to the ultimate strength of the pristine columns ($\sigma_{u_{pristine}}$). The normalised ultimate strength loss of the different confined RC columns is plotted relative to the percentage of corrosion mass loss. Afterwards, linear trend lines are fitted to the test data to estimate the strength reduction due to corrosion and confinement ratios. The R-square goodness of fit values obtained from the trend lines ranges from 0.78 to 0.96 for the circular columns at different confinement ratios (Fig. 4.15(a)), while the variation for the square columns is from 0.84 to 0.95 (Fig. 4.15(b)).

The ultimate strength of the confined corroded RC columns is reduced with an increase in the confinement degree and corrosion mass loss. For example, the well-confined circular columns with *L/D* = 5 (Fig. 4.15(a)) have a strength reduction range of 13.1%, 22.5%, 25.8% and 37.3% for the 4.4%, 5.2%, 14.4% and 19.1% corrosion mass loss, respectively. Also, the well-confined square columns with *L/D* = 5 (Fig. 4.15(b)) have a strength reduction range of 13.1%, 18.3%, 24.8% and 31.4% for the 4.3%, 5.7%, 12.1% and 15.9% corrosion mass loss, respectively. A similar trend is

also observed in the mediumly confined (*L/D* = 8) and sparsely confined (*L/D* = 13) columns. The strength reduction increases with increased corrosion mass losses in the circular and square columns.

The axial strain variation of the confined RC columns to corrosion loss was also investigated by normalising the ultimate strain of the corroded columns ($\epsilon_{u_{corr}}$), to the ultimate strain of the pristine columns ($\epsilon_{u_{pristine}}$). Figures 4.15(c) and (d) show the circular and square column plots. The plot of the circular columns (Fig. 4.15(c)) generally indicates a reduction in the ultimate strain with an increase in the corrosion and confinement levels, except in some columns in the medium and low, confined ranges with ultimate strain greater than their corresponding pristine column. This results from the failure of the GFRP ends, reducing the uncorroded columns' capacity under load.

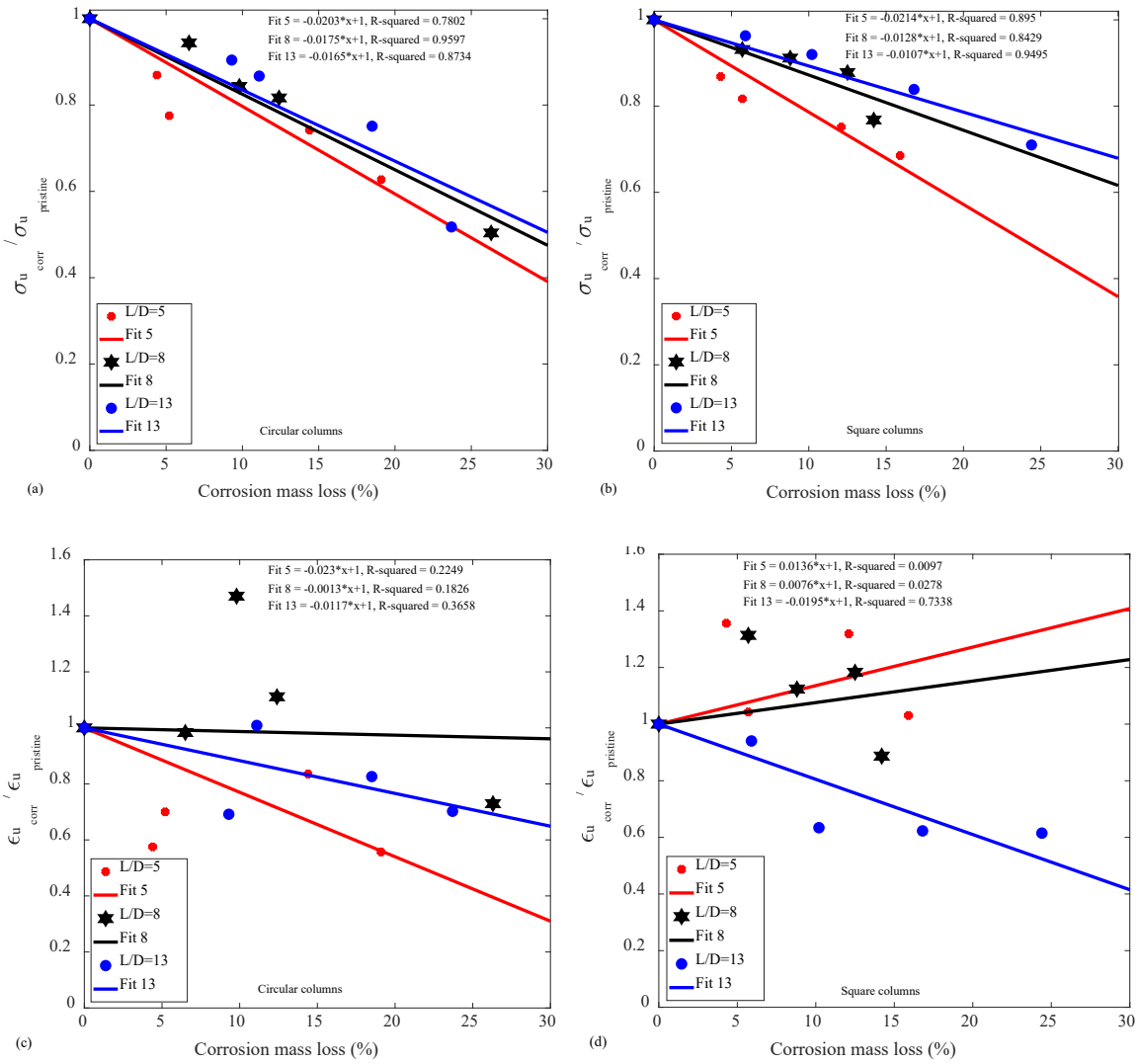


Figure 4.15: The variation of stress and strain with corrosion of confined RC columns; strength (a-b) and strain (c-d)

## 4.6 Comparison of the response of circular and square RC columns

Figure 4.16 (a-o) compares the normalised stress-strain response of the circular and square RC columns with similar confinement configurations and corrosion mass losses. First, the axial stress resulting from the loading of the columns is normalised against the ultimate strength of each column and plotted against the corresponding axial strain values. The columns show similar responses and stiffness within the elastic region until the peak strength is reached. Afterwards, the corrosion and confinement resulted in a loss of stiffness and reduced ductility of the RC columns (Liang & Sritharan, 2018; Vu et al., 2017).

Generally, the highly confined columns (*L/D* = 5) at the lower corrosion mass loss have a higher ductility (especially the square columns) than columns in the mediumly confined (*L/D* = 8) and lowly confined (*L/D* =13) at the same corrosion levels. This behaviour is observed to be the same in the columns within the same configurations as the corrosion level increases. Furthermore, the columns' ductility was reduced with increased confinement levels in all the columns (Hoshikuma et al., 1997; Mander et al., 1988; Saatcioglu & Razvi, 1992).

The circular columns have a higher ultimate strain corresponding to the maximum strength of the columns (Figs. 18(a-l, m-o)) than the square columns except in some of the lowly confined columns (Figs. 18(k and l)). This results from the uniform confinement of the circular columns, which gives rise to a constant stress distribution of the concrete along the cross-section (Ayough et al., 2021; Colajanni et al., 2014; Liang et al., 2015; Liang & Sritharan, 2018). In contrast, the square columns have their stress concentration at the edges, which in some cases led to the failure of the GFRPs.

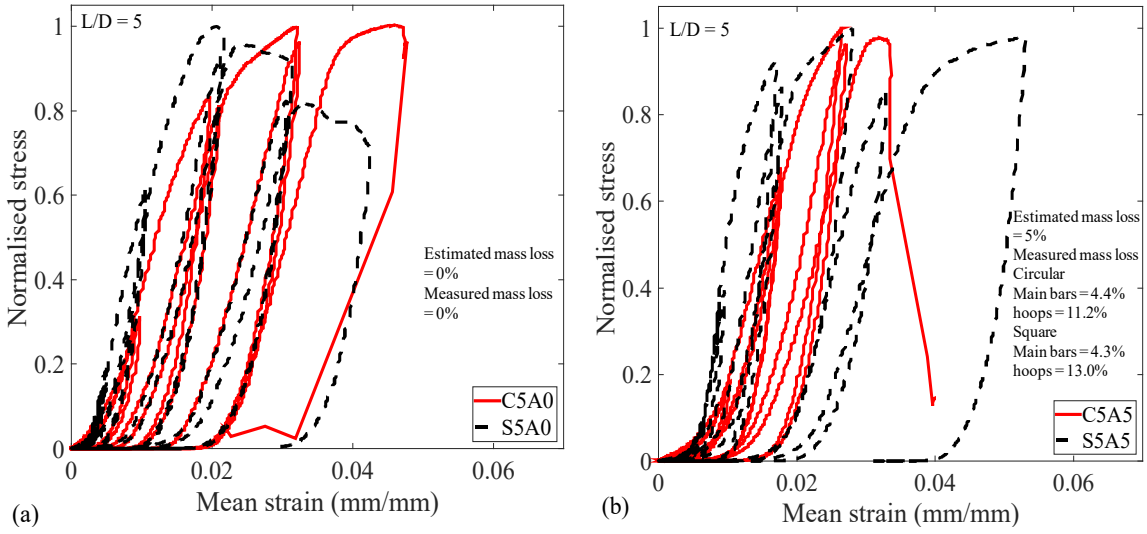

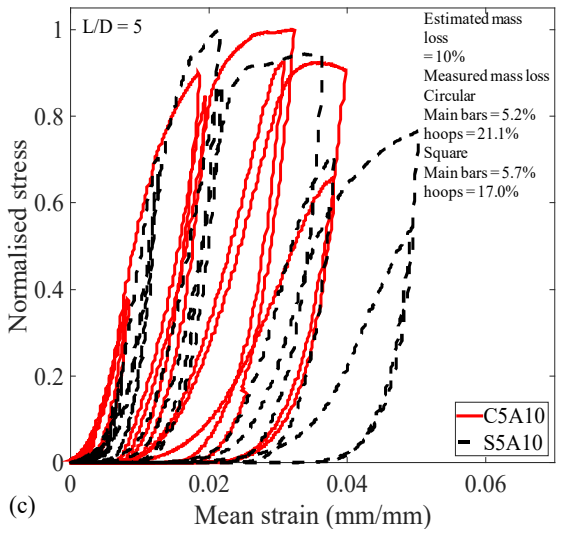
L/D = 5
Estimated mass loss = 10%
Measured mass loss
Circular
Main bars = 5.2%
hoops = 21.1%
Square
Main bars = 5.7%
hoops = 17.0%
C5A10
S5A10
Normalised stress
Mean strain (mm/mm)

(c)

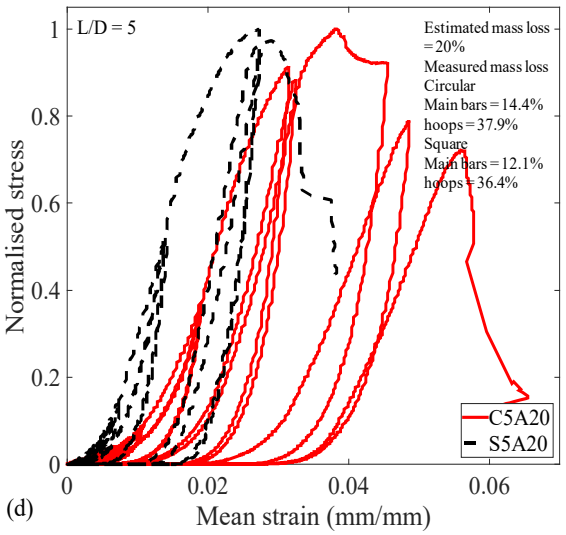
L/D = 5
Estimated mass loss = 20%
Measured mass loss
Circular
Main bars = 14.4%
hoops = 37.9%
Square
Main bars = 12.1%
hoops = 36.4%
C5A20
S5A20
Normalised stress
Mean strain (mm/mm)

(d)

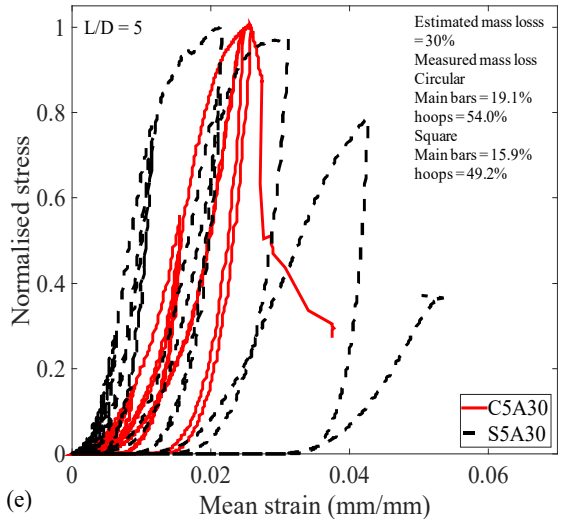
L/D = 5
Estimated mass losss = 30%
Measured mass loss
Circular
Main bars = 19.1%
hoops = 54.0%
Square
Main bars = 15.9%
hoops = 49.2%
C5A30
S5A30
Normalised stress
Mean strain (mm/mm)

(e)

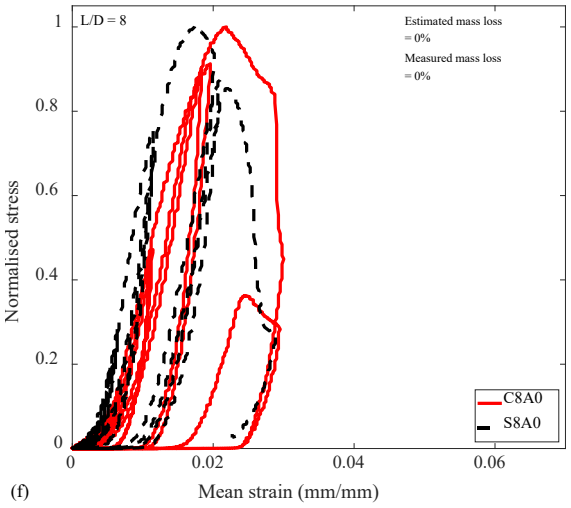
L/D = 8
Estimated mass loss = 0%
Measured mass loss = 0%
C8A0
S8A0
Normalised stress
Mean strain (mm/mm)

(f)

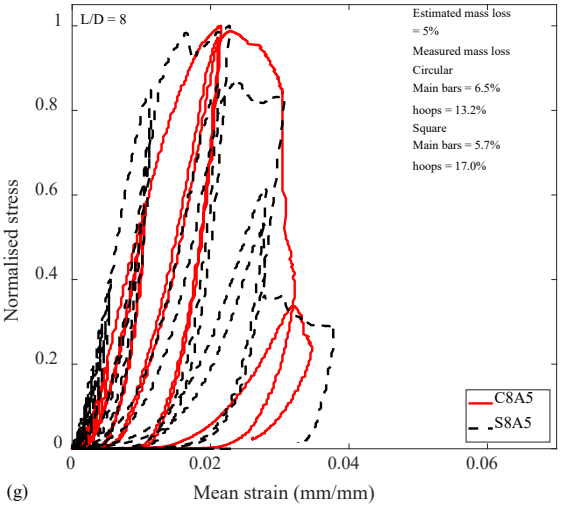
L/D = 8
Estimated mass loss = 5%
Measured mass loss
Circular
Main bars = 6.5%
hoops = 13.2%
Square
Main bars = 5.7%
hoops = 17.0%
C8A5
S8A5
Normalised stress
Mean strain (mm/mm)

(g)

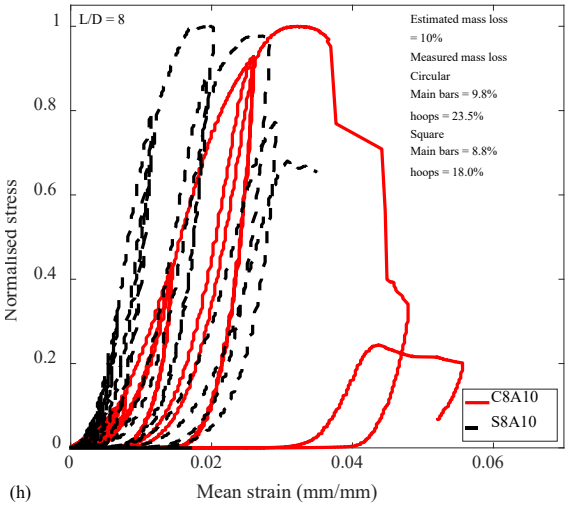
L/D = 8
Estimated mass loss = 10%
Measured mass loss
Circular
Main bars = 9.8%
hoops = 23.5%
Square
Main bars = 8.8%
hoops = 18.0%
C8A10
S8A10
Normalised stress
Mean strain (mm/mm)

(h)

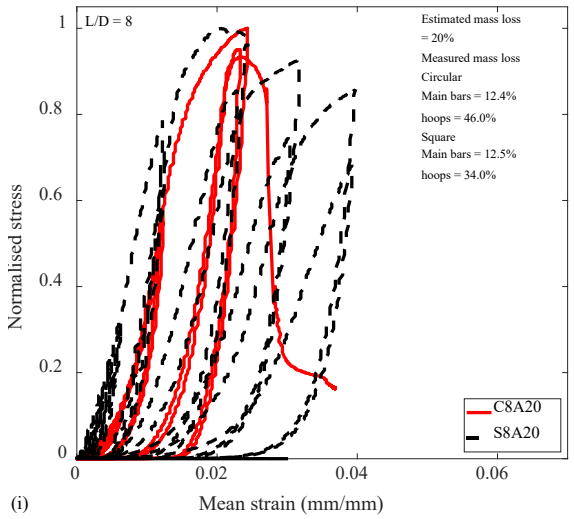
L/D = 8
Estimated mass loss = 20%
Measured mass loss
Circular
Main bars = 12.4%
hoops = 46.0%
Square
Main bars = 12.5%
hoops = 34.0%
C8A20
S8A20
Normalised stress
Mean strain (mm/mm)

(i)

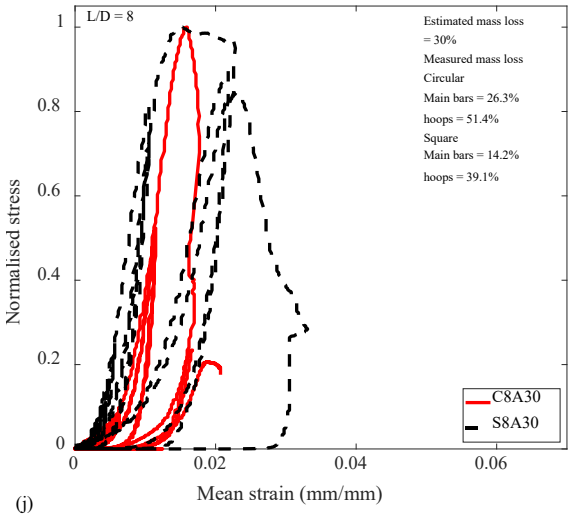
L/D = 8
Estimated mass loss = 30%
Measured mass loss
Circular
Main bars = 26.3%
hoops = 51.4%
Square
Main bars = 14.2%
hoops = 39.1%
C8A30
S8A30
Normalised stress
Mean strain (mm/mm)

(j)

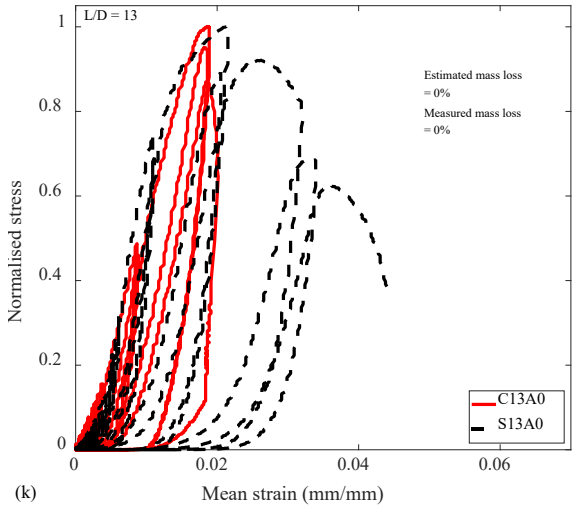
L/D = 13
Estimated mass loss = 0%
Measured mass loss = 0%
C13A0
S13A0
Normalised stress
Mean strain (mm/mm)

(k)

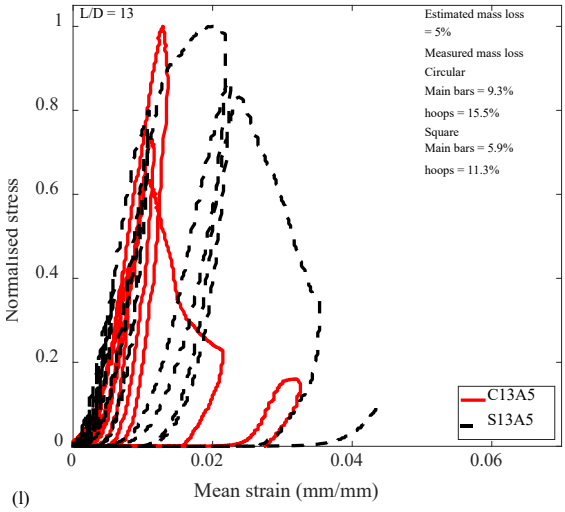
L/D = 13
Estimated mass loss = 5%
Measured mass loss
Circular
Main bars = 9.3%
hoops = 15.5%
Square
Main bars = 5.9%
hoops = 11.3%
C13A5
S13A5
Normalised stress
Mean strain (mm/mm)

(l)

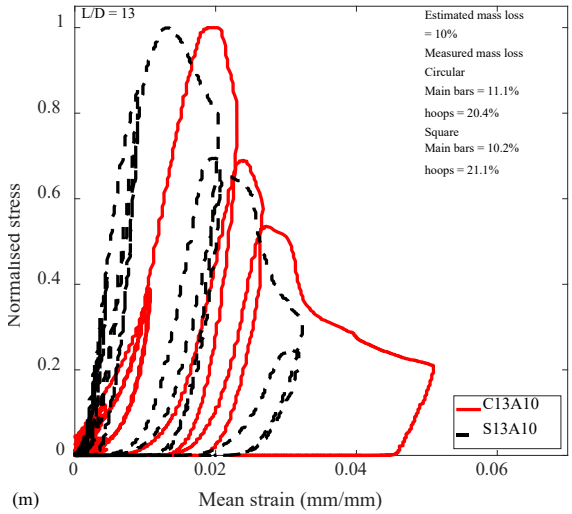
L/D = 13
Estimated mass loss = 10%
Measured mass loss
Circular
Main bars = 11.1%
hoops = 20.4%
Square
Main bars = 10.2%
hoops = 21.1%
C13A10
S13A10
Normalised stress
Mean strain (mm/mm)

(m)

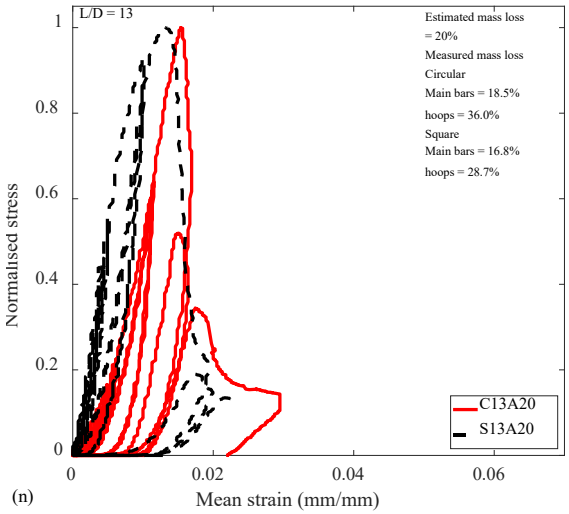
L/D = 13
Estimated mass loss = 20%
Measured mass loss
Circular
Main bars = 18.5%
hoops = 36.0%
Square
Main bars = 16.8%
hoops = 28.7%
C13A20
S13A20
Normalised stress
Mean strain (mm/mm)

(n)

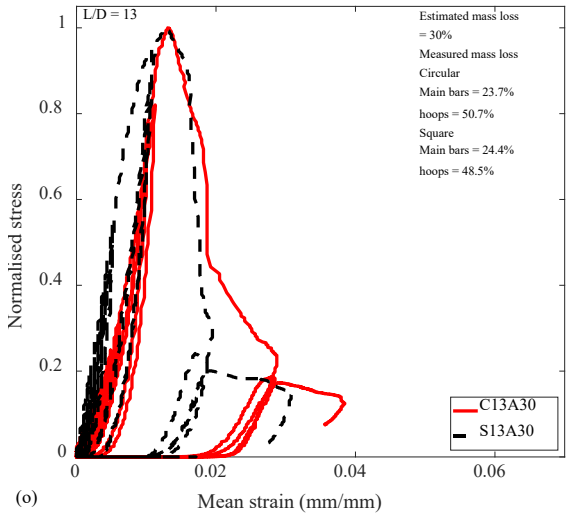


Figure 4.16: Comparison of the normalised stress response of circular and square columns with varying corrosion and confinement levels; *L/D*=5 (a-d), *L/D*=8 (e-h) and *L/D*=13(i-l)

## 4.7 Conclusions

Thirty RC column specimens with five reinforcement corrosion levels and three confinement configurations were tested under cyclic compressive load. Moreover, the relationship between the seismic behaviour, such as rebar corrosion loss ratio, ultimate strength, normalised dissipated energy and inelastic buckling of the rebar, was investigated. The following conclusions can be drawn from this study.

1. The circular columns have higher axial cyclic load-carrying capacities, gradually decreasing with increased corrosion and confinement than the square columns. The well-confined circular columns (*L/D*=5) have 41.32MPa, 35.93MPa, 32.04 MPa, 30.66 MPa and 25.92 MPa axial cyclic load carrying capacities for the 0%, 5%, 10%, 20% and 30% corrosion losses respectively. Meanwhile, the square columns with the same confinement and corrosion losses have 29.91MPa, 25.98MPa, 24.44MPa, 22.48MPa and 20.50MPa axial cyclic compressive load-carrying capacities. A similar trend was observed in the medium-confined and low-confined columns. This results from the effectiveness of the transverse ties in the circular column, which has more significant confinement effectiveness coefficients than the square columns.
2. The total energy dissipated by the RC columns reduced with increased levels of corrosion and confinement except in columns with reduced capacity due to failure of the GFRP ends. The energy dissipated by the columns at the lower loading cycles are similar until after the 10th cycle when the circular columns have more energy dissipated. This results from the

ineffective confinement of the square columns in comparison to the circular columns within the same configuration.

3. Corrosion of transverse confining steel affects the strength and deformability of confined concrete. The effectiveness of confinement reinforcements in confining the core concrete reduces as the corrosion increases. The strength of the highly confined circular column between the uncorroded and 30% corroded was decreased by about 37%, while the mediumly confined and lowly confined with the same corrosion mass loss were reduced by 50% and 48%, respectively.
4. Transverse reinforcement showed much higher vulnerability to chloride-induced deterioration than the respective longitudinal reinforcement in the RC columns. Consequently, the ultimate strength of the columns reduced as corrosion damage increased and confinement effectiveness diminished. Well-confined specimens showed a lesser loss in strength and deformability after corrosion than under-confined specimens.
5. With the strength and ductility losses experienced by old RC columns from the lack of adequate confinement and corrosion degradation, there is a need to improve their structural response with composite strengthening materials such as fibre-reinforced polymers and jacketing.

# Chapter 5 X-ray Computed Tomography (CT) Scan of corroded RC column

## 5.1 Introduction

The nonlinear stress-strain behaviour of low-strength concrete confined corroded RC columns under axial monotonic and axial cyclic compression loading was discussed in Chapters 3 and 4, respectively. It was found that corrosion and confinement affect the stress-strain response of RC columns, reducing the corroded RC columns' load-carrying capacity, ductility, stiffness and energy dissipation capacity. Furthermore, the inelastic buckling of the longitudinal bars is also affected by the confinement and corrosion of the reinforcement in the RC columns. Despite all this, the accurate measurement and location of corrosion, especially pitting or localised corrosion in RC, still pose a serious challenge to engineers and researchers. This chapter thus presents an investigation into the use of X-ray CT scan to estimate corrosion mass loss in RC column and the occurrence of corrosion on the bars in the columns.

## 5.2 Non-destructive investigation of corrosion loss in RC column

X-ray computed tomography (CT) scan is one of the newly introduced non-destructive non-contact techniques in assessing the behaviour and degradation of materials. The technique provides an insight into the inner structure, giving details of a sample's microstructure and macrostructure behaviour without breaking or destroying the specimen (Balázs et al., 2017). Furthermore, the CT image analysis grants three-dimensional (3D) quantitative information from the observations, contrary to most techniques requiring extrapolation from the two-dimensional analysis (de Mendonça Filho et al., 2021). This technique has been used extensively to investigate the degradation of concrete and mortar cement in the construction industry (González et al., 2018a, 2018b; González et al., 1996; Kong et al., 2020; Mínguez et al., 2019; Vicente et al., 2019; Vicente et al., 2021; Vicente et al., 2018).

X-ray CT scan technology has been used extensively in applications as diverse as metals, alloys, composite processing, and manufacturing industries to investigate the defects arising from the manufacturing process for quality control (Vicente et al., 2019). It is also combined with mechanical and thermal characterization tests to investigate the response of the materials to loadings and deformations. The data obtained from the X-ray CT scan is typically used to generate FE models that can be subsequently exported to the FEM software package for numerical

simulation and analysis of the results for comparison with experimental results (Vicente et al., 2019). It could also be used to show the crack distribution pattern inside a concrete specimen that has been subjected to one form of deformation or another.

This technique has been used extensively to investigate the degradation of concrete and mortar cement in the construction industry (González et al., 1996; Mínguez et al., 2019; Vicente et al., 2019; Vicente et al., 2018). In the last two decades, the use of X-ray CT scans in the concrete and construction industry to investigate the properties and behaviour of materials has intensified. For example, it has been used to investigate the different phases of concrete materials such as the cement matrix, aggregates composition, void spaces, water, cracks and also the fibres (Vicente et al., 2019) (Fig. 5.1).

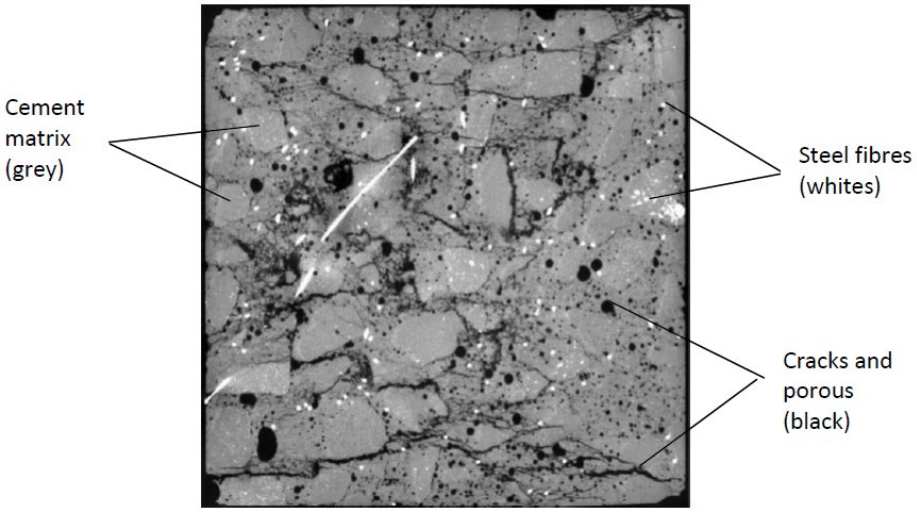


Figure 5.1: Steel-Fibre Reinforced Concrete specimen (Vicente et al., 2019)

RC is the most versatile material used in construction projects worldwide due to its component materials' availability and suitability for various construction applications (Yeomans, 2004). However, RC is affected by steel corrosion resulting from exposure to chloride ions and carbonation in marine and dry environments (Glass, 2003). Chloride-induced steel corrosion in RC structures destroys the passive film around the reinforcement, making it corrode and form rust, thereby introducing expansive stresses between the steel and concrete (Gao et al., 2017; Jiang et al., 2016), causing concrete cracking. This rust leads to the formation of both pitting and generalised corrosion of the steel reinforcement and a reduction in the cross-section of the geometry of the steel. This, in turn, results in the progressive deterioration of the concrete leading to the spalling of the cover concrete. Hence, it is imperative to understand better the reinforcement corrosion mechanisms to implement preventive measures and perform the more effective and efficient repair (Alhusain & Al-Mayah, 2021).

Additionally, a reliable inspection method is required at an early stage before the functionality of the RC structure is seriously damaged due to steel corrosion. The inspection method usually provides information about the current condition of the RC structures so that their future performance can be predicted (Zaki et al., 2015). Furthermore, the inspection method is almost a prerequisite for efficient and cost-effective rehabilitation of existing RC structures, especially in marine and seismic-prone regions susceptible to rapid corrosion damage. The inspection should be done without damaging the RC structures, both new and old ones (Zaki et al., 2015).

Corrosion loss consumes a considerable portion of the country's budget through either restoration measures or reconstruction. Therefore, there have been many investigations on the problems of concrete deterioration and the consequent corrosion of steel in concrete. To study the corrosion of reinforcement embedded in concrete, non-destructive testing (NDT) is often used. However, it usually provides qualitative assessments and lacks precision (e.g., half-cell potential and electrical resistivity) (Broomfield, 2007).

Several NDT methods have been used for monitoring the degradation of RC structures from steel corrosion. Some of these methods are visual inspection (Elsener et al., 2003), electrochemical methods (González et al., 2005; Koleva et al., 2007; Koleva et al., 2006; Poursaee, 2010; Rodrigues et al., 2021; Rodríguez et al., 1994; Shi et al., 2011; Song & Saraswathy, 2007), elastic wave methods (EW) (Sharma & Mukherjee, 2010, 2011, 2013), electromagnetic (EM) methods (Klewe et al., 2021; Lai et al., 2011; Sbartaï et al., 2007), optical sensing methods (OSM) (Fan et al., 2020; Hassan et al., 2012; Lv et al., 2017), and infrared thermography (IRT) (Baek et al., 2012; Doshvarpassand et al., 2019; Fan & Shi, 2022; Kwon et al., 2011; Poelman et al., 2020). These methods can show the existence and progress of deterioration of steel due to corrosion but are limited in establishing the surface discontinuity of the steel reinforcement. In addition, the methods do not accurately estimate the rebar mass loss resulting from corrosion and the location of the most critical areas for strengthening.

Furthermore, several numerical models have been used to predict the occurrence of corrosion in RC structures. However, these models lack accuracy and reliability in predicting the performance and life cycle analysis of RC structures due to the difficulties and complexities in estimating the corrosion of reinforcement in concrete (Kashani et al., 2019). Hence, a more accurate and less disruptive method is needed to quantify the corrosion loss while also identifying the location of more severe corrosion in RC structures.

### 5.2.1 Research Contribution and Novelty of this Chapter

Corrosion of steel in concrete is a significant cause of impaired safety and durability of infrastructure. As existing structures deteriorate over time due to corrosion, assessing the residual performance of RC structures accurately becomes imperative for engineers and managers to carry out safe, economical maintenance and rehabilitation operations (Chen et al., 2020). Unfortunately, it has been challenging to satisfactorily quantify the damage caused by corrosion in RC structures due to the difficulties in quantifying corrosion levels accurately and non-destructively. Hence, experimental studies usually use higher corrosion rates resulting in a change in corrosion morphologies and behaviour of the corrosion products (Chen et al., 2020; Wang et al., 2021).

Generally, the use of X-ray CT scans in the investigation of the reinforcement degradation in concrete is limited in the literature, with the few ones confined to the use of single bars in small concrete samples (de Mendonça Filho et al., 2021; Skarżyński et al., 2021; Skarżyński & Suchorzewski, 2018; Skarżyński & Tejchman, 2021; Van Steen et al., 2017; Vicente et al., 2019; Xi & Yang, 2019). However, this does not effectively represent the corrosion of steel reinforcement in a typical RC member. Most of the work in the literature on CT scanning of RC and concrete with material degradation was on cement mortar and concrete samples with single embedded bars without using whole reinforcement cages (Chandrasekaran, 2019; Lei et al., 2018; Skarżyński et al., 2021; Skarżyński et al., 2015). These works showed the close relationship between some of the corrosion models and the use of CT scans. However, it does not truly show the extent of corrosion in estimating the mass loss, as corrosion in RC is often not uniform. Thus, this research has investigated the use of CT scan data to examine the degradation of RC columns with the complete reinforcement cage embedded inside and estimated the corrosion mass loss of the entire reinforcement cage while also visualising the location of pitting corrosion on the transverse bars. Since the transverse bars provide the confinement needed by the columns to increase the structural behaviour, early identification of the location of pitting corrosion will aid in adequately strengthening the transverse bar positions on the RC column and prevent premature buckling and collapse of the structure.

## 5.3 X-ray CT scan process

The X-ray CT scan involves taking 2D images of a sample placed on a pedestal rotating at a central rotation axis through which multiple X-ray images are captured. Images are taken in the form of slices and recorded on a computer (Fig. 5.2). The slices are displayed as individual images or

stacked together. Afterwards, they are digitally reconstructed into 3D images for further analysis (Farber, 2019).

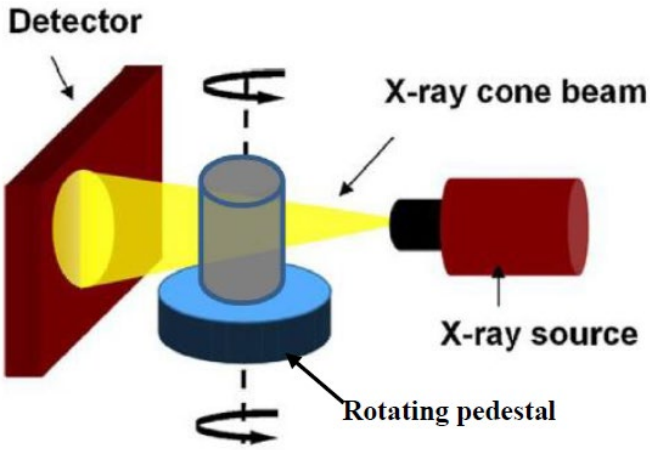


Figure 5.2: Typical CT-scan setup (Farber, 2019)

In CT scanning, the sample is rotated, and many 2D projection images (typically between 500 and 4000) are recorded during a full 360° rotation (du Plessis & Boshoff, 2019). After scanning, these images are used to compute (reconstruct) the volumetric dataset representing the sample. This reconstruction process is typically based on the Feldkamp back-projection algorithm, usually performed with software provided with the hardware (Feldkamp et al., 1984). The reconstructed data comprises a 3D grid of volumetric pixels (voxels) with brightness values related to the X-ray density of the material it represents. X-ray density is associated with physical density and atomic mass; therefore, a denser object will appear brighter in the CT data (du Plessis & Boshoff, 2019; du Plessis et al., 2017).

The basic procedure for X-ray CT scanning is highlighted below and shown in the workflow (Fig. 5.3) (Hermanek et al., 2018):

- X-ray generation, propagation and attenuation,
- signal detection and processing of scanned images
- reconstruction and
- post-processing of volumetric data

The outlined procedure was used to investigate the mass loss resulting from the corrosion of RC columns and is explained in section 5.4 of this thesis.

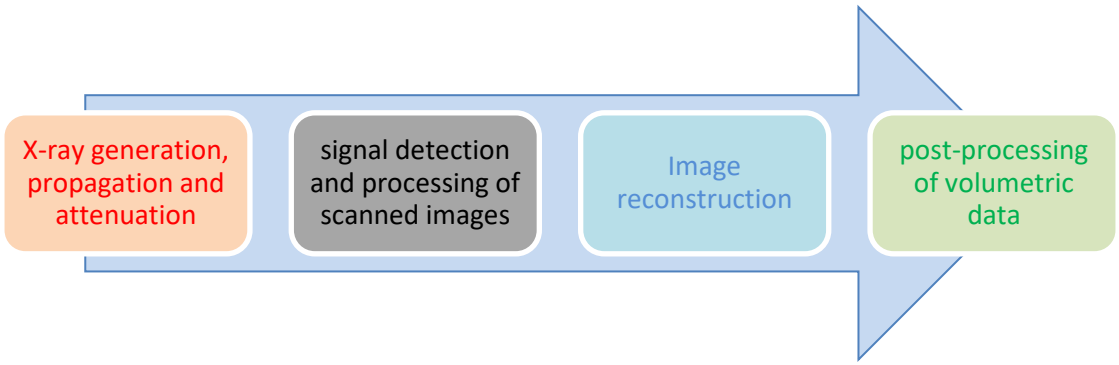


Figure 5.3: Schematic representation of a typical X-ray CT scanning workflow (Hermanek et al., 2018)

## 5.4 Sample preparation

### 5.4.1 Sample selection and preparation

Four RC columns (two circular and two square cross sections) were selected for the CT scan and other structural investigations. The RC columns were made with British standard B500B ribbed threaded steel bars, as shown in Figure 3.1(d). The cuboid samples have a 125 × 125 × 600mm dimension incorporating 4 No. 10mm diameter longitudinal bars, while the cylindrical samples (125mm diameter and 600mm long) have 5 No. 10mm longitudinal bars (Table 1). In addition, the columns have transverse bars in the middle 400mm zone spaced at 133.33mm, while the top and bottom (100mm) ends transverse bars were spaced at 25mm. This prevents localised failure from concentrated loading at the ends and ensures the failure occurs at the 400mm middle zone. Furthermore, both cross section type columns had 10% and 30% corrosion levels.

**Table 5.1: Reinforcements details**

| **Column type** | **Longitudinal reinforcement** | | **Transverse reinforcement** | |
|---|---|---|---|---|
| | **Diameter (mm)** | **Number in column** | **Diameter (mm)** | **Spacing (mm)** |
| **Circular** | 10 | 5 | 6 | 133.33 |
| **Square** | 10 | 4 | 6 | 133.33 |

The details of the tensile tests on the reinforcement and compressive strength tests on the concrete samples have been provided in the earlier part of the thesis in Chapters 3 and 4, respectively. Furthermore, the RC column samples were corroded using the accelerated corrosion

technique (described in Chapter 3). The result of the measured corrosion mass loss of the four RC columns after cleaning is presented in Table 5.2.

**Table 5.2: Measured mass loss from the accelerated corrosion process.**

| Specimen No. | Corrosion current density (mA/cm2) | Corrosion duration (days) | Estimated mass loss (Eq. 3.7) (%) | Measured mass loss of longitudinal bars (Eq. 3.8) (%) | Measured mass loss of transverse bars (Eq. 3.8) (%) |
|---|---|---|---|---|---|
| **C13A10** | 1.28 | 5.0 | 10 | 11.1 | 20.4 |
| **C13A30** | 1.28 | 15.0 | 30 | 23.7 | 50.7 |
| **S13A10** | 1.33 | 4.6 | 10 | 10.2 | 21.1 |
| **S13A30** | 1.33 | 13.9 | 30 | 24.4 | 48.5 |

## 5.5 X-ray CT scan of RC columns

Most of the work in the literature on CT scanning of RC and concrete with material degradation were on cement mortar and concrete samples with singly embedded bars, as discussed in section 2.6.1, without any on samples possessing whole reinforcement cages. Nevertheless, these works were able to show the close relation between some of the corrosion models and the use of CT scans. However, it does not truly show the extent of corrosion in estimating the volume loss as corrosion in RC is usually not uniform.

This research was carried out to investigate the use of CT scans to estimate the material degradation of RC samples with the whole reinforcement cage embedded. The scan was done at the Muvis (μ-VIS) X-Ray Imaging Centre, University of Southampton, using the custom 450/225 kVp Hutch CT system, equipped with a large, temperature-controlled walk-in scanning/testing bay ideal for large and heavy specimens. The high-energy 450 kVp source and 2000 × 2000 pixels flat panel detector enable sub-millimetre density measurements at the central regions of large or highly attenuating specimens.

The CT scanning technology is based on the fact that the material can attenuate the X-ray passing through it. The attenuation rate depends on the X-ray energy and the object's composition. The X-ray system generates a range of energy spectrum (polychromatic beam), and it is not attenuated uniformly when passing through an object (Xi & Yang, 2019). For example, when passing through

the centre area of the steel bar, the X-ray would be enhanced compared with that passing through the edges. As such, the edge of the steel bar in the reconstructed image has brighter voxels. The difference in the grey value of the voxels at different locations of the steel bar is not caused by the density of the material but by the technique itself; such an artefact is known as a beam hardening or cupping artefact (Šavija et al., 2015). The beam-hardening is impossible to eliminate but could be reduced by placing a surrounding metal as a filter between the X-ray source and the object. The filter can not only reduce the soft X-ray from the source but also reduce the scattering effect.

The RC samples used in this investigation were low levels of confinement with corrosion levels of 10% and 30% (two circular and two square cross sections) so that the effect of the corrosion on the reinforcements could be seen clearly in the scanned images. The samples were scanned in their pristine state to obtain the reference images and were further scanned after the corrosion to get the distorted images. The schematic CT scan setup is shown in Figure 5.2, and the image acquisition parameter was set up using the Inspect-X Control Software. First, the sample was positioned on the rotating pedestal to capture the best view of the region of interest. The image enhancer was afterwards turned off while the X-ray beam energy and intensity were adjusted until the detail in the darkest part of the image became visible (darkest pixels $>$10000). Next, the filter was applied to the image and adjusted to reduce beam hardening. Afterwards, the current and detector were modified so the X-ray beam did not introduce saturated grey levels in the images.

The scanning of the circular samples was much easier due to the shape of the sample as it rotates on the pedestal, while the square samples were not as easy to scan due to the cross-section and the sharp edges.

## 5.6 Processing the scanned images/data

### 5.6.1 2D image processing of the RC columns

The scanned images of the RC samples were recorded in the form of 2D slices having about 2886 images (stacks) with the Tagged Image File Format (.tiff, .tif) images in the vertical z-axis (Fig. 5.4(a – d)). The images are loaded using the virtual stack command on the workstation with less memory to load large data. These scanned images were subsequently imported into the image processing Imagej software (Rueden et al., 2017) to reconstruct the images into the 3D format for further processing. First, the image slices were adjusted so that the background's grey value was as close to zero (0) as possible to avoid images with uneven backgrounds. The thresholding (range

between 0 – 255, 0 for black and 255 for white) was afterwards used to adjust the brightness and saturation pixels of the images.

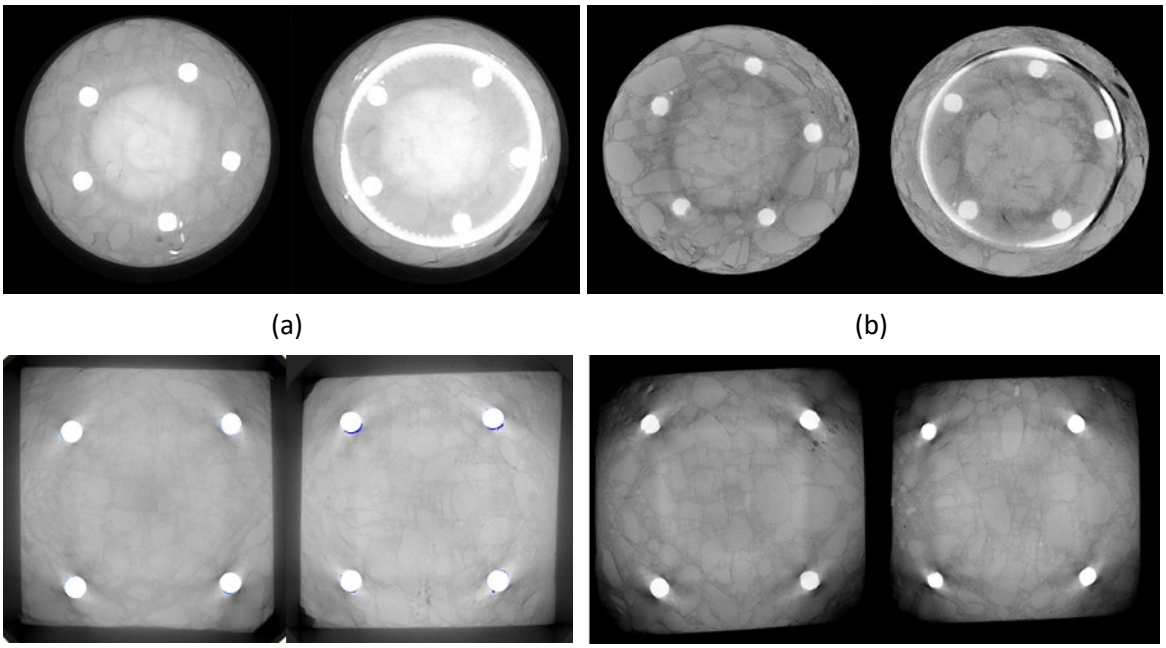

(a) (b)

(c) (d)

Figure 5.4: 2D CT scan image of the RC column; circular (a) before corrosion (b) after corrosion, square (c) before corrosion (d) after corrosion

### 5.6.2 3D image processing of the RC columns

The scanned images of the RC columns were imported into the image processing Imagej software (Rueden et al., 2017) as stacks of 2D images. The stacks menu was afterwards used to concatenate and reconstruct all the stacked images into the 3D format using the filtered back projection algorithm in the Inspect-X control software. Next, the images are filtered using the 3D filtering command to reduce the noise and enhance the 3D signal of the images. The filtered images are then discretised such that it comprises only black and white images.

By using the segmentation thresholds, the 3D images of the RC columns were separated into the reinforcement steel cage and the concrete component. Figure 5.5(a-d) shows the before and after corrosion images of the reinforcement cages separated from the concrete. Afterwards, the separated reinforcement cages were processed further to estimate the mass loss after the corrosion using a more robust 3D volumetric analysis software (Avizo). It should be noted that it was much easier to process the circular columns than the square columns due to the cross-section. Segmentation of the square columns presented some challenges as it was not easy to separate the reinforcements from the concrete due to beam hardening during the scanning process.

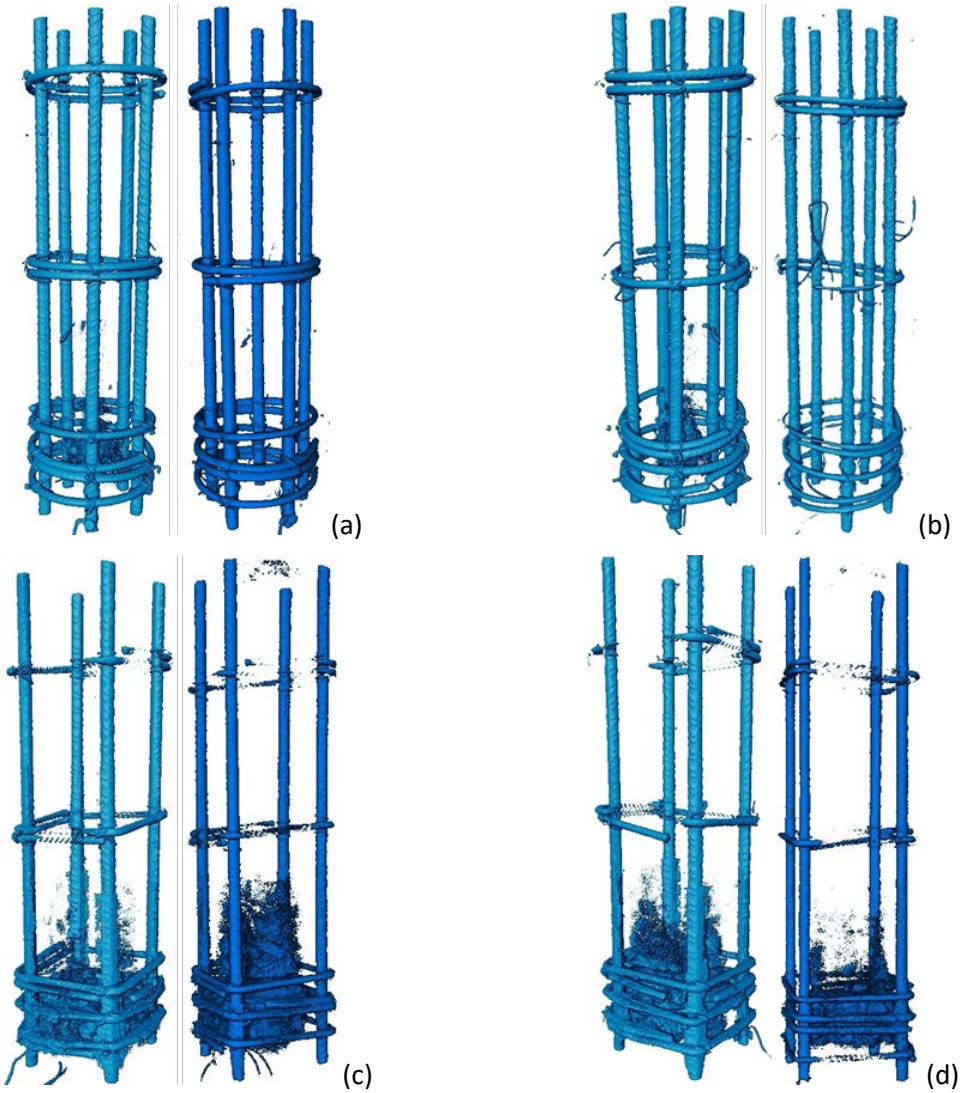


Figure 5.5: 3D CT scan image of the RC column; circular (a) 10% before and after corrosion, (b) 30% before and after corrosion, square (c) 10% before and after corrosion, (d) 30% before and after corrosion

### 5.6.3 Estimation of corrosion loss from CT scan images

The concatenated and reconstructed samples were processed further to estimate the mass loss resulting from the corrosion of the RC samples using the Thermo Scientific™ Avizo™ Software (Version 2020.1). The images were loaded as a file, and the interactive thresholding menu was used to separate the concrete from the reinforcement bars (Figures 9(a,b, e and f). The volume rendering settings and voxelised rendering commands were then applied to the data in the RC columns, which had been subject to a threshold, to view the samples for further refinement. The voxelised volume was further refined by using the fill holes, dilation, erosion, and remove small spots commands to remove small particles of concrete not removed by the thresholding process. Finally, the materials were estimated using the material statistics command. The material

statistics measured the voxel of the reinforcement's scanned images and converted it to measurement in pixels and volumes in cubic millimetres ($mm^3$).

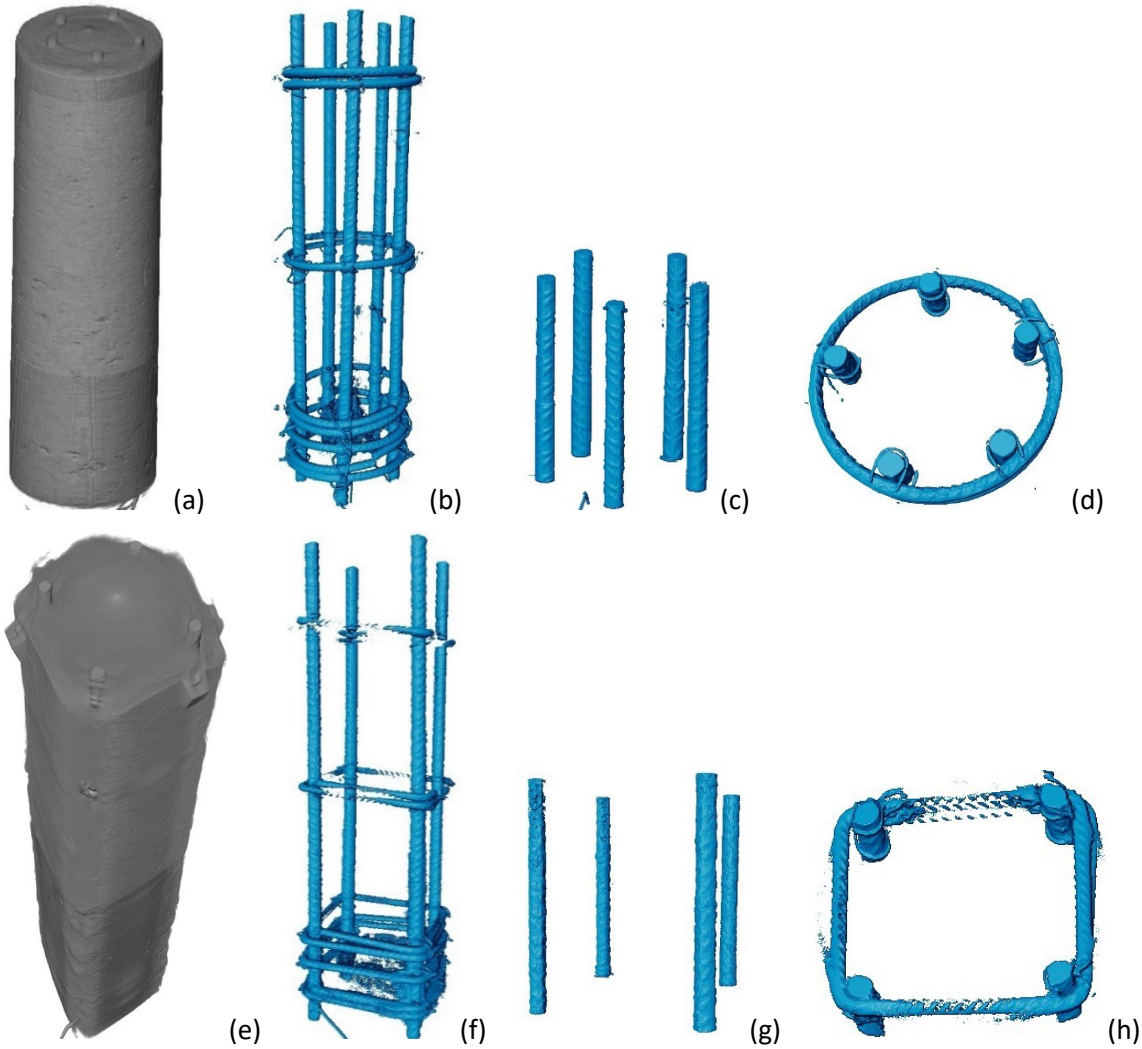


Figure 5.6: Corrosion estimation of extracted reinforcement bars; Circular columns (a – d) and square columns (e – h).

The measured mass loss of the longitudinal reinforcement bars corrosion is presented in Table 5.3. The mass loss was measured by cutting a sub-volume from the reinforcement bars to isolate the longitudinal bars from the transverse bars (Fig. 5.6 (c and g)). The mass loss showed an increase in the mass loss measured with the CT scan data than the actual measurement. The mass loss increased by 4.86% and 2.62% for the 10% and 30% corroded circular columns, respectively, while the square columns also increased by 8.04% and 9.63%, respectively. This increment is due to rust and concrete particles on the surface of the reinforcement bars. These rust and concrete particles were cleaned and brushed off the surface of the reinforcement bars in the actual measurement. Still, they were evident in the CT scan processed images, adding to the voxel measurement in the CT scan mass loss measurement.

**Table 5.3: Mass loss comparison between actual and CT scan of longitudinal bars**

| Specimen No. | Estimated mass loss (Eq. 7) (%) | Measured mass loss of longitudinal bars (Eq. 8) (%) | Measured mass loss CT scan longitudinal bars (%) | mass loss diff. (%) |
|---|---|---|---|---|
| **C13A10** | 10 | 11.1 | 11.64 | 4.86 |
| **C13A30** | 30 | 23.7 | 24.32 | 2.62 |
| **S13A10** | 10 | 10.2 | 11.02 | 8.04 |
| **S13A30** | 30 | 24.4 | 26.75 | 9.63 |

Similarly, the transverse reinforcements are isolated from the longitudinal bars by using the sub-volume command (Fig. 9(d and h)). Table 5 presents the estimated mass loss from the transverse reinforcements' CT scan compared to the measured mass loss. The mass loss difference is 0% and 1.85% for the 10% and 30%, respectively, for the corroded circular columns, while the 10% and 30% corroded square columns have 6.68% and 3.71% increments, respectively.

**Table 5.4: Mass loss comparison between actual and CT scan of transverse bars**

| Specimen No. | Estimated mass loss (Eq. 7) (%) | Measured mass loss of transverse bars (Eq. 8) (%) | Measured mass loss CT scan transverse bars (%) | Mass loss diff. (%) |
|---|---|---|---|---|
| **C13A10** | 10 | 20.4 | 20.40 | 0 |
| **C13A30** | 30 | 50.7 | 51.64 | 1.85 |
| **S13A10** | 10 | 21.1 | 22.51 | 6.68 |
| **S13A30** | 30 | 48.5 | 50.30 | 3.71 |

### 5.6.4 Identifying the location of pitting corrosion from CT scanned images

Pitting (localised) corrosion is considered, among others, as the primary degradation mechanism for most metals exposed to a corrosive environment. It can lead to accelerated failure/collapse of a structural member (Akpanyung & Loto, 2019; Frankel, 1998). Chloride is the most encountered aggressive agent, which causes the pitting of many metals. However, the pitting corrosion on steel reinforcement is not easily detected because of its microscopic nature (Akpanyung & Loto, 2019;

Burstein et al., 2004). On the other hand, transverse bars provide the needed confinement, increasing the ultimate strength and ductility of RC columns under load. Hence, the loss of the transverse bars results in the loss of the adequate confinement of the RC column and subsequently weakens the core concrete and ultimate load-carrying capacity of the RC column. Therefore, the early identification of the presence and position of the pitting could be used for the effective retrofitting and strengthening of the RC columns to prevent premature buckling and failure of the structure. Furthermore, the processed CT scan image also showed clearly, especially in the highly corroded (30%) samples (Fig. 5.7(b)), the location of the pitting corrosion on the transverse bars.

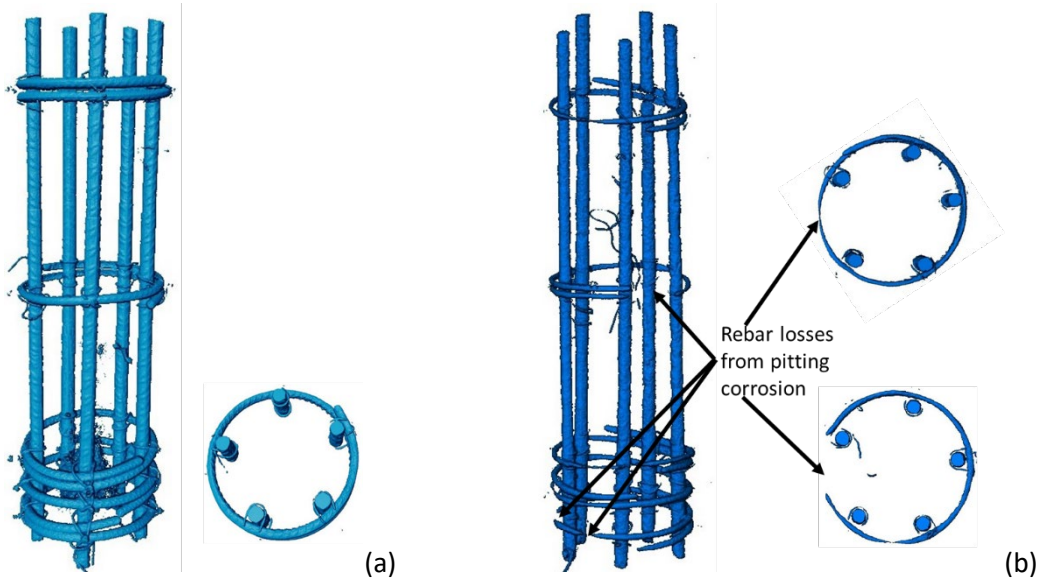


Figure 5.7: Reinforcement cages (a) Reference images (before corrosion) and (b) After corrosion showing pitting location

## 5.7 Structural testing of the RC columns

### 5.7.1 Stress-strain response of the RC columns

The stress-strain responses of the circular and square columns to the applied axial compressive load are presented in Fig. 5.8 (a-b). These stress-strain responses were plotted from the LVDTs data, since it shows the deformation of the 400mm middle zone section rather than the readings from the machine load cell that captures the deformation of the whole column under loading. The cyclic responses of the corroded columns under loading were compared with the corresponding behaviour of the non-corroded columns in each confinement configuration.

The RC column samples all have similar stress-strain responses under axial cyclic load. The deformation started with minor vertical cracks, which subsequently enlarged with further loading,

leading to spalling of the concrete cover as the longitudinal bars buckled due to lateral expansion of the RC columns. The observed cyclic responses of the RC columns are similar at the elastic range until yield and afterwards becomes nonlinear beyond the peak stress due to the corrosion and confinements of the rebars. The hysteretic curve of the corroded columns within each confinement's configuration was compared with the non-corroded ones. It showed a gradual decrease in the columns' strength, stiffness and ductility as the corrosion loss increased. The corrosion of longitudinal and transverse bars reduces the column's ultimate strength and load-carrying capacity.

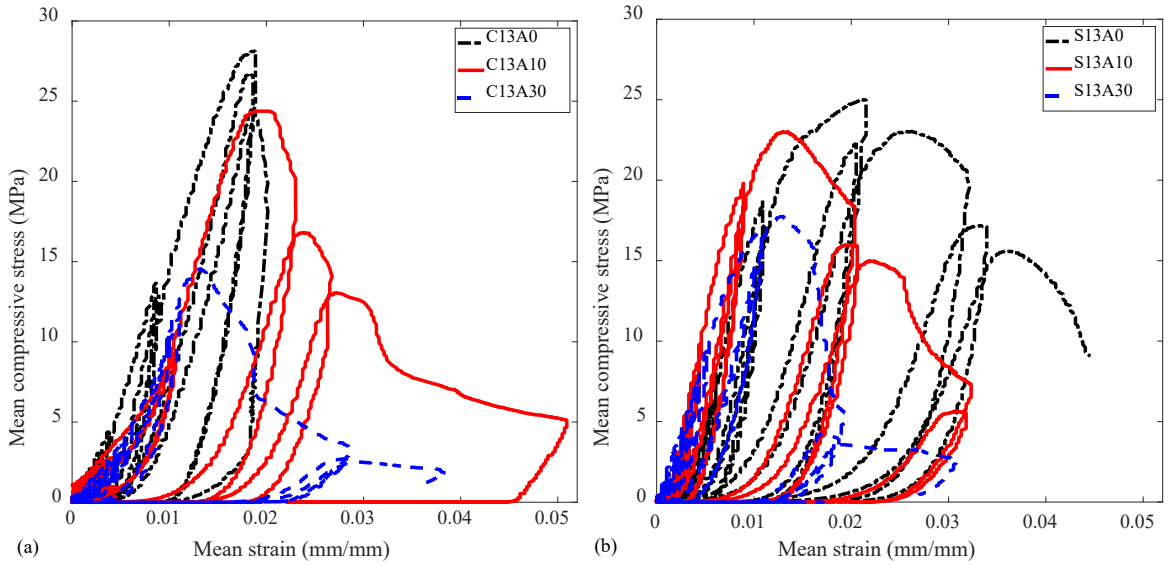


Figure 5.8: Axial cyclic compressive stress-strain response of RC columns; (a) circular and (b) square

The applied cyclic compressive load results in different failure modes of the RC columns (Fig. 5.9 (a-f)). The applied cyclic load led to concrete cover spalling and hence buckling of the longitudinal bars (Fig. 5.9(b)) and, in some cases, fracture of the transverse bar (Fig. 5.9(b)). The longitudinal bars buckled mostly at the expected middle 400mm zone, with some columns having shear buckling due to inadequate confinement (Fig. 5.9(a and c)), loss of confinement resulting from pitting corrosion (Fig. 5.9(c)) and the transverse bars' fracture (Fig. 5.9(e and f)).

(a) (b) (c) (d) (e) (f)

Figure 5.9: Observed failure modes of the RC columns after testing; circular (a-c) and square (d-f)

### 5.7.2 DIC images of corroded columns

The DIC tracks the RC columns' strain response and crack damage to the applied compressive load. Figure 5.10(a) shows the stress-strain response of the circular column with 10% estimated corrosion loss and the locations of the processed images (before yielding, at the ultimate load and beyond the ultimate load). The processed images within the column's middle zone section showed the column's strain contour with the cracks, spalling of the cover concrete and captured the buckling of the reinforcement. Figures 5.10(b - d) are the Von Mises strain processed from the captured images during loading. These values correspond to the strain estimated from the LVDTs at yield stress, ultimate stress and beyond the ultimate stress.

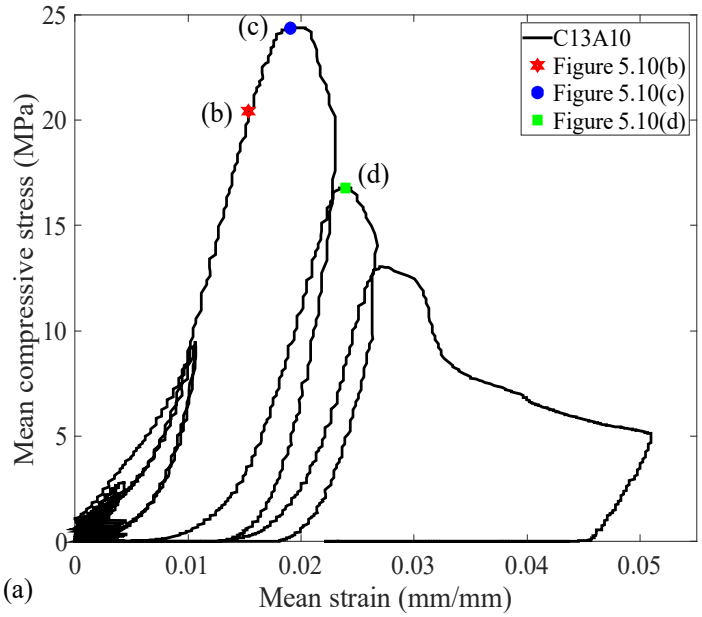


(a)

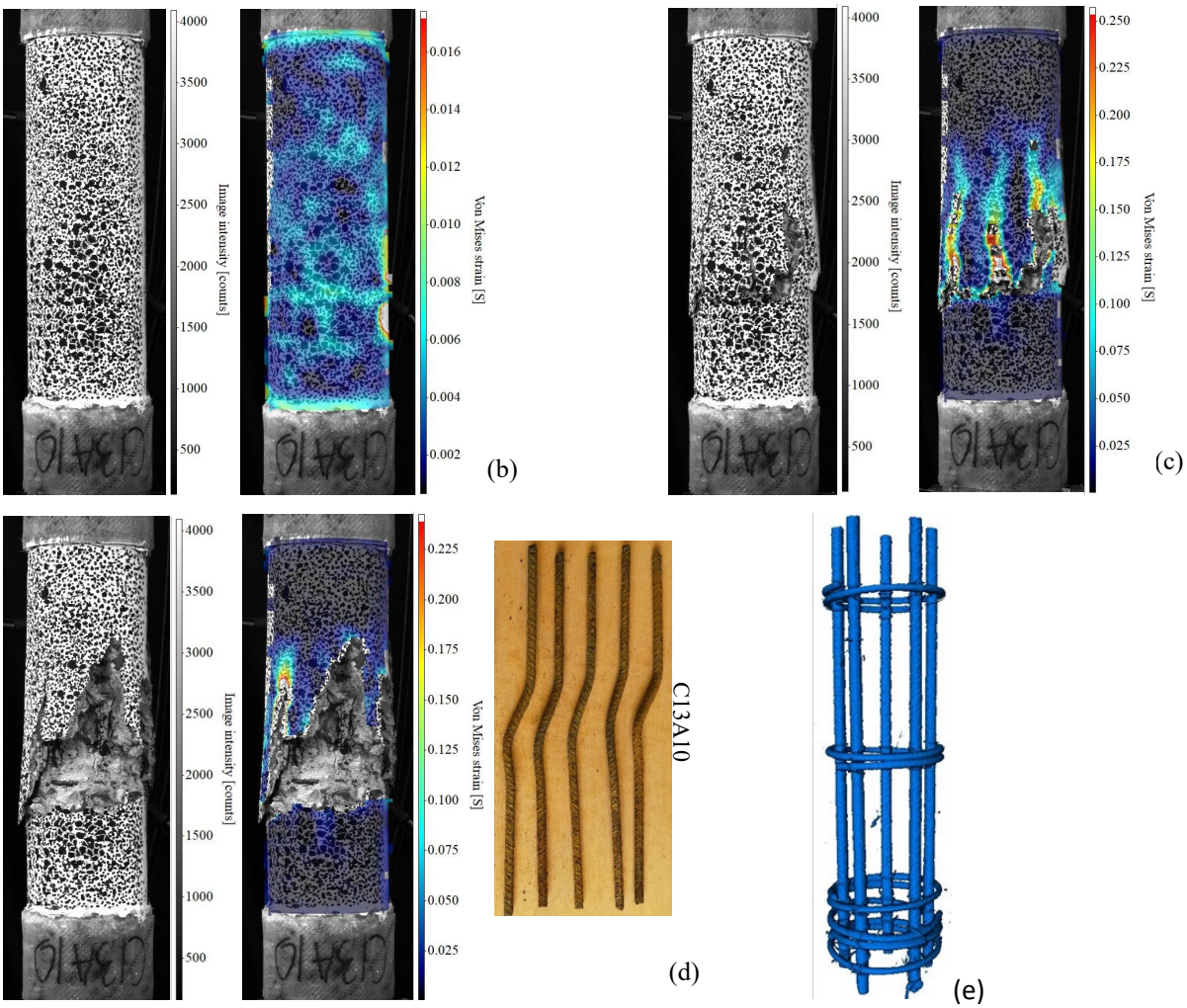


Figure 5.10: Processed DIC images of circular column (a) stress-strain response showing location of processed images (b) at yield stress, (c) at ultimate stress and (d) between ultimate stress and collapse with the rebar buckling at the end of the test (e) CT scan image of rebars at 10% corrosion mass loss

Similarly, the stress-strain response of the square RC column with an estimated 10% corrosion mass loss is presented in Figure 5.11(a), while the processed DIC images are shown in Figure 5.11(b - d). Figure 5.11(e) further indicates the state of the buckled longitudinal bars at the end of the test after removal and cleaning.

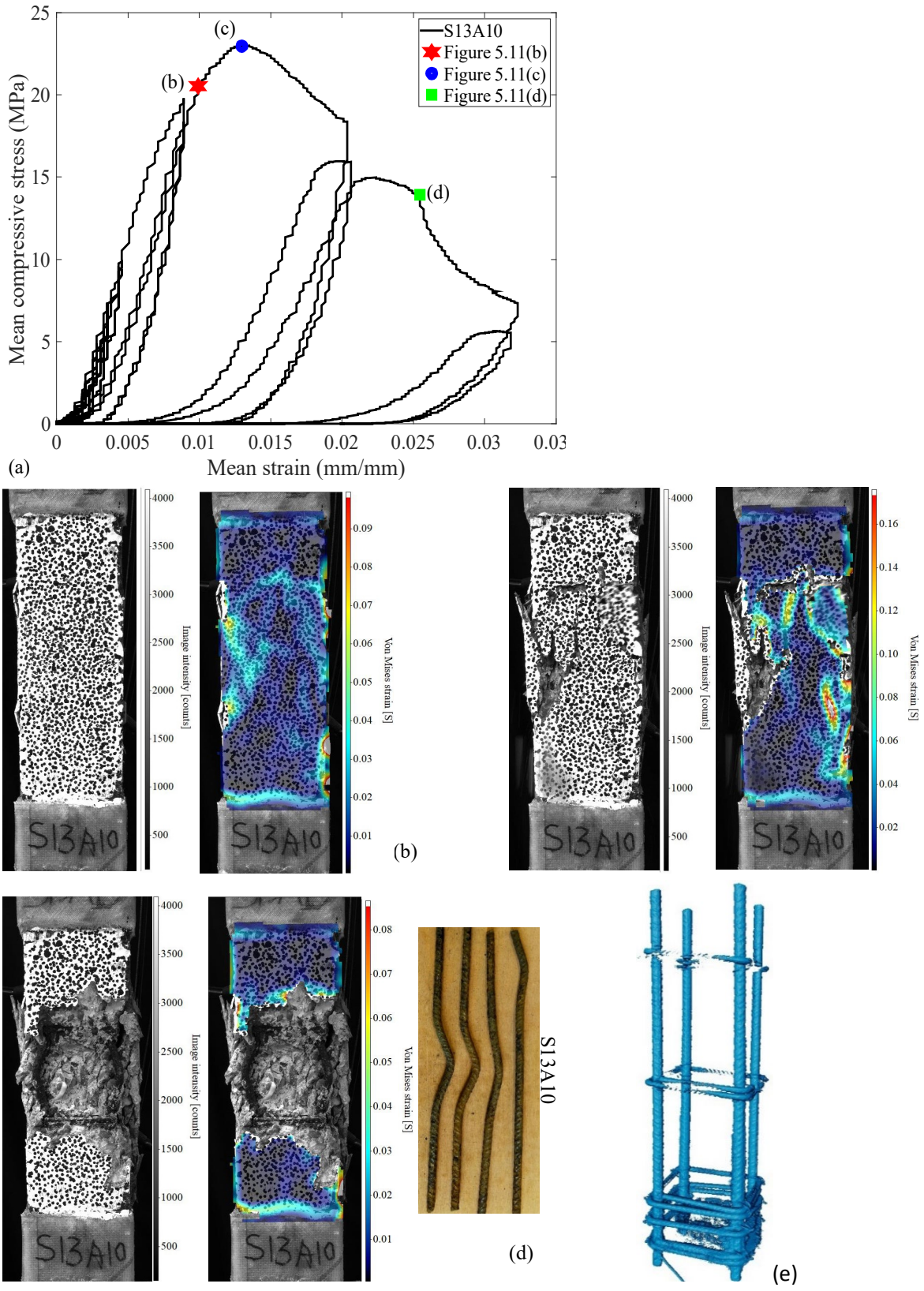


Figure 5.11: Processed DIC images of square column (a) stress-strain response showing location of processed images (b) at yield stress, (c) at ultimate stress and (d) between ultimate stress and collapse with the rebar buckling at the end of the test (e) CT scan image of rebars at 10% corrosion mass loss

### 5.7.3 Impact of corrosion on cumulative energy dissipation capacity of the RC columns

Experimental studies on the cyclic behaviour of corroded beams and columns (Akiyama et al., 2011; Ma et al., 2012; Ou et al., 2012) showed that buckling and/or fracture of corroded bars significantly affects the global response and plastic rotation capacity and plastic hinging mechanisms of the corroded RC elements. Consequently, in the seismic assessment and evaluation of existing corroded structures, consideration needs to be given to the buckling of the reinforcement bars, even if the structure is designed initially to have sufficient confinement reinforcement.

The plots of the normalised accumulated hysteretic energy versus the number of cycles are presented in Figure 5.12. Figure 12(a-b) shows the influence of corrosion on the accumulated energy dissipation of circular and square RC columns with different corrosion mass loss. The plots showed similar behaviour for all the columns with very low energy dissipated at the smaller cycles and a steep increase in the dissipated energy after the 10th cycle. The steep increase in the dissipated energy is more significant at high corrosion in both the circular and square columns.

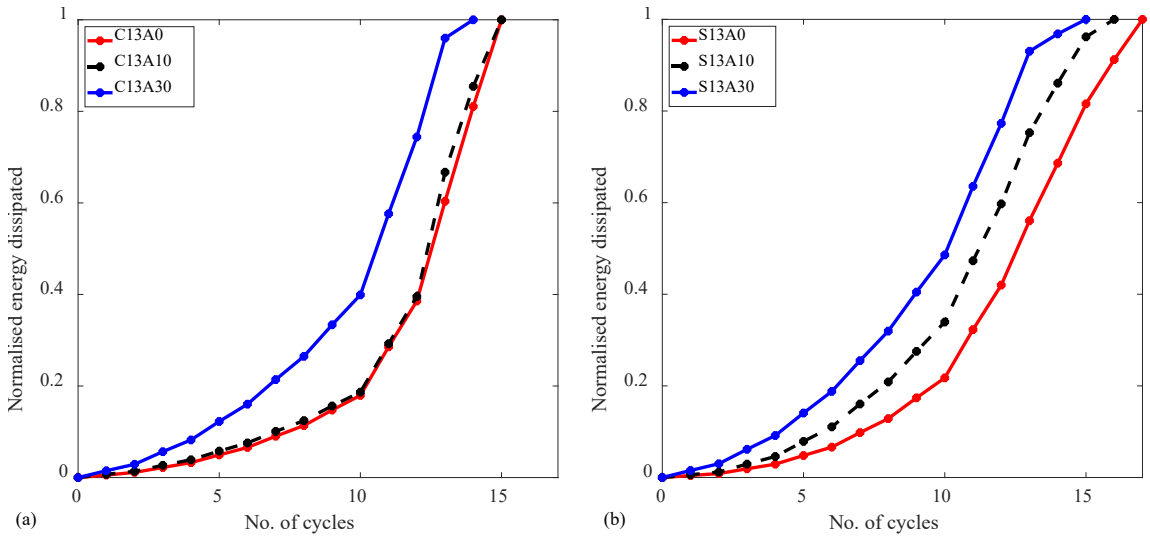


Figure 5.12: Normalised dissipated energy of the RC columns; (a) circulars and (b) squares

## 5.8 Conclusions

The CT scan of RC was briefly investigated to understand the process involved and the previous work related to RC samples. It was discovered that a lot of work has been done on concrete and concrete-related materials. The few works done on RC had been on small samples with fibres or single-embedded rebars. There is presently no work in the literature on scanned RC elements with the whole reinforcement cage embedded. This work investigated the corrosion mass loss of an

entire reinforcement cage embedded in RC columns. The following conclusions can be drawn from this study.

- The CT scan was used to accurately estimate the corrosion mass loss of the reinforcement cages in the circular and square columns and agreed well with the more established method.
- The corrosion mass loss from the CT scan of the longitudinal and transverse reinforcement bars is higher than the otherwise measured mass loss of the same bars. The increase in mass loss is due to the rust and concrete particles on the reinforcement, which could be identified in great detail from the CT scanned images.
- The CT scan can show the location of the pitting corrosion on the reinforcement cage, especially the transverse rebars, which could be used to strengthen the RC structure with materials such as fibre-reinforced polymers and steel jackets.

# Chapter 6 Numerical Modelling of Low strength corroded RC columns

## 6.1 Introduction

The previous chapter 5 discussed the investigation into using an X-ray CT scan to measure corrosion mass loss in the RC column. Furthermore, the CT scan was used to identify pitting corrosion's location on the RC columns' reinforcement bars. Identifying the location of pitting corrosion could be used to strengthen and retrofit the RC columns. This could aid in preventing the buckling of the longitudinal bars and the imminent collapse of the structure. Meanwhile, this chapter introduced numerical simulation to validate the experimental results of the tests on the corroded RC columns in Chapters 3 and 4. The simulation will enable parametric studies to be conducted, which will assist in developing constitutive material models for corrosion-damaged low-strength concrete structures.

The nonlinear finite element method (FEM) provides an essential option for studying corroded RC structures' response and residual load-carrying capacity. In the past years, significant efforts have been devoted to this field (Li et al., 2017). Nonlinear FEM simulation of degraded RC structures is often conducted by incorporating the corrosion-induced damage into the computational model for non-corroded structures by modifying various input parameters. Most previous efforts focused on the numerical simulation of RC members' flexural and shear performance (Bahraq et al., 2019; Junlong & Dongsheng, 2022; Li et al., 2017; Saadah et al., 2021; Shomali et al., 2020).

These studies considered the cross-sectional loss, strength and ductility of the reinforcing steel and the reduction of the bond between concrete and steel (Horrigmoe & Sand, 2002). Furthermore, in some studies, the decrease in the compressive strength of the cracked concrete caused by the steel corrosion was also considered to simulate better the structural response (Coronelli & Gambarova, 2004; Hanjari et al., 2011; Kallias & Rafiq, 2010). However, most of the studies were dedicated to simulating the behaviour of corroded RC beams (Biswas et al., 2019; Biswas et al., 2020; Coronelli & Gambarova, 2004; Kioumarsi et al., 2016). Hence, more numerical and analytical assessment methods are needed to evaluate the behaviour of corroded RC columns under different loading effects. Kioumarsi et al. (2014) performed a detailed 3D nonlinear finite element simulation of the residual flexural capacity of a corroded RC beam. In their work, the damage induced by the steel corrosion was simulated by reducing the cross-sectional area, the

yield and the ultimate strength of the rebars, decreasing the bond strength, modifying the bond-slip behaviour between concrete and steel, and reducing the strength of cracked concrete..

## 6.2 Research contribution and novelty of this chapter.

The nonlinear finite element method (FEM) provides an important option for studying corroded RC structures' response and residual load-carrying capacity. In the past years, significant efforts have been devoted to this field. Nonlinear FEM simulation of corroded RC structures is often conducted by incorporating the corrosion-induced damage into the computational model for non-corroded structures by modifying various input parameters (Li et al., 2017).

Numerical and analytical studies were used to investigate the effect of corrosion on the response of corroded confined RC columns due to the problem associated with full-scale experimental testing of RC columns (Ahamed et al., 2022; Jin et al., 2018; Kashani et al., 2016a; Rao et al., 2017a). Furthermore, most of this analysis was on RC structures with normal or high-strength concrete. Hence, there is a need to investigate the responses and behaviour of ageing low-strength RC structures to proffer adequate maintenance and retrofitting/strengthening to prevent premature failure and collapse.

This research aims to numerically investigate the response of low-strength concrete corroded confined RC columns to axial monotonic and cyclic compressive load and compare the result with the experimental tests conducted in Chapters 3 and 4 of this thesis. This will pave the way for further investigation, leading to the development of constitutive models for low-strength RC structures in high seismic regions.

## 6.3 Preliminary FEA of RC columns

The numerical analysis in Abaqus is based on the CDPM, which requires the material properties to determine the stress-strain relations for uniaxial behaviour in compression and the evolution of damage variables in compression and tension. The Abaqus property module defines the material properties sections, assigns section orientation and defines the material calibrations (Abaqus, 2011). The accuracy of numerical analysis is dependent on the results of the calibration of the material used in the production of the samples. These material properties are determined during the experimental tests on material samples. Preliminary investigations were carried out in Abaqus using typical values of material properties in modelling the RC samples. Tables 6.1 – 6.3 give one of such typical material properties for a grade 20 concrete (Hafezolghorani *et al.,* 2017), while Table 6.4 and Table 6.5 are the properties of steel and GFRP, respectively.

**Table 6.1: Material properties for concrete (B20) with CDPM (M. Hafezolghorani et al., 2017)**

| Properties | Parameter | Values |
|---|---|---|
| **Concrete elasticity** | Young's modulus (GPa) | 21.2 |
| | Poisson's ratio | 0.2 |
| **Concrete plasticity** | Dilation angle | 31 |
| | Eccentricity | 0.1 |
| | $f_{bo}/f_{co}$ | 1.16 |
| | k | 0.67 |
| | viscosity parameter | 0 |

**Table 6.2: Compressive behaviour of Concrete (B20) in CDPM (M. Hafezolghorani et al., 2017)**

| **Concrete compressive behavior** | | **Concrete compression damage** | |
|---|---|---|---|
| **Yield stress (MPa)** | **Inelastic strain** | **Damage parameter C** | **Inelastic strain** |
| **10.2** | 0 | 0 | 0 |
| **12.8** | 0.0000773585 | 0 | 0.0000773585 |
| **15** | 0.000173585 | 0 | 0.000173585 |
| **16.8** | 0.000288679 | 0 | 0.000288679 |
| **18.2** | 0.000422642 | 0 | 0.000422642 |
| **19.2** | 0.000575472 | 0 | 0.000575472 |
| **19.8** | 0.00074717 | 0 | 0.00074717 |
| **20** | 0.000937736 | 0 | 0.000937736 |
| **19.8** | 0.00114717 | 0.01 | 0.00114717 |
| **19.2** | 0.001375472 | 0.04 | 0.001375472 |
| **18.2** | 0.001622642 | 0.09 | 0.001622642 |
| **16.8** | 0.001888679 | 0.16 | 0.001888679 |
| **15** | 0.002173585 | 0.25 | 0.002173585 |
| **12.8** | 0.002477358 | 0.36 | 0.002477358 |
| **10.2** | 0.0028 | 0.49 | 0.0028 |
| **7.2** | 0.003141509 | 0.64 | 0.003141509 |

| | | | |
|---|---|---|---|
| **3.8** | 0.003501887 | 0.81 | 0.003501887 |

**Table 6.3: Tensile behaviour of Concrete (B20) in CDPM (M. Hafezolghorani et al., 2017)**

| **Concrete tensile behavior** | | **Concrete tension damage** | |
|---|---|---|---|
| **Yield stress (MPa)** | **Inelastic strain** | **Damage parameter C** | **Inelastic strain** |
| **2** | 0 | 0 | 0 |
| **0.02** | 0.000943396 | 0.99 | 0.000943396 |

**Table 6.4: Material properties for steel**

| **Properties** | **Parameter** | **Values** |
|---|---|---|
| **Steel elasticity** | Young's modulus (GPa) | 210 |
| | Poisson's ratio | 0.3 |
| **Steel plasticity** | Yield stress | 420 |
| | Plastic stress | 0 |

## 6.4 Nonlinear Finite Element modelling with ABAQUS

The use of ABAQUS FEA software in the modelling and analysis of RC structures has been ongoing, with many researchers using the software to analyse structural elements and investigate their response to loadings and deformations. Some of the published existing work using ABAQUS were presented in the literature review; see section 2.3 of this thesis. The 3D nonlinear finite element (FE) modelling of the test specimen was performed using the ABAQUS 2022 FE package (Dassault Systemes, 2022) to evaluate the response and behaviour of the RC columns to the applied load. This involves using the material properties determined from the experimental tests on the concrete (mass concrete) and steel rebar samples and other details available in the literature to estimate and validate the experimental results from the tests and published results. ABAQUS has some in-built models used to analyse RC structures, but the Concrete Damage Plasticity Model (CDPM) is used for this work.

The CDPM is a generalised Drucker-Prager failure criterion. It is the most widely used model to stimulate the linear and nonlinear behaviour of brittle materials loaded in tension and compression. The models use the concepts of isotropic damaged elasticity and isotropic tensile

and compressive plasticity to represent the inelastic behaviour of concrete (ABAQUS, 2019). The Drucker – Prager type concrete material modelling in ABAQUS has been proven very efficient for steel confinement applications (Charalambidi et al., 2012; Karabinis & Kiousis, 1996).

### 6.4.1 FE model description of RC tests specimens

Using the part module tools, the RC columns were modelled with the geometrical sections embedded in the ABAQUS software (Dassault Systemes, 2022). The concrete and GFRP elements are modelled using the three-dimensional (3D) deformable solid elements known as the hexahedral element with eight nodes and three degrees of freedom per node (C3D8R), which is the general-purpose linear brick element with reduced integration used to represent solid sections. In contrast, the steel reinforcements (transverse and longitudinal) are modelled as 2-node 3D deformable beam elements used for solid sections. The beam elements were utilised in this analysis to account for the resistance of the reinforcing bar to bending and shear by restricting relative rotation between adjacent beam elements. The B31 element, which represents a Timoshenko beam element that accounts for transverse shear deformation in beams, was selected for the role, enabling buckling to form under load. The concrete element is the host element, while the reinforcements are embedded in the concrete volume. Figures 6.1 and 6.2 show the model of the different parts used in modelling the circular and square RC columns, respectively.

The circular column is modelled as a solid element with 125mm dia. and 600mm long, the 6mm stirrup has 105mm dia. the 10mm longitudinal rebar is 550mm long. The GFRP was modelled as a solid element with a hollow centre having 600mm internal diameter, 6mm thickness (approximate measurement of the thickness of the GFRP after wet layup) and 100mm length.

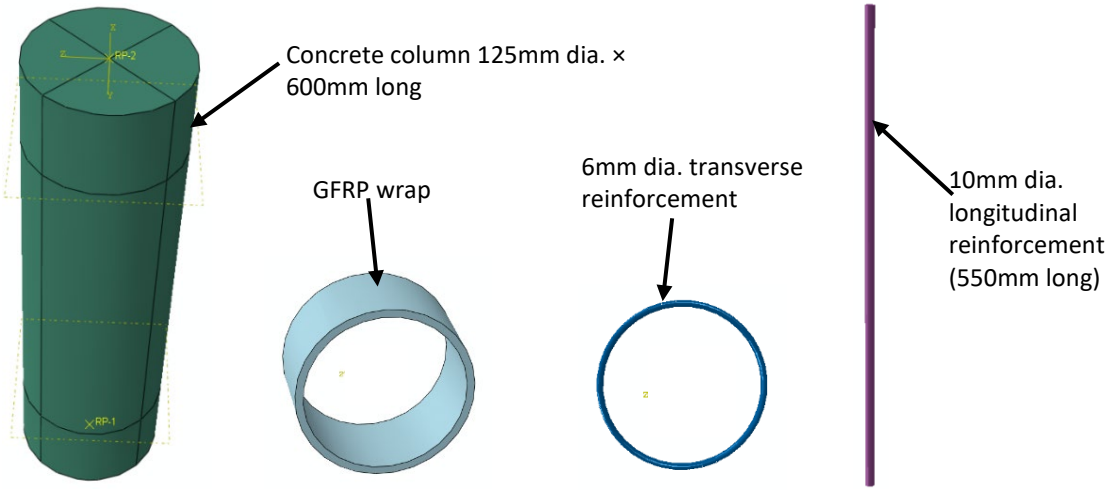


Figure 6.1. Part models of the circular RC column and GFRP elements

The square column is modelled as a solid element 125mm × 125mm and 600mm long, the 6mm stirrup was 105mm × 125mm while the 10mm longitudinal rebar is 550mm long. The GFRP was modelled as a solid element with internal dimension 600mm × 600mm, 6mm thickness and 100mm long.

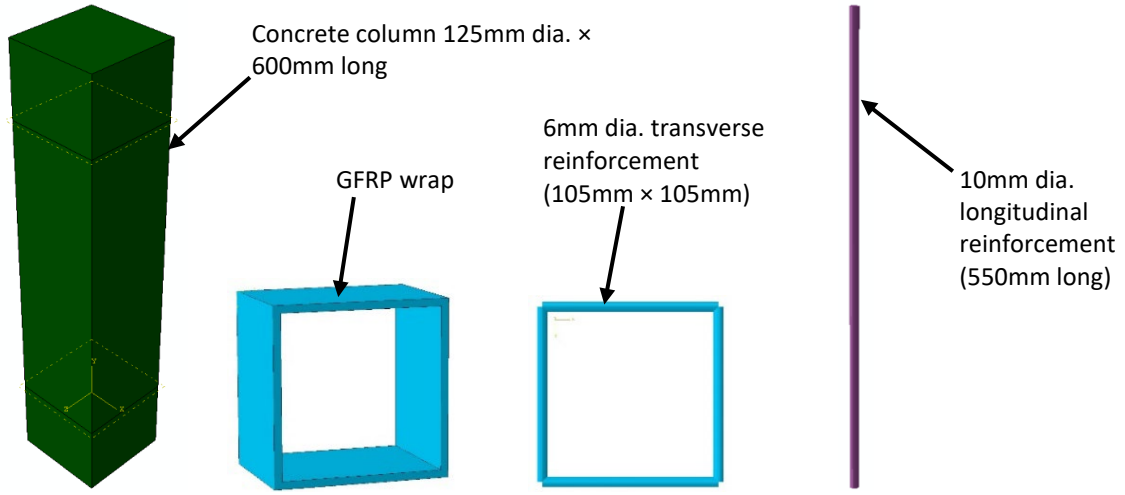


Figure 6.2. Part models of the square RC column and GFRP elements

### 6.4.2 Material properties

The numerical analysis in Abaqus is based on the CDPM, which requires the material properties for the determination of the stress-strain relations for uniaxial behaviour in compression as well as the evolution of damage variables in compression and tension. The Abaqus property module is used to define the material properties, sections, assign section orientation and also to define the material calibrations (Dassault Systemes, 2022).

#### 6.4.2.1 Constitutive material models of the concrete

The available CDP model in ABAQUS (ABAQUS, 2019), comprised of the plasticity model and linearly damaged model, is used to simulate the behaviour of concrete. The linearly damaged model is usually used to model concrete's stiffness degradation and stiffness recovery under cyclic loading by defining the damage variables. Hence, the plasticity and linearly damaged models were used to simulate the concrete nonlinearity (Le Minh et al., 2021).

In the model, the critical plastic parameters, including dilation angle, eccentricity, the ratio of the biaxial compression strength to uniaxial compression strength of concrete, the ratio of the second stress invariant on the tensile meridian to that on the compressive meridian estimated from the laboratory test on the mass concrete and presented in Table 6.5. According to ACI 318-19 (2019), the modulus of elasticity of concrete in compression is estimated from the equation below.

$$E_c = 4700\sqrt{f_c} \quad (6.1)$$

where,

$f_c$, is the cylinder strength of concrete at 28 days (MPa).

Also, the International Federation for Structural Concrete (fib) (2013) recommends 0.2 as Poisson's ratio for concrete in compression. In the modelling of RC in Abaqus, the parameters required to define the yield surface consist of four constitutive parameters determined from experimental concrete tests. The effect of the parameters on the CDPM in ABAQUS are explained below:

#### 6.4.2.2 Parameters used in the ABAQUS CDPM

##### 6.4.2.2.1 Dilation angle, (ψ)

Dilation angle is also called shear strain to volume strain ratio as it represents the angle of friction within a material. The dilation angle for concrete is usually 20 to 40, which affects material ductility (Milad Hafezolghorani et al., 2017). The dilation angle (Ψ) is also associated with the growth of the cracking mechanisms that affect the concrete during the inelastic period. Consequently, the dilation angle had considerable effects on the entire model. An increase in the dilation angle increased the system's flexibility. From a practical viewpoint, the internal dilation angle depended on specific parameters, including plastic strain and confined pressure. An increase in plastic strain and confined pressure decreased the internal dilation angle.

##### 6.4.2.2.2 Flow potential eccentricity, ϵ

A Flow potential eccentricity, which is continuous and smooth, ensures that flow direction is always unique. As confining pressures increase, the function approaches the linear Drucker-Prager flow potential asymptotically at $90^0$. The default flow potential eccentricity was 0.1. As a result, the dilation angle of the material is almost the same for a wide range of confining pressure stress values. Hence, raising the value of flow potential eccentricity increases the curvature of the flow potential. If the flow potential eccentricity had a value much lower than the default value, there could be convergence problems when the confining pressure is not high.

##### 6.4.2.2.3 Ratio of biaxial stress to uniaxial stress, $f_{b0}/f_{c0}$,

This is the ratio of the ultimate biaxial compressive stress to the uniaxial compressive ultimate stress, and its default value was 1.16 (Dassault Systemes, 2022).

#### 6.4.2.2.4 The ratio of the tensile to compressive stress invariants, $K_c$

Ratio between the second stress invariant on the tensile meridian and that on the compressive meridian must satisfy the condition $0.5 < K_c \leq 1$, with the standard value being 0.667 (Dassault Systemes, 2022)

#### 6.4.2.2.5 Viscosity parameter, μ

The ABAQUS software (ABAQUS, 2019; Dassault Systemes, 2022) used a null default viscosity parameter to avoid viscoplastic regularisation. This parameter enhanced the convergence rate of the model when the softening process occurred, and it gave good results. In the FE program, the tension recovery parameter equal to zero denoted that this parameter contributed to the cyclic behaviour and monitored the modulus of elasticity when compression behaviour changed to tension behaviour and vice versa. A zero value for tension recovery implied that the material tangent in the tension phase was wholly affected by compression damages. However, compression recovery was taken as 1, meaning tension damage did not affect the material tangent.

Table 6.5 and Figure 6.3 give the concrete material properties used in the analysis as extracted from the experimental test data of the mass concrete. The full tables of the concrete material properties used in the concrete damage plasticity model showing the values for the compression behaviours and damage parameters in tension and compression are presented in Appendix C.

**Table 6.5. Material properties for concrete**

| Properties | Parameter | Values |
|---|---|---|
| Concrete elasticity | Young's modulus (GPa) | 17.5 |
| | Poisson's ratio | 0.2 |
| Concrete plasticity | Dilation angle, ψ | 30 |
| | Eccentricity, ϵ | 0.1 |
| | $f_{bo}/f_{co}$ | 1.16 |
| | $K_c$ | 0.67 |
| | viscosity parameter, μ | 0 |

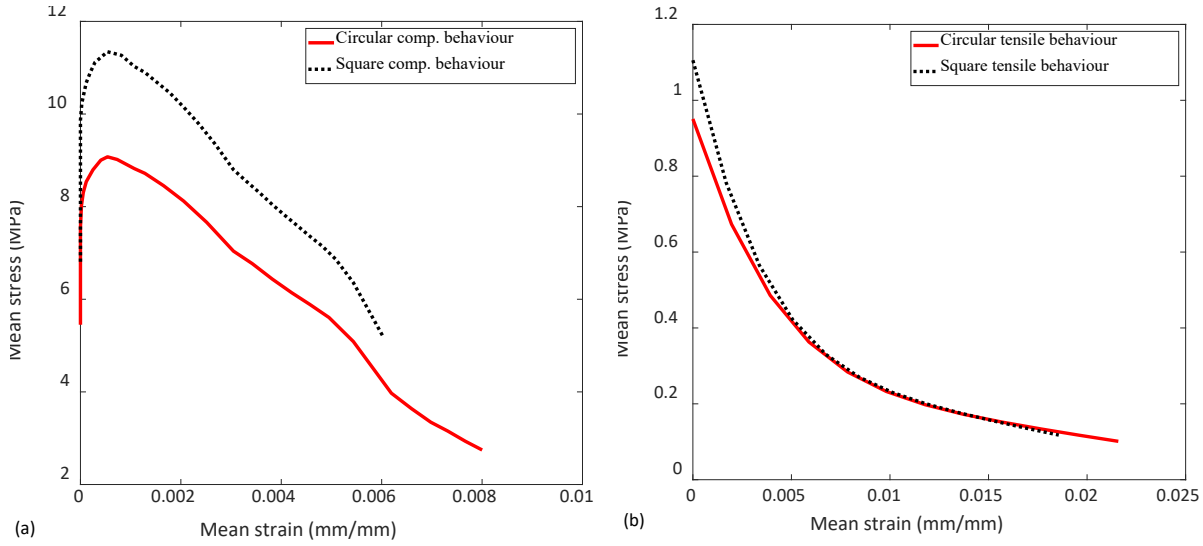


Figure 6.3. Stress-strain behaviour of concrete in the circular and square RC columns (a) compressive behaviour and (b) tensile behaviour

#### 6.4.2.3 Material properties of steel reinforcement

An isotropic elastic-plastic model was used to model the steel reinforcements (longitudinal and transverse), and the stress-strain relation was characterised as a bilinear strain-hardening curve. Generally, the steel reinforcing bars were modelled using the classical metal plasticity model in ABAQUS using the Mises yield surface, which provides an isotropic yield surface. However, for this study, the behaviour of the reinforcing steel was simplified as an effectively elastic-perfectly plastic behaviour (Earij et al., 2017; Hu et al., 2003). The inputs are based on a linear elastic response up to yielding and constant stress from yielding to the ultimate strain obtained from the experimental tests on the steel reinforcements. Table 6.6 gives the properties of steel used in the analysis.

**Table 6.6. Material properties for steel (Extract from Table 3.4)**

| Properties | Parameter | 6mm bars | 10mm bars |
|---|---|---|---|
| Steel elasticity | Young's modulus (GPa) | 185.23 | 196.73 |
| | Poisson's ratio | 0.3 | 0.3 |
| Steel plasticity | Yield stress (GPa) | 531.82 | 551.68 |
| | Ultimate stress (GPa) | 603.05 | 630.11 |

#### 6.4.2.4 Material Modelling of GFRP

The GFRP was used to strengthen the ends of the columns during testing to avoid stress concentration and failure at the ends; as such, it was not tested experimentally to determine its properties. For the purpose of the analysis, typical values in the literature were adopted as its properties. The properties used are presented in Table 6.7.

**Table 6.7. Mechanical properties of GFRP (Xin et al., 2017)**

| Parameter | Values |
|---|---|
| Density (kg/m$^3$) | 2560 |
| Young's modulus (GPa) | 74 |
| Poisson's ratio | 0.2 |

The parameters in Tables 6.5 – 6.7 and Figure 6.3 were used to analyse the circular and square RC columns with the different confinements (*L/D = 5, 8 and 13*) and corrosion levels subject to displacement loading (monotonic and cyclic) in ABAQUS. Sections 6.5 and 6.6 of this thesis show some of the analysis results.

### 6.4.3 Assembly of RC samples

The RC columns comprising the concrete columns (square and circular), which were modelled as C3D8R solid sections, and the transverse and longitudinal reinforcement modelled as beam elements (B31) are assembled using the embedded region constraint in the ABAQUS assembly module. This technique was used to represent the relationship between the reinforcing steel and the concrete. The concrete elements serve as the host, whilst the embedded reinforcing bars are the guest element, having its nodal translational degree of freedom constrained to the corresponding degree of freedom of the host elements.

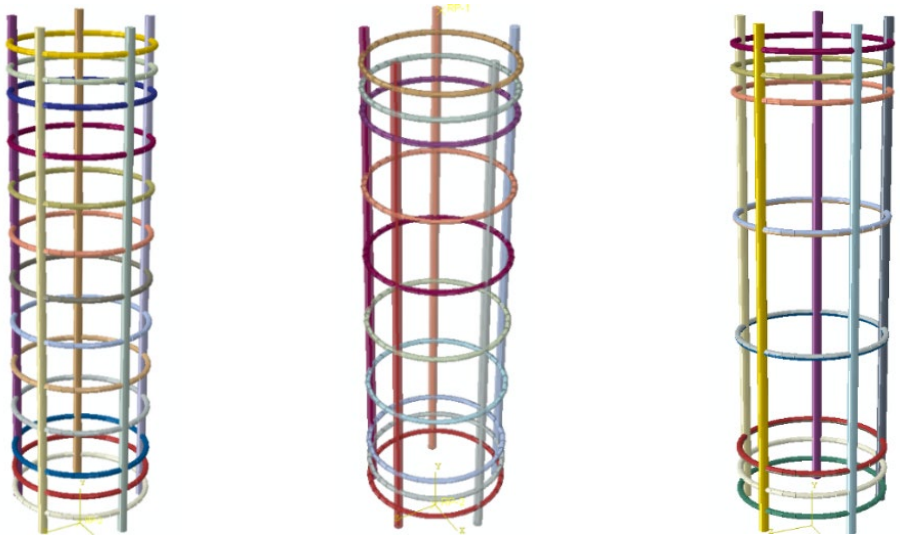

Figure 6.4. 3D assembly of the reinforcements in circular columns in ABAQUS

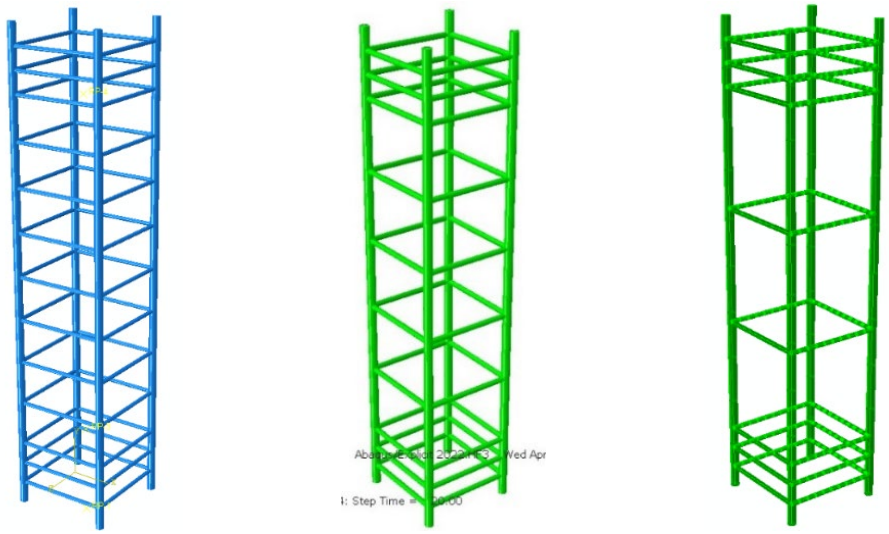

Figure 6.5. 3D assembly of the reinforcements in square columns in ABAQUS

The GFRP elements are attached to both ends of the embedded RC element using the tie technique, where the GFRP becomes the master surface while the RC becomes the slave surface. The ends are tied with the GFRPs to increase the strength and prevent failure at both ends, thereby transferring the stress concentration and loss during loading to the middle region of the RC sample. The complete assembly of the different configurations of the RC columns with the GFRP's presented in Figures 6.6 and 6.7 for circular and square columns, respectively.

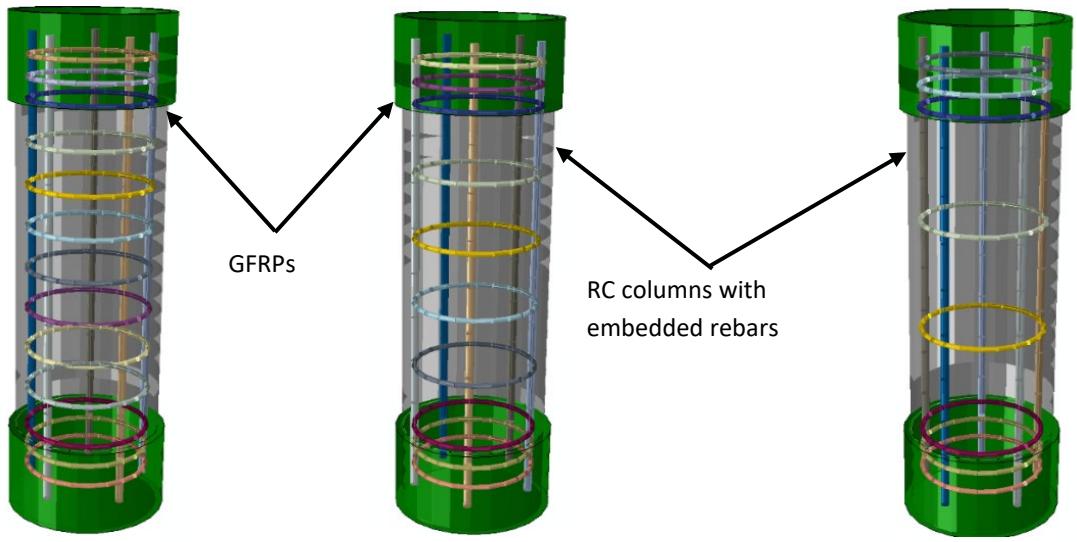


Figure 6.6. 3D assembly of circular columns in ABAQUS

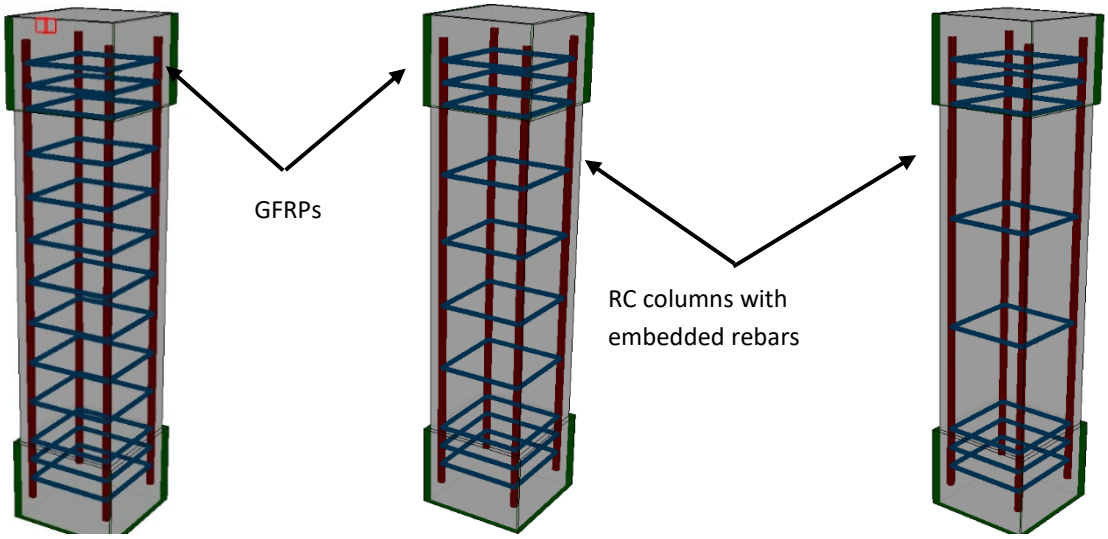


Figure 6.7. 3D assembly of square columns in ABAQUS

### 6.4.4 The step and interaction

The step and interaction module in Abaqus was used to specify the following during the analysis of
the RC columns:

- The type and procedure of the analysis to be done (nonlinear)
- The results/outputs expected such as the stresses, strains, and displacements
- The boundary conditions and the type of loading
- The contact or tie interaction between the elements
- The embedded region constraint

The analysis method used for the RC columns analysed in this research is the Dynamic Explicit. This is found to give a better output for nonlinear analysis; it converges faster and is more efficient and accurate. The displacement constraint was used to apply the 18mm displacement load at the base of the RC columns. The 18mm is applied as a gradually increasing displacement load, which varies with time (quasi-static loading) and is specified using the amplitude toolset in Abaqus.

The embedded region constraint was applied on the concrete host and the reinforcement using the interaction module such that the different elements could work together as a single unit while the tie constraint was used to attach the GFRP's to the ends of the columns.

### 6.4.5 The loading and meshing of samples

The mesh controls the accuracy of the output/result generated by the software and the duration of the analysis, but finer meshes are used for much better results. Mesh sensitivity was conducted to select an appropriate mesh which produce an acceptable simulation result with less computing time. The mesh sensitivity analysis was conducted using five different mesh sizes (10mm, 8mm, 7mm, 5mm and 3mm) in trial analysis of the RC columns.

The optimum mesh size used in the analysis is 5mm. It produces a fine enough mesh that results in a short analysis duration, which was checked under some initial model simulations. The element meshing was done by assigning the individual elements with a specific mesh size. The concrete column and the GFRPs are meshed as 3D stress elements, while the reinforcements (transverse and longitudinal) are meshed as beam elements. Figure 6.8 illustrates the meshing of the different parts of the circular column, including the GFRP wrap.

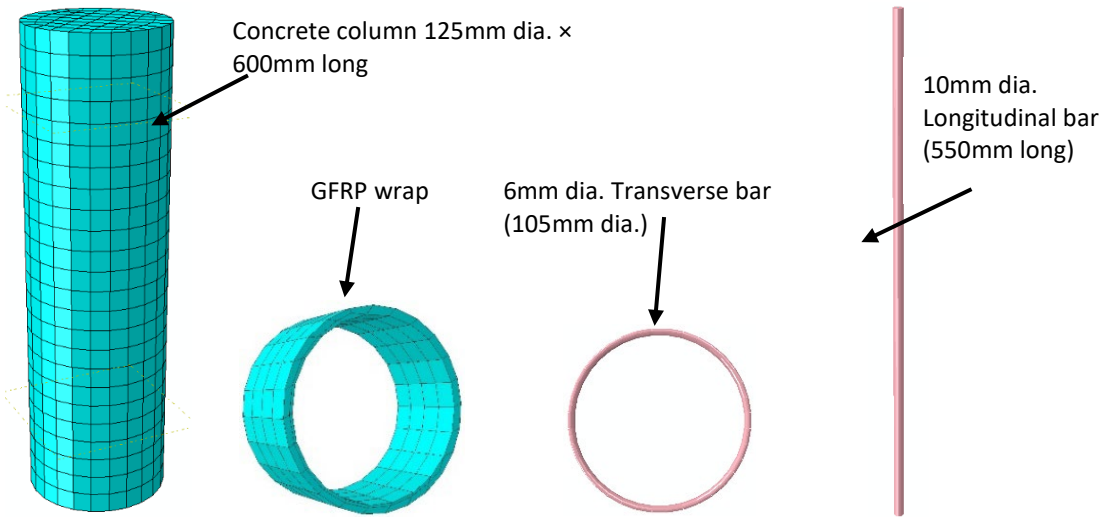


Figure 6.8. The mesh pattern of the circular RC column and GFRP elements

Also, figure 6.9 presents the meshed parts of the square RC column and the GFRP wrap.

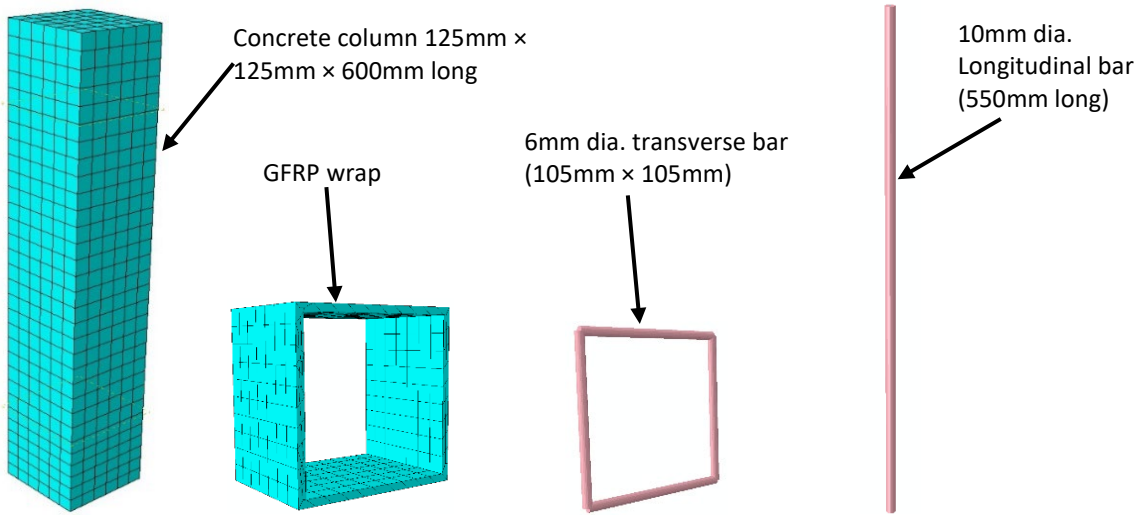


Figure 6.9. The mesh pattern of the square RC column and GFRP elements

The loading and boundary conditions are specified using the load module. For the monotonic analysis, the RC columns were subjected to displacement load (18mm) to investigate the response of the columns to deformation. The displacement output from the experimental test in Chapter 4 was used for the axial cyclic compressive analysis.

For the monotonic analysis, the boundary condition is applied such that the top of the column is subjected to zero displacements and rotations ($U_1 = U_2 = U_3 = U_{r1} = U_{r2} = U_{r3} = 0$), while the loading is applied as a gradually ramped compressive 18mm displacement load from the base ($U_2 = 18mm, U_1 = U_3 = U_{r1} = U_{r2} = U_{r3} = 0$) (Figure 6.10) similar to the operation of the machine used in the experimental test. $U_i$, are the displacements in the x, y and z direction respectively while $U_{ri}$, are the rotations in the x, y and z direction respectively

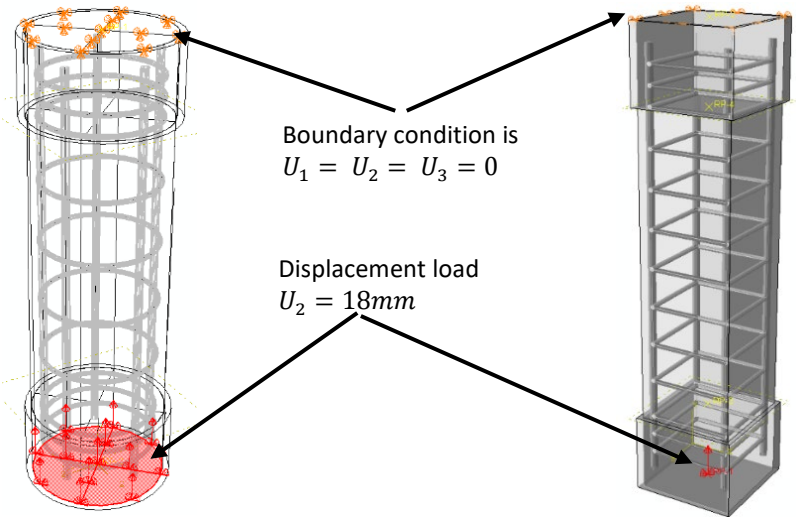


Figure 6.10. Applied boundary condition and load on the RC samples

In the axial cyclic compressive analysis, the displacement loading is applied by using the displacement output from the individual experimental test on the RC columns selected for the analysis.

### 6.4.6 The analysis result/output

The result/output variables of the analysis are defined in the step module using the field and history output. The expected output is defined according to the type of analysis and information needed.

The following is the output obtained from the analysis of the RC columns:

- the stresses (Von Mises)
- the failure modes of the selected RC columns showing the buckling of the bars
- the stress-strain curves resulting from the applied axial monotonic and cyclic load on the RC columns

These outputs from the analysis were presented in section 6.4 of this thesis for the axial monotonic and axial cyclic loading of the corroded and uncorroded RC columns.

### 6.4.7 Modelling impact of corrosion damage on the steel reinforcement

Corrosion affects the load-carrying capacity of RC columns while also leading to the buckling of the longitudinal bars and hence the failure of the structure. The effect of corrosion on the RC columns was reflected by reducing the diameter of the reinforcements leading to a reduction in the cross-sectional area available to sustain the imposed load. Furthermore, the yield strength of both the transverse and longitudinal bars is reduced by applying the effect of corrosion obtained from the mass loss estimate procedure in Chapters 3 and 4.

The area reduction in steel bars depends on whether chloride or carbonation-induced corrosion occurs. The latter causes a more uniform attack with a relatively limited reduction of bar cross-section. On the other hand, chlorides may cause severe pitting in the bars, with highly localized reductions of the sections. The tests performed by Cairns et al. (2008) and Castel et al. (2000) have shown that there is a sort of balance between the strength loss ensuing from the reduced section and the strength increase due to the hardening of the undamaged material in the same section (Coronelli & Gambarova, 2004).

For the numerical analysis, the reduction in the diameter of the steel reinforcement was calculated using Equation 6.1 (Apostolopoulos et al., 2006; Kashani et al., 2013b; Toongoenthong & Maekawa, 2005).

$$D_{corr} = D_o\sqrt{1 - \gamma} \quad (6.2)$$

where $D_{corr}$ is the diameter of reinforcement for a specific mass loss

$D_o$, is the initial diameter of the pristine bar and

$\gamma$, is the corrosion mass loss determined in Eq. 3.7.

This reduced diameter is applied to the reinforcement bars uniformly, which might affect the response of the column under loading as corrosion, especially chloride-induce, occurs non-uniformly in the form of pits and depressions along the length of the reinforcement bars. Hence the mean cross-sectional area of the reinforcement bars becomes

$$A_{corr} = \frac{\pi\,(D_{corr})^2}{4} \quad (6.3)$$

Corrosion of steel reinforcement leads to a reduction in the yield and ultimate strength and hence the load-carrying capacity of RC structures leading to a reduction in their level of safety and, in most serious cases, to their structural collapse (Apostolopoulos et al., 2013; Kashani et al., 2013b; Zhong et al., 2023). The yield strength of the longitudinal bar is adjusted to reflect the corrosion and buckling effect using the equation proposed by Kashani et al. (2013b)

$$\sigma'_{yc} = \sigma_y(1 - \beta\gamma) \quad (6.4)$$

where,

$\sigma'_{yc}$, is the yield stress of corroded longitudinal bars in compression,

$\sigma_y$, is the yield stress of uncorroded/pristine bars,

$\beta = 0.005$ for L/D $\leq$ 5, $\beta = 0.0065$ for 5 $<$ L/D $\leq$ 10, $\beta = 0.0125$ for L/D $>$ 10.

Furthermore, the transverse bars yield and ultimate strength are reduced by using the equation proposed by Vu et al. (2017)

$$\sigma'_{yc} = \sigma_y(1 - \alpha_s\gamma) \quad (6.5)$$

where, $\alpha_s$, is a strength reduction factor = 0.005.

The application of the strength reduction factor on the corroded bars assumed a uniform or generalised corrosion effect on the rebar.

## 6.5 Axial monotonic compressive response of RC columns

The stress-strain response of the circular column to the applied axial compressive load is presented in Figures 6.11 (a-c) and 6.13(a-c) for the circular and square columns, respectively. Furthermore, figures 6.12 (a-c) and 6.14(a-c) show the observed failure modes of the RC columns under load during the numerical analysis. The observed compressive response of the columns is similar at the elastic range until yield. Afterwards, it reduces beyond the peak load due to corrosion and confinements of the reinforcement bars. Following the analysis of the numerical output and comparison with the experimental result.

### 6.5.1 Stress-strain responses of corroded and uncorroded circular columns

Figure 6.11(a-c) shows the stress-strain responses of the differently confined corroded and uncorroded circular RC columns (numerical and experimental). The results showed that the numerical model could accurately predict the axial load-carrying capacity of the RC columns as the ultimate strength in all the columns is approximately equal to the strength from the experimental test. In Figure 6.11(a), the numerical model could predict the stress-strain behaviour of the well-confined circular RC column (uncorroded) better than the experimental test, as the RC column in the experimental test failed prematurely due to failure of the GFRP at the top of the column. The failure of the GFRP leads to stress concentration at the top of the column resulting in a reduction in the ultimate load-carrying capacity of the column.

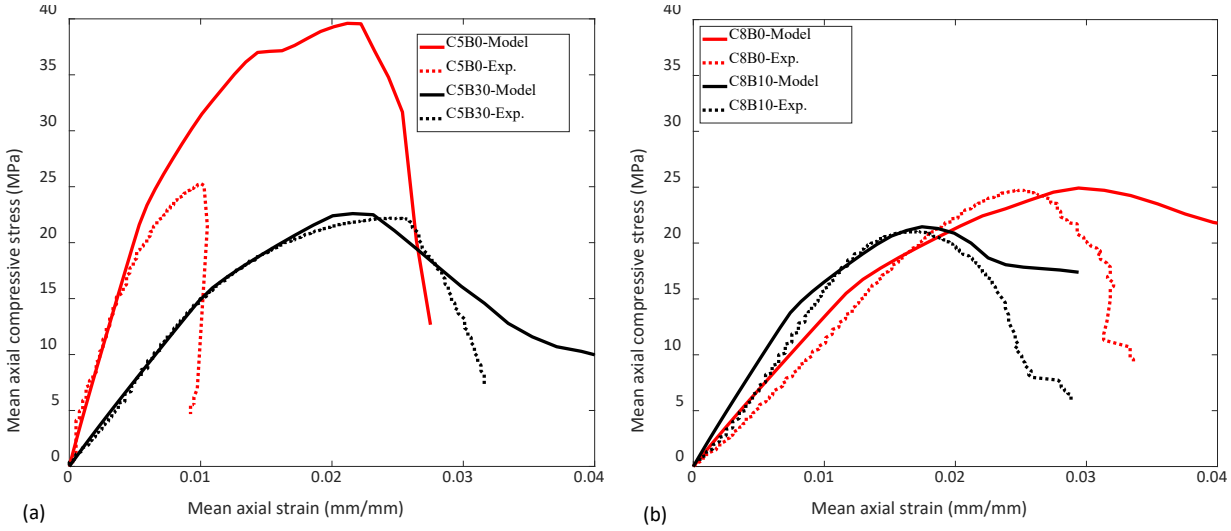

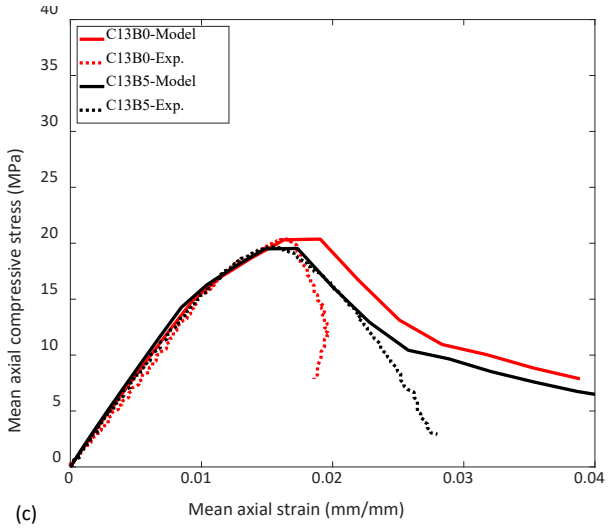


(c)

Figure 6.11. Comparison of the monotonic stress-strain response of circular RC columns under axial compressive load

### 6.5.2 Observed failure modes of circular RC columns under axial compressive load

The observed failure modes of the RC circular columns under axial compressive load are presented in Figure 6.12(a-c). The figures show the buckling of the longitudinal steel reinforcement of the differently confined RC columns. For the highly confined column (*L/D*=5) (Fig. 6.12(a)), there was hardly any noticeable buckling on the pristine (uncorroded) column. In contrast, the column with 30% corrosion mass loss had noticeable buckling below the GFRP end. The buckling of the rebar in the corroded RC columns results from the reduced cross-sectional area and yield stress of the reinforcement bars. The location of the buckling is similar to the observed buckling location of the column during the experimental test.

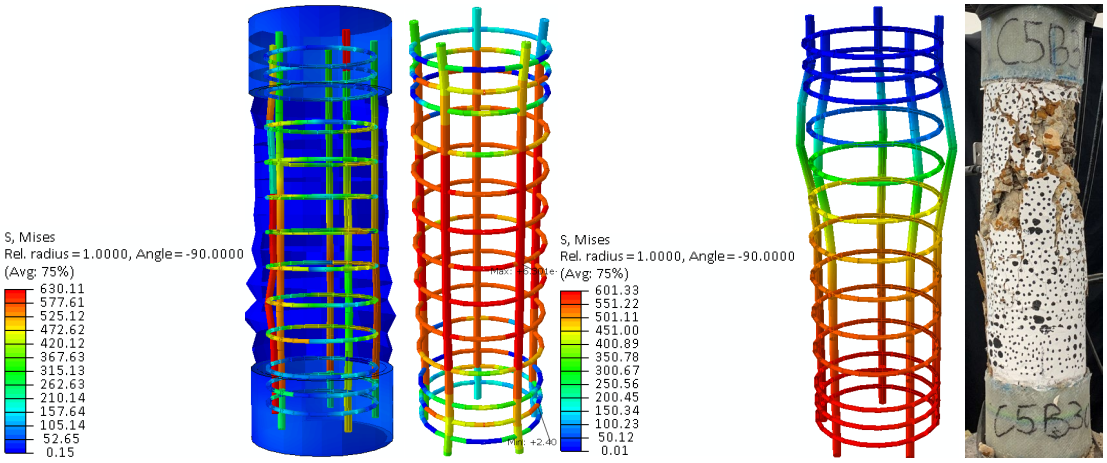


(a) High level of confinement (*L/D = 5*)

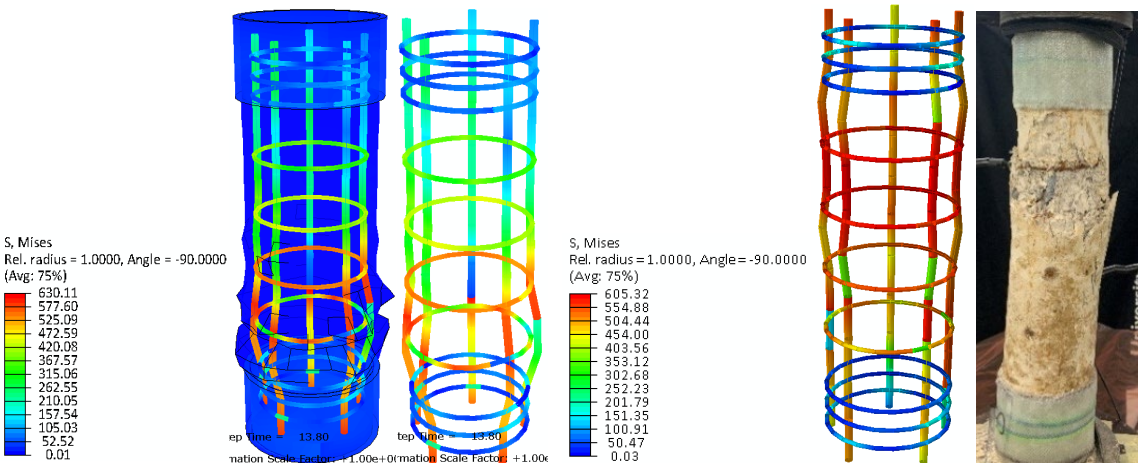


(b) Medium level of confinement (L/D = 8)

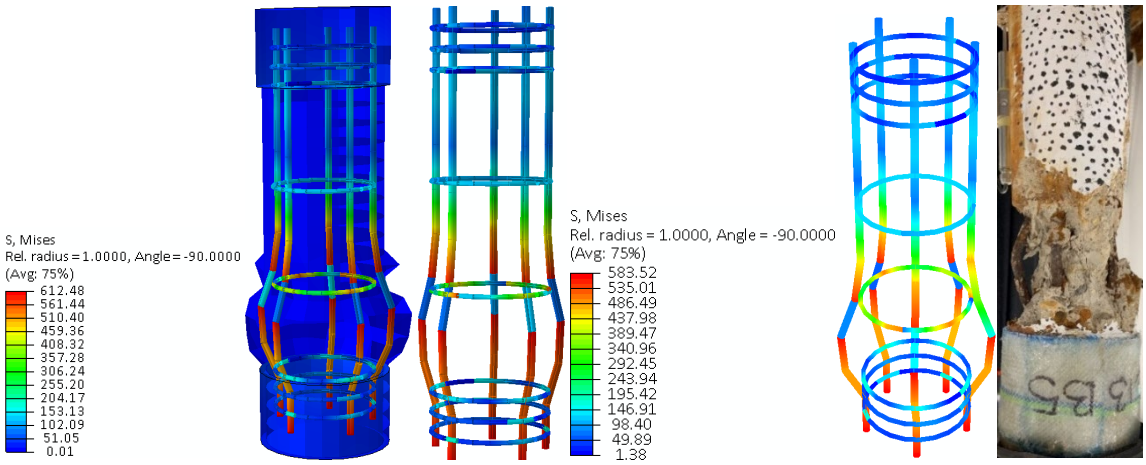


(c) Low level of confinement (L/D = 13)

Figure 6.12. Failure modes of the differently confined uncorroded and corroded circular RC columns under axial compressive load

Meanwhile for the medium and low levels of confined columns, respectively (*L/D*=8) (Fig. 6.12(b)) and (*L/D*=13) (Fig. 6.12(c)), these had rebar buckling even in the uncorroded columns from the inadequate confinement effect of the transverse bars. The buckling of the longitudinal bars is more pronounced in the RC columns analysed posessing corrosion, as the out-of-plane deformation was more significant and more noticeable than in the pristine columns.

### 6.5.3 Stress-strain responses of corroded and uncorroded square RC columns

Similar to the result of the numerical analysis of the circular columns, the square columns' stress-strain behaviour could predict the column's axial load-carrying capacity (Fig. 6.13(a-c)). The RC columns have similar behaviour within the elastic region until yielding, where the effect of the confinement and corrosion results in a decrease in the ultimate strength and carrying capacity. In all the columns analysed, the numerical analysis was able to predict the actual response of the

pristine columns under load in contrast to the experimental test. In the experiments, the pristine RC columns had premature failure resulting from the failure of the GFRP ends, reducing the ultimate load-carrying capacities. This failure is not reproduced in the numerical model and results.

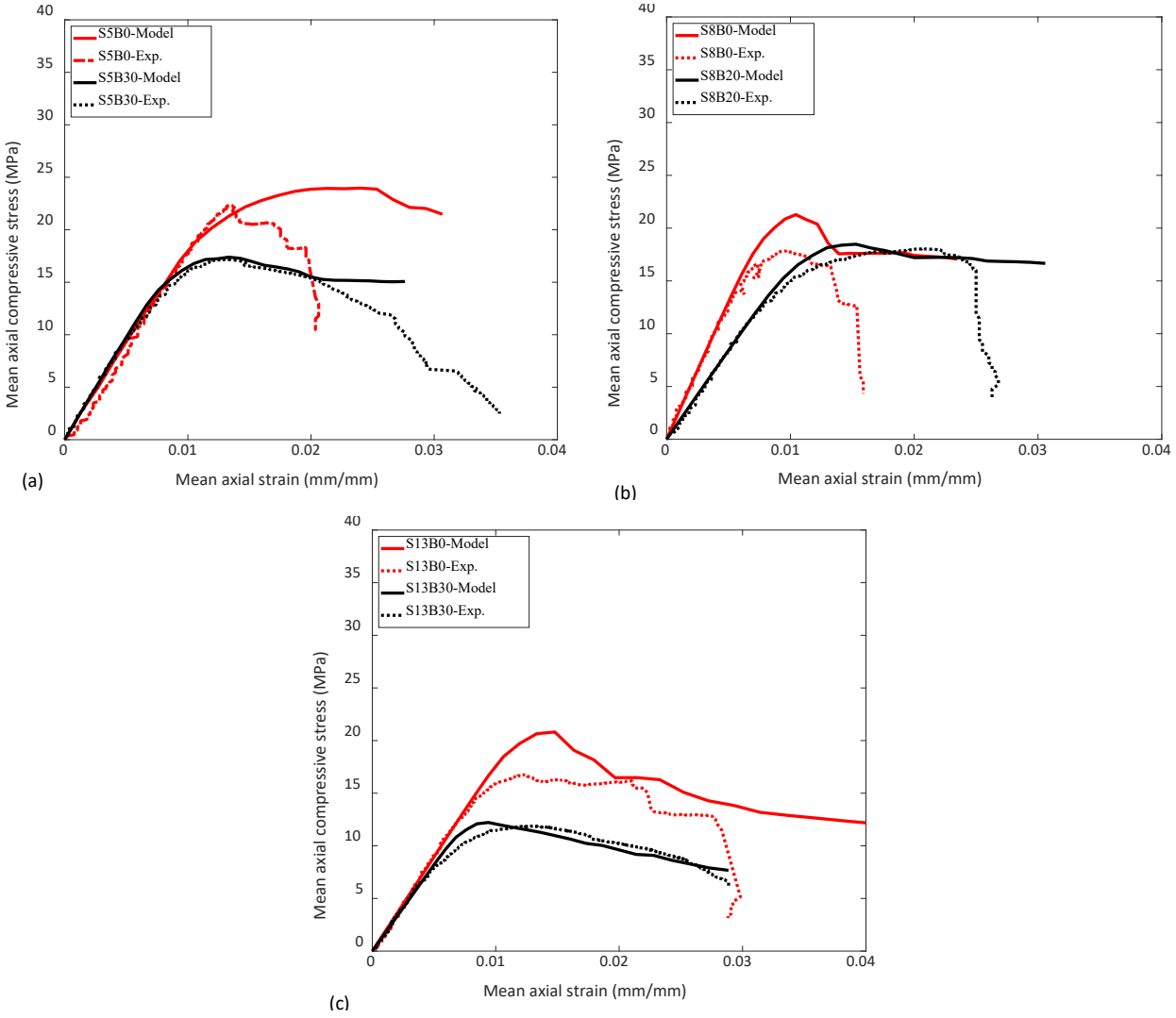


Figure 6.13. Comparison of the monotonic stress-strain response of square RC columns under axial compressive load

### 6.5.4 Observed failure modes of corroded and uncorroded square RC columns under axial compressive load

The observed failure modes of the square RC columns under axial compressive load are presented in Figure 6.14(a-c). The figures show similar behaviour to the buckling of the reinforcements in the circular RC columns. In addition, the highly confined column ($L/D$ = 5) (Fig. 6.14(a)) also had a slightly noticeable buckling on the pristine (uncorroded) column, which was more pronounced in the column with 30% corrosion mass loss primarily in the middle zone of the column.

Furthermore, the numerical analysis captured the buckling of the longitudinal rebars, which occurs at a similar location to the failure observed during the experimental test on the columns.

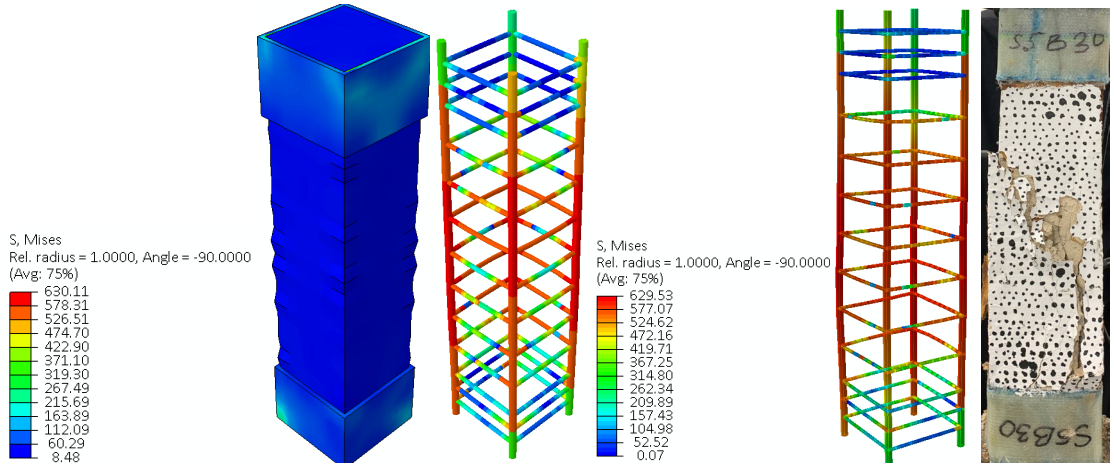


(a) Highly confined (*L/D = 5*)

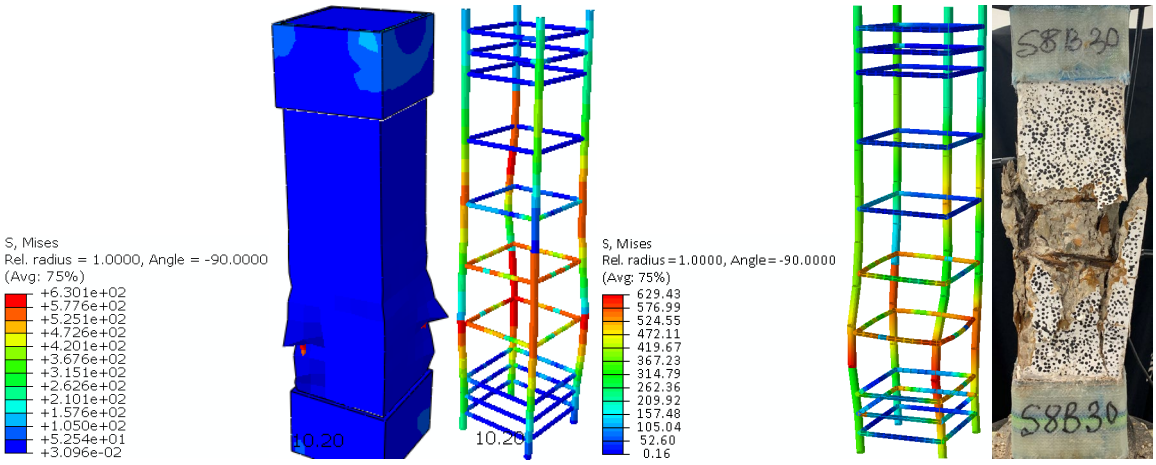


(b) Mediumly confined (*L/D = 8*)

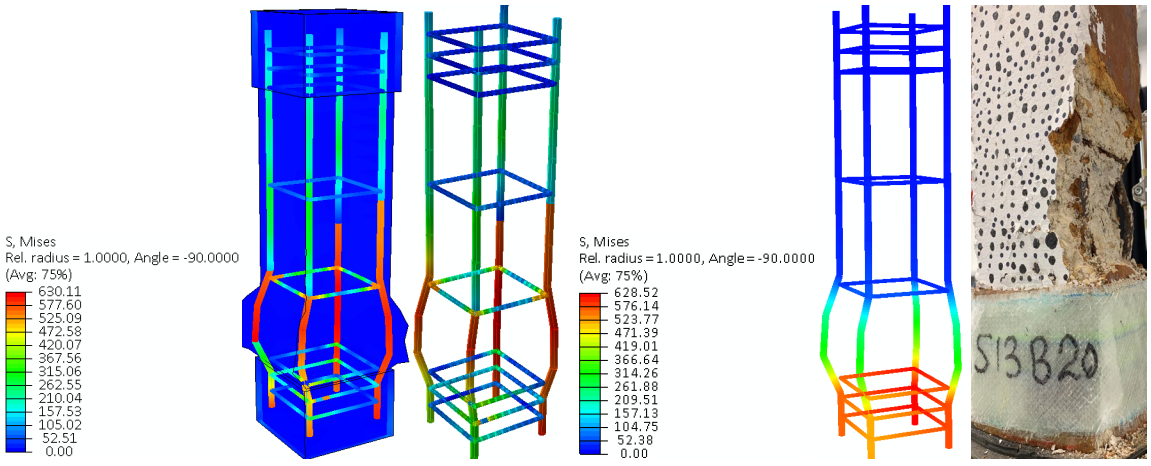


(c) lowly confined (*L/D = 13*)

Figure 6.14. Failure modes of the differently confined uncorroded and corroded square columns under axial compressive monotonic load

## 6.6 Axial cyclic compressive response of RC columns

Cyclic analysis and experimental testing constitute an effective method to provide insight into the seismic performance of the structural component. However, although it is recognised that corrosion-induced damage on coastal bridge piers significantly affects the safety of the structures during the long-term service period, the damage mechanism and the mechanical behaviour are still seldom understood. The effect of corrosion and confinement on the axial cyclic compressive performance of ageing low-strength RC columns was thus investigated numerically and experimentally for better understanding and prediction of the responses. Hence, the axial cyclic response of the RC columns from the numerical analysis was compared with the corresponding responses from the experimental tests. The stress-strain behaviour and the observed modes of failure of the modelled RC columns are presented in Figures 6.16 – 6.19.

### 6.6.1 Modelling the cyclic stress-strain response of the reinforcement bars in Abaqus

The overall cyclic response of RC elements is significantly affected by the behaviour of steel reinforcing bars undergoing repeated loadings into the inelastic range, mainly if corroded. This aspect is worthy of interest because it can impair the structural capacity of the structure (Apostolopoulos, 2007; Apostolopoulos & Papadopoulos, 2007; Kashani et al., 2015). The reinforcement steel rebars (longitudinal and transverse) have been modelled with embedded reinforcement element type. The cyclic behaviour for the stress-strain response steel reinforcement proposed by Monti and Nuti (1992) has been adopted in this analysis. The description of the model is presented below.

Stress-strain relationships for branches between two subsequent load reversal points are incorporated into the model, and material state parameters are updated on each successive load reversal (Fig. 6.15).

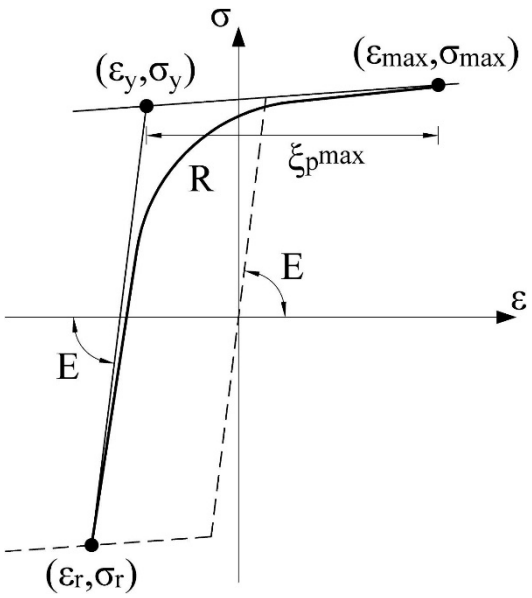


Figure 6.15: Cyclic model for steel reinforcement (Di Carlo et al., 2017a, 2017b)

The model is expressed in terms of a dimensionless stress, $\sigma^*$, and a scaled strain, $\varepsilon^*$.

$$\varepsilon^* = \frac{\varepsilon - \varepsilon_r^n}{\varepsilon_y^{n+1} - \varepsilon_r^n} \tag{6.6}$$

expressed in the strain-stress coordinates of the last reversal point ($\varepsilon_r^n$, $\sigma_r^n$) and in the strain-stress coordinates of the updated yield point ($\varepsilon_y^{n+1}, \sigma_y^{n+1}$).

The Monti-Nuti model is expressed as :

$$\sigma^* = b.\varepsilon^* \frac{(1-b).\varepsilon^*}{(1+\varepsilon^{*R})^{1/R}} \quad \text{(Di Carlo et al., 2017b)} \tag{6.7}$$

where,

b = hardening ratio

R = curvature parameter defined as a function of the initial curvature $R_o$ and is expressed as

$$R = R_o - \frac{A_1.\xi_p^{max}}{A_2 + \xi_p^{max}} \tag{6.8}$$

where,

$\xi_p^{max}$ = maximum plastic excursion developed during a half-cycle

$A_1$ and $A_2$ = material constants

This results in the half-cycle plastic work at the n-th half-cycle expressed as

$$\Phi_p^i = \frac{1}{2}(\sigma_r^n - \sigma_y^n)\xi_p^n \tag{6.9}$$

where,

$\sigma_y^n$ = yield stress at the n-th half cycle, and the corresponding strain is given as

$$\varepsilon_y^{n+1} = \varepsilon_r^n + \frac{\varepsilon_y^{n+1} - \sigma_r^n}{E} \quad (6.10)$$

Hence, the parameters required in the Monti-Nuti constitutive model are Young's Modulus, E, the initial yield stress, $\sigma_y^o$, the initial hardening ratio $b_0$, the initial curvature parameter $R_0$, the two material constants $A_1$ and $A_2$ and the weighting coefficient P.

The behaviour of the corroded steel reinforcement can be simulated, as proposed by Rinaldi et al. (2022), through a variation of the stress-strain relationship of the reinforcement without any change of its nominal section. The influence of corrosion on the yielding and ultimate stress of reinforcement bars with general and pitting corrosion is evaluated with regression analysis based on the least square method. The yield and ultimate stresses of the corroded and uncorroded bars are estimated from Equations 6.4 and 6.5 proposed by Kashani et al. (2013a) for both the longitudinal and transverse bars. Furthermore, the buckling phenomenon of corroded rebars was accounted for using the model proposed by Kashani et al. (2013b).

### 6.6.2 Axial cyclic stress-strain responses of uncorroded and corroded circular RC columns

Figure 6.16(a-f) shows the stress-strain responses of the circular columns to axial compressive cyclic loading. The loading was applied in the numerical analysis using the experimental displacement outputs. The test results showed an agreement between the numerical analysis and experimental results, as the ultimate strength of the columns is similar. The RC columns generally showed identical responses in the elastic range until the yield, where the effect of the confinement and corrosion results in a reduction in the ultimate strength and failure. However, it is observed in all the analyses that the strain outputs are not the same as the experimental test result despite applying the displacement from the experiments. This results from the response of the RC columns during the numerical analysis to the applied displacement loading protocol (compressive), as the columns are tensioned during the unloading phase of the load application.

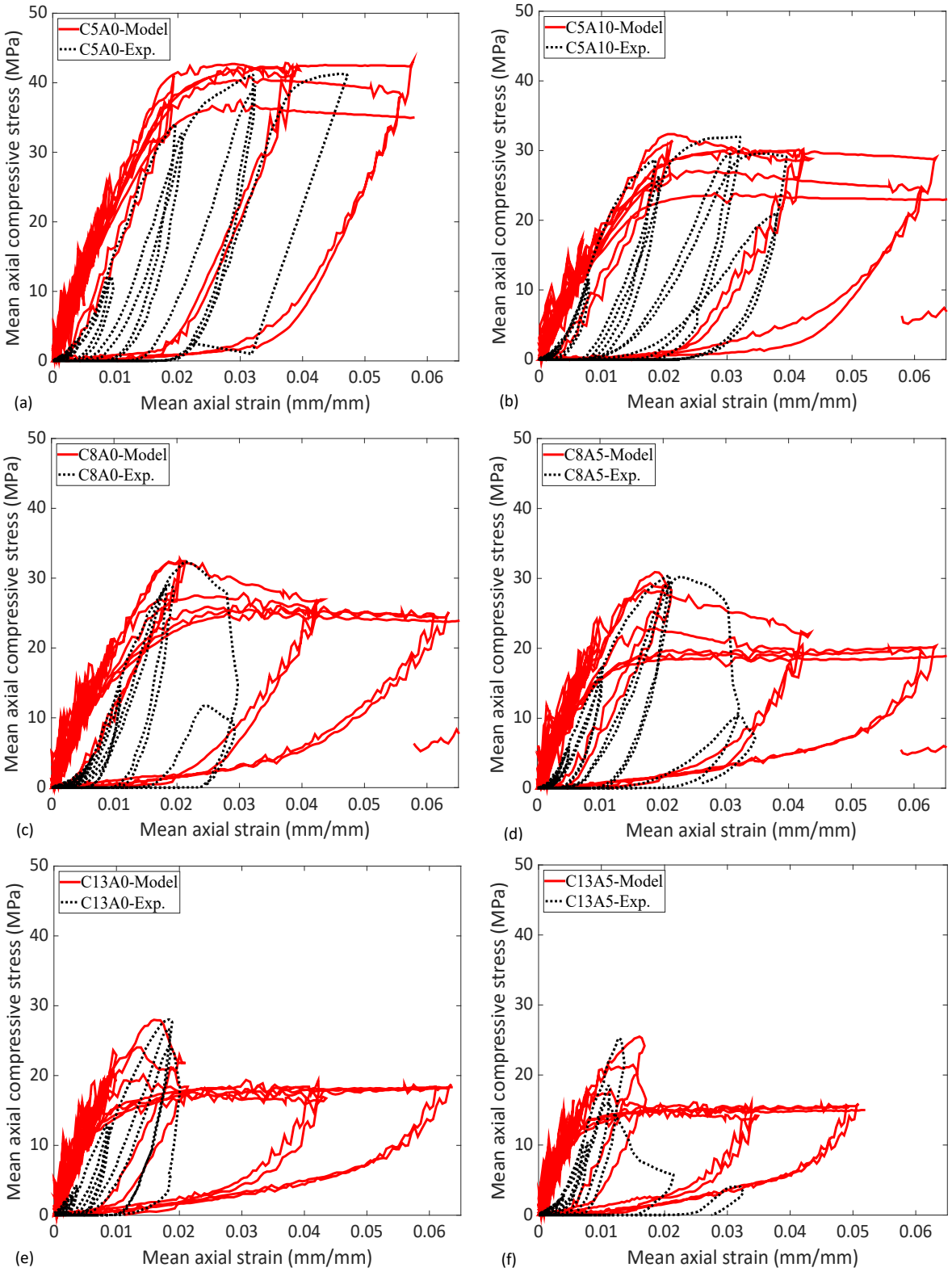


Figure 6.16. Comparing the axial cyclic compressive response of the circular columns

### 6.6.3 Observed failure modes of circular columns under axial cyclic compressive load

The observed failure modes of the RC circular columns under axial cyclic compressive load are presented in Figure 6.17(a-c). The figures show the buckling of the longitudinal steel

reinforcement of the differently confined RC columns. The highly confined (*L/D*=5) (Fig. 6.17(a)) and medium confined (*L/D*=8) (Fig. 6.17(b)) columns buckled in the middle zone in both the pristine (uncorroded) and corroded columns. The location of the buckling is similar to the observed buckling location of the column during the experiments.

Meanwhile, the low confined column (*L/D*=13) (Fig. 6.17(c)) buckled immediately below the GFRP-wrapped ends of the columns. The buckling is more pronounced due to the inadequate confinement provided by the lateral reinforcement.

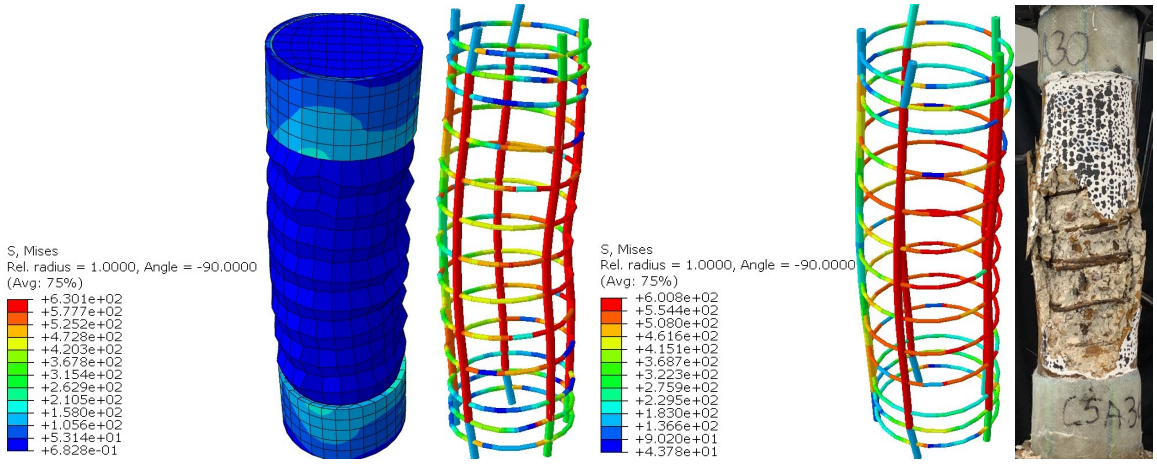


(a) Highly confined (*L/D = 5*)

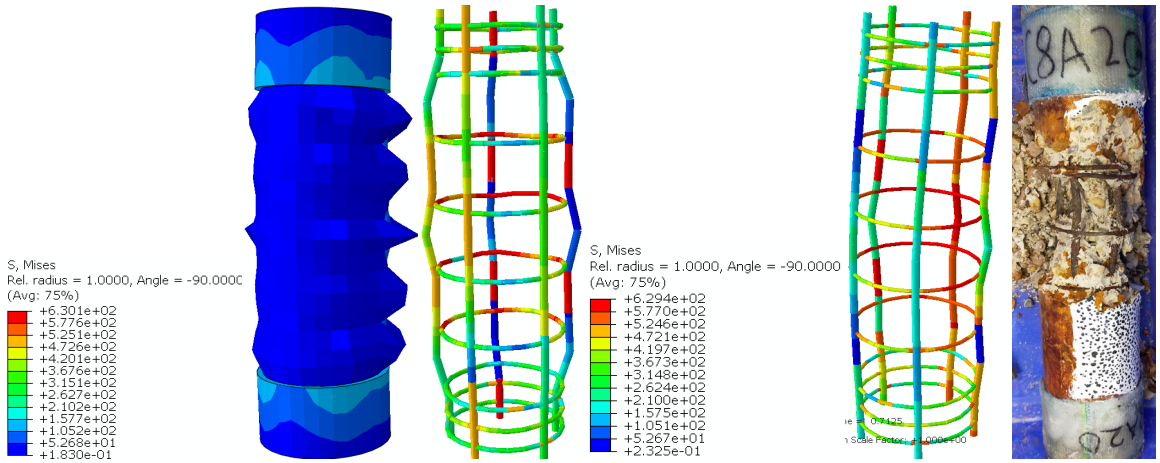


(b) Mediumly confined (*L/D = 8*)

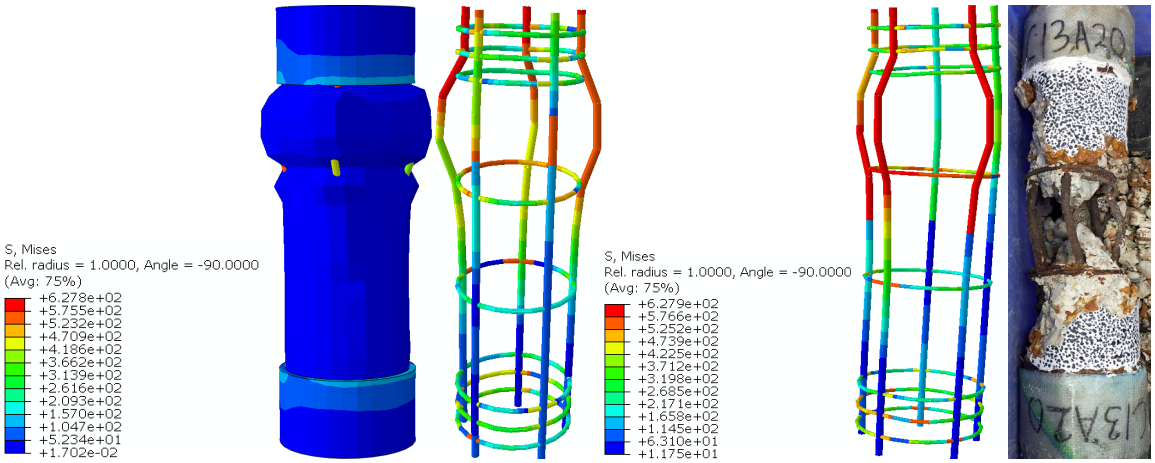


(c) lowly confined (*L/D = 13*)

Figure 6.17. Failure of uncorroded and corroded confined circular columns under axial cyclic compressive loading

### 6.6.4 Axial cyclic stress-strain responses of corroded and uncorroded square columns

Figure 6.18(a-f) presents the stress-strain responses of the confined square RC columns to axial compressive cyclic loading. The loading was applied in the numerical analysis using the experimental test's displacement outputs. The graphs showed an agreement in the load-carrying capacity of the columns between the numerical analysis and experimental results. Similar to the circular columns, the response of the square columns, in the numerical analysis, to the applied displacement load does not match the output from the experimental test as the columns develop tensile stress during the unloading phase of the compressive load application.

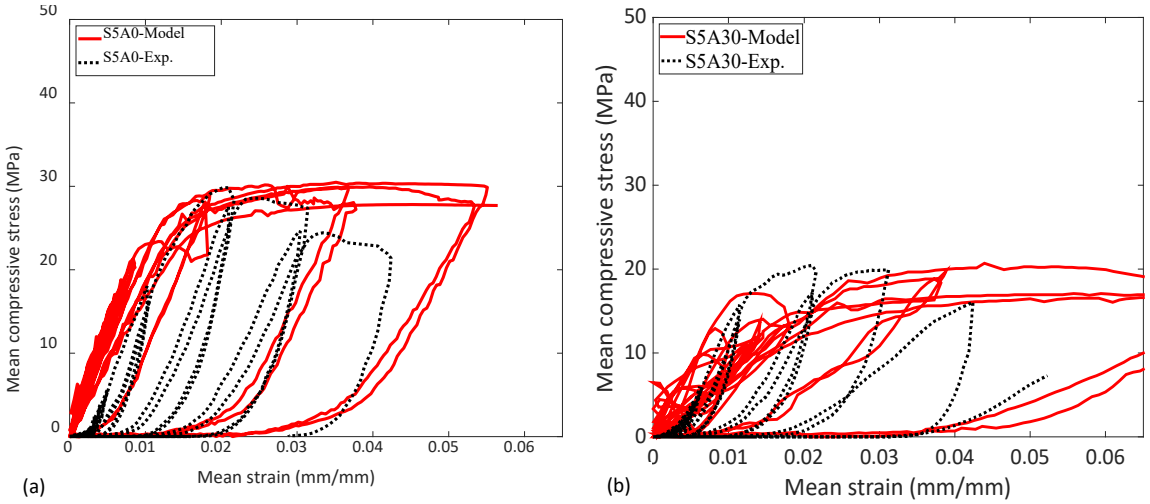

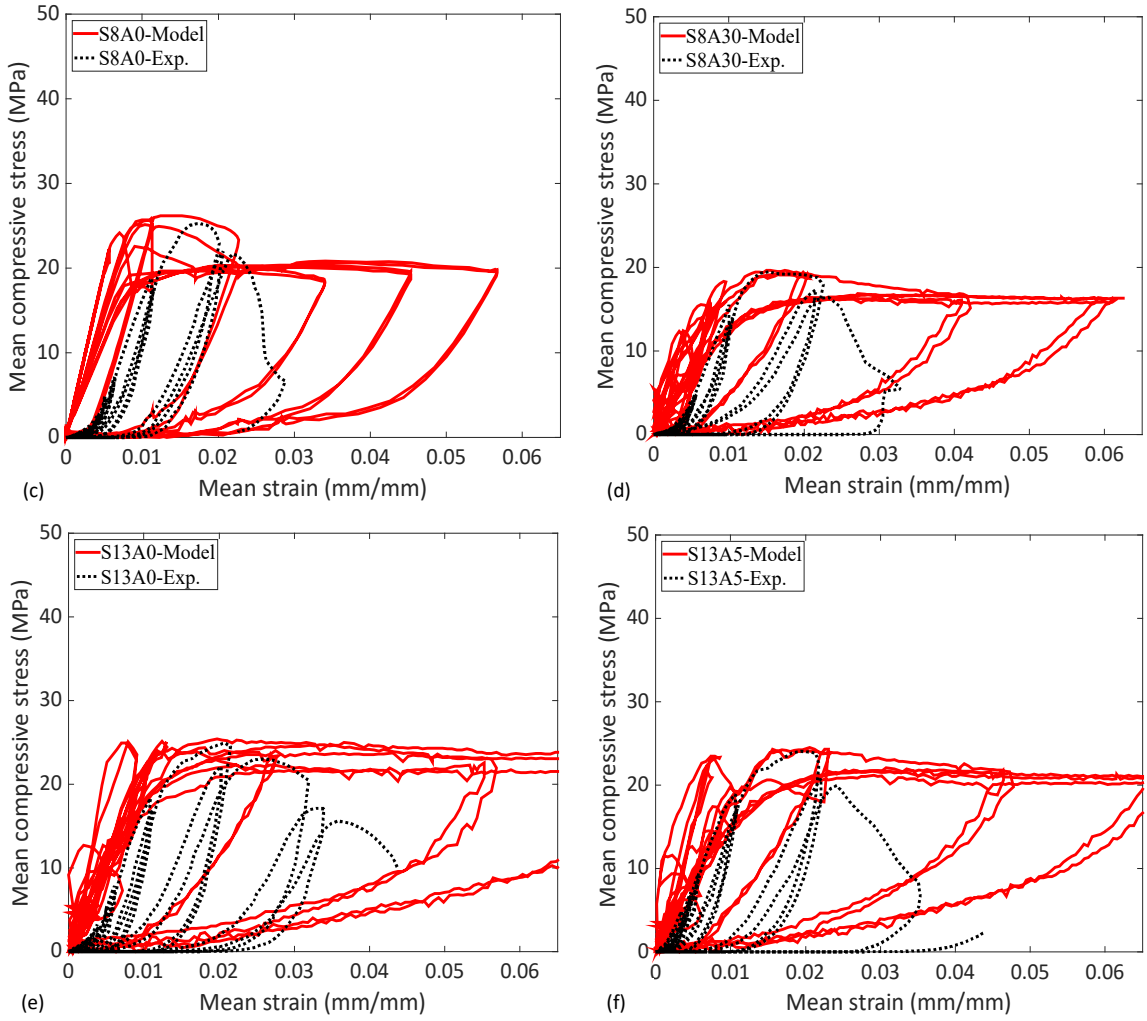


Figure 6.18. Comparing the axial compressive cyclic response of square columns

### 6.6.5 Observed failure modes of corroded and uncorroded square columns under axial cyclic compressive load

The observed failure modes of the RC square columns under axial cyclic compressive load are presented in Figure 6.19(a-c). The figures show the buckling of the longitudinal steel reinforcement of the differently confined RC columns. The highly confined ($L/D$ = 5) (Fig. 6.19(a)) columns buckled in the middle zone in both the pristine (uncorroded) and corroded columns. Additionally, the medium confined ($L/D$ = 8) (Fig. 6.19(b)) and low confined ($L/D$ = 13) (Fig. 6.19(c)) columns experienced buckling failure immediately below the GFRP-wrapped ends of the columns. The buckling is more pronounced due to the inadequate confinement provided by the transverse reinforcement. Nevertheless, the location of the buckling is similar to the observed buckling location of the column during the experimental test.

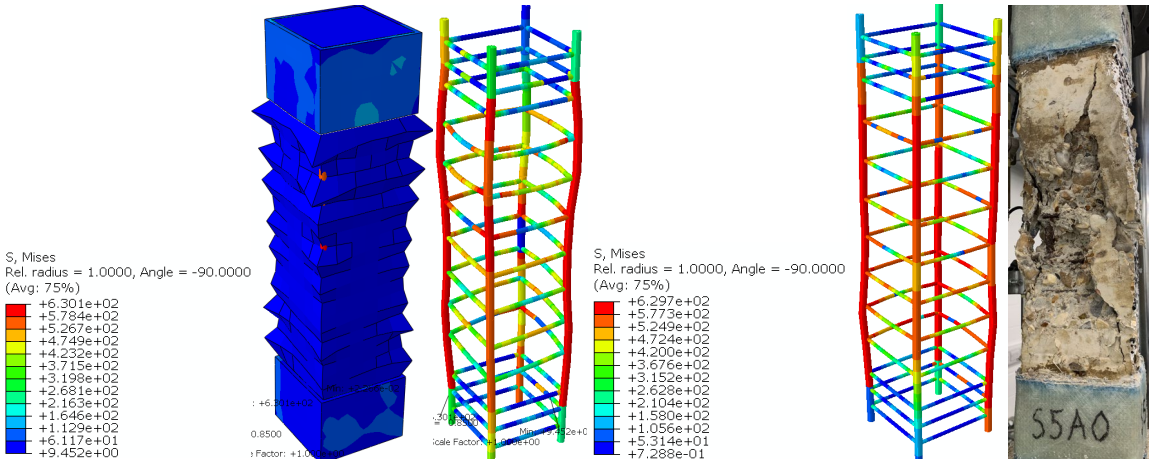


(a) Highly confined (*L/D = 5*)

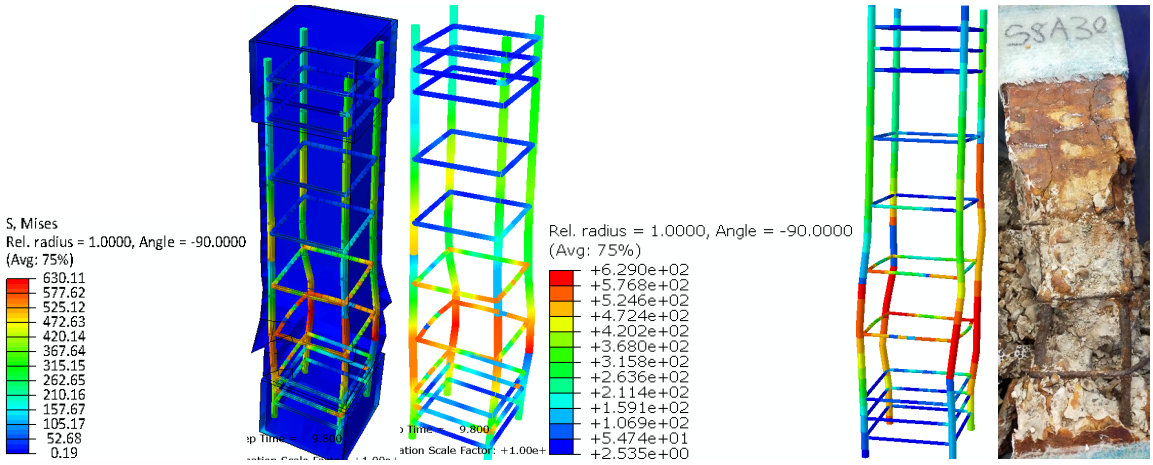


(b) Mediumly confined (*L/D = 8*)

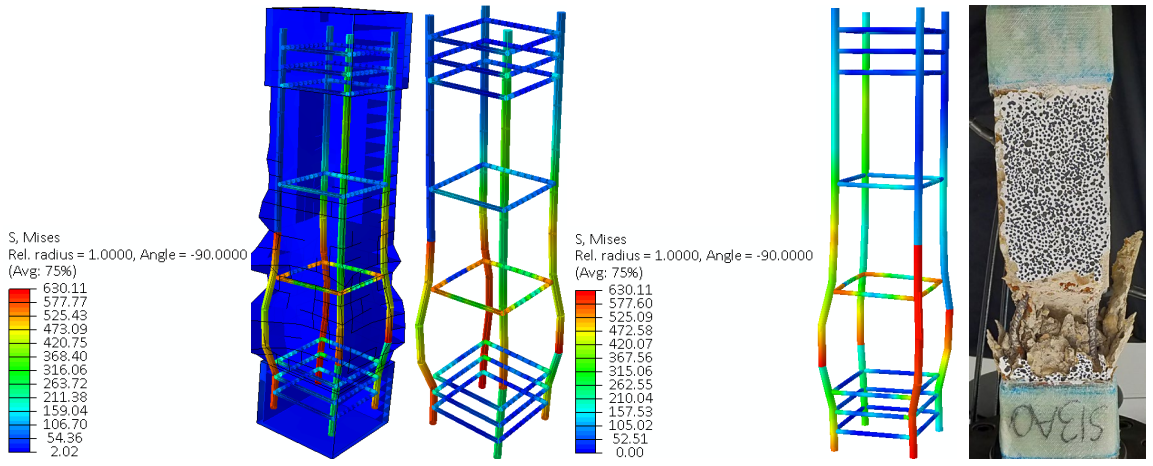


(c) lowly confined (*L/D = 13*)

Figure 6.19. Failure of uncorroded (pristine) and corroded confined square columns under axial cyclic compressive loading

### 6.6.6 Cumulative energy dissipation of the RC columns

The energy dissipation capacity is essential in assessing RC structures' seismic response. Therefore, the cumulative hysteretic dissipation energy was evaluated for the columns analysed,

considering the area of each loading cycle within the hysteretic loop. The cumulative energy dissipated at each loading cycle is normalised against the total energy dissipated at failure. The plots of the normalised accumulated hysteretic energy of the numerical model and experimental data versus the number of cycles are presented in Figures 6.19(a-c) and 6.20(a-c). Figure 6.19(a-c) shows the Influence of corrosion on the accumulated energy dissipation of circular RC columns with different confinement configurations.

In contrast, Figure 6.20(a-c) shows the Impact of corrosion on the accumulated energy dissipation of square RC columns. The plots showed similar behaviour for all the columns, with the numerical analysis having a higher energy dissipated than the experimental data. Also, the numerical data exhibited a higher rate of energy dissipation, especially at the lower cycles than the experimental data. The plots showed a steep increase in the cumulative energy dissipated after the 10th cycle. It should be noted that extensive corrosion significantly reduces the energy dissipated by a column. As such, the highly corroded columns are more likely to have brittle failure than the uncorroded columns (Dai et al., 2021).

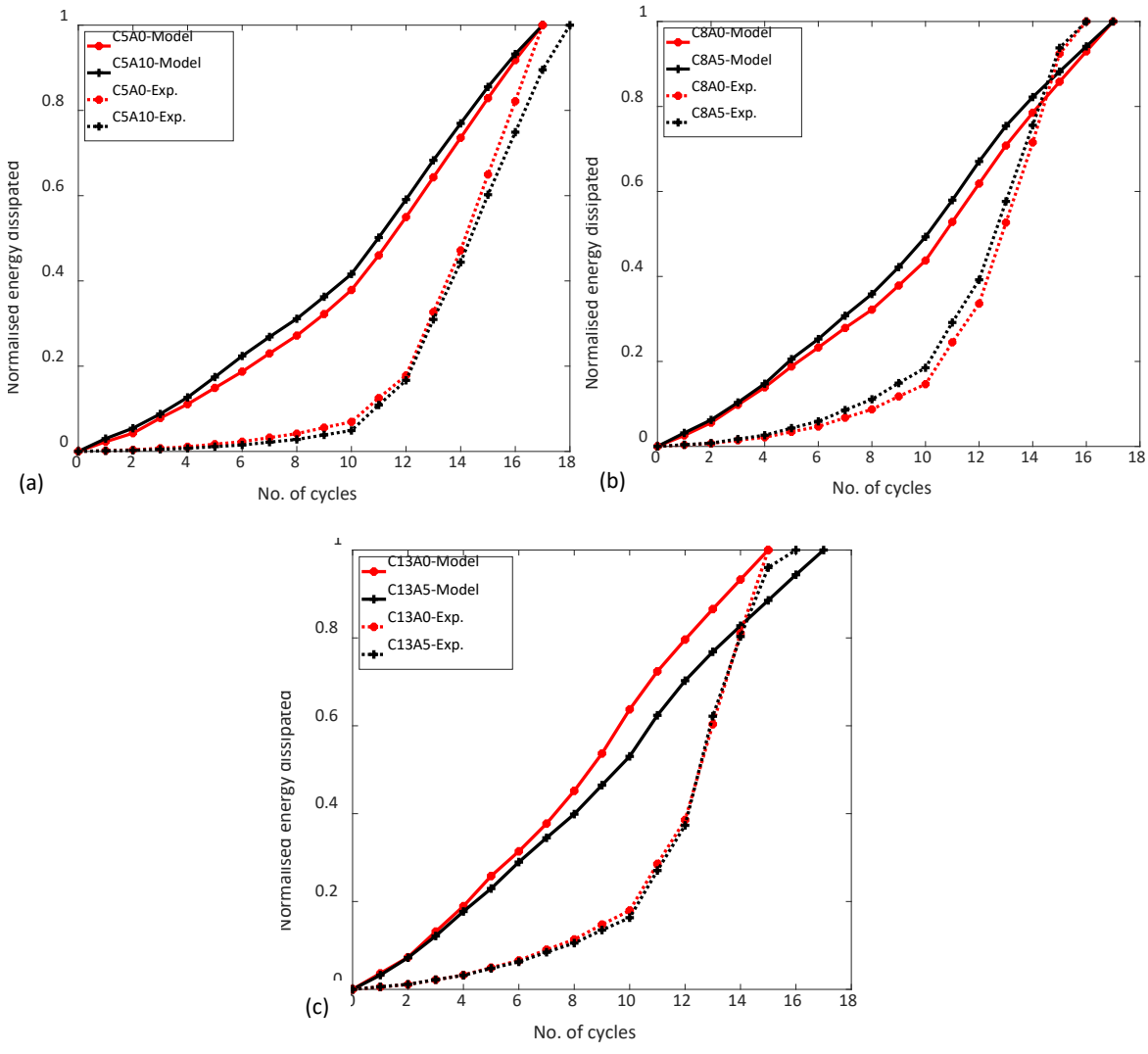

Figure 6.20. Normalised dissipated energy of the uncorroded and corroded circular RC columns; (a) *L/D* = 5, (b) *L/D* = 8 and (c) *L/D* = 13.

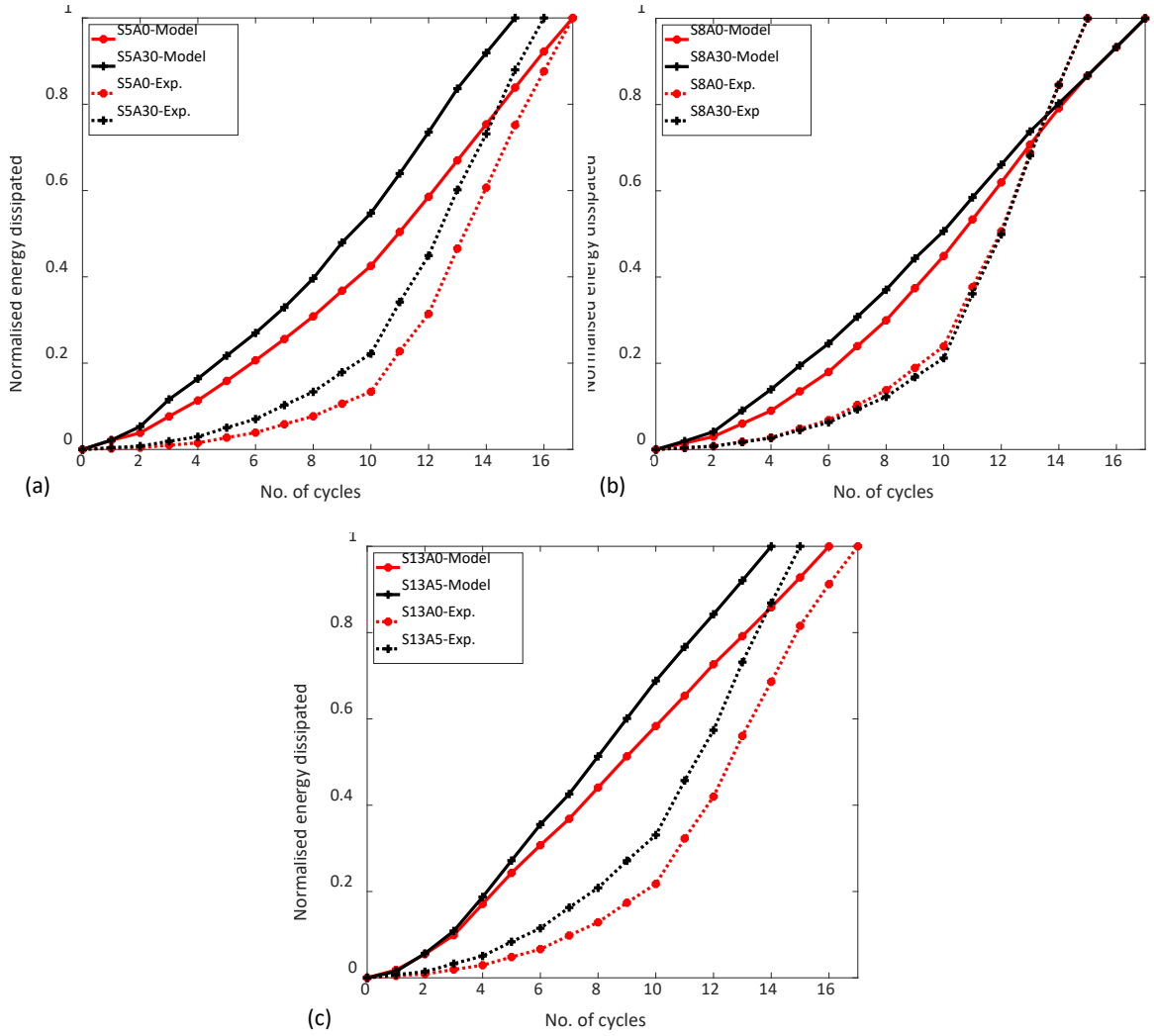


Figure 6.21. Normalised dissipated energy of the uncorroded and corroded square RC columns: (a) *L/D* = 5, (b) *L/D* = 8 and (c) *L/D* = 13.

### 6.6.7 The limitations of the numerical analysis

The axial cyclic compressive analysis aspect of the study has some limitations that affect the behaviour of the analysed corroded RC columns. Some of the limitations are:

i. The accurate simulation of the cyclic loading protocol to reflect loading in compression only. This will require further simulation using the contact protocol in the Abaqus modelling such that the sample is disconnected in the unloading phase of the cyclic loading applications. This will prevent the tension of the sample in the unloading phase.

ii. The corrosion of the reinforcement was presented as general/uniform corrosion by a constant reduction of the cross-sectional area of the rebar. This does not accurately depict the actual corrosion effect on the reinforcement bars, which is primarily non-uniform (pitting). Hence, there is a need to accurately represent the effect of pitting corrosion on the response of the RC columns.

iii. Conducting a parametric study on the response of low-strength RC columns to the effect of size, cross-sections and different axial load ratios.

## 6.7 Conclusions

This chapter presented the numerical modelling (FE) and subsequent numerical investigations of low-strength concrete confined corroded and uncorroded RC columns using the CDPM in ABAQUS software. The numerical results were compared with the experimental results from tests on the same columns under axial monotonic and axial compressive cyclic loadings. The investigation compared the effect of confinement and corrosion on the ultimate strength, axial and cyclic load-carrying capacities of the columns, the failure pattern under load, and the cumulative energy dissipated. Some of the conclusions from the numerical studies are:

1. The numerical model was able to predict the load-carrying capacity of the RC columns correctly and, as a result, matched the experimental data obtained on columns with the same configurations and corrosion mass loss.
2. The circular columns have higher ultimate strength than the square columns, as the circular hoops provide better confinement effects than the square hoops.
3. The numerical data predicts a higher cumulative dissipated energy even at lower loading cycles than the experimental data in all the columns analysed.
4. The numerical analysis was able to accurately predict the location of the buckling of the longitudinal reinforcements in all the columns, which corresponds to the buckling location observed on the columns during the experiments.
5. Having been validated with the experimental data, the numerical model will help in future parametric studies to generate data for developing constitutive models for corrosion-damaged low-strength concrete RC columns.

# Chapter 7 Conclusions and Future Work

## 7.1 Conclusions

The nonlinear stress-strain behaviour of low-strength concrete confined RC columns under axial monotonic and axial cyclic compressive loadings has been investigated. First, previous studies on experimental and numerical investigation of corroded RC columns, including non-destructive, non-contact measurement techniques for corrosion measurements, were reviewed (Chapter 2). Next, the impact of corrosion and confinement on the stress-strain behaviour of low-strength confined corroded RC columns subject to axial monotonic loading was explored experimentally (Chapter 3). Similarly, the impact of corrosion and confinement on the stress-strain behaviour of low-strength confined corroded RC columns subject to axial cyclic compressive loading was explored experimentally (Chapter 4). Next, a non-destructive technique (X-ray CT scan) that accommodates the whole rebar cages was applied to measure the corrosion mass loss and the location of pitting corrosion on the reinforcement bars was identified and presented (Chapter 5). Finally, a numerical (FE) model using the ABAQUS software (Chapter 6) was used to predict the responses of the RC columns and the results compared to the experimental results generated in Chapters 3 (axial monotonic compressive) and 4 (axial cyclic compressive).

The thesis presented the result of the response of ageing low-strength concrete RC columns to both axial and cyclic compressive loading. It also shows the CT scan technique's capability to measure corrosion mass loss in RC structures. Before this work, there was no experimental and numerical investigation into the nonlinear behaviour/response of ageing low-strength concrete confined RC columns/piers despite such structures worldwide. Also, non-destructive techniques have been used mainly for characterising concrete material and investigating the corrosion of single bars embedded in concrete. However, this does not fully reveal the occurrence and distribution of corrosion, especially pitting corrosion on the rebar. Hence, the most significant contribution of this work is that it will enable the accurate measurement of corrosion in RC structures and the location of severe pitting corrosion on the reinforcement bars. This will help develop a more precise and cost-effective maintenance strategy to evaluate and identify structures to be repaired/retrofitted, thus preventing imminent collapse.

The significant detailed technical findings of this thesis are summarised below. However, it should be noted that these conclusions are limited to the specific cases studied in this thesis:

1. Corrosion of reinforcements severely affects RC columns' load-carrying capacity, stiffness, and ductility. This is more significant in ageing low-strength RC concrete where corroded

specimens fail due to fractures of stirrups at corners and buckling of longitudinal reinforcements. Local buckling is more severe for samples with high corrosion rates, and buckling always occurs in areas with more rust products. This is evidence that the local buckling of the rebar is strongly related to its corrosion condition, and the part where the cross-sectional area is weakened by corrosion is more likely to cause buckling of the rebar.

2. The inelastic buckling mechanism of reinforcement bars is affected by non-uniform pitting corrosion. The observed buckling modes showed that the buckling mechanism of corroded bars is a function of the mass loss due to corrosion and the distribution of pits along the bar length. Hence, the bars with more corrosion mass loss experienced more buckling and fracture than columns at low corrosion.
3. Corrosion of transverse confining steel affects the strength and deformability of confined concrete. The effectiveness of confinement reinforcements in confining the core concrete reduces as the corrosion increases in RC structures. The strength of the highly confined circular column was reduced by 5.35%, 15.97%, 27.74%, and 38.11% for the 5%, 10%, 20% and 30% corroded columns to the EC2 estimated uncorroded column. Similarly, the mediumly confined and lowly confined columns have strength reduction varying between 15% to 39% and 17% to 70%, respectively. Furthermore, the adequate confinement of RC columns, especially in the plastic hinge zones, results in less buckling and failure of the RC columns.
4. The degree of corrosion experienced by transverse reinforcement is more severe than longitudinal reinforcements at the same current densities. In the highly confined circular RC columns, the transverse reinforcement corrosion losses are 8.8%, 21.2%, 29.4% and 39.8%, while the longitudinal bars have corrosion losses of 4.1%, 7.3%, 10.8% and 20.6% for the 5%, 10%, 20% and 30% corrosion estimates. This results from the closeness of the transverse bars to the surface of the concrete, leading to a possibly higher concentration of chloride ions and an early start of corrosion of the transverse bars (Q. Li et al., 2022). Similar trends are observed in the other confinement configurations in the circular and square RC columns tested in the axial and cyclic compressive loading.
5. The circular columns have a higher ultimate strain corresponding to the maximum strength of the columns than the square columns, except in some low levels of the confined columns. This results from the uniform confinement of the circular columns, which gives rise to a constant stress distribution of the concrete along the cross-section (Ayough et al., 2021; Colajanni et al., 2014; Liang et al., 2015; Liang & Sritharan, 2018). In contrast, the square columns have their stress concentration at the edges, sometimes leading to the failure of the GFRPs.

6. The circular columns have higher axial cyclic load-carrying capacities, gradually decreasing with increased corrosion and confinement than the square columns. The well-confined circular columns (*L/D*=5) have 41.32MPa, 35.93MPa, 32.04 MPa, 30.66 MPa and 25.92 MPa axial cyclic load carrying capacities for the 0%, 5%, 10%, 20% and 30% corrosion losses respectively. Meanwhile, the square columns with the same confinement and corrosion losses have 29.91MPa, 25.98MPa, 24.44MPa, 22.48MPa and 20.50MPa axial cyclic compressive load-carrying capacities. A similar trend was observed in the medium-confined and low-confined columns. This results from the effectiveness of the transverse ties in the circular column, which has more significant confinement effectiveness coefficients than the square columns.
7. The CT scan was used to accurately estimate the corrosion mass loss of the reinforcement cages in the circular and square columns and agreed well with the more established method. The percentage difference between the measured mass loss and the CT scan measurement in the circular RC columns is 4.86% and 2.62% for the 10% corroded and 30% corroded columns, respectively. Meanwhile, the measured difference in the square columns is 8.04% and 9.63% for the 10% corroded and 30% corroded columns, respectively.
8. The CT scan was used to identify the location of the most severe corrosion (pitting) on the reinforcement cage, which was quite visible in the analysed CT scan images, especially for the transverse rebars. This shows that the CT scan could identify and monitor the development and progression of pitting corrosion on reinforcement bars in RC structures to strengthen and retrofit the RC structure with materials such as fibre-reinforced polymers and steel jackets to prevent collapse.
9. The numerical model was able to predict the load-carrying capacity of the RC columns correctly and, as a result, matched the experimental data obtained on columns with the same confinement configurations and corrosion mass loss. Also, the numerical analysis was able to accurately predict the location of the buckling of the longitudinal reinforcements in all the columns, which corresponds to the buckling location observed on the columns during experimental tests. Furthermore, the numerical models will enable the parametric studies to develop the constitutive models for ageing low-strength concrete confined corroded RC columns.
10. The existing analytical models overestimate the ultimate strength of low-strength confined corroded RC columns. Hence, there is a need for more experimental tests on low-strength concrete structures, especially ageing and old structures located in marine and earthquake-prone environments, to develop a new model that will correctly predict the strength of such columns.

## 7.2 Future work

This research has explored experimentally and numerically the influence of corrosion and transverse reinforcement confinement on some mechanical properties of ageing low-strength concrete RC columns. The work done can further be extended by:

1. Conducting parametric studies to develop constitutive models for low-strength concrete confined RC columns. This will help mitigate the problems associated with ageing RC structures and identify degraded RC structures' maintenance and strengthening needs against premature failure.
2. A full-scale investigation into the effectiveness of CT scan technique to identify and estimate corrosion development and propagation in RC structures. There is a need to investigate the accuracy of the measurements by evaluating the errors propagated in the CT scan measurements.
3. Using FE to analyse the reconstructed CT scanned images of the RC columns. This will be useful in understanding the actual behaviour and responses of the RC columns, especially with measured corrosion under load.
4. Carrying out large-scale experimental tests on ageing low-strength concrete RC elements to investigate the influence of size on the seismic response of old and ageing low-strength RC structures.
5. Since many of these ageing low-strength structures are also located in seismic regions, there is also a need for lateral cyclic tests on low-strength concrete columns. This will help understand their response to seismic load and aid in maintaining and strengthening existing low-strength columns.
6. The shear capacity of concrete columns is an essential mechanical feature for a structure's security and service life performance. However, it could lead to catastrophic consequences if inadequate. Hence, there is a need to investigate the shear strength of concrete columns with low-strength concrete.
7. There is also a need for a comprehensive seismic performance assessment of structural systems (buildings or frames) with low-strength concrete. The evaluation will help propose a suitable retrofitting and strengthening technique for old and ageing structures in earthquake-prone regions.

# Appendix A Corrosion mass loss estimate after cleaning

**Table A.1. Mass loss estimate for circular columns (monotonic)**

| | Longitudinal | | | | Transverse | | | |
|---|---|---|---|---|---|---|---|---|
| | original | final | mass loss | mass loss (%) | original | final | mass loss | mass loss (%) |
| C5B5 | 0.624 | 0.599 | 0.025 | 4.053 | 0.222 | 0.203 | 0.020 | 8.787 |
| C5B10 | 0.624 | 0.578 | 0.046 | 7.309 | 0.222 | 0.175 | 0.047 | 21.223 |
| C5B20 | 0.624 | 0.557 | 0.067 | 10.785 | 0.222 | 0.157 | 0.065 | 29.402 |
| C5B30 | 0.624 | 0.495 | 0.129 | 20.601 | 0.222 | 0.134 | 0.088 | 39.794 |
| C8B5 | 0.624 | 0.593 | 0.031 | 4.896 | 0.222 | 0.193 | 0.029 | 12.946 |
| C8B10 | 0.624 | 0.565 | 0.059 | 9.439 | 0.222 | 0.174 | 0.048 | 21.807 |
| C8B20 | 0.624 | 0.521 | 0.103 | 16.528 | 0.222 | 0.130 | 0.092 | 41.380 |
| C8B30 | 0.624 | 0.493 | 0.130 | 20.887 | 0.222 | 0.090 | 0.132 | 59.557 |
| C13B5 | 0.624 | 0.586 | 0.037 | 5.993 | 0.222 | 0.194 | 0.028 | 12.654 |
| C13B10 | 0.624 | 0.546 | 0.078 | 12.548 | 0.222 | 0.155 | 0.067 | 30.084 |
| C13B20 | 0.624 | 0.523 | 0.100 | 16.082 | 0.222 | 0.140 | 0.083 | 37.193 |
| C13B30 | 0.624 | 0.452 | 0.172 | 27.598 | 0.222 | 0.120 | 0.102 | 45.859 |

**Table A.2. Mass loss estimate for circular columns (cyclic)**

| | Longitudinal | | | | Transverse | | | |
|---|---|---|---|---|---|---|---|---|
| | original | final | mass loss | mass loss (%) | original | final | mass loss | mass loss (%) |
| C5A5 | 0.624 | 0.596 | 0.027 | 4.408 | 0.222 | 0.197 | 0.025 | 11.151 |
| C5A10 | 0.624 | 0.585 | 0.039 | 6.180 | 0.222 | 0.175 | 0.047 | 21.056 |
| C5A20 | 0.624 | 0.534 | 0.090 | 14.383 | 0.222 | 0.138 | 0.084 | 37.860 |
| C5A30 | 0.624 | 0.505 | 0.119 | 19.078 | 0.222 | 0.102 | 0.120 | 54.039 |
| C8A5 | 0.624 | 0.583 | 0.040 | 6.484 | 0.222 | 0.193 | 0.029 | 13.165 |
| C8A10 | 0.624 | 0.563 | 0.061 | 9.797 | 0.222 | 0.170 | 0.052 | 23.536 |
| C8A20 | 0.624 | 0.547 | 0.077 | 12.356 | 0.222 | 0.120 | 0.102 | 46.005 |
| C8A30 | 0.624 | 0.460 | 0.164 | 26.300 | 0.222 | 0.108 | 0.114 | 51.434 |
| C13A5 | 0.624 | 0.572 | 0.052 | 8.259 | 0.222 | 0.188 | 0.034 | 15.478 |
| C13A10 | 0.624 | 0.555 | 0.069 | 11.095 | 0.222 | 0.177 | 0.045 | 20.395 |
| C13A20 | 0.624 | 0.508 | 0.116 | 18.522 | 0.222 | 0.142 | 0.080 | 36.024 |
| C13A30 | 0.624 | 0.476 | 0.148 | 23.651 | 0.222 | 0.110 | 0.113 | 50.679 |

**Table A.3. Mass loss estimate for square columns (monotonic)**

| | Longitudinal | | | | Transverse | | | |
|---|---|---|---|---|---|---|---|---|
| | original | final | mass loss | mass loss (%) | original | final | mass loss | mass loss (%) |
| S5B5 | 0.624 | 0.602 | 0.021 | 3.421 | 0.224 | 0.199 | 0.024 | 10.937 |
| S5B10 | 0.624 | 0.581 | 0.042 | 6.795 | 0.224 | 0.185 | 0.038 | 17.111 |
| S5B20 | 0.624 | 0.538 | 0.086 | 13.754 | 0.224 | 0.141 | 0.083 | 36.981 |
| S5B30 | 0.624 | 0.509 | 0.115 | 18.369 | 0.224 | 0.120 | 0.103 | 46.295 |
| S8B5 | 0.624 | 0.594 | 0.029 | 4.711 | 0.224 | 0.194 | 0.030 | 13.439 |
| S8B10 | 0.624 | 0.563 | 0.061 | 9.818 | 0.224 | 0.181 | 0.042 | 18.913 |
| S8B20 | 0.624 | 0.520 | 0.104 | 16.688 | 0.224 | 0.135 | 0.088 | 39.436 |
| S8B30 | 0.624 | 0.469 | 0.155 | 24.784 | 0.224 | 0.104 | 0.119 | 53.275 |
| S13B5 | 0.624 | 0.585 | 0.039 | 6.202 | 0.224 | 0.197 | 0.026 | 11.757 |
| S13B10 | 0.624 | 0.569 | 0.055 | 8.788 | 0.224 | 0.185 | 0.039 | 17.375 |
| S13B20 | 0.624 | 0.557 | 0.067 | 10.710 | 0.224 | 0.167 | 0.057 | 25.289 |
| S13B30 | 0.624 | 0.498 | 0.126 | 20.178 | 0.224 | 0.156 | 0.068 | 30.292 |

**Table A.4. Mass loss estimate for square columns (cyclic)**

| | Longitudinal | | | | Transverse | | | |
|---|---|---|---|---|---|---|---|---|
| | original | final | mass loss | mass loss (%) | original | final | mass loss | mass loss (%) |
| S5A5 | 0.624 | 0.597 | 0.027 | 4.329 | 0.224 | 0.194 | 0.029 | 13.011 |
| S5A10 | 0.624 | 0.588 | 0.036 | 5.703 | 0.224 | 0.186 | 0.038 | 16.971 |
| S5A20 | 0.624 | 0.548 | 0.076 | 12.128 | 0.224 | 0.142 | 0.081 | 36.360 |
| S5A30 | 0.624 | 0.525 | 0.099 | 15.872 | 0.224 | 0.113 | 0.110 | 49.248 |
| S8A5 | 0.624 | 0.588 | 0.036 | 5.745 | 0.224 | 0.185 | 0.038 | 17.026 |
| S8A10 | 0.624 | 0.569 | 0.055 | 8.784 | 0.224 | 0.183 | 0.040 | 18.031 |
| S8A20 | 0.624 | 0.546 | 0.078 | 12.505 | 0.224 | 0.147 | 0.076 | 34.023 |
| S8A30 | 0.624 | 0.535 | 0.088 | 14.167 | 0.224 | 0.136 | 0.088 | 39.149 |
| S13A5 | 0.624 | 0.587 | 0.037 | 5.913 | 0.224 | 0.198 | 0.025 | 11.347 |
| S13A10 | 0.624 | 0.560 | 0.064 | 10.211 | 0.224 | 0.176 | 0.047 | 21.147 |
| S13A20 | 0.624 | 0.519 | 0.105 | 16.795 | 0.224 | 0.159 | 0.064 | 28.651 |
| S13A30 | 0.624 | 0.472 | 0.152 | 24.369 | 0.224 | 0.115 | 0.108 | 48.498 |

# Appendix B Corrosion estimates from CT scan

**Table B.1. Mass loss estimate of longitudinal bars in circular column**

10% mass loss (before corrosion)

| Nr | Material | Label | Volume | CenterX | CenterY | CenterZ | | |
|---|---|---|---|---|---|---|---|---|
| 1 | Exterior | 0 | 2,543,630.727 | 75.038 | 75.016 | 119.987 | | |
| 2 | Material001 | 1 | 41,808.153 | 74.221 | 75.579 | 121.392 | | |

10% mass loss (After corrosion)

| Nr | Material | Label | Volume | CenterX | CenterY | CenterZ | | |
|---|---|---|---|---|---|---|---|---|
| 1 | Exterior | 0 | 2,402,793.557 | 75.017 | 75.030 | 136.593 | | |
| 2 | Material001 | 1 | 36,939.593 | 75.516 | 74.718 | 137.523 | 4,868.560 | 11.645 |

30% mass loss (before corrosion)

| Nr | Material | Label | Volume | CenterX | CenterY | CenterZ | | |
|---|---|---|---|---|---|---|---|---|
| 1 | Exterior | 0 | 2,389,352.727 | 74.993 | 75.057 | 120.595 | | |
| 2 | Material001 | 1 | 40,214.347 | 76.927 | 73.121 | 121.540 | | |

30% mass loss (After corrosion)

| Nr | Material | Label | Volume | CenterX | CenterY | CenterZ | | |
|---|---|---|---|---|---|---|---|---|
| 1 | Exterior | 0 | 2,375,412.294 | 74.976 | 75.053 | 135.845 | | |
| 2 | Material001 | 1 | 30,435.156 | 78.838 | 72.825 | 136.721 | 9,779.190 | 24.318 |

**Table B.2. Mass loss estimate of transverse bars in circular column**

10% before corrosion

Sample 1

| Nr | Material | Label | Volume | CenterX | CenterY | CenterZ |
|---|---|---|---|---|---|---|
| 1 | Exterior | 0 | 574,916.474 | 74.815 | 74.931 | 52.957 |
| 2 | Material001 | 1 | 21,462.613 | 80.636 | 77.532 | 52.636 |

Sample 2

| Nr | Material | Label | Volume | CenterX | CenterY | CenterZ |
|---|---|---|---|---|---|---|
| 1 | Exterior | 0 | 644,355.615 | 75.196 | 75.082 | 187.445 |
| 2 | Material001 | 1 | 23,182.202 | 70.281 | 73.442 | 187.587 |

10% after corrosion

Sample 1

| Nr | Material | Label | Volume | CenterX | CenterY | CenterZ | | |
|---|---|---|---|---|---|---|---|---|
| 1 | Exterior | 0 | 440,416.317 | 75.277 | 75.260 | 70.178 | | |
| 2 | Material001 | 1 | 17,033.676 | 68.514 | 68.942 | 69.247 | 4,428.937 | 20.636 |

Sample 2

| Nr | Material | Label | Volume | CenterX | CenterY | CenterZ |
|---|---|---|---|---|---|---|
| 1 | Exterior | 0 | 421,999.386 | 74.799 | 74.779 | 203.450 |

| | | | | | | | | | |
|---|---|---|---|---|---|---|---|---|---|
| 2 | Material001 | 1 | 18,508.105 | 80.187 | 80.622 | 203.359 | 4,674.097 | 20.162 | 20.399 |

30% before corrosion

Sample 1

| Nr | Material | Label | Volume | CenterX | CenterY | CenterZ |
|---|---|---|---|---|---|---|
| 1 | Exterior | 0 | 608,829.269 | 74.671 | 75.099 | 188.805 |
| 2 | Material001 | 1 | 24,823.771 | 83.709 | 73.199 | 188.708 |

Sample 2

| Nr | Material | Label | Volume | CenterX | CenterY | CenterZ |
|---|---|---|---|---|---|---|
| 1 | Exterior | 0 | 337,105.971 | 75.141 | 75.238 | 57.247 |
| 2 | Material001 | 1 | 18,688.297 | 72.935 | 71.181 | 56.852 |

30% after corrosion

Sample 1

| Nr | Material | Label | Volume | CenterX | CenterY | CenterZ | | | |
|---|---|---|---|---|---|---|---|---|---|
| 1 | Exterior | 0 | 530,196.195 | 74.843 | 75.157 | 204.199 | | | |
| 2 | Material001 | 1 | 11,966.760 | 83.097 | 69.152 | 204.105 | 12,857.012 | 51.793 | |

Sample 2

| Nr | Material | Label | Volume | CenterX | CenterY | CenterZ | | | |
|---|---|---|---|---|---|---|---|---|---|
| 1 | Exterior | 0 | 384,003.051 | 74.954 | 74.973 | 73.542 | | | |
| 2 | Material001 | 1 | 9,064.875 | 78.035 | 77.209 | 72.719 | 9,623.422 | 51.494 | 51.644 |

**Table B.3. Mass loss estimate of longitudinal bars in square column**

10% mass loss (before corrosion)

| Nr | Material | Label | Volume | CenterX | CenterY | CenterZ |
|---|---|---|---|---|---|---|
| 1 | Exterior | 0 | 1,747,360.243 | 75.043 | 75.045 | 206.445 |
| 2 | Material001 | 1 | 14,668.875 | 72.821 | 72.657 | 207.072 |

10% mass loss (After corrosion)

| Nr | Material | Label | Volume | CenterX | CenterY | CenterZ | | |
|---|---|---|---|---|---|---|---|---|
| 1 | Exterior | 0 | 1,630,514.138 | 75.014 | 74.990 | 219.277 | | |
| 2 | Material001 | 1 | 13,052.415 | 76.389 | 79.481 | 221.125 | 1,616.460 | 11.020 |

30% mass loss (before corrosion)

| Nr | Material | Label | Volume | CenterX | CenterY | CenterZ |
|---|---|---|---|---|---|---|
| 1 | Exterior | 0 | 1,832,513.460 | 74.999 | 75.018 | 209.824 |
| 2 | Material001 | 1 | 14,228.978 | 78.373 | 75.957 | 210.530 |

30% mass loss (After corrosion)

| Nr | Material | Label | Volume | CenterX | CenterY | CenterZ | | |
|---|---|---|---|---|---|---|---|---|
| 1 | Exterior | 0 | 1,853,567.068 | 75.026 | 75.017 | 221.460 | | |
| 2 | Material001 | 1 | 10,422.999 | 74.897 | 76.432 | 223.366 | 3,805.979 | 26.748 |

**Table B.4. Mass loss estimate of transverse bars in square column**

10% before corrosion

Sample 1

| Nr | Material | Label | Volume | CenterX | CenterY | CenterZ |
|---|---|---|---|---|---|---|
| 1 | Exterior | 0 | 490,586.898 | 75.031 | 75.036 | 60.541 |
| 2 | Material001 | 1 | 7,525.282 | 74.634 | 74.283 | 59.857 |

Sample 2

| Nr | Material | Label | Volume | CenterX | CenterY | CenterZ |
|---|---|---|---|---|---|---|
| 1 | Exterior | 0 | 581,903.462 | 75.018 | 75.119 | 159.524 |
| 2 | Material001 | 1 | 11,087.066 | 75.379 | 70.106 | 158.878 |

10% after corrosion

Sample 1

| Nr | Material | Label | Volume | CenterX | CenterY | CenterZ | | |
|---|---|---|---|---|---|---|---|---|
| 1 | Exterior | 0 | 468,712.212 | 75.021 | 74.993 | 70.518 | | |
| 2 | Material001 | 1 | 5,680.243 | 75.344 | 77.632 | 70.585 | 1,845.039 | 24.518 |

Sample 2

| Nr | Material | Label | Volume | CenterX | CenterY | CenterZ | | | |
|---|---|---|---|---|---|---|---|---|---|
| 1 | Exterior | 0 | 533,349.920 | 75.065 | 74.902 | 169.644 | | | |
| 2 | Material001 | 1 | 8,813.035 | 72.597 | 82.471 | 170.070 | 2,274.031 | 20.511 | 22.514 |

30% before corrosion

Sample 1

| Nr | Material | Label | Volume | CenterX | CenterY | CenterZ |
|---|---|---|---|---|---|---|
| 1 | Exterior | 0 | 550,133.775 | 74.863 | 75.058 | 59.627 |
| 2 | Material001 | 1 | 8,971.657 | 84.969 | 73.001 | 59.764 |

Sample 2

| Nr | Material | Label | Volume | CenterX | CenterY | CenterZ |
|---|---|---|---|---|---|---|
| 1 | Exterior | 0 | 631,476.220 | 75.041 | 75.028 | 160.647 |
| 2 | Material001 | 1 | 12,341.847 | 74.211 | 74.851 | 160.221 |

30% after corrosion

Sample 1

| Nr | Material | Label | Volume | CenterX | CenterY | CenterZ | | |
|---|---|---|---|---|---|---|---|---|
| 1 | Exterior | 0 | 503,711.906 | 75.039 | 74.965 | 72.773 | | |
| 2 | Material001 | 1 | 4,565.620 | 73.471 | 81.685 | 72.632 | 4,406.037 | 49.111 |

Sample 2

| Nr | Material | Label | Volume | CenterX | CenterY | CenterZ | | | |
|---|---|---|---|---|---|---|---|---|---|
| 1 | Exterior | 0 | 603,945.967 | 75.018 | 75.028 | 171.151 | | | |
| 2 | Material001 | 1 | 5,987.315 | 75.720 | 74.745 | 171.385 | 6,354.531 | 51.488 | 50.299 |

# Appendix C Concrete material properties for CDPM in ABAQUS FEA

**Table C.1. Compressive behaviour of concrete in circular columns**

| Concrete compressive behaviour | | Concrete compression damage | |
|---|---|---|---|
| Yield stress (MPa) | Inelastic strain | Damage parameter C | Inelastic strain |
| 5.45 | 0 | 0 | 0 |
| 5.899581 | 0 | 0.331269 | 0.004322 |
| 6.305096 | 0 | 0.342663 | 0.004453 |
| 6.677315 | 0 | 0.351425 | 0.004572 |
| 7.075958 | 0 | 0.362069 | 0.0047 |
| 7.555139 | 0 | 0.369901 | 0.004816 |
| 8.020844 | 1.97E-05 | 0.382299 | 0.004951 |
| 8.305162 | 5.65E-05 | 0.395075 | 0.005087 |
| 8.539341 | 0.000116 | 0.414745 | 0.005251 |
| 8.795039 | 0.000249 | 0.439512 | 0.005436 |
| 9.003131 | 0.000405 | 0.465555 | 0.005627 |
| 9.075487 | 0.000539 | 0.540935 | 0.006022 |
| 9.01804 | 0.000732 | 0.562325 | 0.006193 |
| 8.822784 | 0.001071 | 0.574989 | 0.006328 |
| 8.718597 | 0.001284 | 0.586777 | 0.006461 |
| 8.45226 | 0.001656 | 0.599099 | 0.006594 |
| 8.120617 | 0.002055 | 0.610135 | 0.006724 |
| 7.661757 | 0.002514 | 0.622132 | 0.006856 |
| 7.039396 | 0.003048 | 0.631441 | 0.006979 |
| 6.769562 | 0.003422 | 0.637388 | 0.007085 |
| 6.434898 | 0.003822 | 0.644993 | 0.007201 |
| 6.141133 | 0.004208 | 0.652391 | 0.007315 |
| 5.886136 | 0.004572 | 0.661879 | 0.007438 |
| 5.605939 | 0.004951 | 0.668804 | 0.007549 |
| 5.086705 | 0.005436 | 0.676613 | 0.007665 |
| 3.972116 | 0.006193 | 0.684176 | 0.00778 |
| 3.638374 | 0.006594 | 0.691355 | 0.007893 |
| 3.34485 | 0.006979 | 0.697475 | 0.008001 |
| 3.154719 | 0.007315 | 0.704203 | 0.008112 |
| 2.934892 | 0.007665 | 0.712801 | 0.008231 |
| 2.745564 | 0.008001 | 0.72109 | 0.008349 |

**Table C.2. Tensile behaviour of concrete in circular columns**

| Concrete tensile behaviour | | Concrete tensile damage | |
|---|---|---|---|
| Yield stress (MPa) | Inelastic strain | Damage parameter T | Inelastic strain |
| 0.950827 | 0 | 0 | 0 |
| 0.673353 | 0.001962 | 0.291824 | 0.001962 |
| 0.485718 | 0.003925 | 0.489163 | 0.003925 |
| 0.362977 | 0.005887 | 0.618251 | 0.005887 |
| 0.283929 | 0.007849 | 0.701387 | 0.007849 |
| 0.232573 | 0.009812 | 0.755399 | 0.009812 |
| 0.197777 | 0.011774 | 0.791995 | 0.011774 |
| 0.172311 | 0.013736 | 0.818777 | 0.013736 |
| 0.151796 | 0.015699 | 0.840353 | 0.015699 |
| 0.133788 | 0.017661 | 0.859293 | 0.017661 |
| 0.117073 | 0.019623 | 0.876873 | 0.019623 |
| 0.101165 | 0.021585 | 0.893603 | 0.021585 |
| | | 0.909586 | 0.023548 |
| | | 0.924739 | 0.02551 |
| | | 0.938922 | 0.027472 |

**Table C.3. Compressive behaviour of concrete in square columns**

| Concrete compressive behaviour | | Concrete compression damage | |
|---|---|---|---|
| Yield stress (MPa) | Inelastic strain | Damage parameter C | Inelastic strain |
| 6.81 | 0 | 0 | 0 |
| 7.374477 | 0 | 0.331269 | 0.004322 |
| 8.119322 | 0 | 0.342663 | 0.004453 |
| 8.844947 | 0 | 0.351425 | 0.004572 |
| 9.443923 | 0 | 0.362069 | 0.0047 |
| 9.86448 | 0 | 0.369901 | 0.004816 |
| 10.22965 | 0.000027 | 0.382299 | 0.004951 |
| 10.38145 | 0.000056 | 0.395075 | 0.005087 |
| 10.67418 | 0.000115 | 0.414745 | 0.005251 |
| 10.90413 | 0.000198 | 0.439512 | 0.005436 |
| 11.11423 | 0.000289 | 0.465555 | 0.005627 |
| 11.34436 | 0.000538 | 0.540935 | 0.006022 |
| 11.26742 | 0.000816 | 0.562325 | 0.006193 |
| 11.02848 | 0.00107 | 0.574989 | 0.006328 |
| 10.89825 | 0.001283 | 0.586777 | 0.006461 |
| 10.6782 | 0.00153 | 0.599099 | 0.006594 |
| 10.45994 | 0.001777 | 0.610135 | 0.006724 |

| | | | |
|---|---|---|---|
| 10.15077 | 0.002054 | 0.622132 | 0.006856 |
| 9.79591 | 0.002351 | 0.631441 | 0.006979 |
| 9.353914 | 0.00268 | 0.637388 | 0.007085 |
| 8.799245 | 0.003047 | 0.644993 | 0.007201 |
| 8.544602 | 0.003307 | 0.652391 | 0.007315 |
| 8.307341 | 0.00356 | 0.661879 | 0.007438 |
| 8.043622 | 0.003822 | 0.668804 | 0.007549 |
| 7.80727 | 0.004076 | 0.676613 | 0.007665 |
| 7.586323 | 0.004322 | 0.684176 | 0.00778 |
| 7.35767 | 0.004572 | 0.691355 | 0.007893 |
| 7.14807 | 0.004815 | 0.697475 | 0.008001 |
| 6.862483 | 0.005086 | 0.704203 | 0.008112 |
| 6.358381 | 0.005436 | 0.712801 | 0.008231 |
| 5.207795 | 0.006021 | 0.72109 | 0.008349 |

**Table C.4. Tensile behaviour of concrete in square columns**

| Concrete tensile behaviour | | Concrete tensile damage | |
|---|---|---|---|
| Yield stress (MPa) | Inelastic strain | Damage parameter T | Inelastic strain |
| 0.950827 | 0 | 3.02 | 0 |
| 0.673353 | 0.001962 | 2.138692 | 0.000618 |
| 0.485718 | 0.003925 | 1.542728 | 0.001235 |
| 0.362977 | 0.005887 | 1.152881 | 0.001853 |
| 0.283929 | 0.007849 | 0.90181 | 0.00247 |
| 0.232573 | 0.009812 | 0.738695 | 0.003088 |
| 0.197777 | 0.011774 | 0.628176 | 0.003706 |
| 0.172311 | 0.013736 | 0.547293 | 0.004323 |
| 0.151796 | 0.015699 | 0.482133 | 0.004941 |
| 0.133788 | 0.017661 | 0.424935 | 0.005558 |
| 0.117073 | 0.019623 | 0.371845 | 0.006176 |
| 0.101165 | 0.021585 | 0.321319 | 0.006793 |
| | | 0.909586 | 0.007411 |
| | | 0.924739 | 0.008029 |
| | | 0.938922 | 0.008646 |

# List of References


ABAQUS. (2019). *ABAQUS standard user's manual, version 6.14*. Dassault Systèmes, Providence, RI, USA.

Aboutaha, R., Jnaid, F., Sotoud, S., & Tapan, M. (2013). Seismic Evaluation and Retrofit of Deteriorated Concrete Bridge Components [Tech Report]. https://rosap.ntl.bts.gov/view/dot/26113

ACI 318-19. (2019). *Building Code Requirements for Structural Concrete (ACI 318-19): An ACI Standard ; Commentary on Building Code Requirements for Structural Concrete (ACI 318R-19)*. American Concrete Institute. https://books.google.co.uk/books?id=5O_PxQEACAAJ

ACI Committee 222, C. o. M. i. C. (2001). Protection of metals in concrete against corrosion.

Ahamed, A., Nifla, F., Thamboo, J., Asad, M., & Zahra, T. (2022). Finite element modelling of un-corroded and corroded reinforced concrete columns under axial compression: Stirrup corrosion scenario. *Society of Structural Engineers-Sri Lanka: Proceedings of Annual Sessions-2022*, 33-38.

Ahmed, I. (2023). Key Building Design and Construction Lessons from the 2023 Türkiye–Syria Earthquakes. *Architecture*, *3*(1), 104-106. https://www.mdpi.com/2673-8945/3/1/7

Akiyama, M., Frangopol, D. M., & Matsuzaki, H. (2011). Life-cycle reliability of RC bridge piers under seismic and airborne chloride hazards. *Earthquake Engineering & Structural Dynamics*, *40*(15), 1671-1687. https://doi.org/https://doi.org/10.1002/eqe.1108

Akpanyung, K. V., & Loto, R. T. (2019). Pitting corrosion evaluation: a review. *Journal of Physics: Conference Series*, *1378*(2), 022088. https://doi.org/10.1088/1742-6596/1378/2/022088

Al-Amin, S., & Ahsan, R. (2012). Finite Element Modeling of Reinforced Concrete Column under Monotonic Lateral Loads. *International Journal of Computer Applications*, *42*, 53-58. https://doi.org/10.5120/5676-6412

Al-Ostaz, A., Cheng, A., Mullen, C., & Song, C. (2009). Aging Infrastructure: Evaluation, Repair, Improvement and Protection.

Al-Saidy, A. H., Saadatmanesh, H., El-Gamal, S., Al-Jabri, K. S., & Waris, B. M. (2016). Structural behavior of corroded RC beams with/without stirrups repaired with CFRP sheets. *Materials and Structures*, *49*(9), 3733-3747. https://doi.org/10.1617/s11527-015-0751-y

al-Swaidani, A. M., & Aliyan, S. D. (2015). Effect of Adding Scoria as Cement Replacement on Durability-Related Properties. *International Journal of Concrete Structures and Materials*, *9*(2), 241-254. https://doi.org/10.1007/s40069-015-0101-z

Alhusain, M., & Al-Mayah, A. (2021). Three dimensional imaging of reinforcement corrosion using micro-computed tomography: Literature review. *Construction and Building Materials*, *284*, 122813. https://doi.org/https://doi.org/10.1016/j.conbuildmat.2021.122813

Almusallam, T. H., & Alsayed, S. H. (1995). Stress–strain relationship of normal, high-strength and lightweight concrete. *Magazine of Concrete Research*, *47*(170), 39-44. https://doi.org/10.1680/macr.1995.47.170.39

Altoubat, S., Maalej, M., & Shaikh, F. U. A. (2016). Laboratory Simulation of Corrosion Damage in Reinforced Concrete. *International Journal of Concrete Structures and Materials*, *10*(3), 383 - 391. https://doi.org/10.1007/s40069-016-0138-7

Aminulai, H. O., Ferguson, N., & Kashani, M. (2023a). Structural behaviour of axially loaded corroded low-strength RC columns with different confinement ratios. In *Life-Cycle of Structures and Infrastructure Systems* (pp. 3348-3355). CRC Press.

Aminulai, H. O., Ferguson, N., & Kashani, M. (2023b). Structural response of corroded concrete columns with different rebar confinements under cyclic compressive loading. In *Life-Cycle of Structures and Infrastructure Systems* (pp. 3340-3347). CRC Press.

Aminulai, H. O., Robinson, A. F., Ferguson, N. S., & Kashani, M. M. (2023a). Impact of corrosion on axial load capacity of ageing low-strength reinforced concrete columns with different

confinement ratios. *Construction and Building Materials*, *384*, 131355. https://doi.org/https://doi.org/10.1016/j.conbuildmat.2023.131355

Aminulai, H. O., Robinson, A. F., Ferguson, N. S., & Kashani, M. M. (2023b). Nonlinear behaviour of corrosion damaged low-strength short reinforced concrete columns under compressive axial cyclic loading. *Engineering Structures*, *289*, 116245. https://doi.org/https://doi.org/10.1016/j.engstruct.2023.116245

Andisheh, K., Liu, R., Palermo, A., & Scott, A. (2018). Cyclic Behavior of Corroded Fuse-Type Dissipaters for Posttensioned Rocking Bridges. *Journal of Bridge Engineering*, *23*. https://doi.org/10.1061/(ASCE)BE.1943-5592.0001197

Andisheh, K., Scott, A., & Palermo, A. (2016a). Modeling the influence of pitting corrosion on the mechanical properties of steel reinforcement: Modeling the influence of pitting corrosion. *Materials and Corrosion*, *67*. https://doi.org/10.1002/maco.201508795

Andisheh, K., Scott, A., & Palermo, A. (2016b). Seismic Behavior of Corroded RC Bridges: Review and Research Gaps. *International Journal of Corrosion*, *2016*, 1-22. https://doi.org/10.1155/2016/3075184

Andisheh, K., Scott, A., & Palermo, A. (2018). Experimental evaluation of the residual compression strength and ultimate strain of chloride corrosion‐induced damaged concrete. *Structural Concrete*, *20*. https://doi.org/10.1002/suco.201800108

Andisheh, K., Scott, A., & Palermo, A. (2021). Effects of Corrosion on Stress-Strain Behavior of Confined Concrete. *Journal of Structural Engineering*, *147*(7), 04021087. https://doi.org/doi:10.1061/(ASCE)ST.1943-541X.0003005

Andisheh, K., Scott, A., Palermo, A., & Clucas, D. (2019). Influence of chloride corrosion on the effective mechanical properties of steel reinforcement. *Structure and Infrastructure Engineering*, *15*(8), 1036-1048. https://doi.org/10.1080/15732479.2019.1594313

Apostolopoulos, C., Konstantopoulos, G., & Koulouris, K. (2018). Seismic resistance prediction of corroded S400 (BSt420) reinforcing bars. *International Journal of Structural Integrity*, *9*(1), 119-138. https://doi.org/10.1108/IJSI-02-2017-0008

Apostolopoulos, C. A. (2007). Mechanical behavior of corroded reinforcing steel bars S500s tempcore under low cycle fatigue. *Construction and Building Materials*, *21*(7), 1447-1456.

Apostolopoulos, C. A., Demis, S., & Papadakis, V. G. (2013). Chloride-induced corrosion of steel reinforcement – Mechanical performance and pit depth analysis. *Construction and Building Materials*, *38*, 139-146. https://doi.org/https://doi.org/10.1016/j.conbuildmat.2012.07.087

Apostolopoulos, C. A., & Papadopoulos, M. P. (2007). Tensile and low cycle fatigue behavior of corroded reinforcing steel bars S400. *Construction and Building Materials*, *21*(4), 855-864. https://doi.org/https://doi.org/10.1016/j.conbuildmat.2005.12.012

Apostolopoulos, C. A., Papadopoulos, M. P., & Pantelakis, S. G. (2006). Tensile behavior of corroded reinforcing steel bars BSt 500s. *Construction and Building Materials*, *20*(9), 782-789. https://doi.org/https://doi.org/10.1016/j.conbuildmat.2005.01.065

Arya, A. S., Boen, T., & Ishiyama, Y. (2014). *Guidelines for earthquake resistant non-engineered construction*. UNESCO. https://unesdoc.unesco.org/notice?id=p::usmarcdef_0000229059

ASCE. (2021). *2021 Report Card for America's Infrastructure*. https://infrastructurereportcard.org/

ASTM, G.-. (2011). Standard practice for preparing, cleaning, and evaluating corrosion test specimens,. In: ASTM International.

Awd, M., Stern, F., Kampmann, A., Kotzem, D., Tenkamp, J., & Walther, F. (2018). Microstructural characterization of the anisotropy and cyclic deformation behavior of selective laser melted AlSi10Mg structures. *Metals*, *8*(10), 825.

Awd, M., Tenkamp, J., Hirtler, M., Siddique, S., Bambach, M., & Walther, F. (2018). Comparison of Microstructure and Mechanical Properties of Scalmalloy® Produced by Selective Laser Melting and Laser Metal Deposition. *Materials*, *11*(1), 17. https://www.mdpi.com/1996-1944/11/1/17

Ayop, S. S., & Cairns, J. J. (2013). Critical Study of Corrosion Damaged Concrete Structures. *International journal of integrated Engineering*, *5*(2). https://publisher.uthm.edu.my/ojs/index.php/ijie/article/view/737

Ayough, P., Ibrahim, Z., Sulong, N. H. R., & Hsiao, P.-C. (2021). The effects of cross-sectional shapes on the axial performance of concrete-filled steel tube columns. *Journal of Constructional Steel Research*, *176*, 106424. https://doi.org/https://doi.org/10.1016/j.jcsr.2020.106424

Azad, A. K., Ahmad, S., & Al-Gohi, B. H. A. (2010). Flexural strength of corroded reinforced concrete beams. *Magazine of Concrete Research*, *62*(6), 405-414. https://doi.org/10.1680/macr.2010.62.6.405

Azad, A. K., Ahmad, S., & Syed, A. A. (2007). Residual Strength of Corrosion-Damaged Reinforced Concrete Beams. *ACI Materials Journal*, *104*(1). https://doi.org/10.14359/18493

Baek, S., Xue, W., Feng, M. Q., & Kwon, S. (2012). Nondestructive Corrosion Detection in RC Through Integrated Heat Induction and IR Thermography. *Journal of Nondestructive Evaluation*, *31*(2), 181-190. https://doi.org/10.1007/s10921-012-0133-0

Bahraq, A. A., Al-Osta, M. A., Ahmad, S., Al-Zahrani, M. M., Al-Dulaijan, S. O., & Rahman, M. K. (2019). Experimental and Numerical Investigation of Shear Behavior of RC Beams Strengthened by Ultra-High Performance Concrete. *International Journal of Concrete Structures and Materials*, *13*(1), 6. https://doi.org/10.1186/s40069-018-0330-z

Balázs, G. L., Czoboly, O., Lublóy, É., Kapitány, K., & Barsi, Á. (2017). Observation of steel fibres in concrete with Computed Tomography. *Construction and Building Materials*, *140*, 534-541. https://doi.org/https://doi.org/10.1016/j.conbuildmat.2017.02.114

Basdeki, M., Koulouris, K., & Apostolopoulos, C. (2022). Effect of Corrosion on the Hysteretic Behavior of Steel Reinforcing Bars and Corroded RC Columns. *Applied Sciences*, *12*(15), 7451. https://www.mdpi.com/2076-3417/12/15/7451

Bažant, Z., & Kwon, Y. (1994). Failure of slender and stocky reinforced concrete columns: Tests of size effect. *Materials and Structures*, *27*, 79-90.

Bentur, A., Berke, N., & Diamond, S. (1997). *Steel Corrosion in Concrete: Fundamentals and civil engineering practice* (1st Edition ed.). CRC Press. https://doi.org/https://doi.org/10.1201/9781482271898

Biondini, F., Camnasio, E., & Palermo, A. (2014). Lifetime seismic performance of concrete bridges exposed to corrosion. *Structure and Infrastructure Engineering*, *10*(7), 880-900. https://doi.org/10.1080/15732479.2012.761248

Biswas, R., Iwanami, M., Chijiwa1c, N., & Uno, K. (2019). Finite element analysis of RC beams subjected to non-uniform corrosion of steel bars.

Biswas, R. K., Iwanami, M., Chijiwa, N., & Uno, K. (2020). Effect of non-uniform rebar corrosion on structural performance of RC structures: A numerical and experimental investigation. *Construction and Building Materials*, *230*, 116908. https://doi.org/https://doi.org/10.1016/j.conbuildmat.2019.116908

Bossio, A., Monetta, T., Bellucci, F., Lignola, G. P., & Prota, A. (2015). Modeling of concrete cracking due to corrosion process of reinforcement bars. *Cement and Concrete Research*, *71*, 78-92. https://doi.org/https://doi.org/10.1016/j.cemconres.2015.01.010

Boumarafi, A., Abouzied, A., & Masmoudi, R. (2015). Harsh environments effects on the axial behaviour of circular concrete-filled fibre reinforced-polymer (FRP) tubes. *Composites Part B: Engineering*, *83*, 81-87. https://doi.org/https://doi.org/10.1016/j.compositesb.2015.08.054

Broomfield, J. P. (2007). *Corrosion of Steel in Concrete: Understanding, Investigation and Repair* (2nd ed.). Taylor and Francis.

Burstein, G. T., Liu, C., Souto, R. M., & Vines, S. P. (2004). Origins of pitting corrosion. *Corrosion Engineering, Science and Technology*, *39*(1), 25-30. https://doi.org/10.1179/147842204225016859

Cady, P., & Weyers, R. (1983). Chloride Penetration and the Deterioration of Concrete Bridge Decks. *Cement Concrete and Aggregates*, *5*, 81-87.

Cady, P. D., & Weyers, R. E. (1984). Deterioration Rates of Concrete Bridge Decks. *Journal of Transportation Engineering*, *110*(1), 34-44. https://doi.org/doi:10.1061/(ASCE)0733-947X(1984)110:1(34)

Cairns, J., Du, Y., & Law, D. (2008). Structural performance of corrosion-damaged concrete beams. *Magazine of Concrete Research - MAG CONCR RES*, *60*, 359-370. https://doi.org/10.1680/macr.2007.00102

Cao, C., Cheung, M. M. S., & Chan, B. Y. B. (2013). Modelling of interaction between corrosion-induced concrete cover crack and steel corrosion rate. *Corrosion Science*, *69*, 97-109. https://doi.org/https://doi.org/10.1016/j.corsci.2012.11.028

Castel, A., François, R., & Arliguie, G. (2000). Mechanical behaviour of corroded reinforced concrete beams—Part 1: Experimental study of corroded beams. *Materials and Structures*, *33*(9), 539-544. https://doi.org/10.1007/BF02480533

Chandrasekaran, V. (2019). Tomography of reinforced concrete. *Material Design & Processing Communications*, *1*(6), e92. https://doi.org/https://doi.org/10.1002/mdp2.92

Charalambidi, B., Rousakis, T., & Karabinis, A. (2012). *Finite element modeling of reinforced concrete columns seismically strengthened through partial FRP jacketing*.

Chen, E., Berrocal, C. G., Fernandez, I., Löfgren, I., & Lundgren, K. (2020). Assessment of the mechanical behaviour of reinforcement bars with localised pitting corrosion by Digital Image Correlation. *Engineering Structures*, *219*, 110936. https://doi.org/https://doi.org/10.1016/j.engstruct.2020.110936

Chen, W.-F. (2007). *Plasticity in reinforced concrete*. J. Ross Publishing.

Chi, Y., Yu, M., Huang, L., & Xu, L. (2017). Finite element modeling of steel-polypropylene hybrid fiber reinforced concrete using modified concrete damaged plasticity. *Engineering Structures*, *148*, 23-35. https://doi.org/https://doi.org/10.1016/j.engstruct.2017.06.039

Choi, M. H., & Lee, C. H. (2022). Seismic Behavior of Existing Reinforced Concrete Columns with Non-Seismic Details under Low Axial Loads. *Materials (Basel)*, *15*(3). https://doi.org/10.3390/ma15031239

Colajanni, P., Fossetti, M., & Macaluso, G. (2014). Effects of confinement level, cross-section shape and corner radius on the cyclic behavior of CFRCM confined concrete columns. *Construction and Building Materials*, *55*, 379–389. https://doi.org/10.1016/j.conbuildmat.2014.01.035

Coronelli, D., & Gambarova, P. (2004). Structural Assessment of Corroded Reinforced Concrete Beams: Modeling Guidelines. *Journal of Structural Engineering*, *130*(8), 1214-1224. https://doi.org/doi:10.1061/(ASCE)0733-9445(2004)130:8(1214)

Dai, K.-Y., Lu, D.-G., & Yu, X.-H. (2021). Experimental investigation on the seismic performance of corroded reinforced concrete columns designed with low and high axial load ratios. *Journal of Building Engineering*, *44*, 102615. https://doi.org/https://doi.org/10.1016/j.jobe.2021.102615

Darwin, D., Dolan, C. W., & Nilson, A. H. (2016). *Design of concrete structures* (Vol. 2). McGraw-Hill Education New York, NY, USA:.

Dassault Systemes. (2022). *Abaqus*. In Retrieved from https://www.3ds.com/products-services/simulia/products/abaqus/, (Accessed on April 2023)

de Mendonça Filho, F. F., Copuroglu, O., Schlangen, E., & Šavija, B. (2021). Determination of Loss of Reinforcement Due to Corrosion through X-ray Computer Micro-Tomography. *Materials*, *14*(4), 893. https://www.mdpi.com/1996-1944/14/4/893

Deb, S., & Pradhan, B. (2013). A Study on corrosion performance of steel in concrete under accelerated condition. International Conference on Structural Engineering Construction and Management, Kandy, Sri Lanka.

Del Zoppo, M., Di Ludovico, M., Balsamo, A., Prota, A., & Manfredi, G. (2017). FRP for seismic strengthening of shear controlled RC columns: Experience from earthquakes and experimental analysis. *Composites Part B: Engineering*, *129*, 47-57. https://doi.org/https://doi.org/10.1016/j.compositesb.2017.07.028

Dhakal, R. P., & Maekawa, K. (2002). Reinforcement Stability and Fracture of Cover Concrete in Reinforced Concrete Members. *Journal of Structural Engineering*, *128*(10), 1253-1262. https://doi.org/doi:10.1061/(ASCE)0733-9445(2002)128:10(1253)

Di Carlo, F., Meda, A., & Rinaldi, Z. (2017a). Numerical cyclic behaviour of un-corroded and corroded RC columns reinforced with HPFRC jacket. *Composite Structures*, *163*, 432-443. https://doi.org/https://doi.org/10.1016/j.compstruct.2016.12.038

Di Carlo, F., Meda, A., & Rinaldi, Z. (2017b). Numerical evaluation of the corrosion influence on the cyclic behaviour of RC columns. *Engineering Structures*, *153*, 264-278.

Dizaj, E. A., & Kashani, M., M. . (2022). Nonlinear structural performance and seismic fragility of corroded reinforced concrete structures: modelling guidelines. *European Journal of Environmental and Civil Engineering*, *26*(11), 5374-5403 , year = 2022. https://doi.org/10.1080/19648189.2021.1896582

Dizaj, E. A., & Kashani, M. M. (2020). Numerical investigation of the influence of cross-sectional shape and corrosion damage on failure mechanisms of RC bridge piers under earthquake loading. *Bulletin of Earthquake Engineering*, *18*(10), 4939-4961. https://doi.org/10.1007/s10518-020-00883-3

Dizaj, E. A., Madandoust, R., & Kashani, M., M. . (2018). Exploring the impact of chloride-induced corrosion on seismic damage limit states and residual capacity of reinforced concrete structures. *Structure and Infrastructure Engineering*, *14*(6), 714-729 , year = 2018. https://doi.org/10.1080/15732479.2017.1359631

Dizaj, E. A., Salami, M. R., & Kashani, M. (2021). Seismic Vulnerability Assessment of Ageing Reinforced Concrete Structures under Real Mainshock-Aftershock Ground Motions. *Structure and Infrastructure Engineering*. https://doi.org/10.1080/15732479.2021.1919148

Dong, H.-L., Wang, D., Wang, Z., & Sun, Y. (2018). Axial compressive behavior of square concrete columns reinforced with innovative closed-type winding GFRP stirrups. *Composite Structures*, *192*, 115-125. https://doi.org/https://doi.org/10.1016/j.compstruct.2018.02.092

Dong, J., Zhao, Y., Wang, K., & Jin, W. (2017). Crack propagation and flexural behaviour of RC beams under simultaneous sustained loading and steel corrosion. *Construction and Building Materials*, *151*, 208-219. https://doi.org/https://doi.org/10.1016/j.conbuildmat.2017.05.193

Doshvarpassand, S., Wu, C., & Wang, X. (2019). An overview of corrosion defect characterization using active infrared thermography. *Infrared Physics & Technology*, *96*, 366-389. https://doi.org/https://doi.org/10.1016/j.infrared.2018.12.006

du Plessis, A., & Boshoff, W. P. (2019). A review of X-ray computed tomography of concrete and asphalt construction materials. *Construction and Building Materials*, *199*, 637-651. https://doi.org/https://doi.org/10.1016/j.conbuildmat.2018.12.049

du Plessis, A., Broeckhoven, C., Guelpa, A., & le Roux, S. G. (2017). Laboratory x-ray micro-computed tomography: a user guideline for biological samples. *Gigascience*, *6*(6), 1-11. https://doi.org/10.1093/gigascience/gix027

Du, Y., Clark, L. A., & Chan, A., H. C. . (2007). Impact of Reinforcement Corrosion on Ductile Behavior of Reinforced Concrete Beams. *ACI Structural Journal*, *104*(3). https://doi.org/10.14359/18618

Du, Y. G., Clark, L. A., & Chan, A. H. C. (2005). Residual capacity of corroded reinforcing bars. *Magazine of Concrete Research*, *57*(3), 135 –147. https://doi.org/10.1680/macr.2005.57.3.135

Earij, A., Alfano, G., Cashell, K., & Zhou, X. (2017). Nonlinear three–dimensional finite–element modelling of reinforced–concrete beams: Computational challenges and experimental validation. *Engineering Failure Analysis*, *82*, 92-115. https://doi.org/https://doi.org/10.1016/j.engfailanal.2017.08.025

El-Sayed, A. K., Hussain, R. R., & Ahmed, B. S. (2016). Influence of Stirrup Corrosion on Shear Strength of Reinforced Concrete Slender Beams. *ACI Structural Journal*, *113*(6). https://doi.org/10.14359/51689147

El Maaddawy, T., Khaled, S., & Topper, T. (2005). Analytical Model to Predict Nonlinear Flexural Behavior of Corroded Reinforced Concrete Beams. *ACI Structural Journal*, *102*(4), 550 - 559. https://doi.org/10.14359/14559

El Maaddawy, T. A., & Soudki, K. A. (2003). Effectiveness of Impressed Current Technique to Simulate Corrosion of Steel Reinforcement in Concrete. *Journal of Materials in Civil Engineering*, *15*(1), 41-47. https://doi.org/10.1061/(ASCE)0899-1561(2003)15:1(41)

Elbusaefi, A. (2014). The effect of steel bar corrosion on the bond strength of concrete manufactured with cement replacement materials.

Elsener, B., Andrade, C., Gulikers, J., Polder, R., & Raupach, M. (2003). Half-cell potential measurements—Potential mapping on reinforced concrete structures. *Materials and Structures*, *36*(7), 461-471. https://doi.org/10.1007/BF02481526

Erdik, M., Tümsa, M. B. D., Pınar, A., Altunel, E., & Zülfikar, A. C. (2023). *A preliminary report on the February 6, 2023 earthquakes in Türkiye*. Temblor.

Fan, L., & Shi, X. (2022). Techniques of corrosion monitoring of steel rebar in reinforced concrete structures: A review. *Structural Health Monitoring*, *21*(4), 1879-1905. https://doi.org/10.1177/14759217211030911

Fan, L., Tan, X., Zhang, Q., Meng, W., Chen, G., & Bao, Y. (2020). Monitoring corrosion of steel bars in reinforced concrete based on helix strains measured from a distributed fiber optic sensor. *Engineering Structures*, *204*, 110039. https://doi.org/https://doi.org/10.1016/j.engstruct.2019.110039

Feldkamp, L. A., Davis, L. C., & Kress, J. W. (1984). Practical cone-beam algorithm. *Journal of the Optical Society of America A*, *1*(6), 612-619. https://doi.org/10.1364/JOSAA.1.000612

François, R., Laurens, S., & Deby, F. (2018). 1 - Steel Corrosion in Reinforced Concrete. In R. François, S. Laurens, & F. Deby (Eds.), *Corrosion and its Consequences for Reinforced Concrete Structures* (pp. 1-41). Elsevier. https://doi.org/https://doi.org/10.1016/B978-1-78548-234-2.50001-9

Frankel, G. S. (1998). Pitting Corrosion of Metals: A Review of the Critical Factors. *Journal of The Electrochemical Society*, *145*(6), 2186. https://doi.org/10.1149/1.1838615

Gao, Y., Jiang, J., & Wu, K. (2017). Modeling of Ionic Diffusivity for Cement Paste with Solid Mass Fractal Model and Lattice Boltzmann Method. *Journal of Materials in Civil Engineering*, *29*(5), 04016287. https://doi.org/doi:10.1061/(ASCE)MT.1943-5533.0001809

Gao, Y., Zheng, Y., Zhang, J., Wang, J., Zhou, X., & Zhang, Y. (2019). Randomness of critical chloride concentration of reinforcement corrosion in reinforced concrete flexural members in a tidal environment. *Ocean Engineering*, *172*, 330-341. https://doi.org/https://doi.org/10.1016/j.oceaneng.2018.11.038

Gehlen, C., Von Greve-Dierfeld, S., & Osterminsk, K. (2010). Modelling of ageing and corrosion processes in reinforced concrete structures. In C. Maierhofer, H.-W. Reinhardt, & G. Dobmann (Eds.), *Non-Destructive Evaluation of Reinforced Concrete Structures* (Vol. 1, pp. 57-81). Woodhead Publishing. https://doi.org/https://doi.org/10.1533/9781845699536.1.57

Glass, G. K. (2003). 6.07 - Deterioration of Steel Reinforced Concrete. In I. Milne, R. O. Ritchie, & B. Karihaloo (Eds.), *Comprehensive Structural Integrity* (pp. 321-350). Pergamon. https://doi.org/https://doi.org/10.1016/B0-08-043749-4/06140-1

González, A., Norambuena-Contreras, J., Storey, L., & Schlangen, E. (2018a). Effect of RAP and fibers addition on asphalt mixtures with self-healing properties gained by microwave radiation heating. *Construction and Building Materials*, *159*, 164-174. https://doi.org/https://doi.org/10.1016/j.conbuildmat.2017.10.070

González, A., Norambuena-Contreras, J., Storey, L., & Schlangen, E. (2018b). Self-healing properties of recycled asphalt mixtures containing metal waste: An approach through microwave radiation heating. *Journal of Environmental Management*, *214*, 242-251. https://doi.org/https://doi.org/10.1016/j.jenvman.2018.03.001

González, J. A., Andrade, C., Alonso, C., & Feliu, S. (1995). Comparison of rates of general corrosion and maximum pitting penetration on concrete embedded steel reinforcement. *Cement and Concrete Research*, *25*(2), 257-264. https://doi.org/https://doi.org/10.1016/0008-8846(95)00006-2

González, J. A., Feliú, S., Rodríquez, P., López, W., Ramírez, E., Alonso, C., & Andrade, C. (1996). Some questions on the corrosion of steel in concrete. Part II: Corrosion mechanism and monitoring, service life prediction and protection methods. *Materials and Structures*, *29*(2), 97-104. https://doi.org/10.1007/BF02486199

González, J. A., Miranda, J. M., Birbilis, N., & Feliu, S. (2005). Electrochemical Techniques for Studying Corrosion of Reinforcing Steel: Limitations and Advantages. *Corrosion*, *61*(1), 37-50. https://doi.org/10.5006/1.3278158

Gu, X.-L., Dong, Z., Yuan, Q., & Zhang, W.-P. (2020). Corrosion of Stirrups under Different Relative Humidity Conditions in Concrete Exposed to Chloride Environment. *Journal of Materials in Civil Engineering*, *32*(1), 04019329. https://doi.org/doi:10.1061/(ASCE)MT.1943-5533.0003001

Guo, A., Li, H., Ba, X., Guan, X., & Li, H. (2015). Experimental investigation on the cyclic performance of reinforced concrete piers with chloride-induced corrosion in marine environment. *Engineering Structures*, *105*, 1-11. https://doi.org/https://doi.org/10.1016/j.engstruct.2015.09.031

Guohua, X., Haonan, W., & Ozbulut, O. E. (2022). Seismic behavior of multiple reinforcement, high-strength concrete columns: experimental and theoretical analysis. *Earthquake Engineering and Engineering Vibration*, *21*(2), 359-375. https://doi.org/10.1007/s11803-022-2095-2

Hafezolghorani, M., Hejazi, F., Vaghei, R., Bin Jaafar, M. S., & Karimzade, K. (2017). Simplified Damage Plasticity Model for Concrete. *Structural Engineering International*, *27*(1), 68-78. https://doi.org/10.2749/101686616x1081

Hafezolghorani, M., Hejazi, F., Vaghei, R., Jaafar, M. S. B., & Karimzade, K. (2017). Simplified Damage Plasticity Model for Concrete. *Structural Engineering International*, *27*(1), 68-78 https://doi.org/10.2749/101686616X1081

Hanjari, K. Z., Kettil, P., & Lundgren, K. (2011). Analysis of mechanical behavior of corroded reinforced concrete structures. *ACI Structural Journal*, *108*(5), 532-541.

Hany, N. F., Hantouche, E. G., & Harajli, M. H. (2016). Finite element modeling of FRP-confined concrete using modified concrete damaged plasticity. *Engineering Structures*, *125*, 1-14. https://doi.org/https://doi.org/10.1016/j.engstruct.2016.06.047

Hassan, M. R. A., Bakar, M. H. A., Dambul, K., & Adikan, F. R. M. (2012). Optical-Based Sensors for Monitoring Corrosion of Reinforcement Rebar via an Etched Cladding Bragg Grating. *Sensors*, *12*(11), 15820-15826. https://www.mdpi.com/1424-8220/12/11/15820

Heiyantuduwa, R., Alexander, M. G., & Mackechnie, J. R. (2006). Performance of a Penetrating Corrosion Inhibitor in Concrete Affected by Carbonation-Induced Corrosion. *Journal of Materials in Civil Engineering*, *18*(6), 842-850. https://doi.org/doi:10.1061/(ASCE)0899-1561(2006)18:6(842)

Hermanek, P., Rathore, J. S., Aloisi, V., & Carmignato, S. (2018). *Principles of X-ray Computed Tomography , bookTitle= Industrial X-Ray Computed Tomography*. Springer International Publishing. https://doi.org/10.1007/978-3-319-59573-3_2

Horrigmoe, G., & Sand, B. (2002). Residual Strength of Deteriorated and Retrofitted Concrete Structures: A Numerical Approach. IABSE Symposium Report,

Hoshikuma, J., Kawashima, K., Nagaya, K., & Taylor, A. W. (1997). Stress-Strain Model for Confined Reinforced Concrete in Bridge Piers. *Journal of Structural Engineering*, *123*(5), 624 - 633.

Hou, L., Zhou, B., Guo, S., Aslani, F., & Chen, D. (2019). Corrosion behavior and flexural performance of reinforced concrete/ultrahigh toughness cementitious composite (RC/UHTCC) beams under sustained loading and shrinkage cracking. *Construction and Building Materials*, *198*, 278-287. https://doi.org/https://doi.org/10.1016/j.conbuildmat.2018.11.237

Hu, H.-T., Huang, C.-S., Wu, M.-H., & Wu, Y.-M. (2003). Nonlinear analysis of axially loaded concrete-filled tube columns with confinement effect. *Journal of Structural Engineering*, *129*(10), 1322-1329.

Huang, L., Xu, L., Chi, Y., & Xu, H. (2015). Experimental investigation on the seismic performance of steel–polypropylene hybrid fiber reinforced concrete columns. *Construction and Building Materials*, *87*, 16-27.

Instron. (2018). *WAVEMATRIX2*. In Illinois Tool Works Inc. https://www.instron.com/en/products/materials-testing-software/wavematrix2

International Federation for Structural Concrete (fib). (2013). *Fib Model Code for Concrete Structures 2010* (P. Beverly, Ed.). Ernst & Sohn, a Wiley brand. https://books.google.co.uk/books?id=wEUqnwEACAAJ

Jang, B. S., & Oh, B. H. (2010). Effects of non-uniform corrosion on the cracking and service life of reinforced concrete structures. *Cement and Concrete Research*, *40*(9), 1441-1450. https://doi.org/https://doi.org/10.1016/j.cemconres.2010.03.018

Jia, J., Zhao, L., Wu, S., Wang, X., Bai, Y., & Wei, Y. (2020). *Experimental investigation on the seismic performance of low-level corroded and retrofitted reinforced concrete bridge columns with CFRP fabric* (0141-0296). (Engineering Structures, Issue. https://www.sciencedirect.com/science/article/pii/S0141029619338180

Jiang, J., Gao, Y., Sun, W., & Liu, Z. (2016). Multi-scale modeling of the ionic diffusivity of cement-based materials. *Journal of Wuhan University of Technology-Mater. Sci. Ed.*, *31*(1), 123-130. https://doi.org/10.1007/s11595-016-1341-8

Jiang, Y., Jin, Z., Zhao, T., Chen, Y., & Chen, F. (2017). Strain Field of Reinforced Concrete under Accelerated Corrosion by Digital Image Correlation Technique. *Journal of Advanced Concrete Technology*, *15*, 290-299. https://doi.org/10.3151/jact.15.290

Jin, L., Zhang, S., Li, D., Xu, H., Du, X., & Li, Z. (2018). A combined experimental and numerical analysis on the seismic behavior of short reinforced concrete columns with different structural sizes and axial compression ratios. *International Journal of Damage Mechanics*, *27*(9), 1416-1447.

Jones, E. M., & Iadicola, M. A. (2018). A good practices guide for digital image correlation. *International Digital Image Correlation Society*, *10*, 308-312.

Joshi, J., Arora, H. C., & Sharma, U. K. (2015). Structural performance of differently confined and strengthened corroding reinforced concrete columns. *Construction and Building Materials*, *82*, 287-295. https://doi.org/https://doi.org/10.1016/j.conbuildmat.2015.02.056

Junlong, Z., & Dongsheng, L. (2022). Shear-flexural cracking strength of RC beams with external vertical prestressing rebars: Theoretical investigation and numerical simulation. *Advances in Structural Engineering*, *25*(3), 593-610. https://doi.org/10.1177/13694332211060634

Kajastie, N. (2023). *Turkey-Syria earthquakes: Turkish building code updated four years ago*. Available online: https://www.geplus.co.uk/news/turkey-syria-earthquakes-turkish-building-code-updated-four-years-ago-10-02-2023/

Kallias, A. N., & Rafiq, M. I. (2010). Finite element investigation of the structural response of corroded RC beams. *Engineering Structures*, *32*(9), 2984-2994.

Kam, W. Y., Pampanin, S., & Elwood, K. (2011). Seismic performance of reinforced concrete buildings in the 22 February Christchurch (Lyttelton) earthquake. *Bulletin of the New Zealand Society for Earthquake Engineering*, *44*. https://doi.org/10.5459/bnzsee.44.4.239-278

Karabinis, A. I., & Kiousis, P. D. (1996). Strength and Ductility of Rectangular Concrete Columns: A Plasticity Approach. *Journal of Structural Engineering*, *122*(3), 267-274. https://doi.org/doi:10.1061/(ASCE)0733-9445(1996)122:3(267)

Karapetrou, S. T., Fotopoulou, S. D., & Pitilakisa, K. D. (2017). Seismic Vulnerability of RC Buildings under the Effect of Aging. *Procedia Environmental Sciences*, *38*, 461 - 468. https://doi.org/10.1016/j.proenv.2017.03.137

Kashani, M. (2014). *Seismic Performance of Corroded RC Bridge Piers: Development of a Multi-Mechanical Nonlinear Fibre Beam-Column Model* University of Bristol]. United Kingdom.

Kashani, M., Crewe, A. J., & Alexander, N. A. (2013a). Nonlinear cyclic response of corrosion-damaged reinforcing bars with the effect of buckling. *Construction and Building Materials*, *41*, 388-400. https://doi.org/https://doi.org/10.1016/j.conbuildmat.2012.12.011

Kashani, M., Crewe, A. J., & Alexander, N. A. (2013b). Nonlinear stress–strain behaviour of corrosion-damaged reinforcing bars including inelastic buckling. *Engineering Structures*, *48*, 417-429. https://doi.org/https://doi.org/10.1016/j.engstruct.2012.09.034

Kashani, M., Lowes, L. N., Crewe, A. J., & Alexander, N. A. (2015). Phenomenological hysteretic model for corroded reinforcing bars including inelastic buckling and low-cycle fatigue degradation. *Computers & Structures*, *156*, 58-71. https://doi.org/https://doi.org/10.1016/j.compstruc.2015.04.005

Kashani, M., Lowes, L. N., Crewe, A. J., & Alexander, N. A. (2016a). Computational Modelling Strategies for Nonlinear Response Prediction of Corroded Circular RC Bridge Piers. *Advances in Materials Science and Engineering*, *2016*, 2738265.

Kashani, M., Lowes, L. N., Crewe, A. J., & Alexander, N. A. (2016b). Nonlinear fibre element modelling of RC bridge piers considering inelastic buckling of reinforcement. *Engineering Structures*, *116*, 163-177. https://doi.org/https://doi.org/10.1016/j.engstruct.2016.02.051

Kashani, M., Maddocks, J., & Dizaj, E. A. (2019). Residual Capacity of Corroded Reinforced Concrete Bridge Components: State-of-the-Art Review. *Journal of Bridge Engineering*, *24*(7), 1 - 16. https://doi.org/10.1061/(ASCE)BE.1943-5592.0001429.

Kashani, M. M. (2017). Size Effect on Inelastic Buckling Behavior of Accelerated Pitted Corroded Bars in Porous Media. *Journal of Materials in Civil Engineering*, *29*(7), 04017022. https://doi.org/doi:10.1061/(ASCE)MT.1943-5533.0001853

Kashani, M. M., Salami, M. R., Goda, K., & Alexander, N. A. (2018). Non-linear flexural behaviour of RC columns including bar buckling and fatigue degradation. *Magazine of Concrete Research*, *70*(5), 231-247. https://doi.org/10.1680/jmacr.16.00495

Ketcham, R. A., & Carlson, W. D. (2001). Acquisition, optimization and interpretation of X-ray computed tomographic imagery: applications to the geosciences. *Computers & Geosciences*, *27*(4), 381-400. https://doi.org/https://doi.org/10.1016/S0098-3004(00)00116-3

Kett, I. (2009). *Engineered concrete: mix design and test methods*. CRC Press.

Khan, M. U., Ahmad, S., & Al-Gahtani, H. J. (2017). Chloride-Induced Corrosion of Steel in Concrete: An Overview on Chloride Diffusion and Prediction of Corrosion Initiation Time. *International Journal of Corrosion*, *2017*, 5819202. https://doi.org/10.1155/2017/5819202

Kioumarsi, M. M., Hendriks, M., & Geiker, M. R. (2014). Quantification of the interference of localised corrosion on adjacent reinforcement bars in a concrete beam in bending. *Nordic Concrete Research (NCR)*, *49*, 39-57.

Kioumarsi, M. M., Hendriks, M. A., Kohler, J., & Geiker, M. R. (2016). The effect of interference of corrosion pits on the failure probability of a reinforced concrete beam. *Engineering Structures*, *114*, 113-121.

Klewe, T., Strangfeld, C., & Kruschwitz, S. (2021). Review of moisture measurements in civil engineering with ground penetrating radar – Applied methods and signal features. *Construction and Building Materials*, *278*, 122250. https://doi.org/https://doi.org/10.1016/j.conbuildmat.2021.122250

Koleva, D. A., de Wit, J. H. W., van Breugel, K., Lodhi, Z. F., & van Westing, E. (2007). Investigation of Corrosion and Cathodic Protection in Reinforced Concrete: I. Application of Electrochemical Techniques. *Journal of The Electrochemical Society*, *154*(4), P52. https://doi.org/10.1149/1.2436609

Koleva, D. A., Hu, J., Fraaij, A. L. A., Stroeven, P., Boshkov, N., & de Wit, J. H. W. (2006). Quantitative characterisation of steel/cement paste interface microstructure and corrosion phenomena in mortars suffering from chloride attack. *Corrosion Science*, *48*(12), 4001-4019. https://doi.org/https://doi.org/10.1016/j.corsci.2006.03.003

Kong, W., Wei, Y., Wang, S., Chen, J., & Wang, Y. (2020). Research progress on cement-based materials by X-ray computed tomography. *International Journal of Pavement Research and Technology*, *13*(4), 366-375. https://doi.org/10.1007/s42947-020-0119-8

Kruth, J. P., Bartscher, M., Carmignato, S., Schmitt, R., De Chiffre, L., & Weckenmann, A. (2011). Computed tomography for dimensional metrology. *CIRP Annals*, *60*(2), 821-842. https://doi.org/https://doi.org/10.1016/j.cirp.2011.05.006

Kumar, M. K., Rao, P. S., Swamy, B. L. P., & Mouli, C. C. (2012). Corrosion Resistance Performance of Fly Ash Blended Cement Concretes. *International Journal of Research in Engineering and Technology (IJRET)*, *1*(2), 448–454.

Küntz, M., Jolin, M., Bastien, J., Perez, F., & Hild, F. (2006). Digital image correlation analysis of crack behavior in a reinforced concrete beam during a load test. *Canadian Journal of Civil Engineering*, *33*(11), 1418-1425. https://doi.org/10.1139/l06-106

Kwon, S.-J., Xue, H., Feng, M., & Baek, S. (2011). *Nondestructive corrosion detection in concrete through integrated heat induction and IR thermography* (Vol. 7983). SPIE. https://doi.org/10.1117/12.881121

Lai, W. L., Kind, T., & Wiggenhauser, H. (2011). Frequency-dependent dispersion of high-frequency ground penetrating radar wave in concrete. *NDT & E International*, *44*(3), 267-273. https://doi.org/https://doi.org/10.1016/j.ndteint.2010.12.004

Le Minh, H., Khatir, S., Abdel Wahab, M., & Cuong-Le, T. (2021). A concrete damage plasticity model for predicting the effects of compressive high-strength concrete under static and dynamic loads. *Journal of Building Engineering*, *44*, 103239. https://doi.org/https://doi.org/10.1016/j.jobe.2021.103239

Leber, I., & Blakey, F. A. (2017). Some effects of carbon dioxide on mortars and concrete. *ACI Journal*, *28*, 295-308. https://doi.org/10.3989/mc.1957.v07.i079.2151

LeBorgne, M., & Ghannoum, W. (2012). Modeling lateral strength degradation of reinforced concrete columns. The Fifteenth World Conference on Earthquake Engineering,

Lee, C., Bonacci, J. F., Thomas, M. D. A., Maalej, M., Khajehpour, S., Hearn, N. D., Pantazopoulou, S. J., & Sheikh, S. A. (2000). Accelerated corrosion and repair of reinforced concrete columns using carbon fibre reinforced polymer sheets. *Canadian Journal of Civil Engineering*, *27*(5), 941-948.

Lei, G., Han, J., & Dang, F. (2018). Using X-Ray CT Scanning to Study the Failure Mechanism of Concrete under Static and Dynamic Loadings. *Advances in Materials Science and Engineering*, *2018*, 3019158. https://doi.org/10.1155/2018/3019158

Li, J., Gong, J., & Wang, L. (2009). Seismic behavior of corrosion-damaged reinforced concrete columns strengthened using combined carbon fiber-reinforced polymer and steel jacket. *Construction and Building Materials*, *23*(7), 2653-2663. https://doi.org/https://doi.org/10.1016/j.conbuildmat.2009.01.003

Li, J., Markeset, G., & Kioumarsi, M. (2017). Nonlinear FEM Simulation of Structural Performance of Corroded RC Columns subjected to Axial Compression. *Nordic Concrete Research*, *57*(57), 15-22.

Li, P., Ren, Y., Zhou, Y., Zhu, Z., & Chen, Y. (2022). Experimental study on the mechanical properties of corroded RC columns repaired with large rupture strain FRP. *Journal of Building Engineering*, *54*, 104413. https://doi.org/https://doi.org/10.1016/j.jobe.2022.104413

Li, Q., Dong, Z., He, Q., Fu, C., & Jin, X. (2022). Effects of Reinforcement Corrosion and Sustained Load on Mechanical Behavior of Reinforced Concrete Columns. *Materials (Basel)*, *15*(10). https://doi.org/10.3390/ma15103590

Li, Q., Huang, L., Ye, H., Fu, C., & Jin, X. (2020). Mechanical Degradation of Reinforced Concrete Columns Corroded Under Sustained Loads. *International Journal of Civil Engineering*, *18*(8), 883-901. https://doi.org/10.1007/s40999-020-00511-w

Li, Q., Niu, D.-t., Xiao, Q.-h., Guan, X., & Chen, S.-j. (2018). Experimental study on seismic behaviors of concrete columns confined by corroded stirrups and lateral strength prediction. *Construction and Building Materials*, *162*, 704 – 713. https://doi.org/10.1016/j.conbuildmat.2017.09.030

Li, Z., Zhou, X., Ma, H., & Hou, D. (2022). *Advanced Concrete Technology* (2nd ed.). https://doi.org/https://doi.org/10.1002/9781119806219.fmatter

Liang, C.-Y., Chen, C.-C., Weng, C.-C., Yin, S. Y.-L., & Wang, J.-C. (2014). Axial compressive behavior of square composite columns confined by multiple spirals. *Journal of Constructional Steel Research*, *103*, 230-240. https://doi.org/https://doi.org/10.1016/j.jcsr.2014.09.006

Liang, X., Beck, R., & Sritharan, S. (2015). *Understanding the Confined Concrete Behavior on the Response of Hollow Bridge Columns*. C. D. o. Transportation.

Liang, X., & Sritharan, S. (2018). Effects of Confinement in Circular Hollow Concrete Columns. *Journal of Structural Engineering*, *144*(9), 04018159. https://doi.org/doi:10.1061/(ASCE)ST.1943-541X.0002151

Liu, X., Jiang, H., & He, L. (2017). Experimental investigation on seismic performance of corroded reinforced concrete moment-resisting frames. *Engineering Structures*, *153*, 639-652. https://doi.org/https://doi.org/10.1016/j.engstruct.2017.10.034

Lounis, Z., & Amleh, L. (2004). Reliability-based prediction of chloride ingress and reinforcement corrosion of aging concrete bridge decks. In *Life-Cycle Performance of Deteriorating Structures: Assessment, Design and Management* (pp. 113-122).

Luo, X., Cheng, J., Xiang, P., & Long, H. (2020). Seismic behavior of corroded reinforced concrete column joints under low-cyclic repeated loading. *Archives of Civil and Mechanical Engineering*, *20*, 40. https://doi.org/10.1007/s43452-020-00043-z

Lv, H., Zhao, X., Zhan, Y., & Gong, P. (2017). Damage evaluation of concrete based on Brillouin corrosion expansion sensor. *Construction and Building Materials*, *143*, 387-394. https://doi.org/https://doi.org/10.1016/j.conbuildmat.2017.03.122

Ma, G., Li, H., & Hwang, H.-J. (2018). Seismic behavior of low-corroded reinforced concrete short columns in an over 20-year building structure. *Soil Dynamics and Earthquake Engineering*, *106*, 90-100. https://doi.org/https://doi.org/10.1016/j.soildyn.2017.12.006

Ma, J., Yu, L., Li, B., & Yu, B. (2022). Stress–strain model for confined concrete in rectangular columns with corroded transverse reinforcement. *Engineering Structures*, *267*(114710), 1 - 14. https://doi.org/10.1016/j.engstruct.2022.114710

Ma, Y., Che, Y., & Gong, J. (2012). Behavior of corrosion damaged circular reinforced concrete columns under cyclic loading. *Construction and Building Materials*, *29*, 548-556. https://doi.org/https://doi.org/10.1016/j.conbuildmat.2011.11.002

Maire, E., & Withers, P. J. (2014). Quantitative X-ray tomography. *International Materials Reviews*, *59*(1), 1-43. https://doi.org/10.1179/1743280413Y.0000000023

Mander, J. B. (1983). *Seismic design of bridge piers* University of Canterbury]. Christchurch, New Zealand.

Mander, J. B., Priestley, M. J. N., & Park, R. (1988). Theoretical stress-strain model for confined concrete. *Journal of Structural Engineering*, *114*(8), 1804 - 1826.

Markeset, G., Rostam, S., & Klinghoffer, O. (2006). Guide for the use of stainless steel reinforcement in concrete structures.

Matthews, B., Palermo, A., & Scott, A. (2022). Overview of the cyclic response of reinforced concrete members subjected to artificial chloride-induced corrosion. *Structural Concrete*, *n/a*(n/a). https://doi.org/https://doi.org/10.1002/suco.202200365

Meda, A., Mostosi, S., Rinaldi, Z., & Riva, P. (2014). Experimental evaluation of the corrosion influence on the cyclic behaviour of RC columns. *Engineering Structures*, *76*, 112-123. https://doi.org/https://doi.org/10.1016/j.engstruct.2014.06.043

Mínguez, J., Vicente, M. A., & González, D. C. (2019). Pore morphology variation under ambient curing of plain and fiber-reinforced high performance mortar at an early age. *Construction and Building Materials*, *198*, 718-731. https://doi.org/https://doi.org/10.1016/j.conbuildmat.2018.12.010

Mogire, P., Abuodha, S., Mwero, J., & Mang'uriu, G. (2018). The effect of Selected Cement Brands in Kenya on the Critical Penetration Depth of Rust in Reinforced Concrete Water Conveyancing Structures. *International Journal of Scientific and Research Publications (IJSRP)*, *8*. https://doi.org/10.29322/IJSRP.8.11.2018.p8333

Mohammed, A., Almansour, H., & Martín-Pérez, B. (2018). Simplified finite element model for evaluation of ultimate capacity of corrosion-damaged reinforced concrete beam-columns. *International Journal of Advanced Structural Engineering*, *10*(4), 381-400. https://doi.org/10.1007/s40091-018-0204-2

Mohammed, M. K. (2015). *Multi-scale Response of Sustainable Self-compacting Concrete (SCC) to Carbonation and Chloride Penetration* University of Nottingham]. https://books.google.co.uk/books?id=kmEOvwEACAAJ

Monti, G., & Nuti, C. (1992). Nonlinear cyclic behavior of reinforcing bars including buckling. *Journal of Structural Engineering*, *118*(12), 3268-3284.

Monticelli, C., Natali, M. E., Balbo, A., Chiavari, C., Zanotto, F., Manzi, S., & Bignozzi, M. C. (2016). Corrosion behavior of steel in alkali-activated fly ash mortars in the light of their microstructural, mechanical and chemical characterization. *Cement and Concrete Research*, *80*, 60-68. https://doi.org/https://doi.org/10.1016/j.cemconres.2015.11.001

Morshed, A., Mahmood, T., & Begum, M. (2016). Finite Element Modelling of Short Concrete Columns Reinforced with GFRP Bars. *International Journal of Advance Civil Engineering and Technology*, *1*, 1-14.

Neuman, S. (2023). *In Turkey and Syria, outdated building methods all but assured disaster from a quake*. Available online: https://www.npr.org/2023/02/07/1154816277/turkey-syria-earthquake-why-buildings-collapsed

Nguyen, C. V., & Lambert, P. (2018). Effect of current density on accelerated corrosion of reinforcing steel bars in concrete. *Structure and Infrastructure Engineering*, *14*(11), 1535-1546. https://doi.org/10.1080/15732479.2018.1459745

Ni Choine, M., Kashani, M., Lowes, L. N., O'Connor, A., Crewe, A. J., Alexander, N. A., & Padgett, J. E. (2016). Nonlinear dynamic analysis and seismic fragility assessment of a corrosion damaged integral bridge. *International Journal of Structural Integrity*, *7*(2). https://doi.org/10.1108/IJSI-09-2014-0045

Nojavan, A., Schultz, A. E., & Chao, S.-H. (2017). Analytical study of in-plane buckling of longitudinal bars in reinforced concrete columns under extreme earthquake loading. *Engineering Structures*, *134*, 48-60. https://doi.org/https://doi.org/10.1016/j.engstruct.2016.12.003

Ou, Y.-C., & Chen, H.-H. (2014). Cyclic Behavior of Reinforced Concrete Beams with Corroded Transverse Steel Reinforcement. *Journal of Structural Engineering*, *140*(9), 04014050. https://doi.org/doi:10.1061/(ASCE)ST.1943-541X.0000932

Ou, Y.-C., Fan, H.-D., & Nguyen, N. D. (2013). Long-term seismic performance of reinforced concrete bridges under steel reinforcement corrosion due to chloride attack. *Earthquake Engineering & Structural Dynamics*, *42*(14), 2113-2127. https://doi.org/https://doi.org/10.1002/eqe.2316

Ou, Y.-C., Tsai, L.-L., & Chen, H.-H. (2012). Cyclic performance of large-scale corroded reinforced concrete beams. *Earthquake Engineering & Structural Dynamics*, *41*(4), 593-604. https://doi.org/https://doi.org/10.1002/eqe.1145

Ou, Y.-C. O., & Nguyen, D. N. (2014). Plastic Hinge Length of Corroded Reinforced Concrete Beams. *ACI Structural Journal*, *111*(5). https://doi.org/10.14359/51687026

Papadakis, V. G., Vayenas, C. G., & Fardis, M. N. (1989). A reaction engineering approach to the problem of concrete carbonation. *AIChE Journal*, *35*(10), 1639-1650. https://doi.org/https://doi.org/10.1002/aic.690351008

Paulay, T., & Priestley, M. N. (1992). *Seismic design of reinforced concrete and masonry buildings* (Vol. 768). Wiley New York.

Poelman, G., Hedayatrasa, S., Segers, J., Van Paepegem, W., & Kersemans, M. (2020). Multi-scale gapped smoothing algorithm for robust baseline-free damage detection in optical infrared thermography. *NDT & E International*, *112*, 102247. https://doi.org/https://doi.org/10.1016/j.ndteint.2020.102247

Poursaee, A. (2010). Potentiostatic transient technique, a simple approach to estimate the corrosion current density and Stern–Geary constant of reinforcing steel in concrete. *Cement and Concrete Research*, *40*(9), 1451-1458. https://doi.org/https://doi.org/10.1016/j.cemconres.2010.04.006

Prachasaree, W., Limkatanyu, S., Wangapisit, O., & Kraidam, S. (2018). Field Investigation of Service Performance of Concrete Bridges Exposed to Tropical Marine Environment. *International Journal of Civil Engineering*, *16*(12), 1757-1769. https://doi.org/10.1007/s40999-017-0250-3

Pritzl, M. D., Tabatabai, H., & Ghorbanpoor, A. (2014). Laboratory Evaluation of Select Methods of Corrosion Prevention in Reinforced Concrete Bridges. *International Journal of Concrete Structures and Materials*, *8*(3), 201-212. https://doi.org/10.1007/s40069-014-0074-3

Rajagopal, R., Sharma, S., Pillai, R. G., & Subramanian, S. J. (2018). *Assessment of stress-strain behavior of corroded steel reinforcement using digital image correlation (DIC)*. ASTM International.

Rajput, A. S., & Sharma, U. K. (2018a). Corroded reinforced concrete columns under simulated seismic loading. *Engineering Structures*, *171*, 453-463. https://doi.org/https://doi.org/10.1016/j.engstruct.2018.05.097

Rajput, A. S., & Sharma, U. K. (2018b). Seismic Behavior of Under Confined Square Reinforced Concrete Columns. *Structures*, *13*, 26-35. https://doi.org/https://doi.org/10.1016/j.istruc.2017.10.005

Rajput, A. S., Sharma, U. K., & Engineer, K. (2019). Seismic retrofitting of corroded RC columns using advanced composite materials. *Engineering Structures*, *181*, 35-46. https://doi.org/https://doi.org/10.1016/j.engstruct.2018.12.009

Rao, A. S., Lepech, M., D., Kiremidjian, A., S., & Sun, X.-Y. (2017a). Simplified structural deterioration model for reinforced concrete bridge piers under cyclic loading. *Structure and Infrastructure Engineering*, *13*(1), 55-66 , year = 2017. https://doi.org/10.1080/15732479.2016.1198402

Rao, A. S., Lepech, M. D., Kiremidjian, A. S., & Sun, X.-Y. (2017b). Simplified structural deterioration model for reinforced concrete bridge piers under cyclic loading. *Structure and Infrastructure Engineering*, *13*(1), 55-66. https://doi.org/10.1080/15732479.2016.1198402

Raupach, M., & Schießl, P. (2001). Macrocell sensor systems for monitoring of the corrosion risk of the reinforcement in concrete structures. *NDT & E International*, *34*(6), 435-442. https://doi.org/https://doi.org/10.1016/S0963-8695(01)00011-1

Ren, W., Yang, Z., Sharma, R., McDonald, S. A., & Mummery, P. M. (2018). Three-Dimensional In Situ XCT Characterisation and FE Modelling of Cracking in Concrete. *Complexity*, *2018*, 3856584. https://doi.org/10.1155/2018/3856584

Rinaldi, Z., Di Carlo, F., Spagnuolo, S., & Meda, A. (2022). Influence of localised corrosion on the cyclic response of reinforced concrete columns. *Engineering Structures*, *256*, 114037. https://doi.org/https://doi.org/10.1016/j.engstruct.2022.114037

Rodrigues, H., Arêde, A., Varum, H., & Costa, A. G. (2013). Experimental evaluation of rectangular reinforced concrete column behaviour under biaxial cyclic loading. *Earthquake Engineering & Structural Dynamics*, *42*(2), 239-259.

Rodrigues, R., Gaboreau, S., Gance, J., Ignatiadis, I., & Betelu, S. (2021). Reinforced concrete structures: A review of corrosion mechanisms and advances in electrical methods for corrosion monitoring. *Construction and Building Materials*, *269*, 121240. https://doi.org/https://doi.org/10.1016/j.conbuildmat.2020.121240

Rodriguez, J., Ortega, L. M., Aragoncillo, J., Izquierdo, D., & Andrade, C. (2005). Methodology for the Structural Assessment of Concrete Affected by Reinforcement Corrosion. *ACI Symposium Publication*, *229*. https://doi.org/10.14359/14744

Rodriguez, J., Ortega, L. M., & Casal, J. (1997). Load carrying capacity of concrete structures with corroded reinforcement. *Construction and Building Materials*, *11*(4), 239-248. https://doi.org/https://doi.org/10.1016/S0950-0618(97)00043-3

Rodríguez, P., Ramírez, E., & González, J. A. (1994). Methods for studying corrosion in reinforced concrete. *Magazine of Concrete Research*, *46*(167), 81-90. https://doi.org/10.1680/macr.1994.46.167.81

Rueden, C. T., Schindelin, J., Hiner, M. C., DeZonia, B. E., Walter, A. E., Arena, E. T., & Eliceiri, K. W. (2017). ImageJ2: ImageJ for the next generation of scientific image data. *BMC Bioinformatics*, *18*(1), 529. https://doi.org/10.1186/s12859-017-1934-z

Saadah, M., Ashteyat, A., & Murad, Y. (2021). Shear strengthening of RC beams using side near surface mounted CFRP ropes and strips. *Structures*, *32*, 380-390. https://doi.org/https://doi.org/10.1016/j.istruc.2021.03.038

Saatcioglu, M., & Razvi, S. R. (1992). Strength and Ductility of Confined Concrete. *Journal of Structural Engineering*, *118*(6), 1590 - 1607.

Salman, H. M., & Al-Sherrawi, M. H. (2018). Finite Element Modeling of a Reinforced Concrete Column Strengthened with Steel Jacket. *Civil Engineering Journal*.

Šavija, B., Luković, M., Hosseini, S. A. S., Pacheco, J., & Schlangen, E. (2015). Corrosion induced cover cracking studied by X-ray computed tomography, nanoindentation, and energy dispersive X-ray spectrometry (EDS). *Materials and Structures*, *48*(7), 2043-2062. https://doi.org/10.1617/s11527-014-0292-9

Sbartaï, Z. M., Laurens, S., Rhazi, J., Balayssac, J. P., & Arliguie, G. (2007). Using radar direct wave for concrete condition assessment: Correlation with electrical resistivity. *Journal of Applied*

*Geophysics*, *62*(4), 361-374. https://doi.org/https://doi.org/10.1016/j.jappgeo.2007.02.003

Shah, A., & Ribakov, Y. (2011). Recent trends in steel fiber high-strength concrete. *Materials & Design*, *32*, 4122-4151. https://doi.org/10.1016/j.matdes.2011.03.030

Shah, A., & Ribakov, Y. (2012). Evaluation of the hydration of concrete mixtures by ultrasonic testing. *Concrc - Proceedings of Concrete Solutions, 4th International Conference on Concrete Repair*, 299-305. https://doi.org/10.1201/b11570-43

Sharma, S., & Mukherjee, A. (2010). Longitudinal Guided Waves for Monitoring Chloride Corrosion in Reinforcing Bars in Concrete. *Structural Health Monitoring*, *9*(6), 555-567. https://doi.org/10.1177/1475921710365415

Sharma, S., & Mukherjee, A. (2011). Monitoring Corrosion in Oxide and Chloride Environments Using Ultrasonic Guided Waves. *Journal of Materials in Civil Engineering*, *23*(2), 207-211. https://doi.org/doi:10.1061/(ASCE)MT.1943-5533.0000144

Sharma, S., & Mukherjee, A. (2013). Nondestructive Evaluation of Corrosion in Varying Environments Using Guided Waves. *Research in Nondestructive Evaluation*, *24*(2), 63-88. https://doi.org/10.1080/09349847.2012.699609

Shi, J.-j., Sun, W., & Geng, G.-q. (2011). - Steel corrosion in simulated concrete pore solutions using a galvanostatic pulse method. - *Chinese Journal of Engineering*, - *33*(- 6), - 727. https://doi.org/- 10.13374/j.issn1001-053x.2011.06.015

Shomali, A., Mostofinejad, D., & Esfahani, M. R. (2020). Experimental and numerical investigation of shear performance of RC beams strengthened with FRP using grooving method. *Journal of Building Engineering*, *31*, 101409. https://doi.org/https://doi.org/10.1016/j.jobe.2020.101409

Skarżyński, Ł., Kibort, K., & Małachowska, A. (2021). 3D X-ray Micro-CT Analysis of Rebar Corrosion in Reinforced Concrete Subjected to a Chloride-Induced Environment. *Molecules*, *27*(1). https://doi.org/10.3390/molecules27010192

Skarżyński, Ł., Nitka, M., & Tejchman, J. (2015). Modelling of concrete fracture at aggregate level using FEM and DEM based on X-ray µCT images of internal structure. *Engineering Fracture Mechanics*, *147*, 13-35. https://doi.org/https://doi.org/10.1016/j.engfracmech.2015.08.010

Skarżyński, Ł., & Suchorzewski, J. (2018). Mechanical and fracture properties of concrete reinforced with recycled and industrial steel fibers using Digital Image Correlation technique and X-ray micro computed tomography. *Construction and Building Materials*, *183*, 283-299. https://doi.org/https://doi.org/10.1016/j.conbuildmat.2018.06.182

Skarżyński, Ł., & Tejchman, J. (2021). Investigations on fracture in reinforced concrete beams in 3-point bending using continuous micro-CT scanning. *Construction and Building Materials*, *284*, 122796. https://doi.org/https://doi.org/10.1016/j.conbuildmat.2021.122796

Song, H.-W., & Saraswathy, V. (2007). Corrosion Monitoring of Reinforced Concrete Structures - A Review. *International Journal of Electrochemical Science*.

Song, Z., & Lu, Y. (2011). Numerical simulation of concrete confined by transverse reinforcement. *Computers and Concrete*, *8*. https://doi.org/10.12989/cac.2011.8.1.023

Sprung, M. J., Chambers, M., & Smith-Pickel, S. (2018). *Transportation Statistics Annual Report 2018* [Statistical Report]. https://rosap.ntl.bts.gov/view/dot/37861

Stanish, K., Hooton, R. D., & Pantazopoulou, S. J. (1999). Corrosion Effects on Bond Strength in Reinforced Concrete. *ACI Structural Journal*, *96*(6). https://doi.org/10.14359/765

Su, J., Wang, J., Bai, Z., Wang, W., & Zhao, D. (2015). Influence of reinforcement buckling on the seismic performance of reinforced concrete columns. *Engineering Structures*, *103*, 174-188. https://doi.org/https://doi.org/10.1016/j.engstruct.2015.09.007

Sümer, Y., & Aktaş, M. (2015). Defining parameters for concrete damage plasticity model. *Challenge Journal of Structural Mechanics*, *1*(3), 149-155.

Talakokula, V., Bhalla, S., & Gupta, A. (2014). Corrosion assessment of reinforced concrete structures based on equivalent structural parameters using electro-mechanical impedance technique. *Journal of Intelligent Material Systems and Structures*, *25*(4), 484-500. https://doi.org/10.1177/1045389x13498317

The British Standard. (2005). Eurocode 2: Design of concrete structures-part 1–1: general rules and rules for buildings. In (pp. 659-668). London UK: BSI Standards Limited.

The British Standards. (2005). Steel for the reinforcement of concrete — Weldable reinforcing steel — General. In *BS EN 10080:2005*. London, UK: BSI Standards Limited.

The British Standards. (2016). Steel for the reinforcement of concrete — Weldable reinforcing steel — Bar, coil and decoiled product — Specification. In *BS 4449-2005+A3-2016*. London, UK: BSI Standards Limited.

The British Standards. (2020). Metallic materials - Tensile testing - Part 1: Method of test at room temperature. In *BS EN ISO 6892-1:2019*. London, UK: BSI Standards Limited.

Toongoenthong, K., & Maekawa, K. (2005). Multi-mechanical approach to structural performance assessment of corroded RC members in shear. *Journal of Advanced Concrete Technology*, *3*(1), 107-122.

Torres-Acosta, A. A., & Martınez-Madrid, M. (2003). Residual Life of Corroding Reinforced Concrete Structures in Marine Environment. *Journal of Materials in Civil Engineering*, *15*(4), 344-353. https://doi.org/doi:10.1061/(ASCE)0899-1561(2003)15:4(344)

Tuutti, K. (1982). *Corrosion of steel in concrete* (03466906 (ISSN)). (CBI forskning, Issue. http://urn.kb.se/resolve?urn=urn:nbn:se:ri:diva-3051

Van Belleghem, B., Kessler, S., Van den Heede, P., Van Tittelboom, K., & De Belie, N. (2018). Chloride induced reinforcement corrosion behavior in self-healing concrete with encapsulated polyurethane. *Cement and Concrete Research*, *113*, 130-139. https://doi.org/https://doi.org/10.1016/j.cemconres.2018.07.009

Van Steen, C., Wevers, M., & Verstrynge, E. (2017). X-ray computed tomography for the detection of corrosion-induced damage at the reinforcement-concrete interface. 7th Conference on Industrial Computed Tomography (iCT 2017), Leuven, Belgium.

Vecchi, F., & Belletti, B. (2021). Capacity Assessment of Existing RC Columns. *Buildings*, *11*(161), 1 - 19. https://doi.org/10.3390/buildings11040161

Vicente, M. A., González, D. C., & Mínguez, J. (2019). Recent advances in the use of computed tomography in concrete technology and other engineering fields. *Micron*, *118*, 22-34. https://doi.org/10.1016/j.micron.2018.12.003

Vicente, M. A., Mena, Á., Mínguez, J., & González, D. C. (2021). Use of Computed Tomography Scan Technology to Explore the Porosity of Concrete: Scientific Possibilities and Technological Limitations. *Applied Sciences*, *11*(18), 8699. https://www.mdpi.com/2076-3417/11/18/8699

Vicente, M. A., Ruiz, G., González, D. C., Mínguez, J., Tarifa, M., & Zhang, X. (2018). CT-Scan study of crack patterns of fiber-reinforced concrete loaded monotonically and under low-cycle fatigue. *International Journal of Fatigue*, *114*, 138-147. https://doi.org/https://doi.org/10.1016/j.ijfatigue.2018.05.011

Vu, N. S., Yu, B., & Li, B. (2016). Prediction of strength and drift capacity of corroded reinforced concrete columns. *Construction and Building Materials*, *115*, 304 – 318. https://doi.org/10.1016/j.conbuildmat.2016.04.048

Vu, N. S., Yu, B., & Li, B. (2017). Stress-strain model for confined concrete with corroded transverse reinforcement. *Engineering Structures*, *151*, 472 - 487. https://doi.org/10.1016/j.engstruct.2017.08.049

Wallbank, E. J. (1989). The Performance of Concrete in Bridges: a Survey of 200 Highway Bridges.

Wang, L., Zhang, X., Zhang, J., Ma, Y., & Liu, Y. (2015). Effects of stirrup and inclined bar corrosion on shear behavior of RC beams. *Construction and Building Materials*, *98*, 537-546. https://doi.org/https://doi.org/10.1016/j.conbuildmat.2015.07.077

Wang, X., Jin, Z., Liu, J., Chen, F., Feng, P., & Tang, J. (2021). Research on internal monitoring of reinforced concrete under accelerated corrosion, using XCT and DIC technology. *Construction and Building Materials*, *266*, 121018.

Wu, X., Chen, L., Li, H., & Xu, J. (2019). Experimental study of the mechanical properties of reinforced concrete compression members under the combined action of sustained load and corrosion. *Construction and Building Materials*, *202*, 11-22. https://doi.org/https://doi.org/10.1016/j.conbuildmat.2018.12.156

Xi, X., & Yang, S. (2019). Investigating the spatial development of corrosion of corner-located steel bar in concrete by X-ray computed tomography. *Construction and Building Materials*, *221*, 177-189. https://doi.org/https://doi.org/10.1016/j.conbuildmat.2019.06.023

Yang, H., Sun, P., & Deng, Y. (2020). Experiment investigation of the influence of reinforcing bar buckling on seismic behavior of RC columns. *Engineering Structures*, *220*, 110923. https://doi.org/https://doi.org/10.1016/j.engstruct.2020.110923

Yang, S.-Y., Song, X.-B., Jia, H.-X., Chen, X., & Liu, X.-L. (2016). Experimental research on hysteretic behaviors of corroded reinforced concrete columns with different maximum amounts of corrosion of rebar. *Construction and Building Materials*, *121*, 319 – 327. https://doi.org/10.1016/j.conbuildmat.2016.06.002

Ye, Z., Zhang, W., & Gu, X. (2018). Deterioration of shear behavior of corroded reinforced concrete beams. *Engineering Structures*, *168*, 708-720. https://doi.org/https://doi.org/10.1016/j.engstruct.2018.05.023

Yeomans, S. (2004). *Galvanized Steel Reinforcement in Concrete*. Elsevier Science. https://books.google.co.uk/books?id=hbwr0NoovtQC

Yu, L., François, R., Dang, V. H., L'Hostis, V., & Gagné, R. (2015). Structural performance of RC beams damaged by natural corrosion under sustained loading in a chloride environment. *Engineering Structures*, *96*, 30-40. https://doi.org/https://doi.org/10.1016/j.engstruct.2015.04.001

Yu, T., Teng, J. G., Wong, Y. L., & Dong, S. L. (2010a). Finite element modeling of confined concrete-I: Drucker–Prager type plasticity model. *Engineering Structures*, *32*(3), 665-679. https://doi.org/https://doi.org/10.1016/j.engstruct.2009.11.014

Yu, T., Teng, J. G., Wong, Y. L., & Dong, S. L. (2010b). Finite element modeling of confined concrete-II: Plastic-damage model. *Engineering Structures*, *32*(3), 680-691. https://doi.org/https://doi.org/10.1016/j.engstruct.2009.11.013

Yuan, W., Guo, A., & Li, H. (2017). Experimental investigation on the cyclic behaviors of corroded coastal bridge piers with transfer of plastic hinge due to non-uniform corrosion. *Soil Dynamics and Earthquake Engineering*, *102*, 112-123. https://doi.org/10.1016/j.soildyn.2017.08.019

Yuan, W., Guo, A., Yuan, W., & Li, H. (2018). Experimental investigation on cyclic behavior of coastal bridge piers with non-uniform corrosion under biaxial quasi-static loads. *Construction and Building Materials*, *190*, 222-234. https://doi.org/https://doi.org/10.1016/j.conbuildmat.2018.09.151

Yuan, W., Guo, A., Yuan, W., & Li, H. (2018). Shaking table tests of coastal bridge piers with different levels of corrosion damage caused by chloride penetration. *Construction and Building Materials*, *173*, 160-171. https://doi.org/https://doi.org/10.1016/j.conbuildmat.2018.04.048

Zaki, A., Chai, H. K., Aggelis, D. G., & Alver, N. (2015). Non-Destructive Evaluation for Corrosion Monitoring in Concrete: A Review and Capability of Acoustic Emission Technique. *Sensors*, *15*(8), 19069-19101. https://www.mdpi.com/1424-8220/15/8/19069

Zeng, X. (2016). FINITE ELEMENT MODELLING AND ANALYSIS OF CONCRETE CONFINED BY STIRRUPS IN SQUARE RC COLUMNS. *Stavební obzor - Civil Engineering Journal*, *25*. https://doi.org/10.14311/CEJ.2016.03.0017

Zeng, X. (2017). Finite Element Analysis of Square RC Columns Confined by Different Configurations of Transverse Reinforcement. *The Open Civil Engineering Journal*, *11*, 292 - 302.

Zeng, X., Jiang, S.-F., Deng, K., Huang, H., & Cui, E. (2022). Seismic performance of circular RC columns strengthened in flexure using NSM reinforcement and externally bonded BFRP sheets. *Engineering Structures*, *256*, 114033. https://doi.org/https://doi.org/10.1016/j.engstruct.2022.114033

Zhang, M., Ye, G., & van Breugel, K. (2012). Modeling of ionic diffusivity in non-saturated cement-based materials using lattice Boltzmann method. *Cement and Concrete Research*, *42*(11), 1524-1533. https://doi.org/https://doi.org/10.1016/j.cemconres.2012.08.005

Zhang, Q., Zheng, N.-H., Gu, X.-L., Wei, Z.-Y., & Zhang, Z. (2022). Study of the confinement performance and stress-strain response of RC columns with corroded stirrups. *Engineering Structures*, *266*, 114476. https://doi.org/https://doi.org/10.1016/j.engstruct.2022.114476

Zhang, W., Liu, Y., Hu, F., & Gu, X. (2023). Experimental and numerical investigation on seismic performance of corroded RC columns of low-strength concrete. *Bulletin of Earthquake Engineering*, *21*(4), 2103-2140. https://doi.org/10.1007/s10518-022-01593-8

Zhao, J., Sang, Y., & Duan, F. (2019). The state of the art of two‐dimensional digital image correlation computational method. *Engineering reports*, *1*(2), e12038.

Zhong, X., Li, J., Xu, J., Wang, K., Zhu, B., Liu, Y., & Ni, K. (2023). Deterioration of Mechanical Properties of Axial Compression Concrete Columns with Corroded Stirrups Coupling on Load and Chloride. *Applied Sciences*, *13*(4), 2423. https://www.mdpi.com/2076-3417/13/4/2423

Zhou, H., Xu, Y., Peng, Y., Liang, X., Li, D., & Xing, F. (2020). Partially corroded reinforced concrete piers under axial compression and cyclic loading: An experimental study. *Engineering Structures*, *203*, 109880. https://doi.org/https://doi.org/10.1016/j.engstruct.2019.109880

Zhou, Y., Wang, X., Yuan, F., Hu, B., & Zhu, Z. (2023). Seismic retrofitting of coastal structural columns with steel bars locally corroded to fracture using sprayed ECC overlays and FRP jackets. *Composite Structures*, *307*, 116670. https://doi.org/https://doi.org/10.1016/j.compstruct.2023.116670

Zhu, W., & François, R. (2015). Structural performance of RC beams in relation with the corroded period in chloride environment. *Materials and Structures*, *48*(6), 1757-1769. https://doi.org/10.1617/s11527-014-0270-2